

NOVEL STRUCTURED ADSORBER AND OXIDATION CATALYSTS FOR THE REMOVAL OF VOCs IN LOW CONCENTRATION

THÈSE N° 3842 (2007)

PRÉSENTÉE LE 11 JUILLET 2007

À LA FACULTÉ DES SCIENCES DE BASE

Laboratoire de génie de la réaction chimique

SECTION DE GÉNIE ÉLECTRIQUE ET ÉLECTRONIQUE

ÉCOLE POLYTECHNIQUE FÉDÉRALE DE LAUSANNE

POUR L'OBTENTION DU GRADE DE DOCTEUR ÈS SCIENCES

PAR

Kim Martin NIKOLAJSEN

M.Sc. in Engineering, Technical University of Denmark, Kgs. Lyngby, Danemark
et de nationalité danoise

acceptée sur proposition du jury:

Prof. C. Comninellis, président du jury
Dr L. Kiwi-Minsker, Prof. A. Renken, directeurs de thèse
Prof. L. Kershenbaum, rapporteur
Prof. F. Stoessel, rapporteur
Prof. Ph. R. von Rohr, rapporteur



ÉCOLE POLYTECHNIQUE
FÉDÉRALE DE LAUSANNE

Suisse
2007

Acknowledgements

I have worked on this thesis from April 2003 to May 2007 in the Laboratory of Chemical Reaction Engineering (Group of Catalytic Reaction Engineering, since November 2006). First of all I would like to thank Prof. Albert Renken and Dr. MER Liouba Kiwi-Minsker for taking me into their group. I thank you for your advises and the trust you have shown in my work.

Thanks to Prof. Christos Comninellis for having presided the jury and thanks to Prof. Lester Kershenbaum, Prof. Philipp Rudolf von Rohr and Prof. Francis Stoessel for having taken the time to examine.

Thanks to those who have assisted me in the lab. I had the pleasure of working for three months with Sébastien Freymond, who worked as a laboratory apprentice. I wish you the best of luck in your studies Séb. Also thanks to Daniel Imesh and Andrea Brühwiler who did their "Projet de semestre" under my supervision. I couldn't always answer your good questions - so it forced me to learn some things in more detail as well. Thanks to Edi Casali for the BET measurements and your "randonnée trips".

Technical, electronic, computer and administrative problems occur numerous times during a thesis - accept it! and be happy with all the help you can get. Thanks to Bobo and his team of skillful technicians, Gaby and the electricians, PAP for the PC help and thanks to the secretaries: Mme Szuman, Mme Anken, Stéphanie, Vida and Sara.

To everyone in the LGRC team: Pierre, Fabio, Eric, Chrystèle, Pac, Petra, Martin, Marina, Bryan, Hao, Anne-Laure, Natasha, Subbu, Dmitri, Igor and Micaela, thanks for the discussions (professional and non-prof.) as well as the coffees and good moments we have shared.

Thanks to the other members of the k-fêt: Marie-Agnès, Ben, Sophie, Babis, Béa, Justyna, Ilaria, Elena, Gabriele, Erika, Aga, Michal and Blanca, Ben Bioman, Pietro, for the good atmosphere in the cafeteria.

Special thanks to other friends I met around EPFL includes: Elina, Michal Chang, Kris, Andy, Michal Kapalka and Pam.

To the people I owe the most: Mom and Dad, thanks for always believing in me. To Sandra: my wonderful sister (and thanks to Søren for the nice moments and powder we have shared). Thanks to Clara for not crying all the time when I first met you - "Jeg glæder mig til at lære dig bedre at kende". Thanks to Renate, Eric and Wendy who also came to visit and cheer us up when needed.

Special thanks to my lovely wife Lisa: For your love, care, support and all the time we spend together - I cherish it.

The virtuous find delight in mountains, the wise in rivers

-Confucius

Abstract

One possibility for the removal of volatile organic compounds (VOCs) is catalytic oxidation. For the removal of VOCs in low concentration ($\lesssim 3000$ ppmv for propane) it is not possible to sustain the required oxidation temperature over the catalyst without external heating. An approach to overcome this problem is to concentrate the VOC by adsorption, in a "two-step adsorption-incineration" process. This is an unsteady state process in which the VOC laden effluent gas is cleaned by passing it through an adsorber. Once the adsorber is saturated the VOC is desorbed by heating and purging. The concentrated VOC from the desorber can then be oxidized over the catalyst, producing enough heat to sustain the oxidation temperature. Conventional adsorbents have some drawbacks such as tailing during desorption due to the large particle size, high pressure drop and hot-spot formation.

The **objective** of this work was to develop, characterize and test the adsorbent and catalyst, with low resistance to mass transfer resulting from thin films of active material, for the two-step adsorption-incineration process. Both the adsorbent and the oxidation catalysts were supported on sintered metal fibers (SMF). This is a novel, structured support offering several advantages over conventional randomly packed beds:

- Low pressure drop, due to the high porosity of the SMF, which is important where large flow rates and/or high quantities of gas must be treated.
- High thermal conductivity, due to the metallic nature, leading to smaller temperature gradients in the fixed-bed.
- A very high geometric surface area, due to the small fiber size. On the order of $200,000 \text{ m}^2/\text{m}^3$ with a fiber diameter of $20 \mu\text{m}$.

Furthermore, a mathematical model was developed to show the feasibility of the coupling of the two steps in the process.

The **adsorber** was made from a thin, homogeneous film of MFI-type zeolite covering the fibers of the SMF. The film was grown by the seed-film method by hydrothermal treatment. A $3 \mu\text{m}$ film was obtained with 10 wt.% zeolite on the fiber after 24 h synthesis at 125°C . This material had a specific surface area of $30 \text{ m}^2/\text{g}$. The adsorption equilibrium of propane was described well by the Langmuir isotherm and the heat of adsorption was found to be $\Delta H_{ads}^0 = -43.1 \text{ kJ/mol}$.

Isothermal breakthrough curves were measured as a function of temperature and film thickness. A mathematical model, comprised of a tanks-in-series model with a linear driving force (LDF) mass transfer description, successfully described the breakthrough behavior. The overall mass transfer was found to be solely due to diffusion in the zeolite

film. However, the thin films show very low resistance to mass transfer leading to low internal concentration gradients and efficient utilization of the adsorbent. The pressure drop was measured and compared to that of a randomly packed fixed-bed of spheres. The equivalent diameter for a constant volumetric flow rate and superficial cross sectional area was $d_p = 180\ \mu\text{m}$, for a fiber diameter of $d_f = 26\ \mu\text{m}$ at 10 wt.% zeolite loading.

The **oxidation catalysts** were all supported on SMF and cobalt oxide was used as the active phase. Three different groups of catalysts were developed. The support was modified by coating the fibers either with a thin film of fine powder (alumina or catalyst powder) or with a MFI-type zeolite film identical to the adsorbent. The third group was made from cobalt oxide impregnated directly on the oxidized fibers. The latter type of catalyst was found to be the most active during the screening experiments. The base support composition was varied (stainless steel (SS), FeCrAlloy and inconel) to investigate the support effect on the kinetics. The stainless steel and FeCrAlloy supports had similar activities, surpassing that of the inconel supported catalyst, which might be attributed to a Co_3O_4 surface enriched with iron from the support. Between the 1.1 wt.% Co_3O_4 /SMF_{SS} and 1.5 wt.% Co_3O_4 /SMF_{FeCrAlloy} catalyst the FeCrAlloy based had the highest normalized activity at low temperature ($< 310^\circ\text{C}$), low propane mole fraction (0.13 %) and high oxygen mole fraction (16.7 %). The chemical kinetics were determined from a novel and efficient experimental design. The apparent activation energy for this catalyst was found to be $87.5 \pm 2.6\ \text{kJ/mol}$, with reaction orders in propane of 0.38 ± 0.04 and in oxygen of 0.30 ± 0.08 . The catalysts were tested up to 350°C . Mass transfer limitations were absent and the kinetics was described well with the power rate law as compared to the Mars-van Krevelen model.

Catalysts based on Co_3O_4 , supported directly on oxidized SMF, are very active catalysts, simple to prepare, withstand deactivation due to hot-spot formation and show great potential in comparison to the industrial reference catalyst (copper and manganese oxide supported on alumina).

The **adiabatic desorption** process was investigated by mathematical modeling. Simply purging the adsorption bed with the hot exhaust gas from the reactor cannot result in the concentration of the VOC due to the high heat capacity of the fixed-bed. Hence, it will be necessary to use either a high heat carrier like steam, with the adverse effects of drying and separation of water and VOC, or an approach in which the desorber is heated prior to purging the bed, changing the adsorption equilibrium in favor of high gas concentrations. For the latter method, the minimum theoretical propane mole fraction for an autothermal process was found to be 350 ppmv to sustain a catalytic incinerator at 250°C .

Finally, it can be concluded that for the first time zeolite films on SMF were used as structured adsorbents, leading to very low internal mass transfer and increased process efficiency. Furthermore, the advantages of the SMF can be exploited in a catalytic oxidizer, which can be combined with the adsorber to annihilate VOCs in low concentrations. A novel method for the deposition of fine powder catalyst on SMF was also developed for the first time.

Keywords: structured reactor, zeolite coating, sintered metal fibers, adsorption, VOC, structured catalyst, cobalt oxide, total oxidation, adsorption-incineration.

Version abrégée

Une des possibilités pour l'élimination des composés organiques volatils (COV) est l'oxydation catalytique. Pour la destruction des COV en faible concentration ($\lesssim 3000$ ppmv de propane) il n'est pas possible de maintenir la température d'oxydation requise sur le catalyseur sans effectuer un chauffage externe. Une approche contre ce problème est de concentrer les COV par adsorption, dans un procédé d'adsorption-incinération en 2 étapes. Ceci est un procédé non stationnaire où la charge de COV est nettoyée en passant à travers un adsorbant. Une fois que l'adsorbant est saturé, les COV sont désorbés par chauffage et ainsi purgés. Les COV concentrés provenant de cette désorption peuvent ensuite être oxydés sur le catalyseur, produisant suffisamment de chaleur pour maintenir une température suffisante d'oxydation. Les adsorbants conventionnels ont quelques désavantages parmi lesquels on peut citer une faible vitesse de désorption due à de grandes tailles de particules, une perte de charge importante et la formation de "points chauds". L'objectif de ce travail est de développer, caractériser et tester l'adsorbant et le catalyseur, avec une faible résistance au transfert de masse résultant de la fine épaisseur du matériel actif lors d'un procédé d'adsorption-incinération en 2 étapes. L'adsorbant et le catalyseur pour la réaction d'oxydation sont tous deux supportés sur des filtres de fibres métalliques frittées (SMF). Il s'agit d'un support structuré novateur offrant de nombreux avantages par rapport aux lits fixes conventionnels "*randomly packed bed*":

- Faible perte de charges due à la haute porosité des SMF, ce qui est important lorsque des flux élevés et/ou lorsque de grandes quantités de gaz doivent être traités.
- Conductivité thermique élevée, due à la nature métallique du support, amenant un gradient de température faible dans le lit fixe.
- Très grande surface géométrique, due aux faibles dimensions des fibres: de l'ordre de $200,000 \text{ m}^2/\text{m}^3$ avec un diamètre de fibres de $20 \mu\text{m}$.

De plus, un modèle mathématique a été développé afin de montrer la faisabilité du couplage des 2 étapes de ce procédé.

L'adsorbant est fait en un fin film homogène de zéolite de type MFI qui couvre les fibres de SMF. Le film est déposé, par une méthode de pré-déposition de colloïde de zéolite, lors d'un traitement hydrothermal. Une épaisseur de $3 \mu\text{m}$ de film est obtenue avec 10 % en masse de zéolite sur les fibres après 24 h de synthèse à 125°C . Ce matériau possède une surface spécifique de $30 \text{ m}^2/\text{g}$. L'équilibre d'adsorption du propane est bien décrit par l'isotherme de Langmuir. L'enthalpie d'adsorption mesurée vaut $\Delta H_{ads}^0 = -43.1 \text{ kJ/mol}$.

Les courbes de ruptures isothermes sont mesurées en fonction de la température et de l'épaisseur du film. Un modèle mathématique, comprenant un modèle des cuves en série avec une force agissante linéaire "*linear driving force*" de transfert de masse, décrit avec

succès le comportement de la courbe. Il a été montré que le transfert de masse global est dû uniquement à la diffusion dans le film de zéolite. Cependant le film présente une très faible résistance au transfert de masse menant à un faible gradient de concentration interne et à une utilisation efficace de l'adsorbant. La perte de charge a été mesurée et comparée à celle provoquée dans un lit fixe rempli de sphères. Le diamètre équivalent pour un flux volumétrique et une section libre constants est $d_p = 180 \mu\text{m}$, pour une fibre de $d_f = 26 \mu\text{m}$ et une déposition de 10 % en masse de zéolite.

Les catalyseurs d'oxydation sont tous supportés sur des SMF et de l'oxyde de cobalt est utilisé comme phase active. Trois différents groupes de catalyseurs ont été développés. Le support est modifié en recouvrant chaque fibre avec une fine couche de poudre (alumine ou catalyseur en poudre) ou avec une couche de zéolite type MFI semblable à celle de l'adsorbant. Le troisième groupe est fait d'oxyde de cobalt imprégné directement sur les fibres oxydées. Ce dernier type de catalyseur est mesuré comme étant le plus actif durant les expériences de sélection. La composition du support de base est variée (acier inox (SS), FeCrAlloy et inconel) afin d'étudier l'effet du support sur la cinétique d'oxydation. L'acier inox et le FeCrAlloy montrent des activités similaires dépassant celle de l'inconel supporté, ce qui peut être attribué à la surface Co_3O_4 enrichie de fer dans ces premiers supports. Entre les catalyseurs 1.1 wt.% Co_3O_4 /SMF_{SS} et 1.5 wt.% Co_3O_4 /SMF_{FeCrAlloy}, le FeCrAlloy a montré la plus haute activité normalisée à faible température ($< 310^\circ\text{C}$), la plus faible fraction molaire de propane (0.13 %) et la plus haute concentration d'oxygène (16.7 %). La cinétique chimique est déterminée par un plan d'expérience novateur et efficace. L'énergie d'activation apparente pour ce catalyseur est de $87.5 \pm 2.6 \text{ kJ/mol}$ avec un ordre de réaction du propane de 0.38 ± 0.04 et de 0.30 ± 0.08 pour l'oxygène. Le catalyseur a été testé à une température supérieure à 350°C . Les limitations dues au transfert de masse sont absentes et la cinétique est très bien décrite par une loi de puissance comparée au modèle de Mars-van Krevelen.

Les catalyseurs à base de Co_3O_4 , supportés directement sur les filtres SMF oxydés, sont très actifs, simples à préparer, résistants à la désactivation due à la formation de "points chauds" et démontrent un grand potentiel en comparaison des catalyseurs industriels de référence (oxyde de cuivre et de manganèse supportés sur de l'alumine).

Le procédé d'adsorption adiabatique a été étudié par une modélisation mathématique. Une simple purge du lit d'adsorption avec un gaz chaud d'échappement du réacteur ne peut avoir de conséquence sur la concentration de COV à cause de la capacité thermique élevée du lit fixe. Il est donc nécessaire d'utiliser un gaz à plus haute capacité calorifique comme la vapeur, avec le désavantage de devoir sécher et séparer l'eau et les COV, ou une autre approche où l'adsorbant est chauffé au préalable afin de purger le lit, en changeant l'équilibre d'adsorption en faveur d'une plus haute concentration dans le gaz. Pour cette dernière méthode, la fraction molaire de propane théorique minimum pour un fonctionnement autotherme doit être de 350 ppmv afin de maintenir l'oxydation catalytique à 250°C .

Finalement, il peut être conclu que pour la première fois, une couche de zéolite sur des filtres SMF a été utilisée comme structure d'adsorbant, menant à un transfert de masse interne très faible et une augmentation de l'efficacité du procédé. De plus, les avantages des SMF peuvent être exploités lors de l'oxydation catalytique, qui peut être combinée avec l'adsorbant pour annihiler les COV en faibles concentrations. Une nouvelle méthode de déposition de fines couches de poudre catalytique a également été développée.

Mots-clés: réacteur structuré, couche de zéolite, fibres métallique frittées, adsorption, COV, catalyseur structuré, oxyde de cobalt, oxydation totale, adsorption-incinération.

Contents

Acknowledgements	i
Abstract	v
Version Abregée	vii
Contents	ix
Nomenclature	xiii
1 Introduction	1
1.1 VOC Emissions	1
1.2 VOC Removal Techniques	3
1.3 Heterogeneous Catalysis	4
1.4 Structured Materials	5
1.5 Objectives	6
2 Theory	7
2.1 VOC Removal by Two-Step Adsorption - Incineration	7
2.1.1 One-Fixed-Bed-Systems	7
2.1.2 Two-Fixed-Bed-Systems	8
2.2 Structured Fibrous Supports and Catalysts	10
2.2.1 Introduction	10
2.2.2 Comparison Between Conventional and Structured Catalysts	11
2.2.3 Fibrous Structured Materials	11
2.2.4 Metallic Fibrous Materials	12
2.3 Adsorption	14
2.3.1 Activated Carbon Compared to Zeolites	15
2.3.2 MFI-zeolites	17
2.3.3 Zeolite Film Synthesis on Structured Surfaces	19
2.3.4 Small- and Micro-Scale Zeolite Film Systems	20
2.4 Catalytic Total Oxidation of Propane	21
2.4.1 Hydrocarbon Total Oxidation over Metal Oxides	22
2.4.2 Propane Total Oxidation over Cobalt Oxide	24
2.5 Kinetics and Mass Transfer	26
2.5.1 External Mass Transfer	27
2.5.2 Internal Mass Transfer	29
2.5.3 Kinetic Models	30
2.5.4 Nonlinear Regression Analysis	31

2.6	Design of Experiments	33
2.6.1	Definitions in DOE	33
2.6.2	Result Analysis	34
3	Experimental Details	37
3.1	Support - Sintered Metal Fibers	37
3.1.1	Characteristics	37
3.1.2	Pretreatment	38
3.2	Reactors and Experimental Setup	38
3.2.1	Micromeritics Reactor	39
3.2.2	Pilot Reactor	40
3.3	Adsorber	41
3.3.1	Synthesis	41
3.3.2	Adsorption Isotherms	43
3.3.3	Adsorption Breakthrough Curves	44
3.3.4	Pressure Drop	45
3.4	Oxidation Catalyst	45
3.4.1	Powder Preparation and Deposition	45
3.4.2	Catalyst Screening	47
3.4.3	Catalyst Testing and Kinetics	48
3.5	Characterization Techniques	50
3.5.1	Atomic Absorption Spectroscopy	50
3.5.2	X-ray Diffraction	50
3.5.3	Scanning Electron Microscopy	51
3.5.4	Specific Surface Area and Pore Volume	51
3.5.5	Particle Size Distribution	51
3.5.6	X-ray Photoelectron Spectroscopy	51
3.6	Chemicals and Gases	51
4	Adsorber	53
4.1	Synthesis and Characterization of MFI/SMF	53
4.1.1	Film Growth	53
4.1.2	XRD	57
4.1.3	BET Specific Surface Area	57
4.1.4	Atomic Absorption Spectroscopy	58
4.2	Adsorption Isotherms	59
4.3	Isothermal Adsorption Model	63
4.3.1	Governing Model Equations	63
4.3.2	Classification	64
4.3.3	Instantaneous Mass Transfer	66
4.3.4	Finite Mass Transfer	67
4.3.5	Linear Driving Force Approach	69
4.3.6	Tanks-in-Series Model with Linear Driving Force	71
4.4	Adsorption Breakthrough Curves	74
4.5	Activated Mass Transfer Coefficient	79
4.6	Pressure Drop	81
4.7	Conclusion	83

5	Oxidation Catalyst	85
5.1	Preparation and Characterization	86
5.1.1	Powder coatings	86
5.1.2	Cobalt Oxide/Silicalite-1/SMF	88
5.1.3	Cobalt Oxide/Oxidized SMF	89
5.1.4	BET	89
5.2	Coatings on SMF by Powder Deposition	90
5.2.1	Experimental Considerations	91
5.2.2	DOE Scheme	92
5.2.3	Powder Layer Homogeneity	93
5.2.4	ANOVA and Linear Model	94
5.2.5	Model Linearity	97
5.2.6	Powder Adherence	98
5.3	Mass Transfer Limitations	99
5.3.1	External Mass Transfer Limitations	100
5.3.2	Internal Mass Transfer Limitations	107
5.4	Catalyst Screening	109
5.4.1	Screening Results	109
5.5	Kinetics of Cobalt Oxide on SMF	111
5.5.1	Surface Analysis	115
5.5.2	Deactivation	117
5.6	Conclusion	121
6	Two-Step Adsorption-Incineration	123
6.1	Catalytic Fixed-Bed Reactor	123
6.2	Adiabatic Adsorption/Desorption Model	125
6.2.1	Governing Model Equations	125
6.2.2	Tanks-in-Series Model with Linear Driving Force	126
6.3	Modeling of Adsorption/Desorption System	129
6.3.1	Adiabatic Adsorber	129
6.3.2	Adiabatic Desorber	130
6.3.3	Desorption by Hot Gas	131
6.3.4	Steam Purging	136
6.3.5	External Preheating	136
6.3.6	Parametric Study of Adiabatic Desorber	139
6.4	Conclusion	146
7	Chemical Kinetics by Design of Experiments	149
7.1	Models and Experimental Design	150
7.1.1	Design Factors	150
7.1.2	Experimental details	151
7.1.3	One-Factor-at-a-Time	152
7.1.4	Central Composite Design	153
7.1.5	Full Factorial Design	156
7.2	Results and Discussion	156
7.3	Conclusion	162
8	Conclusion	165

8.1 Outlook	167
A Temporal Point Model	169
B Isothermal Adsorption Breakthrough Program	171
C Adiabatic Adsorption/Desorption Program	175
D Parameter Estimation Program	181
E Kinetics of CK-302	185
References	187
Curriculum Vitae	201

Nomenclature

Abbreviations

AAS	Atomic absorption spectrometry
ANOVA	Analysis of variance
CSTR	Continuous stirred tank reactor
DF	Degree of freedom
DOE	Design of experiments
FID	Flame ionization detector
GC	Gas chromatograph
ID	Inner diameter
IWI	Incipient wetness impregnation
LDF	Linear driving force
MS	Mass spectrometer
MS	Mean square
MTZ	Mass transfer zone
NMR	Nuclear magnetic resonance
OD	Outer diameter
OFAT	One factor at a time
PEG	Poly ethylene glycol
PFR	Plug flow reactor
PSD	Particle size distribution
PSV	Pore specific volume [cm^3/g]
PVP	Poly vinyl propylene
QDF	Quadratic driving force

RTD	Residence time distribution
SEM	Scanning electron microscopy
SMF	Sintered metal fiber
SSA	Specific surface area [m^2/g]
<i>ssq</i>	Sum of squares of residuals, see equation (2.31)
SS	Stainless steel (AISI316L) , page 37
SS	Sum of squares
STP	Standard conditions for temperature and pressure (0 °C, 101325 Pa)(IUPAC, 1997, pre-1982 definition)
TCD	Thermal conductivity detector
TPD	Temperature programmed desorption
VOC	Volatile organic compound
WHSV	Weight hourly space velocity [$\text{gC}_3\text{H}_8/\text{g}_{\text{cat}}\cdot\text{h}$] , page 92
XPS	X-ray photoelectron spectroscopy

Dimensionless Groups

Bi_H	Biot number for heat transfer: $\frac{hd_f}{k}$, see equation (6.33)
Ca	Carberry number: $\frac{r_{v,observed}}{k_f a' C_{bulk}}$, see equation (2.16)
Da_{II}	Damköhler II number: $\frac{k_v C_{bulk}^n}{k_f a' C_{bulk}}$, see equation (2.14)
Da_I	Damköhler I number: τk , see equation (4.71)
j_D	j -factor for mass transfer: $\frac{Sh}{Re Sc^{1/3}}$, see equation (2.12)
j_H	j -factor for heat transfer: $Nu Re^{-1} Pr^{-1/3}$, see equation (6.31)
Nu	Nusselt number: $\frac{hd_f}{k}$, see equation (6.32)
Pr	Prandtl number: $\frac{\mu C_p^G}{k}$, see equation (6.32)
Re	Reynolds number: $\frac{v \rho d}{\mu}$, see equation (2.10)
Re_d	Reynolds number based on the wire/fiber diameter: $\frac{v \rho d_f}{\mu}$, see equation (5.2)
Sc	Schmidt number: $\frac{\mu}{\rho D}$, see equation (2.11)
Sh	Sherwood number: $\frac{k_f d_p}{D}$, see equation (2.9)
Φ	Thiele modulus: $\frac{V_p}{A_p} \sqrt{\frac{\frac{n+1}{2} k C^{n-1}}{D_e}}$, see equation (2.19)

Ψ Weisz modulus: $\left(\frac{V_p}{A_p}\right)^2 \frac{n+1}{2} \frac{r_{observed}}{DeC_{surface}}$, see equation (2.20)

Roman Letters

A	Surface area [m ²]
A_p	Outer surface area of particle [m ²]
a	Activity , see equation (5.8)
a	Coefficients of effects, page 34
a'	Specific particle area [m ² /m ³]
b	Model parameters, see equation (2.30)
C	Concentration [mol/m ³]
C_j	Concentration in the j th cell/tank , see equation (4.58)
C_p^f	Heat capacity at constant pressure, metal fiber [J/kg·K] , see equation (6.11)
C_p^G	Heat capacity at constant pressure, gas phase [J/mol·K] , see equation (6.11)
C_p^z	Heat capacity at constant pressure, zeolite [J/kg·K] , see equation (6.11)
D	Diffusivity [m ² /s]
D_{ax}	Axial dispersion coefficient [m ² /s] , see equation (4.10)
D_c	Intracrystalline diffusivity [m ² /s] , see equation (4.36)
D_e	Effective diffusivity [m ² /s] , see equation (4.9)
D_K	Knudsen diffusivity [m ² /s]
D_m	Molecular diffusivity [m ² /s]
d_f	Diameter, fiber [m]
d_p	Diameter, particle [m]
E	Diffusional activation energy [J/mol] , page 71
E_a	Activation Energy[J/mol]
E_{LDF}	Activation energy for mass transfer [J/mol] , see equation (4.57)
F	Fischer distribution
F_{in}	Molar flow rate, inlet , see equation (3.7)
f	Dimensionless gas concentration , see equation (4.66)
H	Enthalpy [J/mol]
ΔH_{ads}^0	Heat of adsorption [J/mol] , see equation (4.6)

ΔH_r	Heat of reaction [J/mol] , see equation (6.1)
h	Heat transfer coefficient [W/m ² ·K] , see equation (6.25)
h	Height [m]
K	Adsorption equilibrium constant [1/Pa] , see equation (4.6)
K'	Adsorption equilibrium constant at reference temperature T' [1/Pa] , see equation (4.6)
K	Kuwabara parameter
k	Permeability [m ²] , see equation (4.72)
k	Reaction rate constant [(mol/kg·s)(m ³ /mol) ^(m+n)] , see equation (2.27)
k_{ax}	Axial thermal conductivity [W/m·K] , see equation (6.4)
k_d	Deactivation rate constant [1/s] , see equation (5.10)
k_e	Effective thermal conductivity [W/m·K] , see equation (6.3)
k_f	Adsorption rate constant [m ³ /mol·s] , see equation (A.3)
k_f	Mass transfer coefficient [m/s]
k_{LDF}	LDF mass transfer coefficient [1/s] , see equation (4.54)
$k'_{0,LDF}$	Preexponential factor of LDF mass transfer coefficient at T' [1/s] , see equation (4.57)
k_{lump}	Overall gas-film mass transfer coefficient [m/s] , see equation (A.1)
k_{QDF}	Quadratic driving force rate constant [1/s] , see equation (4.48)
k^*	Modified rate constant [mol/g·s] , see equation (3.3)
k_v	Reaction rate constant, volumetric [(mol/m ³ ·s)(m ³ /mol) ⁿ] , see equation (2.14)
k_w	Reaction rate constant, weight [(mol/kg·s)(m ³ /mol) ⁿ] , see equation (2.14)
L	Characteristic length [m] , see equation (4.50)
l	Film coordinate [m] , see equation (4.37)
M	Molecular weight [g/mol]
m_{cat}	Catalyst mass [kg], see equation (3.7)
n	Number of moles [mol] , see equation (6.35)
P	Pressure [Pa] , see equation (2.29)
P	Probability
P_i	Partial pressure of species i [Pa] , see equation (4.5)

\dot{Q}	Heat transfer rate [J/s] , see equation (6.25)
Q	Energy flow rate [J/s] , see equation (6.11)
q	Concentration of adsorbed species [mol/kg] , see equation (4.5)
q^*	Maximum adsorption capacity in dynamic equilibrium with C [mol/kg] , see equation (4.54)
\bar{q}	Volume-average adsorbate concentration [mol/kg] , see equation (4.38)
q_m	Maximum adsorption capacity [mol/kg] , see equation (4.5)
R	Gas constant [J/mol·K]
R	Recycle ratio , page 101
r	Reaction rate [mol/g·s]
r_c	Crystal radius [m] , see equation (4.36)
r_p	Pore radius [Å], page 90
C_j^b	Adsorptive bulk gas concentration in the j^{th} tank [mol/m ³] , see equation (A.1)
C_j^s	Adsorptive gas concentration at the fiber surface in the j^{th} tank [mol/m ³] , see equation (A.1)
T'	Reference temperature [K]
T_0	Initial temperature of the desorber [K] , see equation (6.21)
T	Temperature [K] , see equation (6.11)
T_{ads}	Adsorption temperature [°C] , page 145
T_{des}	Desorption temperature [°C] , page 138
T_{eq}	Equilibrium temperature [°C] , page 140
T_m	Maximum temperature of the inlet gas stream to the desorber [K] , see equation (6.21)
T_{max}	Maximum adiabatic reactor temperature [°C] , page 140
T_{rxn}	Reaction temperature [°C] , page 140
T_s	Scaling temperature, $T_s = T_m - T_0$ [K] , see equation (6.21)
t	Toth isotherm parameter [-] , see equation (4.7)
Δt_{ads}	Adsorption time [s] , see equation (4.21)
u	Natural variable, page 33
V	Volume [m ³]

\dot{V}	Volumetric flow rate [m^3/s] , see equation (4.60)
V_{in}	Volumetric inlet flow rate [m^3/s]
V_p	Volume of particle [m^3]
v	Interstitial linear flow rate [m/s] , see equation (5.3)
X	Conversion , see equation (3.6)
x	Factor or variable, page 34
x	Input variables, see equation (2.30)
x	Loading of coating material , see equation (5.1)
x_f	Metallic fiber fraction in fixed-bed , see equation (6.11)
x_z	Zeolite fraction in fixed-bed , see equation (4.52)
y	Measured output variables, see equation (2.31)
\hat{y}	Model value for output variables, see equation (2.30)
z	Axial position [m] , see equation (4.10)

Greek Letters

ϵ	Stochastic, normal distributed error, page 32
ϵ	Volume change by reaction
ε	Porosity
ε_p	Pore fraction , page 29
η	Effectiveness factor , see equation (2.21)
η_H	Effectiveness factor of desorption at 300 °C , page 140
η_L	Effectiveness factor of desorption at 250 °C , page 140
θ	Dimensionless time , see equation (4.66)
θ	Surface coverage , see equation (4.1)
μ	Viscosity [Pa s] , see equation (4.72)
ω	Geometry factor for k_{LDF} , page 78
ρ	Density [kg/m^3]
ρ_f	Density of metal fiber [kg/m^3] , see equation (6.11)
ρ_z	Density of the zeolite adsorbent [kg/m^3] , see equation (4.12)
σ	Standard deviation, page 32

τ_m	Time required for saturating all adsorbent [s] , see equation (4.66)
τ_p	Tortuosity factor , page 29
ξ	Dimensionless adsorbate concentration , see equation (4.66)
ζ_j^C	Dimensionless temperature of the composite phase in the j^{th} tank , see equation (6.26)
ζ_j^G	Dimensionless temperature of the gas phase in the j^{th} tank , see equation (6.26)

Symbols

\varnothing	Diameter [m]
---------------	--------------

Superscript

d	Order of deactivation , see equation (5.10)
f	Metal fiber
G	Bulk gas phase , see equation (6.4)
m	Reaction order in oxygen , see equation (2.27)
n	Reaction order in propane , see equation (2.27)
s	Surface
z	Solid zeolite adsorbent phase , see equation (4.8)
$'$	Reference condition

Subscript

ads	Adsorption , page 145
des	Desorption , page 138
eq	Equilibrium conditions , page 140
HC	Hydrocarbon , see equation (5.7)
i	Chemical species i
j	Tank number
max	Maximum , page 140
min	Minimum , page 140
O_2	Oxygen , see equation (5.7)
p	Particle
R	Particle surface , see equation (6.5)

rxn	Reaction , page 140
v	Volumetric basis , see equation (3.1)
w	Weight basis , see equation (3.2)

Chapter 1

Introduction

Air pollution is the presence of any substance in the atmosphere at a concentration high enough to produce an undesirable effect on humans, animals, vegetation or materials, or to significantly alter the natural balance of any ecosystem. Air pollutants can be solids, liquids or gases.

Health effects associated with chronic exposure to air pollution is a worldwide problem. The World Health Organization (WHO) has estimated that ~ 2.7 million deaths are attributable to air pollution throughout the world each year. Among the air pollutants of greatest concern are ozone, suspended particulate matter, nitrogen dioxide, sulfur dioxide, carbon monoxide, lead and other toxins. Of these pollutants, ozone is one of the most prevalent air pollutants in large cities and has been associated with increased respiratory illness and decreased lung function, particularly in children (Allen, 2004).

Photochemical smog is a complex mixture of constituents that are emitted directly to the atmosphere (primary pollutants) and constituents that are formed by chemical and physical transformations that occur in the atmosphere (secondary pollutants). Ozone (O_3), is generally the most abundant species formed in photochemical smog. Extensive studies have shown that O_3 is both a lung irritant and a phytotoxin. It is responsible for crop damage and is suspected of being a contributor to forest decline in Europe and in parts of the United States (Allen, 2004). Ozone is a secondary pollutant formed by the reactions of hydrocarbons (including volatile organic compounds (VOCs)) and NO_x .

1.1 VOC Emissions

Volatile organic compounds (VOCs) include any organic carbon compound that exists in the gaseous state in ambient air. In some of the older literature the term VOC is used interchangeably with non-methane hydrocarbons (NMHC). VOC sources may be any process or activity utilizing organic solvents, coatings or fuel. Emissions of VOCs are problematic: some are toxic and most are precursors of O_3 and other species associated with photochemical smog. As a result of control measures designed to reduce O_3 , VOC emissions are declining in the United States. Figure 1.1 shows estimates of nationwide emissions of VOCs. Emissions peaked ~ 1970 and have declined by $\sim 40\%$ from that peak. Major sources continue to be industrial processes, solvent use (including solvents used in architectural coatings such as paints and varnishes), non-road sources (such as

marine and garden equipment engines) and vehicular sources.

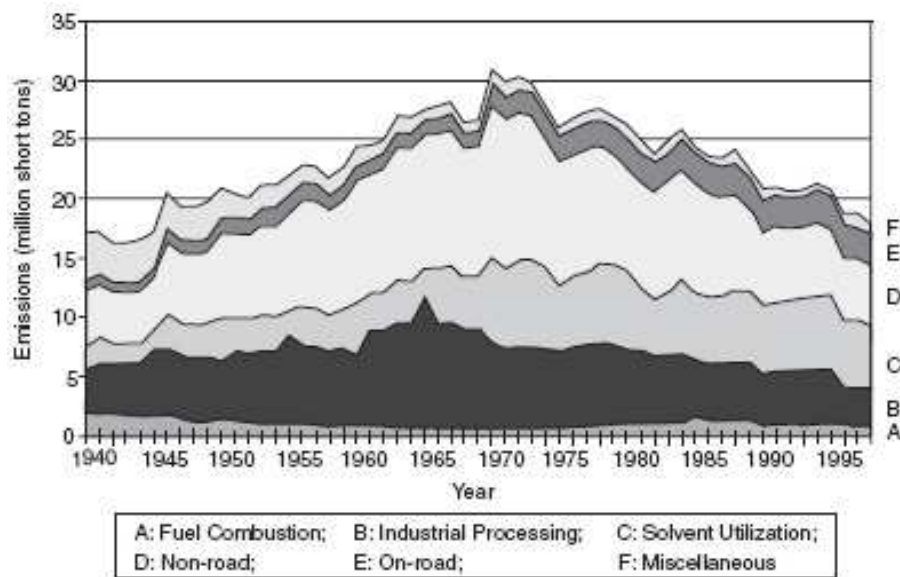


Figure 1.1: Trends in emissions of VOCs 1940-1998, in USA (Allen, 2004).

Regulations on controlling VOCs have been issued world-wide (Ghoshal & Manjare, 2002). Germany having one of the strictest emission regulations: "TA-Luft" (Bundesministerium für Umwelt, 2002), gives an emission limit of gaseous organic compounds of 50 mg/m^3 and 0.50 kg/h . For propane, which is the model molecule in this study, at standard conditions this concentration equals 25 ppmv.

Indoor air quality has become a growing environmental issue over the past 20 years. An increasing number of health and comfort problems have been reported in office buildings, schools, residences and similar nonindustrial settings (Tucker, 2004).

In the 1980s and 1990s, it became clear that there are hundreds of measurable organic compounds in indoor air, present either as gases or associated with particles. Field investigations of residences, office buildings and schools show that these contaminants come predominantly from indoor sources such as new materials, cleaning materials, office machines and appliances and moist areas with favorable conditions for microbial growth. Furthermore, indoor concentrations are highly variable with time and place within a building. Any of hundreds of substances can be the most important with respect to concentration or potential health impact in a given space, at a given time. The health concerns themselves are numerous. They range from vague dissatisfaction to frank irritation to chronic disease.

Governmental regulatory bodies have set very few indoor air quality standards. The U.S. Food and Drug Administration (FDA) has set an indoor limit of 100 mg/m^3 of ozone for spaces where ozone is being generated (FDA, 1988) and the Environmental Protection Agency (EPA) guideline of 4 pCi/L^1 for radon has become a *de facto* standard (EPA, 2007), but there are few others.

¹pico Curies per Liter

1.2 VOC Removal Techniques

Many different techniques for the removal of VOCs exist. An overview of various VOC control techniques is presented in Figure 1.2. They are classified into two different groups:

Process and equipment modification: where control of VOC emissions are achieved by modification of the process equipment, raw materials (including solvents) or a change of process.

Add-on control techniques: which can be added, typically as end-of-line equipment, to control the emissions.

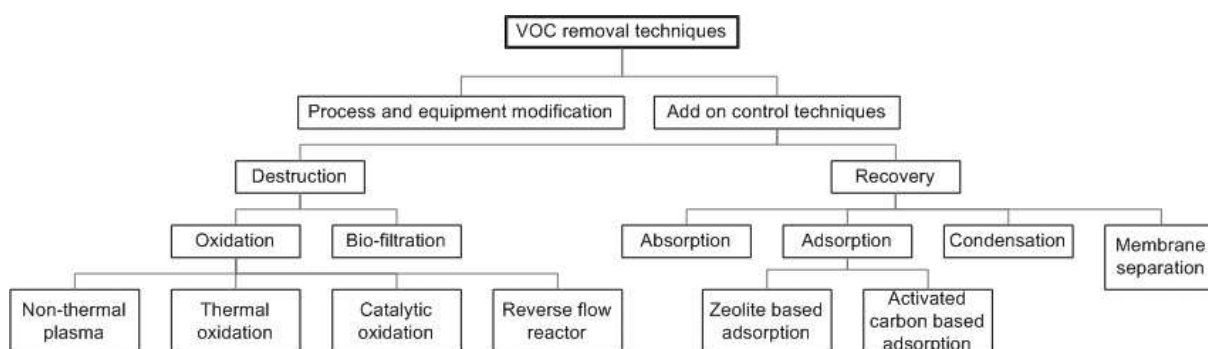


Figure 1.2: Classification of VOC control techniques. Adapted from (Khan & Ghoshal, 2000).

Process and equipment modifications will usually be the most effective, but the applicability of this method is often limited, since the equipment and process have already been optimized. Therefore, add-on control techniques usually have to be used to meet the emission limits. The add-on control techniques are divided into two sub-groups, namely the destruction and the recovery of VOC. The choice of technique for VOC control depends on the type, value and concentration of VOC. The available techniques shown in Figure 1.2 are not all interesting for low concentrations of VOC. Thermal oxidation for example, where the whole gas volume will have to be heated will require additional supply of heat. Furthermore, thermal oxidation happens at temperatures of 700-1000 °C, which can produce elevated levels of nitrogen oxides, NO_x , (from nitrogen in air) that require further treatment of the off-gas. Catalytic oxidizers decrease the operating temperatures to 300-500 °C, leading to lower NO_x levels and lower energy requirements or autothermal conditions. The main problems with catalytic oxidizers are the cost of the catalyst and the possible poisoning by non-VOC materials such as halogens, sulphur containing compounds, phosphorous and heavy metals. Furthermore, the VOC concentration must generally be above 1000 ppmv to function autothermally (McInnes, 1995).

Catalytic oxidation is the method of choice if the concentration of VOC allows performing the process adiabatically. For VOC concentrations lower than 1000 ppmv a two-step adsorber-incinerator process can be used. In this process the VOCs are first concentrated by adsorption at low temperature until the breakthrough occurs. The adsorbent is regenerated by desorption by heating and purging with inert gas. The desorbed, concentrated VOC is then passed through an incinerator and converted to harmless compounds by catalytic oxidation. The heat of combustion can be used for desorption.

Adsorption of VOCs is normally carried out on activated carbon or zeolites. Activated carbon is cheaper, but zeolites have the advantages of being non-flammable, thermally stable and hydrophobic (Khan & Ghoshal, 2000). Therefore, zeolites are preferred for the treatment of waste gases containing large amounts of water and for the processes with repeated adsorber regeneration by heating.

In this study the focus is on an environmentally friendly process for the removal of VOCs in low concentration. We propose to use novel, structured materials for a two-step adsorber-incinerator process to clean up VOC containing effluent gases or indoor air. The VOCs will be eliminated by heterogenous catalytic combustion.

1.3 Heterogeneous Catalysis

A catalyst is a material which influences a chemical process so that it will proceed towards chemical equilibrium faster, without consuming the catalyst. Often, several chemical reactions will take place at the same time, but if the catalyst is appropriately designed it will only lower the barrier for the desired reaction resulting in a much better selectivity and thereby a cleaner product.

Catalysts come in many forms. Most are complex solid materials, where the catalytic processes take place on the surface of the catalyst (heterogeneous catalysis). Heterogeneous catalysts are generally classified as bulk or supported catalysts. An example of a bulk catalyst is the Pt/Rh wire gauzes used for the oxidation of ammonia to NO for the production of nitric acid. However, most heterogeneous catalysts are supported catalysts, where an active catalytic phase (and sometimes promoters) are supported on a high surface area carrier, which serves to facilitate the dispersion and stability of the active catalytic phase. The surface areas of common supports (activated carbon, zeolites, silica gels, activated Al_2O_3) range from about 1.5 to 1500 m^2/g . The final catalyst may be formed into pellets or monoliths optimized for heat and mass transfer as shown in Figure 1.3. There are also catalysts which are dissolved in a fluid (homogeneous catalysis). The biological catalysts, the enzymes, belong to this class and are responsible for most chemical processes in living organisms.

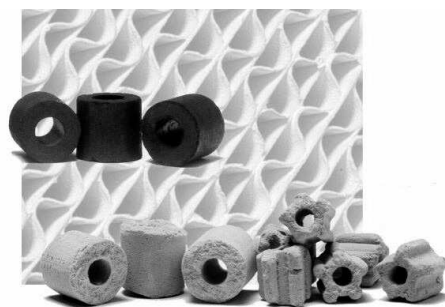


Figure 1.3: Catalysts in the shape of pellets and a monolith.

Catalysts are used widely within chemical production, power production, refinery processes, conversion of natural gases, chiral synthesis, agro chemistry, pharmaceutical processes, polymer and material production and bio-technology. The economic impact of catalysis is perhaps best illustrated by the fact that in the industrialized world hetero-

geneous catalysis is involved in 20-25 % of the gross national products (Maxwell, 1996) and 85-90 % of the products of chemical industry are made in catalytic processes (Chorkendorff & Niemantsverdriet, 2003). Many of the major problems society is encountering, such as the need for creating a production in balance with the environment, better use of fuels, more economical energy production and the reduction of CO₂ and other green house gases, will require solutions where catalysts play an important role. Furthermore, the development of new catalysts and catalytic processes can open for new selective chemical processes which may lead to a considerable reduction of undesired by-products or waste products. Important examples of applications of catalysis in environmental protection are the reduction of toxic emissions from automobiles and energy production. Catalysts are also applied extensively in refineries in order to produce cleaner transport fuels. This area receives currently great attention due to new and strict regulations being introduced worldwide.

1.4 Structured Materials

Conventional adsorbents and catalysts in randomly packed beds are used in form of pellets. Unfortunately, conventional randomly packed beds often have random structural maldistributions of the pellets or particles due to looser packing near the reactor walls. Hence, the fluid tends to bypass the core of the bed, flowing preferentially towards the walls. This can lead to a worsening of the overall process performance and hot-spots and thermal runaway of exothermic reactions. Structured reactors can be used to eliminate these problems and have open macrostructures leading to low pressure drop during gas-passage, narrow residence-time distribution and enhanced heat and mass transfer (Cybulski & Moulijn, 2006).

Three basic types of structured catalysts can be distinguished:

1. **Monolithic catalysts** or honeycomb catalysts, which are continuous unitary structures containing small parallel channels. The catalytically active material is deposited on or inside the walls of the passages. Monolithic catalysts are especially known for their use in automotive 3-way catalysts.
2. **Membrane catalysts** are structures with permeable walls between passages. The membranes show selectivity in mass transport rates for various compounds present and can combine catalytic reaction in the wall with reactant/product separation.
3. **Arranged catalysts**. Particulate catalysts arranged in arrays belong to this class. Furthermore, **structural catalysts** belong to this group. Structural catalysts are derived from structural packings for distillation and absorption columns and static mixers. They are often made from superimposed sheets of different geometric arrangements covered with the catalytically active phase.

In the current study we used a type of arranged, structured support: filters of sintered metal fibers (SMF), which have been designed for filtration purposes and are commercially available in different materials, porosities, fiber diameters and graded/non-graded form (e.g. Bekaert Fibre Technology, Zwevegem, Belgium). SMF have already been used for structured catalytic beds due to their homogeneous and open macro structure (70-90 %

porosity) and low pressure drop (Yuranov *et al.* , 2003, 2005). The metallic fiber matrix of the SMF has a high thermal conductivity, which ensures a radial heat transfer coefficient in the bed two times higher than the one attainable in randomly packed beds. This avoids hot-spots and run-away problems (Cahela & Tatarchuk, 2001). Furthermore, the SMF offer mechanical and thermal stability and acid resistance for stainless steel fibers (Sterte *et al.* , 2001). Hence, this structured material of sintered metal fibers offers several benefits over conventional supports.

1.5 Objectives

This work is concerned with structured adsorbents and catalysts based on filters of sintered metal fibers (SMF) for the removal of volatile organic compounds (VOCs) in low concentration. A two-step adsorber-incinerator process is proposed, in which the VOCs are first concentrated by adsorption at low temperature until breakthrough occurs. The adsorbent is regenerated by desorption with heating and by passing an inert gas through the bed. The desorbed, concentrated VOC is passed through the catalytic fixed-bed reactor and converted to harmless compounds by catalytic oxidation. The heat of combustion can be used for enhancing the desorption. The objectives of this work are summarized in the following:

Structured adsorbent consisting of a thin zeolitic film synthesized on SMF had to be developed. This film should be homogenously grown and stable during use. The adsorption characteristics and effects on the pressure drop should be determined.

Structured catalysts based on SMF had to be developed and tested as a total combustion catalyst.

Adsorption/incineration process: based on the characteristics of the developed adsorbent and catalytic materials, the coupling between desorption and oxidation in the two-step adsorption-incineration process should be simulated theoretically.

Propane was chosen as the model molecule for testing the performances of the synthesized materials.

Chapter 2

Theory

2.1 VOC Removal by Two-Step Adsorption - Incineration

In this section the "state of the art" of removal of VOCs in low concentration by combined adsorption and catalytic combustion is described so as to have a reference point for the current project. Basically two categories exist: adsorbent and catalyst can either be combined in the same fixed-bed or in two separate beds.

2.1.1 One-Fixed-Bed-Systems

Most inventions and research belong to the category of one-fixed-bed-systems, where the adsorbent and catalyst are intimately mixed or with catalytic material deposited on the adsorbent material. With adsorbent and catalyst in the same fixed-bed the heat of reaction from the oxidation reaction is used directly to desorb the adsorbed VOC species. Furthermore, these processes are simpler than having several beds and indirect heat recovery. All processes require an initial heat input to reach the ignition temperature.

All the methods are periodical. First, the VOCs are adsorbed, then the fixed-bed is heated until the desorption and oxidation starts, and in the end the bed will have to be cooled before it can be reused for adsorption and the cycle starts all over. The methods differ in the way they are heated or in the way they are controlled.

The inlet gas, which can still contain VOC, can be heated, thus heating the fixed-bed until the ignition of the bed takes place (Morlec *et al.* , 1993; Campbell & Sanders, 1999; Shore *et al.* , 2001). Conductive bed material can be heated by an electrical current to start the desorption and the catalytic oxidation (Dalla Betta *et al.* , 1994). A "falling furnace" method in which a mobile furnace can heat up the bed periodically has also been proposed (Atwood *et al.* , 1998).

A different, continuous operation approach is a rotary bed in which a number of sections can be controlled by the rotation of the fixed-bed. This concept has been patented by Teller (2000) and is in widespread use McInnes (1995). In this setup one section of the bed is in adsorption mode, the next in oxidation mode and the following in "cooling/preheating of oxidation gas" mode. The rest of the sections have time to cool before they enter

the adsorption mode yet again. A sketch of a commercial rotary honeycomb adsorber system is seen in Figure 2.1. However, the system in the figure belongs to the two-fixed-bed-systems which is discussed in the following section, but the principle of a rotating adsorption/desorption unit is the same.

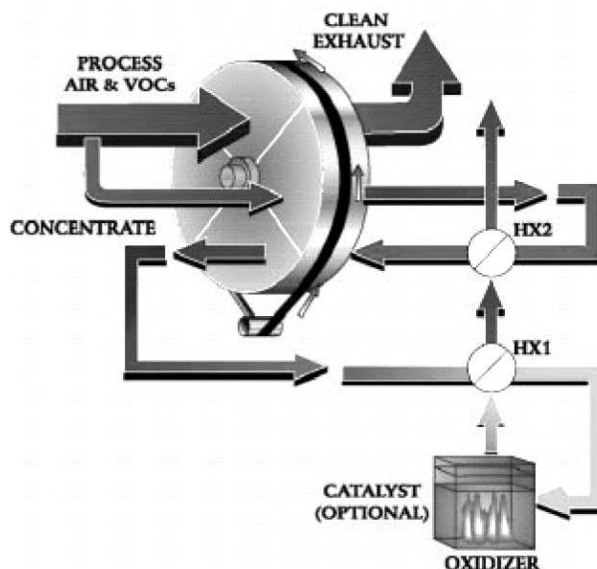


Figure 2.1: Rotary adsorber coupled with catalytic combustion. (Munters Zeol Division, Amesbury, MA, USA;
<http://www.environmental-expert.com/technology/munterszeol/munterszeol.htm>;
 Feb. 2007)

Salden & Eigenberger (2001) developed an adsorption-incineration process for removal of polymerizing organic compounds, which cannot be desorbed by conventional desorption techniques. Styrene was adsorbed on a zeolite containing fixed-bed, which was periodically regenerated by thermal oxidation fronts travelling in upstream direction through the column. The incomplete oxidation products necessitated a catalytic converter downstream, which did not require additional heat input.

A more process control intensive design is the adsorption-catalytic reverse-process by Zagoruiko *et al.* (1996). In this method a heater is placed in the center of the fixed-bed. When the adsorption cycle finishes the heater is turned on and the gas is heated by flow reversals. The flow is reversed when the reaction front reaches one bed-end.

Many of these methods need external heat or power input for every desorption/reaction cycle. Furthermore, all methods (except maybe the last one) suffer from the fact that VOCs will be emitted to the oxidation stream during the heating period until the ignition temperature is reached and might require a second downstream catalytic bed to remove these.

2.1.2 Two-Fixed-Bed-Systems

In these methods the VOCs are first adsorbed in one bed. Once breakthrough occurs the adsorber bed is then heated and VOCs desorb and burn in a second preheated catalytic bed. One example of such a system is the work of Meeyoo *et al.* (1998); Kullavanijaya

et al. (2000, 2002). The benefit of this method is that essentially no VOCs are emitted. However, energy is needed every time the desorption/reaction cycle starts.

An ingenious method of solving the problem of periodic heating and emission of VOCs during the heating period is described in the patent by Schoubye (1980). A flow diagram of the patented apparatus is shown in Figure 2.2. A number of adsorption units, containing adsorbent doped with catalytically active metals or metal oxide, adsorb the VOCs. Once breakthrough happens in an adsorber the VOC containing gas will be switched to a second, "cold" adsorber. The saturated adsorber will switch to desorption mode, heated by a recycled fraction of the exhaust from the main catalytic oxidizer. During desorption, the recycled heat from the main oxidizer enhances the desorption of the VOC. As the adsorbers are heated during desorption it is claimed that they should aid in partly destroying the VOC as the adsorbent is doped with catalytically active material. It is reported that this system only needs heating for the start-up of the process. Furthermore, the system is autothermal or even exothermal for higher concentrations of VOC.

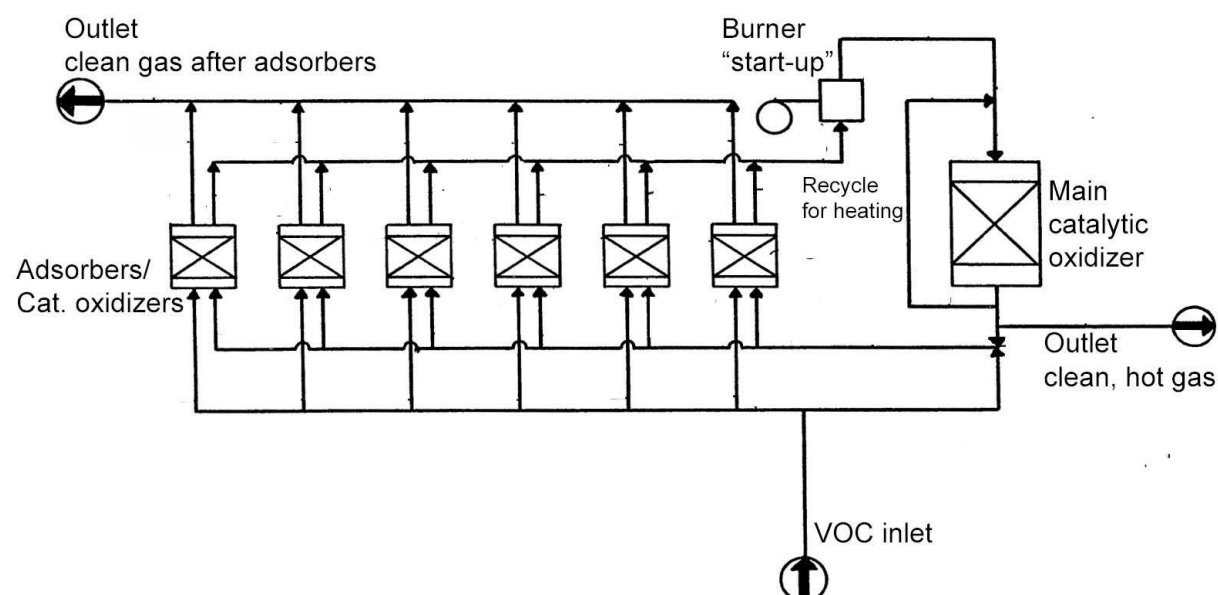


Figure 2.2: Flow diagram of two-step adsorber-incinerator apparatus. Adapted from Schoubye (1980).

The two-fixed-bed-system method has been commercialized e.g. by Munters Zeol Division, Amesbury, MA, USA. A sketch of their system is seen in Figure 2.1. The adsorbent is a zeolite supported in a large honeycomb cylinder. The low concentration VOC laden air stream passes through a section of the hydrophobic honeycomb rotor. The rotor turns several revolutions per hour continuously transporting VOC laden zeolite back into the regeneration sector and regenerated zeolite into the adsorption section, from which clean air is exhausted to the atmosphere. In an isolated section, a small, hot stream of clean air is drawn through the rotor. This stream is normally less than 10 % of the process flow rate. The hot air desorbs the VOCs from the zeolite forming a concentrated VOC laden air stream. The concentrated stream is sent to a small oxidizer. The oxidizer converts the VOCs to carbon dioxide and water vapor which are exhausted to the atmosphere.

2.2 Structured Fibrous Supports and Catalysts

As discussed in Section 1.4 of the Introduction, structured catalysts can be divided into three subgroups. The structured support for the current study was filters of sintered metal fibers (SMF), which belongs to the group of arranged catalysts. In this section the basic characteristics and applications of fibrous catalysts will be presented.

2.2.1 Introduction

The size of catalyst particles in a fixed-bed reactor is a trade-off between a high efficiency of the catalyst and a low pressure drop. Fibrous catalysts are structured catalysts, which can to some degree overcome this problem. The small fiber diameters, on the order of 1-80 μm , makes possible the use of support sizes on the same order of magnitude as powders, but without the disadvantages of handling and pressure drop associated with powders.

Fibrous catalysts in the form of gauze made from precious metals (Pt, Ru, Ag) have been used for a long time in the production of nitric acid, hydrocyanic acid and aldehydes (Satterfield, 1991). However, these bulk catalysts of precious metals are extremely expensive, have problems with deactivation due to loss of platinum through volatile PtO_2 and the applications are limited. During the last decade, fibrous catalysts based on cheaper metals, glass fibers or carbon have been used in several different applications.

The fibrous materials are flexible and can therefore be packed in fixed-beds of different geometries and in many different ways (stacked, rolled, folded etc.) that are not possible with powdered or granular materials. Furthermore, the fibrous materials have very high porosities, 70-90 % (SMF from Bekaert Fibre Technology, Zvevegem, Belgium), compared to randomly packed beds of spheres, cylinders and granules, porosities of 34-60 %, and Raschig rings and Berl saddles with porosities of 60-75 % (McCabe *et al.*, 1993). However, for the conventional packings, high porosities also mean lower specific surface area and higher risk of channeling at the reactor walls. Due to the high porosity of the fibrous materials they lead to low pressure drop compared to fixed-beds of powders and granules. Thus, they can be used as attractive alternatives in three-phase systems such as slurry and trickle-bed reactors.

Fibrous catalytic materials offer the advantages of an immobile structure and a short diffusion time, similar to that in monolith structures. This makes them especially interesting for liquid-phase catalytic reactions. Other advantages of the fibrous catalysts include high geometrical surface area, safer operation, easy scale-up and the absence of maldistribution (provided that the liquid is properly distributed at the inlet). When diffusion inside the fibers is necessary the small diameters available can essentially eliminate the influence of mass transfer. On the other hand, metal loading on the fibers is limited and their mechanical properties limit their use for certain applications (Matatov-Meytal & Sheintuch, 2002).

2.2.2 Comparison Between Conventional and Structured Catalysts

A comparison of some important characteristics of fibers with monolith and pellet structures is given in Table 2.1. The geometric surface area (or SSA_v) and the voidage/porosity of the fibrous structures are generally high compared to packed pellets or in monoliths. When diffusion is not the rate-limiting step, the reaction rates per unit volume of fibrous catalyst will be lower than for pellets, since the reaction takes place only in an outer layer of the fibers as opposed to the entire porous pellet. However, under diffusion-influenced conditions this conclusion may be reversed.

Table 2.1: Contrasting of performance for pellet-, monolith- and fibrous-catalysts. Adapted from (Matatov-Meytal & Sheintuch, 2002).

	Units	Pellet	Monolith	Fibrous structure (wire-mesh, cloths)
Particle/channel diameter	mm	3.0-5.0	1.5	0.01-2
Diffusion length	μm	100-2500 ^a	25-100 ^b	0.15 ^c
Specific surface area	m^2/g	up to 1000	-	2-2000 ^d
Geometric surface area	m^2/m^3	1200	1900	up to 100 000
Voidage		0.42	0.65	0.8

^a Depending on catalyst structure

^b Washcoat thickness

^c Depending on porosity

^d Depending on material

The comparison of catalytic metal wire meshes ($d_f = 0.3$ to 1.65 mm) with monolith (400 - 12 cps¹ and wash coat thickness of 0.2 to 1.1 mm) and pellet catalysts ($d_p = 0.25$, 1 and 4 mm) for catalytic combustion was conducted by Ahlstrom-Silversand & Odenbrand (1999). The performance per volume of catalyst was highest for the small particles ($d_p=0.25$ mm). However, the performance was very sensitive to the particle size due to pore diffusion. The volumetric performance of the wire mesh was similar already at $d_p=1$ mm. On a weight basis the differences were even greater, favoring the fibrous material. The performance of the metal wire meshes was on the same order of magnitude, but better than with monoliths. Performance comparison based on pressure drop showed the opposite trend with the wire-mesh having a pressure drop between the monolith and pellet catalysts. Monoliths clearly have the lowest pressure drop, but the pressure drop over the metal wire meshes were still an order of magnitude lower than in a fixed-bed of pellets. Finally, the authors showed that the thermal response, which is important in combustion applications, was in general 2 to 3 times higher than the corresponding values of the monolith catalyst, due to increased external surface area and improved heat transfer coefficients.

2.2.3 Fibrous Structured Materials

A large number of fibrous materials have been described in the literature with a significant part in the patent literature. Fibrous materials can be used to form composites with

¹Channels per square inch

metallic, ceramic or polymer matrices for applications such as membranes, insulators, medical devices, etc. Catalysis is one area of application. Three classes of materials have been studied profoundly: carbon fibers, glass fibers and metallic wires. Which type of material to use depends on the type of application. Qualitative comparison of mechanical and thermal properties of these three groups of materials is shown in Table 2.2.

Table 2.2: Qualitative comparison of properties of selected fibrous materials (Matatov-Meytal & Sheintuch, 2002)^a.

Material	Tensile strength	Tensile modulus	Ilss ^b	Temperature resistance
Metal	+	+	+	0
Glass	+	-	+	0
Carbon	0	0	0	+

^a +: better than average, 0: average, -: less than average

^b Ilss: interlaminar shear strength

The table shows that metallic fibers have very good overall mechanical and thermal qualities. In the current study metallic fibers were used as support for both the adsorbent and the catalyst. Examples of use of metallic fibrous materials will be described in the following section.

2.2.4 Metallic Fibrous Materials

Metal wires in the form of gauzes have been used as catalysts or catalytic carriers for the conduction of highly exothermic processes since they possess high mechanical strength and high thermal conductivity. These types of reactions are usually very fast and the associated effectiveness factors in porous catalysts are low.

The first bulk metal wire catalysts were developed about a century ago and were made of pure noble metals for the catalytic oxidation of ammonia in the production of nitric acid. 30 years later the Pt-Rh alloys were developed, which improved the mechanical strength compared to the pure Pt gauzes.

High activity of supported catalysts is often linked with a large specific surface area (SSA_w) to allow for a high dispersion of the active phase. In the case of metallic fibers the specific surface area is very small, which can limit their use for extremely fast reactions. To achieve a high surface area several processes have been used. Monnerat *et al.* (2001) used metal grids of nickel, which they treated to produce Raney type metal used for methane cracking. This treatment increases the SSA_w from $< 1 \text{ m}^2/\text{g}$ to $27 \text{ m}^2/\text{g}$. The advantage of this method is that the catalyst remains metallic and thus keeps the benefits of the metal fibers: mechanical strength, flexibility and thermal properties. In a similar approach, Raney type nickel and copper grids were covered by transition metal oxides for the combustion of propane (Yuranov *et al.*, 2002). In this case the SSA_w was increased from $< 1 \text{ m}^2/\text{g}$ to $15\text{-}20 \text{ m}^2/\text{g}$ depending on the metal oxides used.

A second strategy consists in covering the fiber surfaces with porous materials with a high SSA_w . A thin catalyst coating is preferred for fast reactions or when diffusion is

slow (e.g. in liquid-phase). However, wash coating methods, which are commonly used for preparation of metallic monoliths, cannot be applied for coating fibrous materials with thickness as low as $50\text{ }\mu\text{m}$ because of poor adhesion and non-uniformity of the resulting coating (Zwinkels *et al.*, 1993; Maier & Schlangen, 1993). This is the main reason for the development of novel preparation methods for use in fibrous support materials.

Ahlstrom-Silversand & Odenbrand (1999) investigated the preparation of catalytic wire meshes coat by thermal spray deposition, which leads to a ceramic layer with good adhesion to the metal surface. To this layer a composite alumina-polymer powder was added by sol treatment to increase the SSA_w before adding the catalytically active phase by impregnation. Vorob'eva *et al.* (2000) coated stainless steel wires with active alumina by electrophoretic deposition (EPD). EPD is a relatively inexpensive way of depositing particles or colloid suspensions on an electrode driven by an electric field. A layer with a thickness of $5\text{ }\mu\text{m}$ gave a SSA_w of $40\text{ m}^2/\text{g}$ of composite.

Sol-gel methods were used to produce films of alumina, silica, porous glass or SBA-15 mesoporous zeolite on sintered metal filters which were impregnated with Pt for total oxidation of hydrocarbons (Yuranov *et al.*, 2003). Several different methods have been suggested to produce active zeolite coatings on fibrous materials. Jansen *et al.* (1998); Louis *et al.* (2001a,b) immersed the support (stainless steel wire-mesh and grids respectively) in the aqueous sol-gel for in situ hydrothermal synthesis of ZSM-5 zeolite crystals on the surface (see Figure 2.3). By a similar hydrothermal procedure mesoporous MCM-41 zeolites were synthesized on stainless steel metal grids (see Figure 2.4) (Louis *et al.*, 2002). A more controlled method for the growth of a continuous, homogeneous ZSM-5 film was developed and used for the nitration of benzene by Yuranov *et al.* (2005) as seen in Figure 2.5.

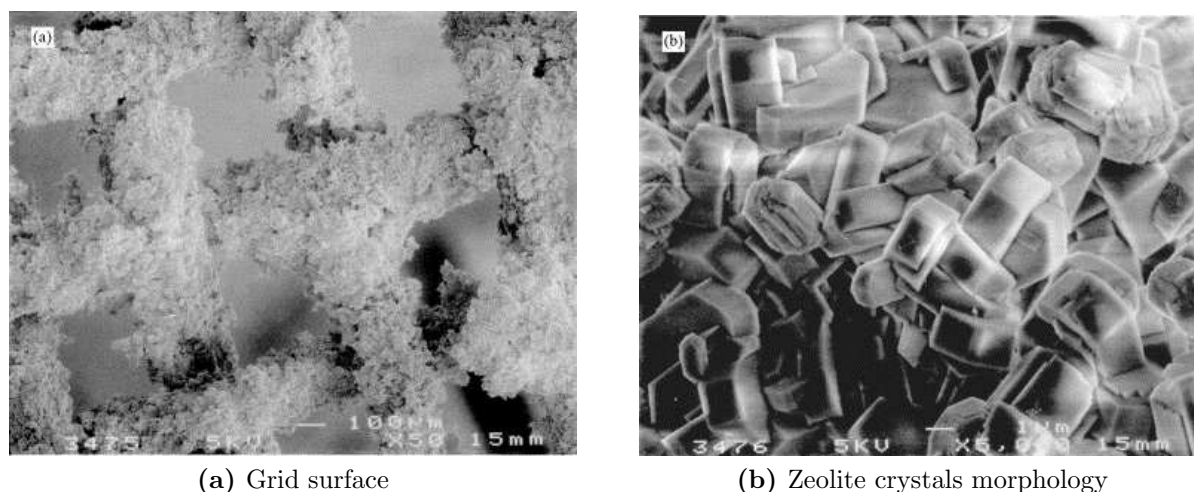


Figure 2.3: SEM images of ZSM-5 zeolite coatings on stainless steel grids (Louis *et al.*, 2001a).

A very different approach to adding SSA_w to the metal fibers is the growth of carbon nanofibers (CNF) on sintered metal fibers of nickel or nickel-containing alloys (Tribolet & Kiwi-Minsker, 2005a,b). SEM images are shown in Figure 2.6. The CNF were formed directly over the SMF by thermal ($650\text{ }^\circ\text{C}$) chemical vapor deposition of an ethane-hydrogen mixture. The CNF are very stable as they are chemically anchored to the metal surface. These types of materials impregnated with palladium have been proposed for the highly exothermic hydrogenation reactions using hydrogenation of acetylene as a model reaction.

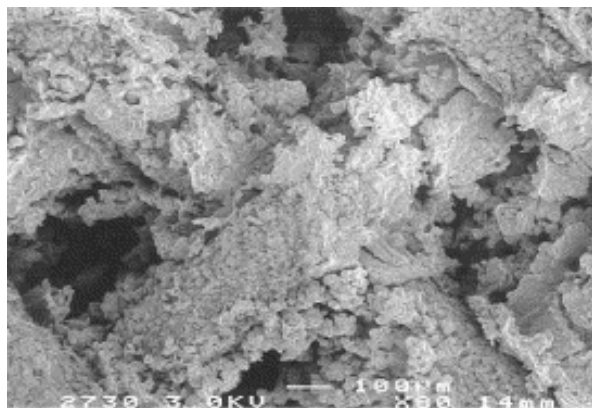


Figure 2.4: SEM image of Si-MCM-41/grid packings (Louis *et al.* , 2002).



Figure 2.5: SEM: sintered metal fibers coated by silicalite-1 (Yuranov *et al.* , 2005).

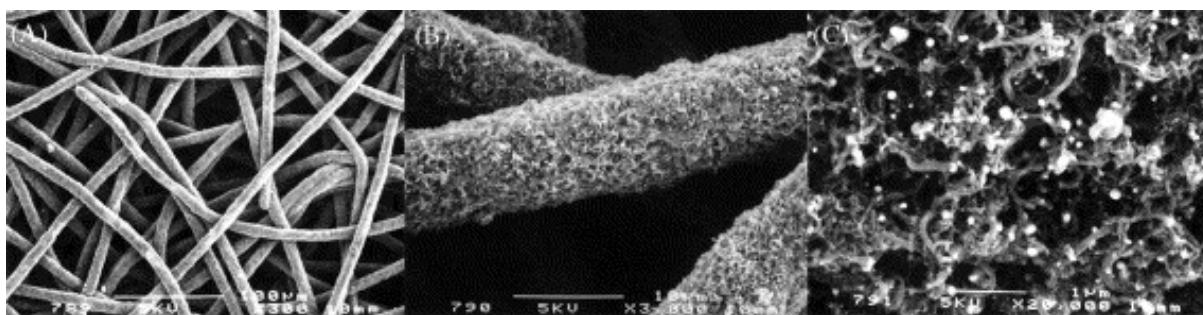


Figure 2.6: SEM images (A: 300 \times , B: 3000 \times and C: 20 000 \times) of carbon nanofibers obtained after 1 h synthesis over SMF_{Inconel} at 655 $^{\circ}$ C, Ar:C₂H₆:H₂ = 85:3:17 (600 ml(STP)/min). (Tribolet & Kiwi-Minsker, 2005a).

Catalysts based on metallic fibers are mainly used in extremely exothermic and fast gas phase reactions, where their excellent heat transfer properties can lead to avoiding hot spot formation and their associated negative effects on activity, reactor selectivity and thermal runaway.

It has also been proposed to use sintered metal fibers in multifunctional reactors by combining reaction and separation. Flue gas treatment with fly ash filtration and catalytic NO_x reduction treatment is one example of a multifunctional application of catalytically active sintered metal fibers (Fino *et al.* , 2006).

2.3 Adsorption

In the current study the VOC in low concentration will be removed from a process stream by adsorption. Upon breakthrough in an adsorber, the VOC will be desorbed with a higher concentration and sent to a catalytic oxidizer for destruction.

Adsorption is the term used to describe the tendency of molecules from an ambient fluid phase to adhere to the surface of a solid. In adsorption, the *adsorptive* accumulates on the *adsorbent* which is then loaded with *adsorbate*. Adsorption is a fundamental property

of matter, due to the attractive forces between molecules. The force field creates a region of low potential energy near the solid surface and, as a result, the molecular density close to the surface is generally greater than in the bulk gas.

The enhanced concentration at the surface accounts, in part, for the catalytic activity shown by many solid surfaces. However, most of the important applications of adsorption depend on the selectivity, i.e. the difference in the affinity of the surface for different components. As a result of this selectivity, adsorption offers, at least in principle, a straightforward means of purification (removal of an undesirable trace component from a fluid mixture).

Adsorption may be classified as chemisorption or physical adsorption (physisorption), depending on the nature of the surface forces. In physical adsorption the forces are relatively weak, involving mainly van der Waals interactions. The process is a nonselective condensation of gaseous molecules on the solid at relatively low temperature (i.e. -200 to -25°C) and with heats of adsorption less than about $15\text{--}20\text{ kJ/mol}$. In chemisorption there is significant electron transfer, equivalent to the formation of a chemical bond between the sorbate and the solid surface. Such interactions are both stronger and more specific than the forces of physical adsorption and are limited to monolayer coverage. The chemisorption is selective and takes place at relatively higher temperatures (i.e. 25 to 400°C) and with heats of adsorption on the order of $50\text{--}300\text{ kJ/mol}$ (Farrauto & Bartholomew, 1997).

Heterogeneous catalysis generally involves chemisorption of the reactants, but most applications of adsorption in separation and purification processes depend on physical adsorption. Chemisorption is sometimes used in trace impurity removal since very high selectivities can be achieved. However, in most situations the low capacity imposed by the monolayer limit and the difficulty of regenerating the spent adsorbent more than outweigh this advantage. The higher capacities achievable in physical adsorption result from multilayer formation and this is obviously critical in such applications as gas storage, but it is also an important consideration in most adsorption separation processes, since the process cost is directly related to the adsorbent capacity.

Water is a small, highly polar molecule and it is therefore strongly adsorbed on a polar surface as a result of the large contribution from the electrostatic forces. Polar adsorbents such as most zeolites, silica gel or activated alumina therefore adsorb water more strongly than they adsorb organic species. Such adsorbents are commonly called hydrophilic. In contrast, on a nonpolar surface where there is no electrostatic interaction water is held only very weakly and is easily displaced by organics. Such adsorbents are termed hydrophobic. The most common hydrophobic adsorbents are activated carbon and silicalite. The latter is of particular interest since the affinity for water is very low (Ruthven, 2001).

2.3.1 Activated Carbon Compared to Zeolites

Activated Carbon Based Adsorption

Activated carbon adsorption is a very common VOC control method. Activated carbon is normally made by thermal decomposition of carbonaceous material followed by activation with steam or carbon dioxide at elevated temperature ($700\text{--}1100^{\circ}\text{C}$). The activation process involves essentially the removal of tarry carbonization products formed during the pyrolysis, thereby opening the pores. Activated carbon is characterized by large surface

areas of between 300 and 4000 m²/g, which exceed those of all other sorbents. It has a polymodal pore size distribution, whereby microporosity (1-2.5 nm) prevails in gas-phase, and mesoporosity (> 3 nm) in liquid-phase applications. The adsorption capacity of activated carbon is determined almost exclusively by the micropores and their volume (Bart & Von Gemmingen, 2005). Once VOC breakthrough occurs the adsorbent is usually regenerated by heating the carbon with steam.

Carbon based systems do have limitations, particularly where the VOC-laden gas stream is hot (above 40 °C) or where the relative humidity is in excess of 60 %, where the VOC adsorptive capacity is reduced by competitive adsorption (McInnes, 1995; Khan & Ghoshal, 2000). Generally, inhomogenities hinder the convective transport of the heat released by adsorption and thus result in hot spots which, when they exceed the carbon ignition temperature, cause fires (Bart & Von Gemmingen, 2005).

Zeolite Based Adsorption

Blocki (1993) pointed out that the applications of activated carbon present some disadvantages as they are flammable, difficult to regenerate for high boiling solvents, promote polymerization or oxidation of some solvents to toxic or insoluble compounds and require humidity control. Therefore, it is necessary for a new type of adsorbent to replace the activated carbon. As a result, hydrophobic zeolite is now considered an alternative adsorbent, since it has good properties such as thermal stability and hydrophobicity (Blocki, 1993; Takeuchi *et al.*, 1995). Hydrophobic zeolite can be manufactured with precise pore size, allowing selective adsorption of some compounds while excluding others.

Zeolites are crystalline, hydrated aluminosilicates with a framework structure. Their three-dimensional, polyanionic networks are constructed of SiO₄ and AlO₄ tetrahedra linked through oxygen atoms (Breck, 1974; Barrer, 1979). Depending on the structure type, they contain regular channels or interlinked voids whose aperture diameters are in the micropore range. These pores contain water molecules and the cations necessary to balance the negative charge of the framework. The cations, which are mobile and can be exchanged, are mainly alkali metal or alkaline earth metal ions.

The homogeneous pore size prevents molecules larger than a certain size from entering the lattice, so zeolites are sometimes called molecular sieves, which allow them to adsorb selectively. Figure 2.7 shows the effective pore size of different zeolites and the kinetic molecular diameter of selected compounds. The non-flammable, thermal-stable and hydrophobic characteristics of zeolites can also play an important role in adsorption. The thermal stability and hydrophobicity of zeolites increase with the Si/Al-ratio in the zeolite framework. Synthetic hydrophobic zeolite, a pure crystalline silica molecular sieve, is non-flammable and capable of withstanding temperatures as high as 850 °C (Deng & Lin, 1995). Furthermore, hydrophobic zeolite has a low affinity for water, which is a useful physical property. McInnes (1995) reported that up to 90 % relative humidity could be handled with little adverse effect on the capacity of hydrophobic zeolite. Takeuchi *et al.* (1995) reported that the presence of water was found to reduce the amount of adsorption of the solvent-hydrophobic zeolite system, but water vapor showed no effect on the adsorption kinetics (thus overcoming the major limitation encountered in carbon adsorption). Hydrophobic zeolites are also non-flammable, so it can be used for some compounds that might catch fire with activated carbon (e.g. cyclohexane). The cost of

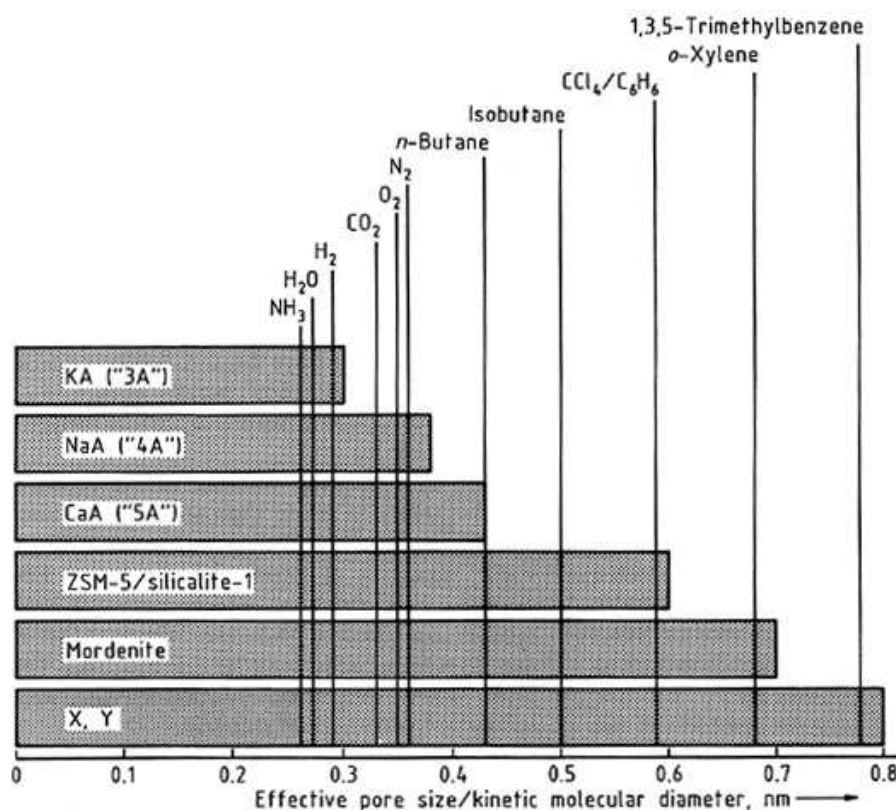


Figure 2.7: Correlation between the effective pore size of industrially important zeolites and the kinetic molecular diameter of selected compounds (room temperature) (Bart & Von Gemmingen, 2005).

hydrophobic zeolite is still very high, so its use is economically limited to applications for which activated carbon is not well suited.

2.3.2 MFI-zeolites

The hydrophobic zeolite silicalite (or silicalite-1) belongs to a family of zeolites which have the MFI structure (Meier *et al.*, 1996). Silicalite is a pure SiO₂ structure, whereas ZSM-5, which also has the MFI structure, covers a wide range of Si/Al-ratios (12-∞). ZSM-5 was first synthesized by Mobil in 1969 (Argauer & Landolt, 1969). The MFI structure belongs to the pentasil family of silica-rich zeolite structures based on a double five-ring secondary building unit. The structure of a characteristic layer of a pentasil zeolite is shown in Figure 2.8. The double five-ring unit can be stacked in different sequences to arrive at e.g. ZSM-5 or ZSM-11 structures. The MFI structure has pores built of 10-membered rings, resulting in pores of apertures 5.3×5.6 Å and 5.1×5.5 Å shown in Figure 2.9. The MFI structure is easier to visualize if only the cavity structure is represented, and not the framework structure. Linear parallel ten-ring channels are linked together by zig-zag shaped continuous pores with ten-ring apertures perpendicular to the channels, resulting in a three-dimensional cavity system as shown in Figure 2.10.

The MFI structure can adsorb molecules up to a kinetic molecular diameter of approximately 6 Å, which is equivalent to cyclohexane or toluene (see Figure 2.7).

The synthesis of ZSM-5 is usually carried out at 120-180 °C in pressure vessels. ZSM-5 can

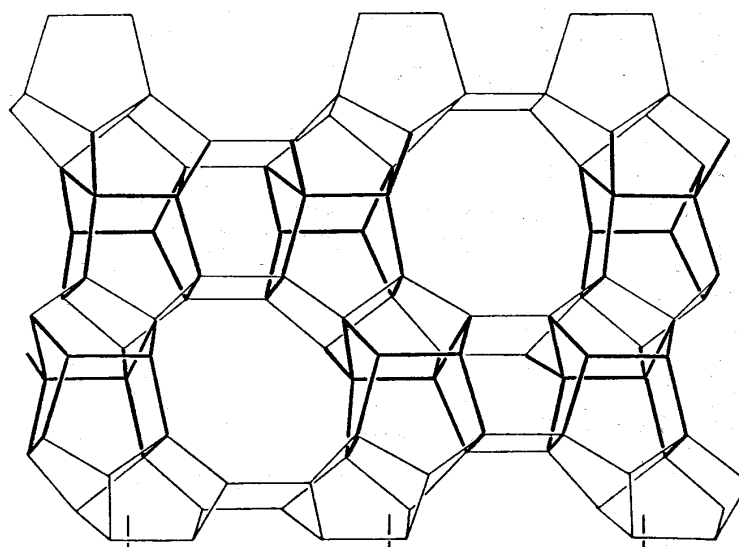


Figure 2.8: Schematic diagram of one layer of a pentasil zeolite structure showing how the framework is built up from the five-ring units (Kokotailo & Meier, 1979).

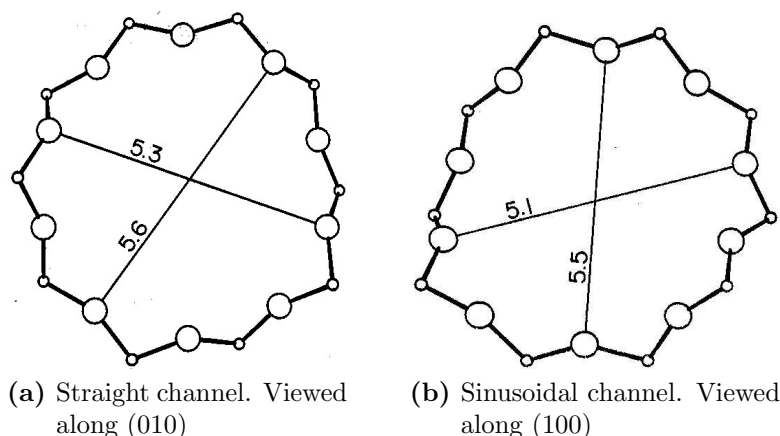


Figure 2.9: Scheme of 10-membered rings creating pore structure in MFI (Meier *et al.* , 1996).

be crystallized with or without template compounds. Tetrapropylammonium (TPA) salts are mainly used as template, but hexamethylenediamine and a series of other compounds are also suitable (Bart & Von Gemmingen, 2005). However, the ranges of Si/Al-ratios achievable in the product by varying the initial stoichiometry by the two methods are not identical. Thus, without a structure-directing agent, Si/Al-ratios between ca. 12 and 50 can be obtained, while adding a template compound significantly widens the range from ca. 15 to the aluminum-free (∞) form (silicalite-1).

The composition $17.1 (\text{TPA})_2\text{O} : \text{Na}_2\text{O} : \text{Al}_2\text{O}_3 : 27.7 \text{SiO}_2 : 453 \text{H}_2\text{O}$ is a typical example of a synthesis mixture for which tetrapropylammonium bromide (TPABr) is used as the template. After 5.5 days at 125°C , this gives ZSM-5 with a Si/Al-ratio of ca. 22 (Argauer & Landolt, 1969). In contrast, the synthesis mixture $11.2 \text{Na}_2\text{O} : \text{Al}_2\text{O}_3 : 70 \text{SiO}_2 : 3213 \text{H}_2\text{O}$, without a template and using colloidal silica as the source of silica, gives a zeolite with a Si/Al-ratio of 22 after 24 h at 190°C (Dai *et al.* , 1988).

The crystal suspension obtained is worked up by washing and filtration. The products are obtained in powder form by spray drying the zeolite suspension or by directly drying

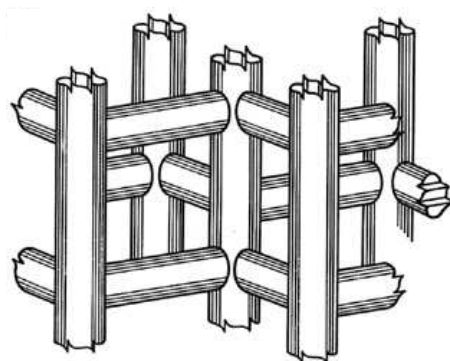


Figure 2.10: Hollow tube representation of ZSM-5 (structure type MFI) (Bart & Von Gemmingen, 2005).

the zeolite filter cake. If an organic template compound is used, it must be calcined from the ZSM-5 pores by heating to ca. 650 °C in air.

2.3.3 Zeolite Film Synthesis on Structured Surfaces

The synthesis of MFI zeolites (as well as other types of zeolites) can be controlled to produce layers, films or membranes of zeolite on different types of supports (e.g. polymers, metals, ceramics and glass) and by various procedures (Bein, 1996). Furthermore, Jansen *et al.* (1998) reviewed the supports, such as ceramics, crystal wafers, glass and steel, that have been used in direct synthesis of zeolitic coatings. Regarding synthesis of zeolitic films on structured supports an overview will be given in the following based on the review of Meille (2006). Most publications are dealing with zeolitic coatings meant for membrane applications or as catalytic materials. However, many of the materials will have similar benefits when used in adsorbers.

The simplest methods of preparing zeolite films or layers are based on a suspension of zeolite (Beers *et al.* , 2003; Wan *et al.* , 2001), but direct synthesis on the structured object is applied more often. Applying the zeolite crystals by a dip-coating technique results in a coating consisting of randomly oriented zeolite crystal layers useful for adsorption and catalysis purposes. The support is immersed in a suspension of the zeolite crystals in a solvent containing a binder and other additives followed by evaporation of the solvent and calcination. Since various zeolites are commercially available, this is a relatively simple coating method, as synthesis issues concerning the zeolite itself do not need to be considered. A binder, e.g. colloidal silica, is added to the suspension for better adherence of the zeolite crystals onto the support. Films of BEA zeolites on ceramic monoliths and metal gauze packing is described by Beers *et al.* (2003).

The advantage of directly grown zeolite layers compared to the dip-coated support is that a complete coverage of an oriented zeolite crystal layer can be achieved. The preparation of directly grown MFI zeolite coatings by hydrothermal synthesis on structured supports is largely reported (Louis *et al.* , 2001b; Rebrov *et al.* , 2001; Mies *et al.* , 2005; Nikolajsen *et al.* , 2006). The synthesized film can be deposited as a uniform layer at the surface or in localized positions (e.g. in microchannels) (Wan *et al.* , 2001, 2003).

To facilitate the zeolite synthesis on various substrates, Sterte *et al.* (2001) use the seed-film method, which consists of adsorbing some colloidal crystals of molecular sieve to

induce its growth as a continuous film. This method is also used to deposit an adhering monolayer of ZSM-5 on microchannels (Rebrov *et al.*, 2001; Chau *et al.*, 2002). Other pretreatments than seeding have been studied. In the case of Wloch *et al.* (2006), FeCrAlloy foils were pretreated thermally to obtain alumina whiskers on the surface. Small crystals of zeolite were synthesized to favor a better contact between the metal foil and the zeolite coating. In the case of Mies *et al.* (2005), molybdenum-containing plates were coated with ZSM-5. Different pretreatments, including chemical etching, atomic layer deposition (ALD, modification of chemical vapor deposition) of TiO_2 and Al_2O_3 , UV treatment of the TiO_2 layer, the use of a solution of templating agent, etc. were applied before zeolite synthesis. These treatments resulted in growth rate and/or nucleation rate enhancement.

In the current study the "seed-film method" (Hedlund *et al.*, 1997, 1999; Lassinantti *et al.*, 2001; Ohrman *et al.*, 2001; Sterte *et al.*, 2001) was applied on sintered metal fibers of stainless steel.

2.3.4 Small- and Micro-Scale Zeolite Film Systems

As discussed above in Section 2.2.4 and 2.3.3 there have been remarkable achievements in the development and applications of zeolite films on supports of different nature and characteristics. The same can be stated for zeolite membranes (Bein, 1996; Coronas & Santamaria, 2004b).

The majority of the applications proposed to date for zeolite membranes, both for separations and for reaction processes are of a relatively large scale. Laboratory examples include the use of zeolite membranes for the dehydrogenation of isobutane or ethylbenzene, Fischer-Tropsch synthesis, isobutene oligomerization, etc. (Coronas & Santamaria, 2004a). Large-scale processes are also prevalent in separation applications, where zeolite membranes have been applied, among other processes, to the separation of isomers (e.g., butane isomers, xylene isomers), of carbon dioxide from methane and of methanol from MTBE (Coronas & Santamaria, 1999). In spite of the promising results obtained in these laboratory studies, the only example of an industrial application of zeolite membranes is the solvent dehydration with zeolite-A membranes (Morigami *et al.*, 2001). In this process, zeolite membranes are used to separate a minority component (water) at a moderate total flux. Meindersma & de Haan (2002) believes that the price of zeolite membranes must undergo a reduction of a factor 10 for large-scale industrial implementations to be undertaken.

The current high price of zeolite membranes stems on the one hand from the cost of the materials used in synthesis (expensive templates, chemicals and porous supports) and, on the other, from the fact that syntheses are in most cases carried out in batch processes. Research has been undertaken to overcome these problems, but the goal of affordable, large-scale zeolite membrane units still seems a long way off (Coronas & Santamaria, 2004b).

Due to the difficulties with the large-scale applications, as discussed above, an alternative for the use of zeolite films and membranes have been intensely investigated in small- and micro-scale systems. Small-scale is defined as systems with a characteristic length in the mm to cm range and micro-scale with a characteristic length on the order of 10 to several hundred micrometers. Scaled-down systems have some general advantages over

conventional reactors, which make them especially suitable for fast, highly exothermic or endothermic chemical reactions (Kolb & Hessel, 2004; Kiwi-Minsker & Renken, 2005):

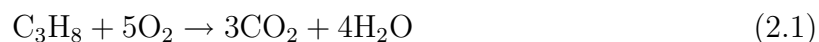
- Process intensification
- Inherent reactor safety
- Broader reaction conditions including up-to the explosion regime
- Distributed production
- Faster process development, due to easier scale-up

Most of these beneficial features of microstructured chemical reactors stem from their high surface to volume ratio in the range of $10,000\text{--}50,000\text{ m}^2/\text{m}^3$, which is 1 to 2 orders of magnitude higher than conventional chemical reactors (Kiwi-Minsker & Renken, 2005). This leads to heat transfer coefficients one order of magnitude higher than in traditional heat exchangers (Ehrfeld *et al.*, 2003). The high heat transfer rate also leads to full utilization of the catalysts during highly exo- and endothermic reactions, the avoidance of hot-spots formation and allows fast heating and cooling of reaction mixtures.

Zeolite interfaces are excellent candidates for micro-scale applications because of their high specificity in adsorption and catalysis, on account of which zeolites have been considered as the inorganic counterparts of enzymes (Derouane, 1998). Micro-scale devices tend to be highly demanding in terms of specificity and can therefore make use of these zeolitic materials. As discussed above (Section 2.2.4 and 2.3.3) several examples of microstructured, zeolite coated materials have been developed for catalytic purposes. Examples of small-scale applications used for removal of VOC by adsorption have also been presented recently. Shiraishi *et al.* (2003) built an apparatus for the removal of VOC from indoor air. The system consist of a photocatalytic reactor coupled with an adsorption/desorption device containing zeolites or activated carbon to concentrate formaldehyde, thus favoring the subsequent photocatalytic reaction. The adsorber was a honeycomb rotor measuring $D = 300\text{ mm}$, $h = 50\text{ mm}$ with 3 mm wide channels. Aguado *et al.* (2004) used MFI-type zeolite membranes to remove VOCs (n-hexane, formaldehyde and benzene) at only a few ppmv from air. Santamaria and co-workers also showed that these zeolite membranes doped with Pt could be used to retain the VOCs and eventually destroy them by oxidation aided by extra oxygen supplied from the other side of the membrane (Coronas & Santamaria, 2004b).

2.4 Catalytic Total Oxidation of Propane

In the current study the VOC model molecule was propane. After the concentration by adsorption the propane will be destroyed by total (deep, complete) oxidation according to the following reaction scheme:



Catalytic combustion is an alternative to conventional thermal combustion. The two main advantages offered by catalytic combustors over flame combustors are:

1. Catalytic combustion can be carried out over a wide range of fuel concentration in air and at lower temperatures.
2. The lower temperatures result in attaining NO_x emission levels substantially lower than possible with conventional combustors.

Historically, oxidation reactions have been carried out over either noble metal (e.g. Pt, Pd, Au and Ag) or transition metal oxides. Noble metals are more active. The main advantage of metal oxide catalysts is the lower cost of raw materials. By choosing the proper catalyst composition, higher thermal stability can be achieved with metal oxides. Noble metal catalysts are sometimes expensive and thermally unstable due to sintering or formation of volatile oxide compounds (Zwinkels *et al.* , 1993).

Most often supported rather than unsupported catalysts are applied, because they combine a high dispersion with a high degree of thermostability of the catalytic components (Farrauto & Bartholomew, 1997). The support, which is itself usually not catalytically active, is a thermostable, highly porous material onto which active component is applied. Frequently used supports are: Al_2O_3 , SiO_2 , active carbon and TiO_2 .

2.4.1 Hydrocarbon Total Oxidation over Metal Oxides

In this section the total oxidation of VOC over transition metal oxides (oxides of the metals from groups 3-12 of the periodic table) will be discussed based mainly on the discussions of Spivey (1987) and the references therein. The reaction conditions considered are oxygen rich, as would be encountered using air as the oxygen source and low concentration of VOC ($< 1\%$).

Oxidation catalysts have been classified according to the stability of the oxides of the metals. Those forming the most stable oxides ($\Delta H_{298\text{K}}^\circ > 270 \text{ kJ/mol O}$) are the alkali and alkali earth metals such as Sc, Ti, V, Cr and Mn; the rare earth metals, and the actinides Ge, In, Sn, Zn and Al. The metal oxides with intermediate stability ($\Delta H_{298\text{K}}^\circ = 170\text{--}270 \text{ kJ/mol O}$): Fe, Co, Ni, Cd, Sb and Pb. The unstable oxides ($\Delta H_{298\text{K}}^\circ < 170 \text{ kJ/mol O}$) are those of the noble metals: Ru, Rh, Pd, Pt, Ir, Au and Ag. This classification suggests that the metals with the unstable oxides remain mainly in reduced form and that the mechanism of the oxidation may therefore only involve molecular O_2 from the gas phase. On the contrary, the lattice oxygen of some metals forming stable or intermediately stable metal oxides is known to be involved in the oxidation of hydrocarbons. This has been shown by isotope studies using $^{18}\text{O}_2$ in the gas stream and measuring the ^{16}O and ^{18}O content of the products.

Another consequence of this metal oxide classification is that there is an optimum in the metal-oxygen interaction in an oxide catalyst. This is often referred to as a "volcano-plot". If the chemisorption is weak, only a small fraction of the surface sites will be covered and the reaction will be slow. As the chemisorption becomes too strong, the reaction rate will diminish as the active surface sites are covered irreversibly. Thus, the reaction rate can be observed to go through a maximum versus the metal oxide stability. Another example of this is shown for the CO dissociation in the methanation reaction over various metals (Bligaard *et al.* , 2004; Andersson *et al.* , 2006) as represented in Figure 2.11.

Metal oxides can also be classified according to their electrical conductivity, which is

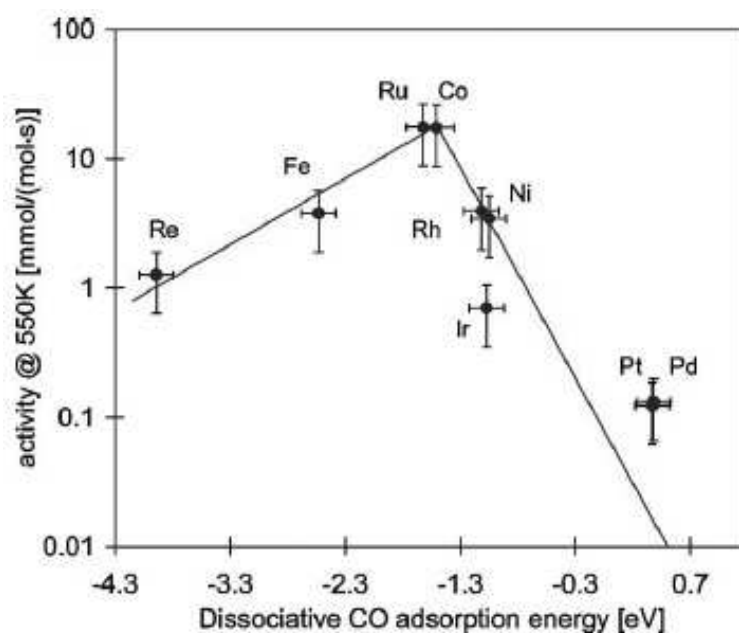


Figure 2.11: Activities of different supported transition metals as a function of the reaction energy for dissociative CO chemisorption (Bligaard *et al.*, 2004).

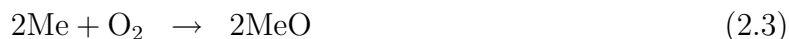
related to their catalytic activity. The three groups are:

1. n-type semiconductors
2. p-type semiconductors
3. Insulators

Electrical conductivity in n-type metal oxides arise from quasi-free electrons that exist due to an excess of electrons present in the lattice. N-type metal oxides are in general not active oxidation catalysts (V_2O_5 being an exception). P-type metal oxides are electron deficient in the lattice and conduct electrons by means of positive "holes". These oxides are generally active oxidation catalysts. The insulators have very low electrical conductivities and are generally not active catalysts. As a result of these different electrical properties oxygen adsorption occurs much easier on p-type oxides, because electrons can be easily removed from the metal cations to form active species such as O^- . Such a mechanism is not present on the n-type metal oxides, where oxygen adsorption can only take place on prerduced surfaces, so as to replace the oxide ions, O^{2-} , that were removed in a reducing pretreatment. The different oxygen species, adsorbed O^- on p-type metal oxides and lattice O^{2-} in n-type oxides lead to very different activities in the total oxidation reactions. Because, the adsorbed oxygen species are more active than the lattice oxide ions, p-type oxides are generally more active for total oxidation reactions.

The Mars-van Krevelen mechanism (or redox mechanism, which involves a reduction-oxidation cycle of the catalyst surface) proposed by Mars & van Krevelen (1954) is widely accepted as the mechanism for selective oxidation reactions over metal oxide catalysts (Spivey, 1987; Satterfield, 1991). The mechanism involves a first step, Equation 2.2, in which the oxidized metal surface (Me is a metal cation) oxidizes the reactant (R, which is a hydrocarbon) and a second step, Equation 2.3, where the metal surface is reoxidized

by gas-phase O_2 .



The active oxygen species in selective oxidation is generally believed to be lattice oxide O^{2-} species (Satterfield, 1991), which have nucleophilic behavior.

Haber and coworkers (Bielanski & Haber, 1991; Haber, 1997) propose that electrophilic, chemisorbed oxygen species (O_2^- and O^-) formed on the catalyst surface ensure a highly active non-selective catalytic behavior. The formation of O_2^- and O^- species on the oxide surface proceeds during the step of surface reoxidation via diatomic oxygen adsorption and electron transfer:



where the O^{2-} is directly incorporated into the oxide lattice and $[]$ indicates an adsorption site. However, other authors are not fully convinced of this (Sokolovskii, 1990; Satterfield, 1991; Busca, 1996).

The activity of the catalyst in total oxidation is known to depend on the oxygen mobility on the catalyst surface, which results from the so-called "weak" metal-oxygen bonds. "Weak" metal-oxygen bonds means low energies of oxygen binding to the oxide surface. It has been reported that a high number of these weakly bonded oxygen species are required for total oxidation reactions (Sokolovskii, 1990).

The most active single metal oxides for the total oxidation of a variety of organic compounds are known to be oxides of V, Cr, Mn, Fe, Co, Ni and Cu. These p-type semiconductor oxides (except V) can adsorb oxygen by donation of an electron from the metal cation. This leads to the formation of electrophilic oxygen species (O_2^- and O^-), which are known to be active in total oxidation. The oxidation mechanism on mixed metal oxides is thought to be similar to that on single metal oxides. However, the activity over mixed metal oxides is generally higher compared to the single metal oxides. This is believed to be due to the readily available multiple energy levels of the metals and their associated oxygen anions, making them more mobile on the surface and more accessible to the organic reactant as compared to single oxides.

2.4.2 Propane Total Oxidation over Cobalt Oxide

It has been reported that among the single metal oxides, Co_3O_4 is the most active in hydrocarbon catalytic combustion (Boreskov, 1982). For the total oxidation of the model molecule, propane, it has also been reported that the most active single metal oxide is Co_3O_4 (Kummer, 1980; Neyestanaki & Lindfors, 1995; Yu Yao, 1974, 1975; Spivey & Butt, 1992; O'Connell *et al.*, 1999; Pope *et al.*, 1976; Torncrona *et al.*, 1997) including studies of Co_3O_4 supported on a structured, metal grid support by Yuranov *et al.* (2002) and on structured SMF (Yuranov *et al.*, 2003). However, the practical use of Co_3O_4 is limited to temperatures below 730 °C, where it decomposes to CoO. Furthermore, reactivity towards supports such as alumina have been reported. Garbowski *et al.* (1990) found that the

Co(II) ions react with alumina to form the much more inactive CoAl_2O_4 at temperatures as low as 500°C .

Solid-state chemical studies showed that Co_3O_4 adsorbs oxygen from the gas phase resulting in the surface being covered by a layer containing Co^{3+} cations and excess oxygen in the form of the electrophilic O^- species (Tyuliev & Angelov, 1988). This is in agreement with the general theory for metal oxides discussed above (Section 2.4.1). However, it has been reported that nucleophilic oxygen species (lattice O^{2-} at the oxidized surface) are involved in the catalytic combustion of propane over Co_3O_4 . This should occur via overoxidation of adsorbed partially oxidized compounds (Finocchio *et al.*, 1996).

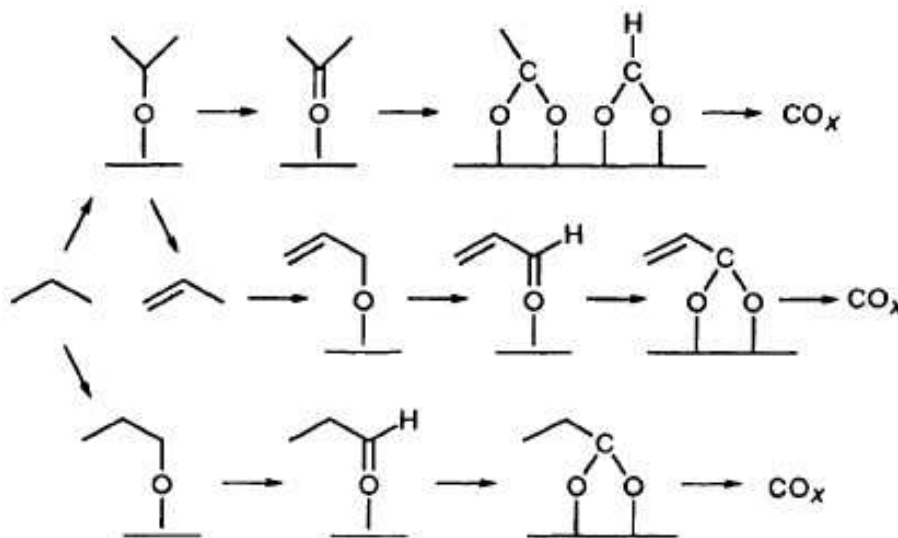


Figure 2.12: Proposed reaction scheme for total oxidation of propane over Co_3O_4 . (Finocchio *et al.*, 1996).

Finocchio *et al.* (1996) proposed the reaction scheme shown in Figure 2.12 based on Fourier-transform infrared (FTIR) spectroscopy studies of Co_3O_4 . The powder was pressed into disks and the experiments were performed in the absence of gas phase oxygen using preoxidized and outgassed catalyst. Three pathways were proposed:

1. Reaction through activation of the weak C-H bond at the C(2) was predominant.
2. Attack at C(1) to form propanoate species.
3. Attack at C(3) of propene produced from propane from the first surface reaction route.

At approximately 250°C they start finding total propane oxidation over the preoxidized Co_3O_4 catalyst.

It seems evident that the oxidation of organic compounds occur at the expense of the oxygen excess at the preoxidized ($\text{Co}_3\text{O}_{4+\epsilon}$) surface, which is reduced by the hydrocarbon to nearly stoichiometric Co_3O_4 upon reaction. The oxidized surface has been found to contain almost exclusively Co^{3+} cations that are reduced to Co^{2+} cations by hydrocarbons and hydrogen (Tyuliev & Angelov, 1988; Busca *et al.*, 1990). Electrophilic oxygen species (O_2^- and O^-) are thought to be easily formed on the surface of this oxide and to take part of the oxidized overlayer (Bielanski & Haber, 1991; Tyuliev & Angelov, 1988). According

to Haber and coworkers (Bielanski & Haber, 1991) such oxygen species are expected to attack the C=C double bonds of alkenes causing oxidative cleavage to carbonyl compounds (e.g. formaldehyde and acetaldehyde from propene) leading finally to their total oxidation. In contrast to this proposed mechanism, the data of Finocchio *et al.* (1996) show that propene oxidation on the preoxidized $\text{Co}_3\text{O}_{4+\varepsilon}$ surface clearly gives rise to acrylate species as the first intermediates, which is a typical product of nucleophilic oxidation at the allylic C-H bonds (Bielanski & Haber, 1991). In fact, all observed oxidation reactions could be explained by the activity of the nucleophilic oxygen species. It was therefore concluded that no molecular oxygen species were found adsorbed on the catalyst. Finally, they concluded that the catalytic total oxidation over Co_3O_4 catalysts most probably takes place via a typical Mars-van Krevelen mechanism, with the trivalent cobalt oxidizing center and nucleophilic oxygen species (i.e. lattice O^{2-} anions at the oxidized surface) as the active oxygen species.

Prereduction of the cobalt oxide has been reported to increase the catalytic activity (Torn-crona *et al.* , 1997; Yuranov *et al.* , 2002). However, since the cobalt oxide surface adapts itself to the reaction conditions the activity will quickly decrease in an oxygen rich atmosphere, where the reduced cobalt species are oxidized. In contrast, the high activity obtained with the prereduced cobalt oxide catalyst could be retained in stoichiometric reaction mixture. It is believed that the reduced cobalt species stabilize the electrophilic oxygen (O_2^- and O^-) active in the total oxidation (Yuranov *et al.* , 2002).

2.5 Kinetics and Mass Transfer

Heterogeneous catalysis takes place on the surface of solids, often in the form of porous particles. In general, the reaction path of a heterogeneous catalytic reaction proceeds through 7 different physical and chemical steps.

Starting with a reactant molecule A and ending with product molecule B :

1. External diffusion: transfer of A from the fluid phase surrounding the catalyst particle (bulk fluid phase) to the external particle surface.
2. Internal diffusion: transport of A from external surface through the pores towards active sites on the internal surface.
3. Chemisorption of A on an active site $[]$ forming $[A]$
4. Surface reaction of $[A]$ to $[B]$
5. Desorption of $[B]$ to reach B and $[]$
6. Internal diffusion: transport of B from the active site through the pores towards the external surface.
7. External diffusion: transfer of B from the external particle surface to the bulk fluid phase.

Depending on the reaction parameters (e.g. temperature, flow rate, catalyst particle size and concentrations) each one of these steps can be rate determining for the overall reaction rate.

The reaction kinetics relates to steps 3-5 above and refers to the rates of chemical reactions. The kinetics is important for a number of reasons:

- Knowledge of kinetics, especially the orders of reaction with respect to reactants and products, is essential (but not always sufficient) for the definition of the mechanism of the reaction.
- The best design of the catalytic reactor, including the size and shape of the catalyst bed, depends critically upon information concerning the reaction kinetics as well as on the thermo chemistry of the system.
- The effect of temperature on the rate can provide a useful clue to the nature of the slowest elementary step.

The kinetics of any reaction is dependent on temperature. This is accounted for by the Arrhenius description of the rate constant. The activation energy of the reaction, E_a , can be found directly from the Arrhenius equation for a homogeneous reaction. However, for a heterogeneous reaction the surface coverage will also vary with temperature which will have to be taken into account. Hence, the true activation energy found at lower temperatures can change to the apparent activation energy at higher temperatures.

Mass transfer relates to steps 1, 2 and 6, 7 above. Mass transfer is one of the big problems in heterogeneous catalysis and in general we try to avoid it, since it does not allow an optimal utilization of the catalyst. There are two types of mass transfer: external and internal.

2.5.1 External Mass Transfer

The transfer of reactants from the bulk fluid phase to the external surface of the catalyst is described by the film model:

$$r_{v,observed} = k_f a' (C_{bulk} - C_{surface}) \quad [\text{mol}/\text{m}^3 \cdot \text{s}] \quad (2.7)$$

$$r_{w,observed} = \frac{k_f a'}{\rho_{cat}} (C_{bulk} - C_{surface}) \quad [\text{mol}/\text{kg} \cdot \text{s}] \quad (2.8)$$

where k_f is the mass transfer coefficient, $a' = A_p/V_p$ the outer specific particle area and ρ_{cat} the density of the catalyst. The subscripts v and w denotes quantities on volumetric and weight basis respectively. The virtual film thickness depends primarily on the hydrodynamics of the system and hence on the Reynolds number, Re and the Schmidt number, Sc . Various correlations have been developed for different reactor types and varying shapes of particles in terms of the following dimensionless variables:

Sherwood number:

$$Sh = \frac{k_f d_p}{D} = f(Re, Sc) \quad (2.9)$$

Reynolds number:

$$Re = \frac{v \rho d}{\mu} \quad (2.10)$$

the Reynolds number is based on the diameter of a pipe d or on the characteristic length of the catalyst particle, d_p appropriate to the geometry of the particular system; and the

Schmidt number:

$$Sc = \frac{\mu}{\rho D} \quad (2.11)$$

Sometimes the mass transfer correlations use the j -factor:

$$j_D = \frac{Sh}{ReSc^{1/3}} \quad (2.12)$$

as an alternative to the Sherwood number due to the analogies with heat transfer given by the Chilton-Colburn j -factor analogy (Chilton & Colburn, 1934). These correlations are used to estimate the value of the mass transfer coefficient k_f .

When a heterogeneous catalytic reaction is strongly influenced by external mass transfer the apparent activation energy will be in the range 4-12 kJ/mol for gases and the apparent reaction order will appear to be one, since mass transfer is a first-order process (Satterfield, 1980, p. 320).

To test to which degree a reaction is limited by external diffusion, the dimensionless number DamköhlerII relates the intrinsic reaction rate to the rate of mass transfer. However, the Carberry number, Ca , is often more applicable since it relates the observed rate of reaction to the maximum rate of external mass transfer (Kapteijn & Moulijn, 1997, p.1365):

DamköhlerII:

$$DaII_v = \frac{k_v C_{bulk}^n}{k_f a' C_{bulk}} \quad (2.13)$$

$$DaII_w = \frac{k_w C_{bulk}^n \rho_{cat}}{k_f a' C_{bulk}} \quad (2.14)$$

Carberry Number:

$$Ca_v = \frac{r_{v,observed}}{k_f a' C_{bulk}} \quad (2.15)$$

$$Ca_w = \frac{r_{w,observed} \rho_{cat}}{k_f a' C_{bulk}} \quad (2.16)$$

where k_v and k_w are the reaction rate constants on a volumetric (v) and weight (w) basis, respectively. A criterion for the absence of extra-particle gradients can be derived from the definition of an effectiveness factor for a particle. The deviation of the observed reaction rate from the intrinsic rate should be less than 5 %:

$$\eta = \frac{\text{observed reaction rate}}{\text{rate without gradients}} = \frac{r_{v,observed}}{r_{v,intrinsic}(C_{bulk}, T_{bulk})} = 1 \pm 0.05 \quad (2.17)$$

The minus sign applies to positive reaction orders and endothermal reactions, the plus sign to negative reaction orders and exothermal reactions. For an isothermal n^{th} -order irreversible reaction this results in (Kapteijn & Moulijn, 1997):

$$Ca < \frac{0.05}{|n|} \quad (2.18)$$

2.5.2 Internal Mass Transfer

Diffusion within the porous catalyst particles can also affect the overall rate. Internal mass transfer limitations result in concentration gradients inside the catalyst particles. When a heterogeneous catalytic reaction is strongly influenced by internal mass transfer the apparent activation energy will tend to one-half the intrinsic activation energy and the apparent reaction order will tend to one half the real reaction order (for single reactant reactions and bulk diffusion in the pores) (Satterfield, 1970, p. 138-139).

To test to which degree a reaction is influenced by internal diffusion the dimensionless number Thiele modulus, Φ , relates the intrinsic kinetics to the maximum effective rate of internal diffusion. However, in analogy with the DamköhlerII and Carberry numbers, the Weisz Modulus, Ψ , is often more applicable since it relates the observed rate of reaction to the rate of internal mass transfer (Emig & Dittmeyer, 1997, p.1217):

Generalized Thiele Modulus:

$$\Phi = \frac{V_p}{A_p} \sqrt{\frac{\frac{n+1}{2} k_v C^{n-1}}{D_e}} \quad (2.19)$$

Generalized Weisz Modulus:

$$\Psi = \left(\frac{V_p}{A_p} \right)^2 \frac{n+1}{2} \frac{r_{v,observed}}{D_e C_{surface}} \quad (2.20)$$

where n is the reaction order, $r_{v,observed}$ the observed (effective) rate of reaction and D_e the effective diffusivity.

The Thiele modulus and the Weisz modulus are linked through the effectiveness factor, η :

$$\Psi = \eta \Phi^2 \quad (2.21)$$

The effective diffusivity is $D_e = (\varepsilon_p D) / \tau_p$, where $\varepsilon_p \sim 0.3-0.6$ is the pore fraction in the catalyst and τ_p is the tortuosity factor $\sim 2-8$. When these are not known by measurement the values: $\varepsilon_p = 0.5$ and $\tau_p = 4$ can be used (Perry *et al.*, 1997, p. 23-29). The diffusivity in a porous media is increasingly influenced by redirecting collisions between the pore walls and the diffusing molecules as the pore size becomes smaller. This can lead to transition regime diffusion given by the Bosanquet equation (Bosanquet, 1944):

$$\frac{1}{D} = \frac{1}{D_m} + \frac{1}{D_K} \quad (2.22)$$

where D_m is the molecular diffusivity corresponding to intermolecular collisions and D_K is the Knudsen diffusivity corresponding to collisions of the molecules with the pore walls:

$$D_K = 9700 r_p \sqrt{\frac{T}{M}} \quad (2.23)$$

where r_p is the pore radius in centimeters, T the temperature in degrees kelvin and M the molecular weight of the diffusing molecule (Satterfield, 1970).

In the case of zeolites, the pore sizes are so small that the pore diffusion becomes even slower than described by the Knudsen diffusivity. This type of diffusion is called "configurational diffusion" (Weisz, 1973). In transitional regimes between Knudsen and configurational diffusion the Bosanquet equation (Equation 2.22) can be used with D_m replaced by the configurational diffusivity.

2.5.3 Kinetic Models

First, for a homogeneous, elementary, bimolecular reaction (occurring at the instant of collision of two molecules) between two species A and B the reaction rate is given by:

$$r = kC_A C_B \quad [\text{mol}/\text{m}^3 \cdot \text{s}] \quad (2.24)$$

$$= k_0 \exp\left(\frac{-E_a}{RT}\right) C_A C_B \quad (2.25)$$

Equation 2.25 is known as the Arrhenius expression when k_0 , the preexponential factor, is taken to be temperature independent. From collision theory, k_0 varies as the square root of the temperature, but since the effect of temperature on the exponential term is much more important k_0 may be taken to be temperature independent with little error.

By analogy, a simple expression for the reaction rate of a heterogeneously catalyzed reaction between species A and B can be defined as:

$$r = k_0 \exp\left(\frac{-E_a}{RT}\right) \cdot f(C_A, C_B) \quad [\text{mol}/\text{kg} \cdot \text{s}] \quad (2.26)$$

The function of the concentrations which is usually the easiest to use in correlating data, consists of simple power functions and is called the power rate law.

Power Rate Law:

$$r = kC_A^n C_B^m \quad [\text{mol}/\text{g} \cdot \text{s}] \quad (2.27)$$

where, the exponents n and m are the reaction orders. This is an empirical rate expression, which is not based on a specific reaction mechanism. For this expression to be useful, the intrinsic reaction orders should be constant over the concentration range of interest. The reaction orders can be integer, fractional, negative, zero or positive. However, many catalytic reactions follow a simple relationship like the power rate law over a sufficiently wide range of conditions to be useful. Despite this model being empirical, the theoretically derived models based on reaction mechanisms often reduce to power law forms in which n and m are integers or half-integers (Satterfield, 1980).

It is frequently observed that the reaction orders yield fractional orders, when expressing the rate by the simple power rate law. This is because the driving force for the reaction has been assumed to be a function of the gas phase concentration. A more logical approach in heterogenous catalysis would be to use the concentration of species on the surface of the catalyst, since this is where the reaction takes place. This can be done by using knowledge from adsorption phenomena. Furthermore, the reaction takes place through a series of steps (e.g. reactant adsorption, surface reaction, product desorption). It is often assumed that one of these steps is rate-limiting and all the other steps are assumed to be in equilibrium with one another, which simplifies the theoretical formulation. In many cases it appears that the rate of reaction of one or more chemisorbed species is the rate-limiting step, rather than the rate of adsorption or desorption. The kinetic formulations based on this assumption is called the Langmuir-Hinshelwood. For reactions assumed to be between a chemisorbed species and a molecule in the fluid phase the models are termed Eley-Rideal.

Mars-van Krevelen Model:

The Mars-van Krevelen model is often used to describe the reduction-oxidation cycle of the catalyst surface in partial oxidation of hydrocarbons (Mars & van Krevelen, 1954; Satterfield, 1980; Finocchio *et al.*, 1996). The model has been used successfully to describe many oxidation reactions including total oxidation of VOCs (Jaswal *et al.*, 1969; Gangwal *et al.*, 1988; Abdullah *et al.*, 2003; Cellier *et al.*, 2006). The derivation of the model makes no assumption about the form of oxygen on the catalyst (i.e. chemisorbed, O^- and O_2^- , or lattice oxygen, O^{2-}). However, lattice oxygen seem to follow this model, whereas some chemisorbed systems can better be described and understood by Langmuir-Hinshelwood or Eley-Rideal models.

The model assumes that the rate of oxidation of the reactant is proportional to the fraction of active sites in oxidized state and to the hydrocarbon partial pressure. The rate of reoxidation of the catalyst is taken to be proportional to the fraction of sites on the catalyst in the reduced (empty) state and to $P_{O_2}^n$:

$$r = kP_{HC}(1 - \Theta) = \frac{k^*}{\beta} P_{O_2}^n \Theta \quad (2.28)$$

where

P_{HC} : partial pressure of hydrocarbon

k : reaction rate constant for oxidation of hydrocarbon

k^* : reaction rate constant for surface reoxidation

β : moles O_2 consumed per mole of hydrocarbon reacted

Θ : fraction of active sites in reduced state

Equation 2.28 can be rearranged by eliminating Θ to give:

$$r = \frac{1}{\frac{\beta}{k^* P_{O_2}^n} + \frac{1}{k P_{HC}}} \quad [\text{mol/g.s}] \quad (2.29)$$

The parameters of these kinetic models were estimated by nonlinear regression analysis as discussed in the following section.

2.5.4 Nonlinear Regression Analysis

The kinetics of the model reaction over different catalysts and for different kinetic models were fitted by nonlinear regression to the output data from the experiments. The regression estimates the parameters in the rate expression by a least squares method.

The program used for this parameter estimation was a Marquardt-Levenberg program, with the SUBROUTINE VA07AD, from the Harwell Subroutine Library (Hopper, 1978). An example of the program is shown in Appendix D.

Least Squares Method

A mathematical model consists in an output variable \hat{y} , which is a function of the p model parameters b_1, b_2, \dots, b_p and the k input variables x_1, x_2, \dots, x_k :

$$\hat{y} = f(\mathbf{b}, \mathbf{x}) \quad (2.30)$$

To experimentally estimate the model parameters it is necessary to fit the parameters to a number of measured output variables y . This fitting can be done by a least squares method. The vector \mathbf{b} of parameters is evaluated through n observations of y for different values of the input variables \mathbf{x} . The least squares method estimates \mathbf{b} by minimizing the sum of squares of the residuals:

$$ssq_{min} = \min_{\mathbf{b}} \sum_{u=1}^n (y_u - \hat{y}_u)^2 \quad (2.31)$$

where y_u is the output value for the u^{th} observation.

This is the best estimation of the parameters, \mathbf{b} , according to the theory of estimation, if

$$y = \hat{y} + \epsilon \quad (2.32)$$

where ϵ is a stochastic, normal distributed error on the measurement with the mean 0 and a constant variance, σ^2 (Kittrell, 1970; Himmelblau, 1970). ϵ is the inevitable error on the measurements, but will also include any error caused by the model, where it deviates from the true behavior of the system. The least squares method will seek to minimize the error of the model by distributing it evenly on the input variables, \mathbf{x} .

Variance Stabilizing Transformation of Model

For an unweighted least-squares estimation it is an important requirement for the efficiency and validity that, to a rough approximation, the variance of the response y is independent of the magnitude of y . In the catalyst activity measurements for the kinetics the relative error of the response was found to be approximately constant. In this case a constant standard deviation can be obtained by transforming output variable y to $y' = \ln y$ (Box & Draper, 1987, p.283). In this transformed model, an unweighted least-squares method can be employed. The residuals were changed and the problem for minimization, Equation 2.31, was changed to:

$$ssq_{min} = \min_{\mathbf{b}} \sum_{u=1}^n (\ln y_u - \ln \hat{y}_u)^2 \quad (2.33)$$

Rescaling the Arrhenius Expression

In the Arrhenius expression of the rate constants there is a tendency to be a close correlation between the activation energy E_a and the preexponential factor k_0 . This can be removed by making experiments over a wide range of temperatures or by rearranging the expression. In order to remove this correlation and get a better fit of the data, the Arrhenius expression

$$k = k_0 \exp\left(-\frac{E_a}{RT}\right) \quad (2.34)$$

could be rescaled to

$$k = k' \exp \left\{ -\frac{E_a}{R} \left(\frac{1}{T} - \frac{1}{T'} \right) \right\} \quad (2.35)$$

where k' is the new rate constant at the reference temperature T' , which should be chosen in the region of experimental temperatures, preferably centrally (Bates & Watts, 1988; Kondratenko & Perez-Ramirez, 2006).

2.6 Design of Experiments

To ease the understanding of the applied methods some basic concepts in design of experiments (DOE) will be introduced in the following. The theory is based on Fürbringer (2005) and Box *et al.* (2005).

2.6.1 Definitions in DOE

Some definitions that are used to evaluate a design of experiment:

- A **response** is any consequence of a phenomenon. It can be qualitative or quantitative, but it is easier to work with a quantifiable response. Response = dependent variable.
- A **factor** is any variable (or parameter) which has an influence on the studied phenomenon. The factors are considered as the possible causes of the response. Factor = independent variable.
- The **level** is the state or value of a factor.
- For numerical accuracy and to generate the designs, natural variables are **standardized** (coded) so that the variable is centered on zero and varying in the interval $[-1,1]$. The coded variable x_j is obtained by the transformation of the natural variable u_j :

$$x_j = \frac{u_j - u_j(0)}{\Delta u} \quad (2.36)$$

u : natural variable

$u(0)$: center of the interval of the natural variable

x : coded variable

Δu : half of the natural interval

The advantage of using the factorial design over a normal "one factor at a time" (OFAT) design is that the interactions between the factors are taken into account, due to the structured, simultaneous variation of the factors. The full factorial design allows the determination of main effects and linear interactions of the factors. The results can then

be represented in the form of a first order polynomial with interactions as presented in Equation 2.37.

$$Y(x) = a_0 + \sum_{i=1}^N a_i x_i + \sum_{i \neq j}^N a_{ij} x_i x_j + \sum_{i \neq j \neq k}^N a_{ijk} x_i x_j x_k + \dots + a_{i\dots N} x_i \dots x_N \quad (2.37)$$

This polynomial counts 2^N coefficients ($a_0, a_i \dots$) and each factor appears only in first degree. The optimal² design for determining the coefficients of this model is a factorial design. The coefficients are called the effects of the factors (x_i) and are distinguished as follows:

a_0 : constant effect

a_i : main half effects

a_{ij} : first order interaction half effects

a_{ijk} : second order interaction half effects

The a_i are called "half" effects because they correspond to the variation between the center of the domain and the border.

2.6.2 Result Analysis

Results are normally treated by one of two ways:

1. Comparison of the data with a statistical distribution (such as the normal distribution)
2. Comparison of a subset of the data with another subset of the data. This can be done by comparing the effects with the residual error, as is the case of the analysis of variance (ANOVA).

To test the validity of a constant effect model the ANOVA procedure compares the sum of the squares of the effects with the sum of the squares of the residual. The sum of squares (SS) must be standardized by the degree of freedom (DF). The total degrees of freedom is equal to the number of data. For each factor the degree of freedom is the number of levels minus one. The degree of freedom of the mean is 1. Then the mean squares (MS) are obtained by dividing the sum of square by the degree of freedom.

The MS of the effects are then compared with the mean square of the residual errors. It is expected that the mean square of a significant effect be significantly greater than the mean square of the residual errors. The evaluation of the ratio is done in an objective way by comparing it with the probability (P) of such a ratio between two random variables following a χ^2 distribution. This comparison is then done with the distribution $F_{\alpha\nu}$ of Fisher. A higher probability means that the effect is less significant. The distribution

²Optimal with respect to information. In relation to the cost or other types of experimental limitations this optimum could change.

$F_{\alpha\nu}$ depends on the degrees of freedom α and ν of the considered effect as well as on the residual error.

The results of the experiments were treated by ANOVA. The criterion for choosing the factors with a significant effect on the response was chosen to be a probability (of the effect to be noise) lower than 5 %.

Chapter 3

Experimental Details

3.1 Support - Sintered Metal Fibers

The support for both the adsorbent and the oxidation catalyst was filters of sintered metal fibers, SMF.

3.1.1 Characteristics

The characteristics of the applied SMF are given in Table 3.1.

Table 3.1: Characteristics of filters of sintered metal fibers, SMF. [†]

Name	Material	Composition [wt.%]	Fiber diameter [μm]	Filter thickness [mm]	Porosity
SMF _{SS}	AISI316L (stainless steel)	Cr: 16.5 %, Ni: 12 %, Mo: 2.5 %, Mn: 2 %, Si: 1 %, P: 0.05 %, C: 0.03 %, S: 0.03 %, Fe: balance	20	0.30	0.83
SMF _{FeCrAlloy}	FeCrAlloy	Cr: 20 %, Al: 4.75 %, Ni: 0.35 %, Mn: 0.35 %, Si: 0.35 %, Y: 0.3 %, Cu: 0.15 %, P: 0.035 %, C: 0.03 %, S: 0.01 %, Fe: balance	20	0.30	0.71
SMF _{Inconel}	Inconel 601	Ni: 60.5 %, Cr: 23 %, Al: 1.25 %, Cu: 1 %, Mn: 1 %, Si: 0.5 %, C: 0.1 %, S: 0.015 %, Fe: balance	8	0.49	0.81

[†] Data given by the supplier: Southwest Screens & Filters (Sprimont, Belgium), now: Bekaert Fibre Technology (Zwevegem, Belgium).

The specific surface area (SSA_w) of the sintered metal fibers is difficult to measure by the BET method, since the fibers are not porous and the SSA in relation to weight is very

low. However, the geometry of the fibrous matrix is well defined and the SSA can thus be estimated, by considering the fibers infinite cylinders and $V_{fiber} = V_{bed}(1 - \varepsilon)$:

$$SSA_v = \frac{A_{fiber}}{V_{bed}} = \frac{A_{fiber}}{V_{fiber}}(1 - \varepsilon) = \frac{\pi d_f L}{\pi/4 d_f^2 L}(1 - \varepsilon) = \frac{4}{d_f}(1 - \varepsilon) \quad [\text{m}^2/\text{m}^3] \quad (3.1)$$

$$SSA_w = \frac{A_{fiber}}{V_{fiber}\rho}(1 - \varepsilon) = \frac{4}{d_f\rho}(1 - \varepsilon) \quad [\text{m}^2/\text{kg}] \quad (3.2)$$

where A is the surface area, V the volume and ρ the metal density. The values of the fiber diameter d_f and the filter porosity ε are taken from Table 3.1, the results are shown in Table 3.2.

Table 3.2: Estimated values of the specific surface area of SMF filters.

Name	Density [kg/m ³]	SSA _v [m ² /m ³]	SSA _w [m ² /g]
SMF _{SS}	8000	34000	0.03
SMF _{FeCrAlloy}	7200	58000	0.03
SMF _{Inconel}	8110	95000	0.06

3.1.2 Pretreatment

Calcination

All filters were cleaned and calcined before use. They were washed three times in acetone, followed by half an hour in boiling toluene. After air drying the filters were calcined according to Table 3.3.

Table 3.3: Calcination details.

Filter type	Calcination temperature [°C]	Calcination time [h]
SMF _{SS}	550	3
SMF _{FeCrAlloy}	650	3
SMF _{Inconel}	650	3

3.2 Reactors and Experimental Setup

Two different reactors were used in the current study:

Micromeritics reactor: A quartz reactor ($\varnothing=10$ mm), fitting the Micromeritics AutoChem 2910 system.

Pilot reactor: A stainless steel, pilot reactor ($\varnothing=19$ mm), used in a setup from Vinci Technologies, Lyon, France.

The general features of the two systems are described in the following. More details regarding their use for the specific measurements can be found in Sections 3.3 and 3.4. Table 3.4 gives an overview of the experiments the two systems/reactors were used for.

Table 3.4: Overview of experiments and reactor use.

Micromeritics reactor			Pilot reactor		
Experiments	Section		Experiments	Section	
	Exp. details	Results		Exp. details	Results
Adsorption isotherms	3.3.2	4.2	Breakthrough curves	3.3.3	4.4
Catalyst screening	3.4.2	5.4	Pressure drop	3.3.4	4.6
			Catalyst testing	3.4.3	5.2.1, 5.5, 7

3.2.1 Micromeritics Reactor

Reactor

The quartz reactor is shown in Figure 3.1. It was used with disks of SMF placed coaxially in the tube. Some inert quartz wool was always placed in the bottom, conical part of the tube to avoid active particles to enter the apparatus.

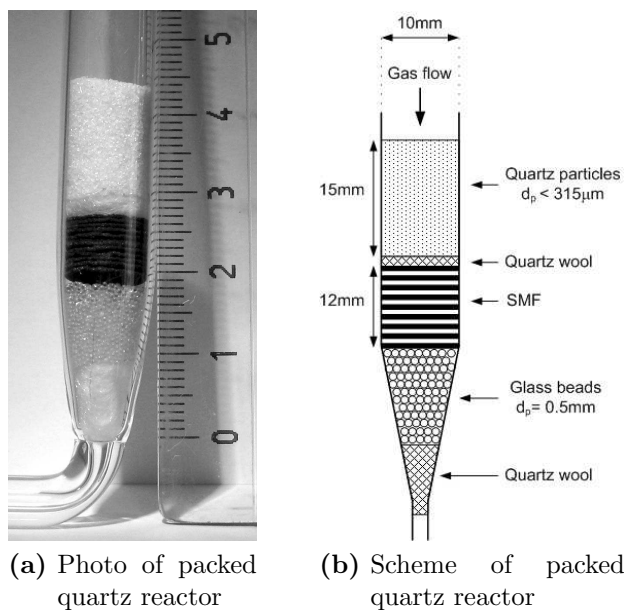


Figure 3.1: Quartz reactor for the Micromeritics setup. Packed for catalyst activity screening.

Experimental Setup

The Micromeritics setup was equipped with mass flow controllers for the gases. Two different gases could be mixed and led to the reactor. The analysis was done with a mass spectrometer (MS), (Balzers Quadstar 422, Version 6.02). Figure 3.2 shows a photo of the Micromeritics setup and a scheme of the setup is shown in Figure 3.5.



Figure 3.2: Photo of the Micromeritics AutoChem 2910 system.

3.2.2 Pilot Reactor

Reactor

A sketch of the pilot reactor is shown in Figure 3.3

The tubular pilot reactor was made in stainless steel and measured: ID = 19 mm, length = 390 mm. The SMF filters were cut into disks (diameter = 19 mm) and placed coaxially in the middle of the reactor. There was always an inner tube (stainless steel, ID = 16.0 mm, OD = 18.7 mm) placed in the reactor to support the fixed-bed.

The temperature profile of the reactor was measured at different temperatures and recycle ratios to locate the isothermal region of the reactor, where the catalysts and adsorbents were placed.

Experimental Setup

A scheme of the pilot reactor experimental setup is shown in Figure 3.4.

Three mass flow controllers (Brooks, Smart Mass Flow, model 5850S) were used to control the gas flow. Thermocouples (type TCG3K750, Pyro-Contrôle, France) for the temperature measurements and a membrane pump (type N026 ST.16E, KNF Neuberger, Switzerland) for the recirculation. The gas flows and temperatures were controlled with a software (Intellution FIX MMI® 7.0, Intellution Inc.).

The gas analysis was done with a Siemens Infrared Spectrometer for CO and CO₂ and a Perkin Elmer, Auto System XL, Gas Chromatograph (GC) equipped with a thermal

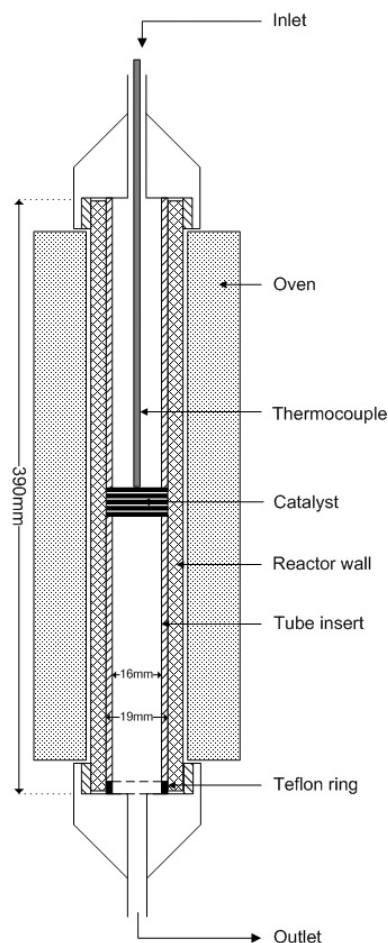


Figure 3.3: Scheme of the pilot reactor.

conductivity detector (TCD) and flame ionization detector (FID). The GC was used for the analysis of the propane mole fraction. For the separation of propane from the remaining gases (mainly: Ar, O₂, CO₂, H₂O) a Supelco Carboxen 1010 capillary column was used. The oven temperature was kept at 230 °C for the fastest possible analysis time, which was 11 min.

3.3 Adsorber

3.3.1 Synthesis

The adsorbent was made from a thin film of MFI-type zeolites grown on sintered metal fibers (SMF) by hydrothermal synthesis.

Zeolite Film Growth

The synthesis is based on the "seed-film method" (Hedlund *et al.*, 1997, 1999; Lassinantti *et al.*, 2001; Ohrman *et al.*, 2001; Sterte *et al.*, 2001). The support was SMF made from stainless steel (AISI 316L), 20 μm fiber diameter, available as panels of 0.30 mm thickness

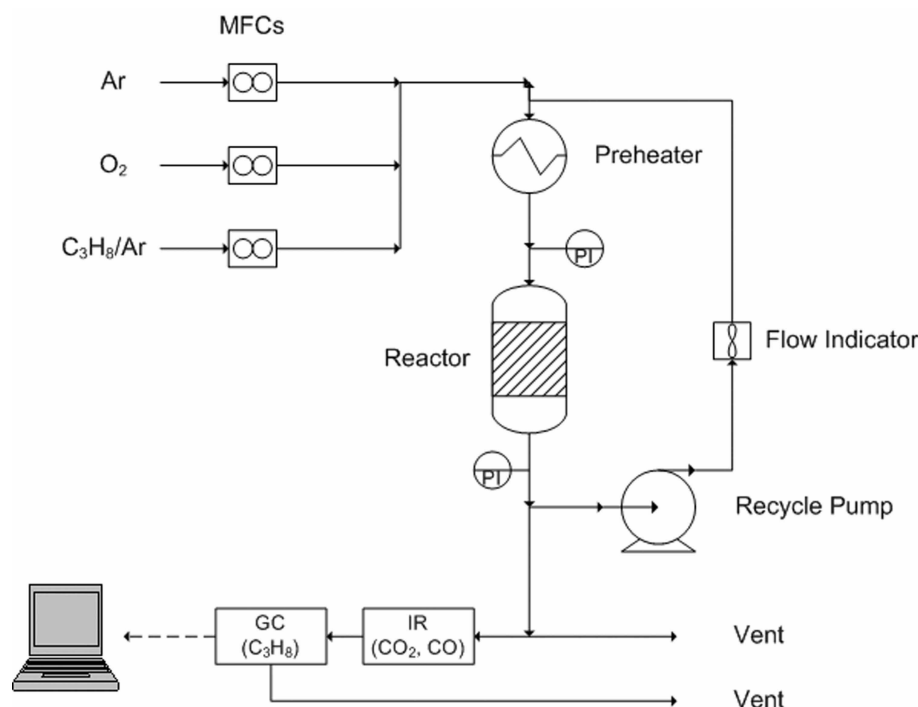


Figure 3.4: Scheme of the pilot experimental setup.

(see Table 3.1). Pieces of SMF ($5\text{ cm} \times 7\text{ cm}$) were calcined in air at 550°C to create an oxide layer on the metal surface. The calcined support was treated with a 0.4 % aqueous solution of a cationic polymer (Poly(dimethylamine-co-epichlorohydrin) for 20 min, rinsed in 0.1 M $\text{NH}_3(\text{aq})$ and air dried. Next, the support was treated with a seed solution of anionic, colloidal silicalite-1 crystals for 20 min to adsorb silicalite-1 seeds on the surface through electrostatic forces, rinsed four times in 0.1 M $\text{NH}_3(\text{aq})$ with ultra sound, dried and calcined at 550°C .

The seed solution was prepared by a method outlined by Persson *et al.* (1994). Tetraethoxysilane (TEOS) was used as silicon source, Tetrapropylammoniumhydroxide (TPAOH) as template in distilled water and ethanol (EtOH, purum). The molar composition of the solution was: 100 EtOH : 500 H_2O : 25 TEOS : 9 TPAOH. The solution was hydrolyzed for 48 hours with reflux at 100°C . Afterwards, the seeds were rinsed 3 times by centrifugation and redispersion in distilled water. The final solids concentration in the seed sol was adjusted to approximately 1 wt.% and pH 10 by adding NH_3 .

A film was grown by hydrothermal synthesis. The seeded SMF panels were placed in a 200 mL Polytetrafluoroethylene (PTFE) lined autoclave with a synthesis solution and kept at 125°C for 8-24 hours. The synthesis solution was prepared from the same chemicals as the seed solution, but in the molar ratio: 2000 H_2O : 4 TEOS : 1 TPAOH. Sodium aluminate (NaAlO_2) was added when synthesizing ZSM-5. This solution was hydrolyzed at room temperature by stirring until the solution became clear ($\sim 2.5\text{ h}$). After the synthesis, the samples were washed in deionized water for $\sim 20\text{ min}$ and calcined at 550°C . The obtained Na-ZSM-5 was ion-exchanged three times in 0.1 M $\text{NH}_4\text{NO}_3(\text{aq})$ at 85°C and calcined at 550°C to obtain H-ZSM-5.

3.3.2 Adsorption Isotherms

Adsorption isotherms of propane on the SMF filters covered with a zeolitic MFI-type film were determined from the adsorption capacity obtained by a transient step-up, step-down method.

The measurements were made using the Micromeritics quartz reactor (Section 3.2.1). The vertical reactor was packed from the bottom (downstream) in the following way: first quartz wool, then 10-20 disks cut from the synthesized SMF panels ($d = 10$ mm), quartz wool, 4 cm quartz powder (< 450 nm) and the rest (~ 11 cm) with quartz beads ($d_p = 4$ mm). The reactor packing was very similar to that shown in Figure 3.1 for the catalyst screening. The reactor was placed in a thermostat for temperature control (± 0.05 °C). A scheme of the experimental setup is shown in Figure 3.5.

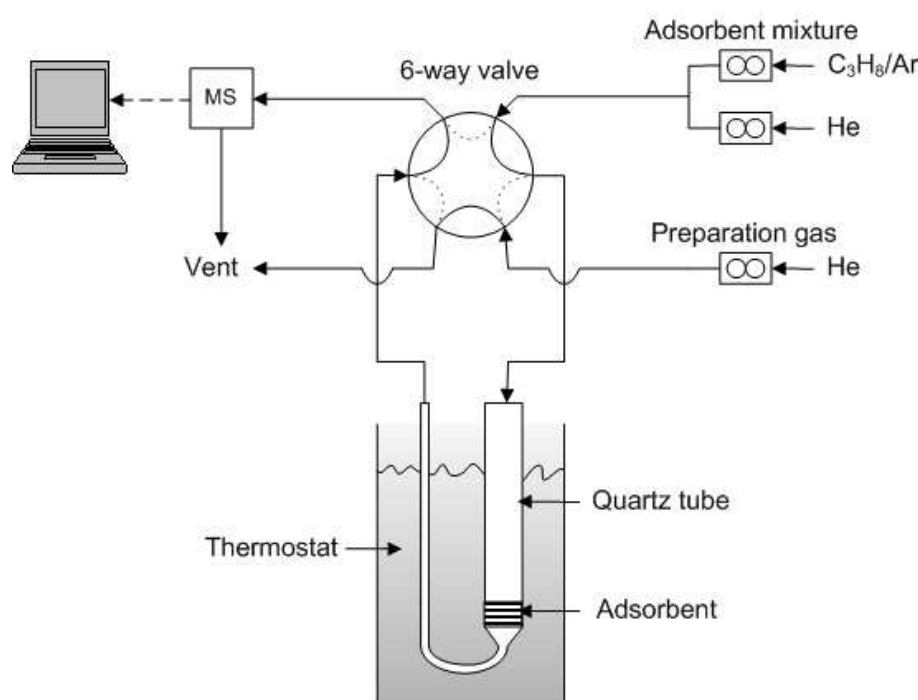


Figure 3.5: Experimental setup of Micromeritics quartz reactor for adsorption isotherm measurements.

The concentration of propane was varied by diluting the mixture containing 5 or 10 % of propane in Argon with He. The total volumetric flow for all experiments was in the range of 40 to 100 mL(STP)/min. The gas flows were controlled with the mass flow controllers of the Micromeritics apparatus. The desorption was carried out in He at the same flow rates as used for the propane adsorption. Isotherms were constructed by varying temperature and propane concentration. An example of the adsorption cycle measurements is shown in Figure 3.6. The adsorption capacity measurements consisted of 3 steps:

1. Stabilization: stabilization of the MS-signal of the propane containing gas in the bypass (30-60 min).
2. Adsorption: the propane containing gas with tracer (Ar) was passed through the reactor and adsorption occurred (5-15 min).

3. Desorption: by purging in He for 30-60 min at the same flow rates as used for the adsorption followed by temperature programmed desorption (TPD): $5\text{ }^{\circ}\text{C}/\text{min}$ in He keeping the flow rate constant.

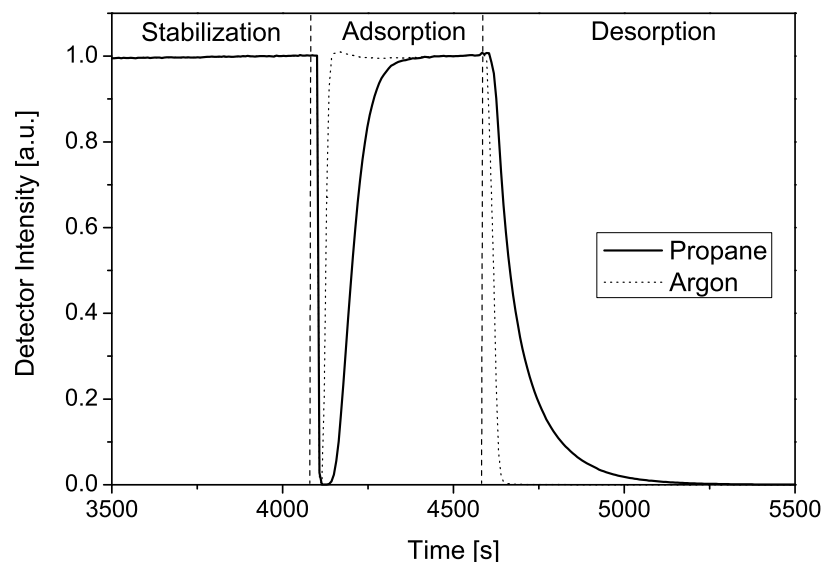


Figure 3.6: Propane adsorption procedure. Sample: 0.665 g of 5.7 % silicalite-1 on SMF at $50.0\text{ }^{\circ}\text{C}$. 2.58 % propane in Ar, flow = $19.5\text{ mL(STP)}/\text{min}$, pressure = 101 kPa.

The amount of propane adsorbed was determined by integrating the area between the curves at the reactor outlet of the tracer (Ar) and the propane in the adsorption part (see Figure 3.6) and multiplying by the molar flow rate of propane. The tracer does not adsorb on the zeolite and therefore gives the "empty reactor" response. The amount of desorbed propane was calculated in a similar manner from the step-down response integrating the area between the two curves in the desorption step.

3.3.3 Adsorption Breakthrough Curves

Adsorption breakthrough curves of propane through a fixed-bed of zeolite/SMF composites were obtained from dynamic measurements in the tubular pilot reactor (Section 3.2.2) at atmospheric pressure. The inner tubes and filter disks were pressed together by placing rings of PTFE or graphite at the ends sealing the space between the walls of the inner and outer tube to avoid any gas bypass. The space above and below the fixed-bed was filled with glass beads.

The samples were pretreated at $450\text{ }^{\circ}\text{C}$ for 3 hours in $67\text{ mL(STP)}/\text{min}$ Ar flow and cooled down in Ar. 800 ppmv propane in argon was used for the adsorption breakthrough curve with a total flow rate of $100\text{ mL(STP)}/\text{min}$. The measurements were made at atmospheric pressure and $30\text{ }^{\circ}\text{C}$. The concentration was monitored at the outlet using an FID detector.

3.3.4 Pressure Drop

The pressure drop was measured in the tubular pilot reactor described above (Section 3.2.2). For the pressure drop measurements the reactor space above and below the fixed-bed was left empty. The pressure drop was measured using air and a membrane pump. A water containing U-tube was used as a manometer. One side was open to the atmosphere and the other side was attached to the reactor upstream of the fixed-bed at the Swagelok fitting for the temperature probe. The absolute pressure drop for a certain fixed-bed packing was corrected for the pressure drop of the empty reactor. Again, the inner tubes and filter disks were pressed together by placing rings of PTFE or graphite at the ends sealing the space between the walls of the inner and outer tube to avoid any gas bypass.

The pressure drop over packed beds of 10-20 layers with varying zeolite loadings was measured in this way.

3.4 Oxidation Catalyst

Metal Impregnation

The filters for catalytic oxidation were prepared by wetness impregnation. The filters' wetness capacity was estimated from weight difference before and after dipping the filters into water. From this wetness capacity the concentration of the metal salts could be calculated in order to arrive at the desired, final loading of metal or metal oxide on the filters. The filters were left to dry in air overnight.

Cobalt oxide catalysts were impregnated with an aqueous solution of $\text{Co}(\text{NO}_3)_2 \cdot 6\text{H}_2\text{O}$. The platinum containing catalyst was impregnated with an aqueous solution of $\text{Pt}(\text{NH}_3)_4\text{Cl}_2 \cdot \text{H}_2\text{O}$ with pH 9.8 (NH_3).

Activation by Calcination

The dry filters containing metal salts were calcined in air at 450 °C for 1 h in order to decompose the nitrate salts and end up with the metal oxides.

3.4.1 Powder Preparation and Deposition

For developing and testing the novel structured catalyst based on sintered metal fibers covered with a thin film of finely powdered catalyst, SMF of stainless steel (AISI 316L) and the following industrial catalyst were used:

Catalyst: CK-302, Haldor Topsøe, Lyngby, Denmark. 2-4 mm spherical particles containing 6.9 % CuO, 13.1 % Manganese oxides on a mixture of α and γ -alumina.

The goal was to deposit the finely ground, industrial catalyst (CK-302) on the SMF. In the following, the steps of the preparation procedure are outlined. The preparation method was chosen from a method previously applied in our lab with similar catalyst materials, which resulted in mainly sub-micron size distributions of the attrition milled powder (Reuse, 2003).

Milling of the CK-302 catalyst:

1. 50 g of the original catalyst was crushed in a ball mill (Centrifugal ball mill Pulverisette 6, Fritsch, Idar-Oberstein, Germany) for 1 h at speed 8.
2. The powder obtained was transferred to an attrition ball mill (PE 075 moliNEx, Netzsch SA, Altendorf, Switzerland) using an alumina impeller shown in Figure 3.7. The powder was mixed with zirconia (ZrO_2) beads of 2 mm diameter and filled with just enough distilled water to cover the contents of the attrition pot. The powder was milled for 3 h at 1700 rpm.
3. The mixture of powder, water and zirconia beads was transferred to a sieve and the obtained powder was washed out with enough water to obtain a final volume of 750 mL. Hence, the final suspension concentration was 67 g/L.



(a) Attrition ball mill



(b) Impeller

Figure 3.7: Attrition ball mill and impeller rod with three alumina disks.**Suspension for deposition:**

1. Suspensions were prepared from the attrition milled batch by dilution with distilled water.
2. Water soluble polymers (PEG 600, PEG 35,000 and PVP 360,000) were added to obtain the desired concentration.
3. The solutions were stirred rigorously for ca. 5 min followed by 15 min in ultrasonic bath (to break up agglomerates). This procedure was repeated three times before taking a sample from the attrition milled batch.
4. The solutions were stored in air tight containers.

Deposition:

1. The prepared solutions were stirred vigorously for 5 min followed by 15 min in an ultrasonic bath (47 kHz, 30 W). This procedure was repeated 3 times before using the solutions for the deposition.
2. During the deposition period the solution was kept in an ultrasonic bath. The samples (SMF disks) were dipped into the solution for 5 seconds.
3. The SMF filter disks were gently swept over the edge of the beaker to avoid an excess of suspension. Furthermore, small droplets on the surface area were absorbed with a paper towel. If this procedure of removing excess suspension covering the external surface of the fiber matrix was not followed it resulted in inhomogeneous deposition and "bridging" or "blocking" between the fibers.
4. The SMF filters were dried either in vacuum (min. 2 h) or at ambient conditions overnight. The samples were finally calcined in air at 300 °C for 3 hours.

Six disks of SMF were dip-coated with powder catalyst for each prepared batch of powder suspension. Each of the 6 disks was weighed and some of the batches were tested in the pilot reactor for their catalytic activity.

3.4.2 Catalyst Screening

The catalysts were synthesized by impregnation or powder deposition on $\varnothing = 10$ mm SMF filter disks made of stainless steel (AISI316L). They were stacked and tested in the Micromeritics quartz reactor tube, $\varnothing = 9.8$ mm (Section 3.2.1) with a slight space between each layer. Figure 3.1 shows the packing of the reactor. The gas flow arrived from the top of the tube flowing downwards. A reactor performance approaching plug flow was desired. A fixed-bed of inert quartz particles ($d_p \sim 250 - 315 \mu\text{m}$), height $h = 15$ mm was placed on top of the stack of catalytically active SMF disks to ensure plug flow already before the catalyst. A ratio $h/d_p > 50$ was achieved, which ensures plug flow performance (Levenspiel, 1996, p. 66.5). The tubular reactor was slightly smaller than the SMF disks resulting in these being slightly concave in the tube and ensured full contact with the glass walls to minimize the risk of gas bypass. The fixed-bed of stacked SMF disks measured 12 mm in height for 12 layers each having a thickness of 0.30 mm. This leaves ≈ 0.7 mm between the layers, which in turn will lead to mixing between each layer and aiding in obtaining plug flow. Furthermore, glass beads ($\varnothing = 0.5$ mm) were placed just below the stack to support it. Quartz wool was used to protect the outlet and to separate the quartz particles from the catalyst. The setup was tested for possible bypass by heating the reactor to 538 °C, at which temperature the conversion reached 99.8 %, which showed that the reaction was complete and bypass could be neglected. For comparison, the temperature for homogeneous autoignition is 540 °C (<http://www.propanecarbs.com/propane.html>).

The quartz reactor was fixed to the Micromeritics instrument in the same way as in the adsorption isotherm experiments as shown in Figure 3.5. However, the oven was used in place of the thermostat for heating the samples. The gas analysis was done with the mass spectrometer as described in Section 3.2.1.

The inlet gas used for the screening was composed of 0.38 vol.% propane and 5 vol.% oxygen. The flow rate was 24 mL(STP)/min. The experiments were performed by step-wise heating, leaving the sample enough time to reach steady state conditions at each temperature. The temperature was raised until the conversion reached 20 %. The reactor was assumed differential allowing an approximative calculation of the apparent activation energy, E_a , and rate constant from the modified power rate law (Equation 2.27) and Arrhenius equation (Equation 2.34):

$$\ln(r) = \ln(k^*) - \frac{E_a}{RT} \quad (3.3)$$

in which $k^* \cong k' C_{C_3H_8}^m C_{O_2}^m$, since the concentration terms were assumed constant. 8-9 temperatures were used for the calculation of E_a .

3.4.3 Catalyst Testing and Kinetics

The prepared SMF catalysts were packed in a fixed-bed with the SMF disks separated by rings as seen in Figure 3.8. The dimensions of the rings were: height = 2 mm, OD = 18.7 mm, see sketch in Figure 3.9. These rings would only touch the filters along the edge of the tube, due to the tapered structure. The separation of the layers leads to mixing between each layer and results in less chance of gas bypassing.

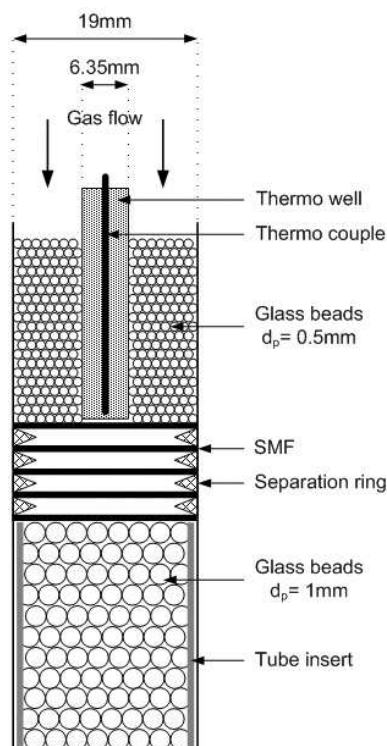


Figure 3.8: Scheme of the pilot reactor. Packed for the kinetics measurements with SMF.

The time needed to achieve steady state conditions varied with the flow rate. For most experiments steady state conditions would be reached within 45 min, where three consecutive measurements were taken.

Glass beads ($d_p = 1$ mm) were placed in the tube underneath the fixed-bed and glass beads with $d_p = 0.4 - 0.6$ mm were placed in the tube above the fixed-bed. The glass beads

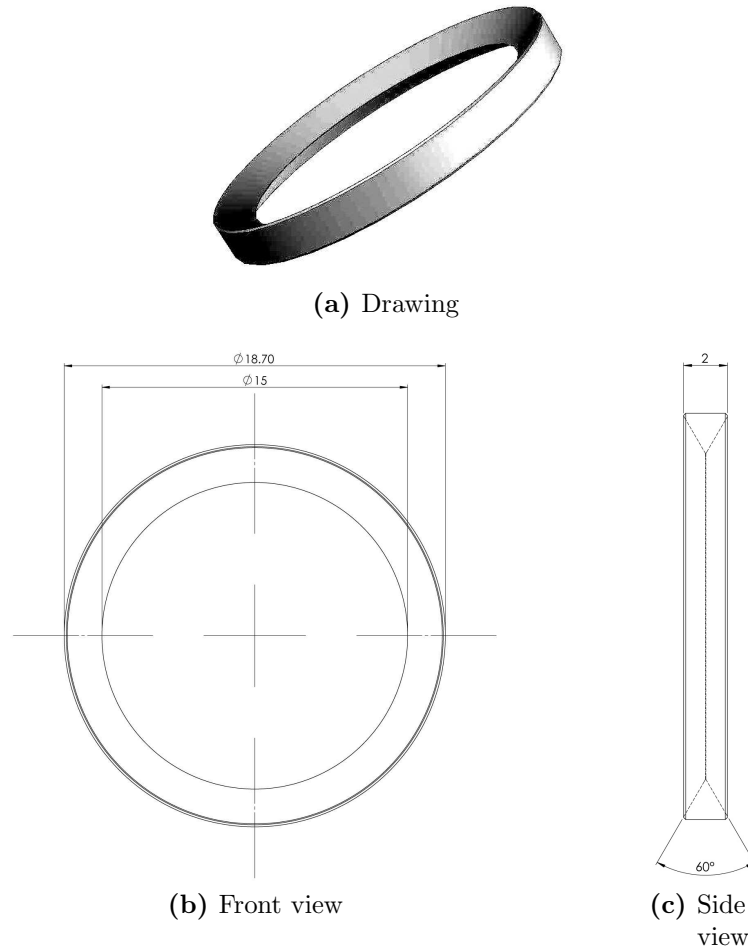


Figure 3.9: Scheme of rings for separating catalyst disks in reactor.

above the fixed-bed were necessary for the gas mixing in order to obtain an isothermal region in the center of the tubular reactor, where the fixed-bed was placed. Furthermore, the glass beads decreased the system volume, thereby decreasing the time to obtain steady state conditions. The latter was particularly important, since the reactor was used as a recycle reactor to obtain a mixed flow/CSTR hydrodynamic pattern. The flow pattern for the system was determined by making a step experiment and fitting a tanks-in-series model to the data. The output F-curve from a series of N ideal stirred tanks are:

$$F(\Theta) = 1 - \exp(-N\Theta) \left[1 + N\Theta \frac{(N\Theta)^2}{2!} + \cdots + \frac{(N\Theta)^{N-1}}{(N-1)!} \right] \quad (3.4)$$

$$F(\Theta)_{N=1} = 1 - \exp(-\Theta) \quad (3.5)$$

The step experiment was made with glass beads in the reactor. A step change of the gas feed from pure Ar to 2% CO_2 in Ar was made, the CO_2 mole fraction at the outlet was followed as a function of time. The measurements could be modeled by the F-curve of a CSTR ($N = 1$), given by Equation 3.5, with a volume of 0.300 L (Figure 3.10). The concentration difference over the fixed-bed during reaction was generally kept well below 5% to ensure a differential reactor.

The test reaction was the total oxidation of propane. This reaction converts 6 molecules to 7 and has a volume change at full conversion of $\epsilon = 1/6$. However, the propane was very diluted with maximum inlet mole fractions of about 1.5% and Ar mole fractions of

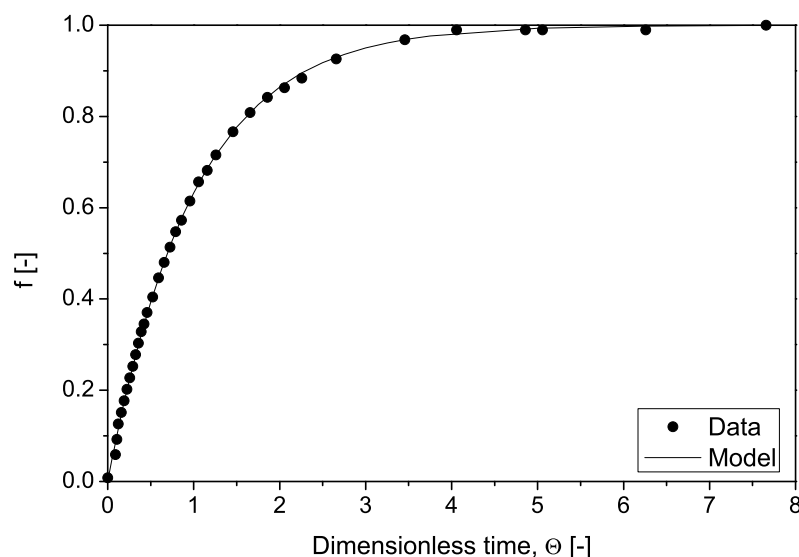


Figure 3.10: F-curve in pilot reactor with recycle. Flow rate, $V = 66.7 \text{ mL(STP)/min}$, recycle ratio, $R = 44$.

about 80-95 %. Hence, $\epsilon \approx 0$ and the conversion, X , could be calculated directly from the mole fractions of propane in the inlet and outlet:

$$X = \frac{y_{\text{C}_3\text{H}_8, \text{in}} - y_{\text{C}_3\text{H}_8, \text{out}}}{y_{\text{C}_3\text{H}_8, \text{in}}} = 1 - \frac{y_{\text{C}_3\text{H}_8, \text{out}}}{y_{\text{C}_3\text{H}_8, \text{in}}} \quad (3.6)$$

The reaction rate from the recycle reactor was calculated from the performance equation of a CSTR:

$$r = \frac{F_{\text{C}_3\text{H}_8, \text{in}} X}{m_{\text{cat}}} \quad [\text{mol/g}\cdot\text{s}] \quad (3.7)$$

where $F_{\text{C}_3\text{H}_8, \text{in}}$ is the inlet molar flow rate of propane and m_{cat} is the catalyst mass, considered here as the active phase of the catalyst i.e. excluding the mass of SMF and inert powder or zeolite layers.

3.5 Characterization Techniques

3.5.1 Atomic Absorption Spectroscopy

The Si/Al-ratio of the zeolite film was determined by atomic absorption spectrometry (AAS) on a Shimadzu Atomic Absorption Spectrometer AA-6650 after dissolving the film in an aqueous HF (1 %) solution.

3.5.2 X-ray Diffraction

For the analysis of crystalline phases X-ray diffraction (XRD) was used. The spectra were recorded with a Siemens D500 Diffractometer, Munich, Germany, with a $\text{CuK}\alpha$ radiation

source, with a wavelength of 0.15405 nm. Steps of $2\Theta = 0.04^\circ$ and a scanning speed of 4 s/step were used. The reference spectra were taken from the JCPDS database (by: International Centre for Diffraction Data, <http://www.icdd.com/>).

3.5.3 Scanning Electron Microscopy

The surface morphology of the samples was analyzed by scanning electron microscopy (SEM) (JSM-6300F, JEOL Ltd, Tokyo, Japan and Philips XL 30 SFEG, Netherlands).

3.5.4 Specific Surface Area and Pore Volume

The specific surface area (SSA_w) was measured by adsorption-desorption of nitrogen at 77 K, after pretreatment at 250 °C for 2 h in vacuum, with a Sorbtomatic 1990 (Carlo Erba (Thermo Electron S.p.A), Milan, Italy). The specific surface area was calculated by the method of Brunauer-Emmet-Teller (BET) (Brunauer *et al.*, 1938), which takes multilayer adsorption into account. The pore volume and the pore distribution was determined by the Dollimore-Heal method (Dollimore & Heal, 1964).

3.5.5 Particle Size Distribution

The particle size distribution (PSD) of the prepared powders was measured by laser diffraction (Malvern Mastersizer S).

3.5.6 X-ray Photoelectron Spectroscopy

X-ray photoelectron spectroscopy (XPS) was done with a Kratos AXIS Ultra, XPS spectrometer with monochromator $K\alpha$ radiation of aluminium with an X-ray power of 150 W. The analysis allows an estimation of the chemical composition of the surface as well as the relative amounts of oxidation states of a metal at the surface by deconvolution of the metal peaks.

3.6 Chemicals and Gases

The employed chemicals and gases are shown in the following Tables 3.5 and 3.6. All gases were supplied by Carbagas (Lausanne, Switzerland).

Table 3.5: Employed chemicals.

Compound	Purity	Supplier
Poly(dimethylamine-co-epiclorohydrin)	50 wt. %	Aldrich
NH ₃ (aq)	purum ~ 28 %	Fluka
Tetraethoxysilane (TEOS)	> 98 %	Acros
Tetrapropylammoniumhydroxide (TPAOH)	Technical, 20 % in H ₂ O	Fluka
Ethanol, purum absolute	> 99.8 % (v/v)	Fluka
NaAlO ₂	Anhydrous, technical	Riedel-de-Haën
NH ₄ NO ₃	ACS, > 98 %	Aldrich
HF	puriss p.a. > 40 %	Fluka
Toluene (C ₇ H ₈)	Technical	Schweizerhalle
Acetone (C ₃ H ₆ O)	Technical	Schweizerhalle
Co(NO ₃) ₂ ·6H ₂ O	ACS, p.a. 98 %	Acros
Pt(NH ₃) ₄ Cl ₂ ·H ₂ O	purum, (Pt-08)	Johnson Matthey
Polyethylene glycol (PEG) 600	purum, 600 g/mol	Fluka
PEG 35000	purum, 35,000 g/mol	Fluka
Polyvinyl-pyrrolidone (PVP) 360000	purum, 360,000 g/mol	Sigma

Table 3.6: Purity of employed gases.

	Gas	Purity [%]
Micromeritics reactor		
Gas mixture	5.06 % C ₃ H ₈	> 99.95
	Rest Ar	> 99.996
Gas mixture	10.03 % C ₃ H ₈	> 99.95
	Rest Ar	> 99.996
Gas mixture	0.50 % C ₃ H ₈	> 99.95
	0.98 % He	> 99.996
	Rest Ar	> 99.998
Gas mixture	21.03 % O ₂	> 99.998
	Rest He	> 99.9990
	Helium	> 99.9990
Pilot reactor		
Gas mixture	2.00 % C ₃ H ₈	> 99.95
	Rest Ar	> 99.998
	Helium (GC)	> 99.996
	Oxygen	> 99.95
	Argon	> 99.998
	Hydrogen (FID)	> 99.995

Chapter 4

Adsorber

This chapter describes the development and testing of the structured adsorber based on a thin zeolite (MFI-type) film on SMF. This material can be beneficial in small scale operations, where low diffusion resistance and low pressure drop are needed for an efficient adsorption/desorption system.

4.1 Synthesis and Characterization of MFI/SMF

4.1.1 Film Growth

The oxidized SMF surface was modified by a polyelectrolyte to obtain a positive surface charge. The filters were then submerged in a colloidal solution of silicalite-1 nanocrystals called "seeds". Seeds were adsorbed on the support and treated by ultra sound in 0.1 M ammonia. The film of MFI-type zeolite was grown on the seeded support by hydrothermal synthesis and calcined. The amount of zeolite loading was varied by using different synthesis times or by repeated synthesis. The effect of varying the synthesis time is shown in Figure 4.1. Some initial time to heat up the autoclave is needed before the reaction takes place resulting in the non-zero values of the regressions at $t = 0$. Once these conditions are obtained the growth rate is a linear function of time until the approach of full conversion, at which time the reaction will stop. In the case of silicalite-1 the loading will hardly change after 20 h of synthesis. The two points at 40 h and 10.5 wt.% loading were the maximum conversions achieved at which point approximately 70 % of the silicon in the synthesis solution had been grown as a film on the SMF and 30 % nucleated in the solution and precipitated as a white powder. The Na-ZSM-5 film growth also follows a linear trend, but grows considerably slower than the silicalite-1 due to the more difficult introduction of Al-atoms into the molecular structure.

Finally, in the case of ZSM-5 films the obtained Na-ZSM-5 was ion-exchanged and calcined to give H-ZSM-5. This synthesis method gives a homogeneous film consisting of $1\ \mu\text{m}$ sized prismatic crystallites of MFI zeolite as seen on the SEM images, Figure 4.2, where the difference between oxidized and MFI coated SMF is seen. Homogeneity of the coating was observed for all synthesized Si/Al-ratios of the synthesis solution. Few cracks in the film were observed after the synthesis. Furthermore, the thermal stability of the film was controlled qualitatively by SEM after fast heating up to $550\ ^\circ\text{C}$ in a preheated oven

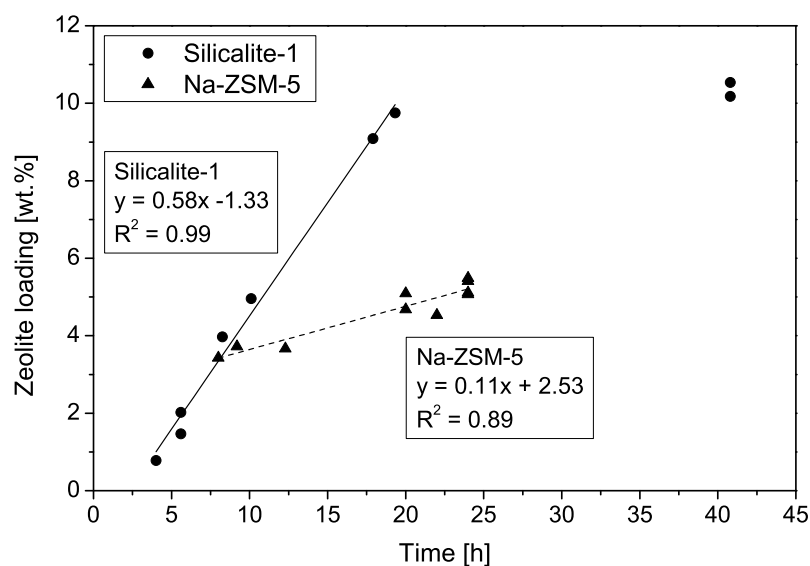


Figure 4.1: MFI-zeolite loading on SMF as a function of synthesis time.

followed by quenching to room temperature. This procedure was repeated 10 times. After this treatment a few cracks or holes in the film were observed in the outer regions of the fiber matrix, but no major damage was visible, confirming the stability of the synthesized zeolite film.

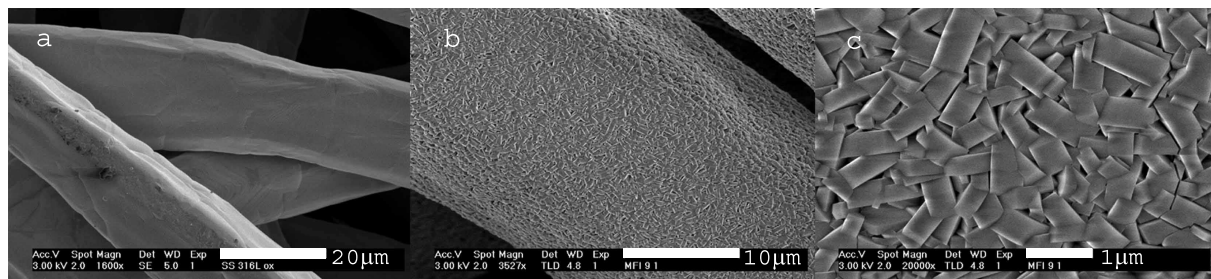


Figure 4.2: SEM images of the SMF/MFI composite: a) calcined fibers, b) and c) coated by silicalite-1 (loading 9.1 wt.%).

The MFI zeolite film on the SMF could be mechanically broken by strong bending or when cutting the filters with scissors. Such a crack in the zeolite film is seen in Figure 4.3 from which the thickness of the film as a function of the loading could be estimated.

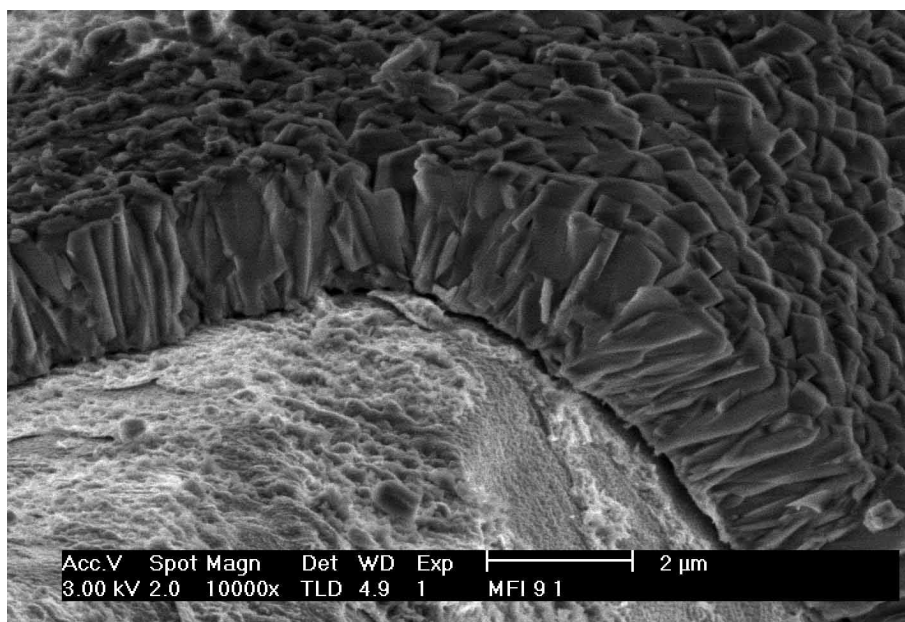


Figure 4.3: SEM image of a damaged MFI film on SMF. Silicalite-1 (loading 9.1 wt.%).

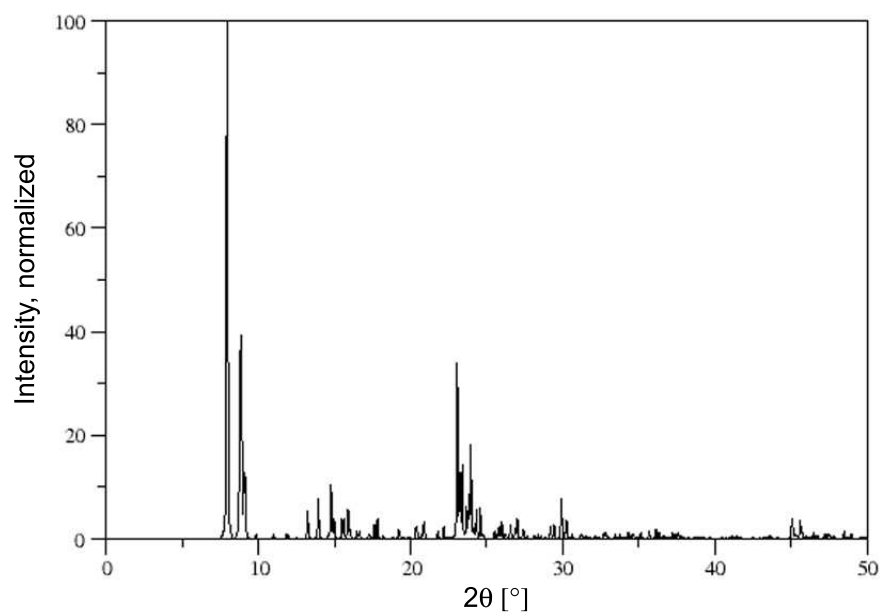


Figure 4.4: Simulated XRD powder pattern for calcined ZSM-5 (normalized) (Treacy & Higgins, 2001).

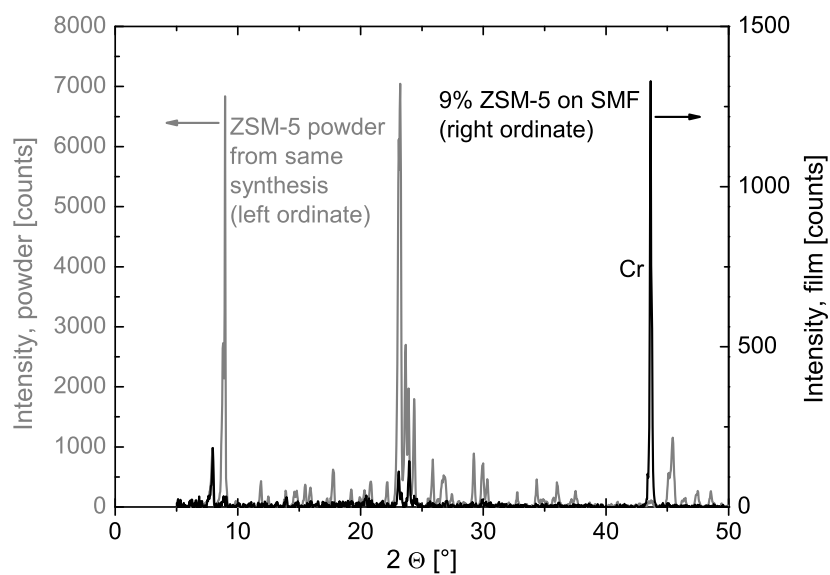


Figure 4.5: XRD pattern of 9% ZSM-5 film on SMF filter ($\text{Si}/\text{Al} = 184$) and the powder precipitated during the synthesis.

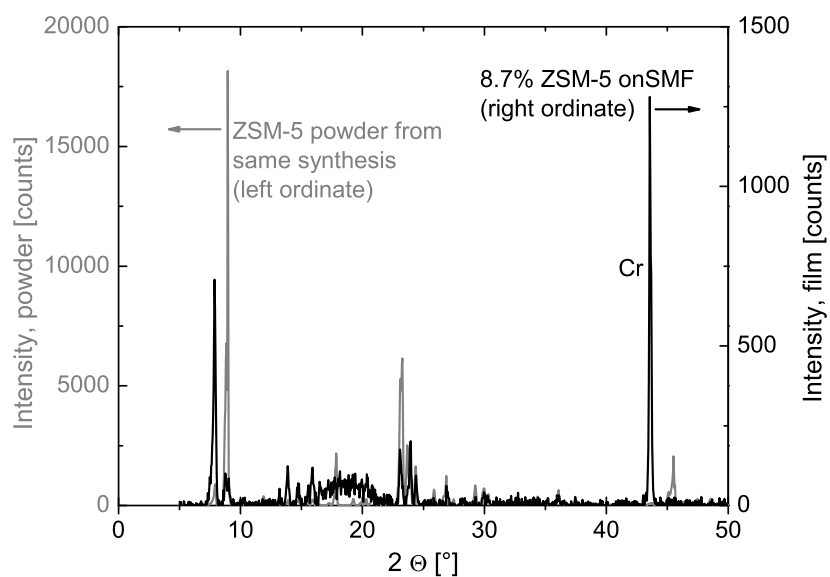


Figure 4.6: XRD pattern of 8.7% ZSM-5 film on SMF filter ($\text{Si}/\text{Al} = 536$) and the powder precipitated during the synthesis.

4.1.2 XRD

X-ray diffraction measurements were used to check if the synthesized zeolite film was crystalline and if it was the expected MFI-structure. The reference spectrum (Treacy & Higgins, 2001) for the MFI-structure (silicalite-1 and ZSM-5) is shown in Figure 4.4 and was compared to the measured spectra, Figure 4.5 and 4.6.

Figure 4.5 and 4.6 show the XRD spectra of the zeolite film on the SMF filters as compared to the precipitated crystals formed during the same synthesis. These precipitated crystals form a white powder after washing and drying. Both of the powder patterns are in very good agreement with the reference spectrum (Figure 4.4). The characteristic peaks at $8-9^\circ$ and $23-25^\circ$ are present for both ZSM-5 powders, indicating that the MFI-structure is obtained in both cases.

The XRD spectra for the zeolite film on the SMF filters show the same characteristic peaks as the respective precipitated powders and the reference spectrum, indicating that the MFI-structure was also obtained in the film. Spectra of the powder and the films show a 100 % crystalline structure. The peak intensities are approximately 10 times lower than for the powders. This is thought to be due to the high porosity of the filters ($\approx 75\%$). It was never possible to get an XRD spectrum with less than approximately 9 wt.% film on the support because of the low intensities. The differences in the relative peak intensities between the powder and film samples indicates that a preferred crystal orientation of the ZSM-5 crystals grown by the seed-film method exists, whereas the powder crystals have all orientations present.

Both film spectra show a very intense peak at approximately 43.5° . This peak is attributed to the chromium in the stainless steel support, which is expected at 43.5° .

The film spectrum in Figure 4.6 shows a broad peak from 15 to 22° . It is not clear if this is due to the high noise in the spectrum or if it could be a sign of some amorphous zeolite deposition on the SMF filter, but ZSM-5 is definitely present as seen by the characteristic peaks of both film and powder spectra.

Due to the characteristic peaks from the film on the filters and the powder spectra it seems that the synthesized film is indeed of the MFI-structure.

4.1.3 BET Specific Surface Area

A linear correlation was found between the ZSM-5 loading and the BET specific surface area (SSA) of the composite as shown in Figure 4.7(a). The SSA calculated for the zeolite was $300-370 \text{ m}^2/\text{g}$ (Figure 4.7(b)) and this material was nanoporous. For MFI-films on SMF from FeCrAlloy and Inconel alloys (Yuranov *et al.*, 2005) the SSA_w was found to be $300-320 \text{ m}^2/\text{g}$. This agrees with the values reported for crystalline ZSM-5 powders: $376-430 \text{ m}^2/\text{g}$ (Narayanan *et al.*, 1996; Seijger *et al.*, 2000; Nijkamp *et al.*, 2001) and that of ZSM-5 crystals supported on metal grids: $302 \text{ m}^2/\text{g}$ (Louis *et al.*, 2001a). No effect on the BET surface area was due to the Si/Al-ratio or the film loading.

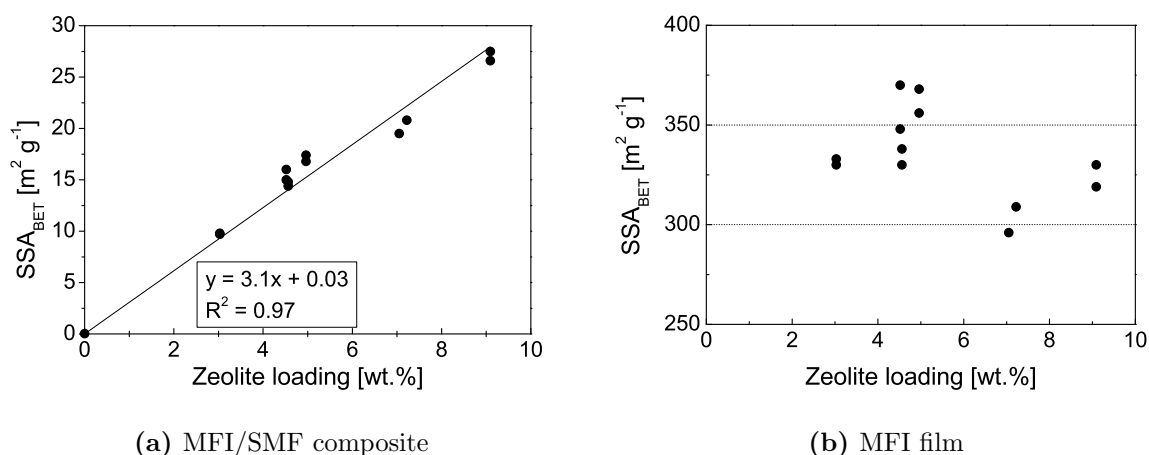


Figure 4.7: BET SSA_w as a function of the zeolite loading.

4.1.4 Atomic Absorption Spectroscopy

The chemical composition was analyzed by atomic absorption spectroscopy (AAS). A significantly higher Si/Al-ratio in the synthesized film compared to the synthesis solution was observed as shown in Figure 4.8. This indicates the hindering of the isomorphous substitution of Si^{4+} by Al^{3+} in the MFI lattice during the slow, controlled growth when applying the seeding method (Ulla *et al.*, 2003).

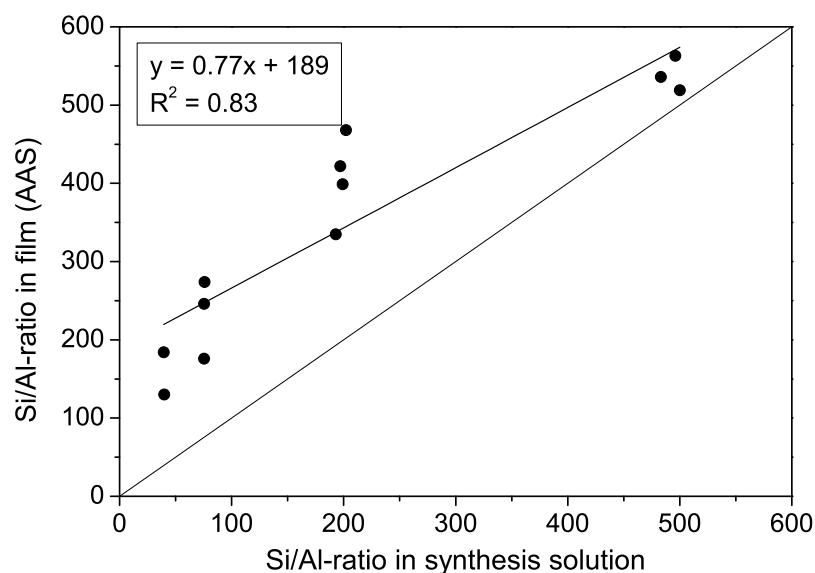


Figure 4.8: Chemical composition of MFI-zeolite film by AAS.

The AAS measurements were verified by testing standard, industrial zeolites in powder

form¹. Furthermore, a study of the mass balance during the synthesis was done. For the mass balance the silicon and aluminium contents were measured in the synthesis solution before and after the synthesis as well as in the deposited powder and the zeolite-film on the SMF filters. The result of the mass balance is shown in Table 4.1. There was an excellent agreement between the amounts before and after the synthesis. Furthermore, the analysis shows how the aluminium atoms are more difficult to introduce into the powder and film crystals, since the Si/Al-ratio is lower in the synthesis solution after the synthesis. The method of estimation of the Si/Al-ratio seems to be valid and indeed the experimental error on repeated concentration measurements was never higher than 7 %.

By the dissolution of the film by HF, some of the metal support will also be dissolved. It was investigated if these dissolved metal atoms could have an influence on the concentration measurements of Si and Al. Where the silicon measurements are not affected about 10 % positive interference is given if Ti and Fe coexist with Al in 10 to 50-fold concentration (Shimadzu-Corporation, n.d.). In one sample the iron concentration was found to be 19 times higher than the aluminium concentration, thus introducing an error of approximately 10 % on the Si/Al-ratio.

Table 4.1: Mass balance for the synthesis of a 3 wt.% ZSM-5 (Si/Al = 132) film on a SMF filter.

		Si[mmol]	Al[mmol]	Si/Al-ratio
BEFORE	Syn sol	21	0.51	41.2
AFTER	Syn sol	15	0.46	32
	Bottom crystals	0.81	0.0022	372
	Film on SMF	4.6	0.035	132
	Total (AFTER)	20	0.50	40.9
Difference [%]		-2.8	-2.1	-0.8

4.2 Adsorption Isotherms

The adsorption equilibrium isotherm can often be described by the Langmuir isotherm (Langmuir, 1918). The derivation of the isotherm can be done by the kinetic approach, which was originally used by Langmuir. The assumptions are:

1. The adsorbed species are held onto definite points of attachment on the surface. This implies that the maximum adsorption possible corresponds to a monolayer. Each site can accommodate only one adsorbed species.
2. The differential energy of adsorption is independent of surface coverage. This implies that the surface is completely uniform so that there is the same probability of adsorption on all sites. A further implication is that adsorbed molecules are localized. Attractive or repulsive forces between adjacent adsorbed molecules are taken to be negligible, so the energy of an adsorbed species or the probability of adsorption onto an empty site are independent of whether or not an adjacent site is occupied.

¹Zeocat PZ-2/25 H from Zeochem AG, Uetikon, Switzerland

Consider then a single pure vapor A at a pressure P_A that adsorbs without dissociation onto a surface. Let the occupied fraction of sites on which adsorption is possible be Θ_A . The rate of adsorption, $r_{A,ads}$, is proportional to the rate of molecular collisions with unoccupied sites:

$$r_{A,ads} = k_{ads}(1 - \Theta_A)P_A \quad (4.1)$$

The rate of desorption is proportional to the number of molecules adsorbed:

$$r_{A,des} = k_{des}\Theta_A \quad (4.2)$$

at equilibrium the rates of adsorption and desorption are equal, so that

$$k_{ads}(1 - \Theta_A)P_A = k_{des}\Theta_A \quad (4.3)$$

$$\Theta_A = \frac{k_{ads}P_A}{k_{des} + k_{ads}P_A} = \frac{K_AP_A}{1 + K_AP_A} \quad (4.4)$$

where the adsorption equilibrium constant $K_A = k_{ads}/k_{des}$. The surface coverage can be related to measurable quantities of adsorbed species $\Theta_A = q/q_m$.

The adsorption of propane was carried out by the dynamic method as described in Section 3.3.2. An example of the isotherms is shown in Figure 4.9.

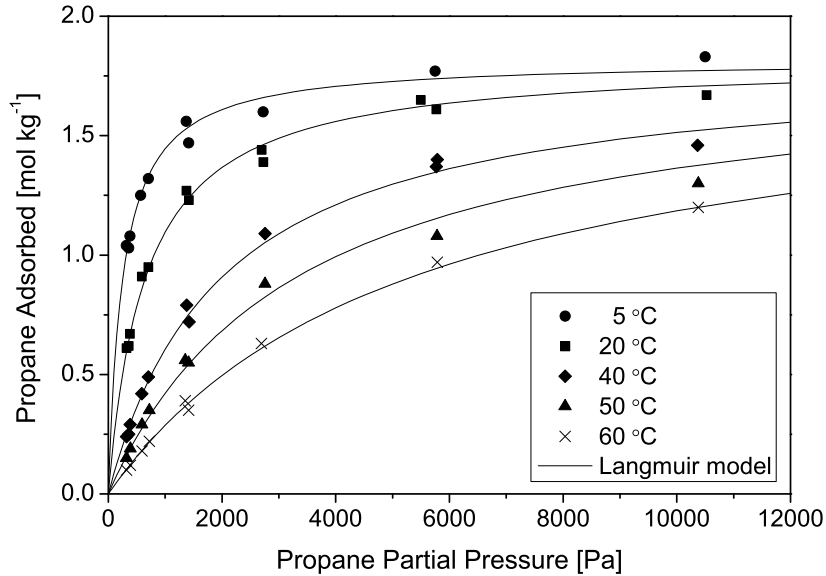


Figure 4.9: Propane isotherms. Sample: 0.696 g of 10 % H-ZSM-5 (Si/Al \sim 200) on SMF.

The Langmuir model has been fitted to the experimental data using a multivariable, non-linear least-squares method by minimizing the sum of the squared residuals (SSR) between the model predictions and the experimental data (program code given in Appendix D). The variables of the model were: saturation capacity (q_m), the preexponential factor of the adsorption equilibrium constant (K') at the reference temperature T' and the heat of adsorption (ΔH_{ads}^0) according to the Langmuir model:

$$q = q_m \frac{KP_{C_3H_8}}{1 + KP_{C_3H_8}} \quad (4.5)$$

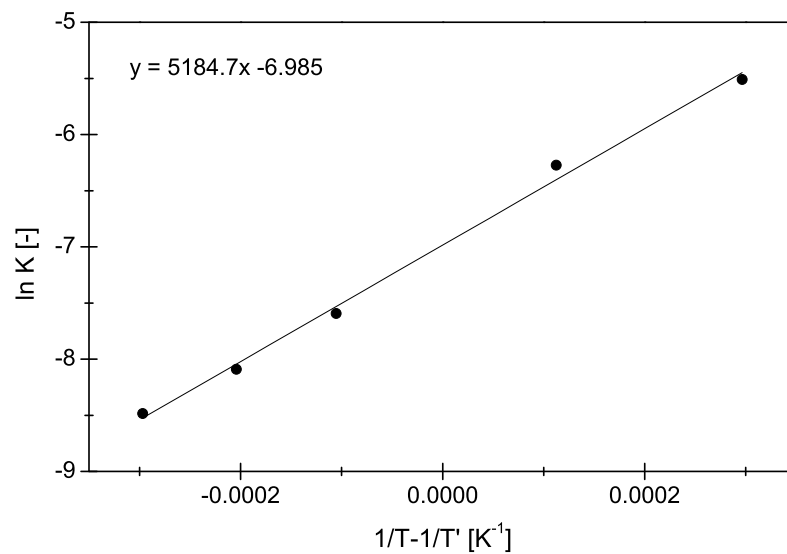


Figure 4.10: Arrhenius plot for the adsorption constants. $T' = 30\text{ }^{\circ}\text{C}$. Sample: 0.696 g of 10 % H-ZSM-5 (Si/Al ~ 200) on SMF.

where the adsorption constant follows a van't Hoff equation:

$$K = K' \exp \left\{ \frac{-\Delta H_{ads}^0}{R} \left(\frac{1}{T} - \frac{1}{T'} \right) \right\} \quad (4.6)$$

The fitted values of the model parameters for three different samples are shown in Table 4.2.

Table 4.2: Langmuir isotherm model parameters^b. Si/Al-ratio = ∞ corresponds to silicalite-1; the two other samples are H-ZSM-5.

Si/Al-ratio:		∞	~ 500	~ 200
q_m	mol/kg	1.85 ± 0.06	1.80 ± 0.08	1.81 ± 0.05
$K' \dagger$	1/Pa	$(9.14 \pm 0.68) \cdot 10^{-4}$	$(7.45 \pm 0.63) \cdot 10^{-4}$	$(8.73 \pm 0.49) \cdot 10^{-4}$
ΔH_{ads}^0	kJ/mol	-43.1 ± 1.6	-43.1 ± 1.8	-43.1 ± 1.2
Standard error*		0.047	0.061	0.041
$ssq_{min} \ddagger$		0.0836	0.146	0.0414
Data points		41	42	51

^b Parameter values with $(\pm) 2\sigma$ -confidence levels

[†] Adsorption equilibrium constant at reference temperature, $T' = 30\text{ }^{\circ}\text{C}$ (see Section 2.5.4)

[‡] Minimal sum of squares of residuals

* Approximate standard error on the output variable ($\ln q$)

Table 4.3: Langmuir and Toth isotherm model parameters^b. For all data of Table 4.2.

Model:		Langmuir	Toth
q_m	mol/kg	1.83 ± 0.06	1.77 ± 0.08
$K'{}^\dagger$	1/Pa	$(8.34 \pm 0.53) \cdot 10^{-4}$	$(8.36 \pm 0.55) \cdot 10^{-4}$
ΔH_{ads}^0	kJ/mol	-43.1 ± 1.4	-43.1 ± 1.5
t	-	-	1.06 ± 0.10
Standard error*		0.0773	0.0775
$ssq_{min}{}^\ddagger$		0.0783	0.0781

^b Parameter values with (\pm) 2σ -confidence levels[†] Adsorption equilibrium constant at reference temperature, $T' = 30^\circ\text{C}$ (see Section 2.5.4)[‡] Minimal sum of squares of residuals* Approximate standard error on the output variable ($\ln q$)

The Langmuir model fits the results very well with a standard error on the order of 5 %. The heat of adsorption is very well estimated with an error of $\approx 4\%$ as is also evident from the Arrhenius plot of the adsorption constants in Figure 4.10, which has a coefficient of determination of $R^2 = 0.996$. The Toth isotherm is an empirical equation similar to the Langmuir isotherm, but with one extra parameter:

$$q = q_m \frac{K P_{\text{C}_3\text{H}_8}}{[1 + (K P_{\text{C}_3\text{H}_8})^t]^{1/t}} \quad (4.7)$$

where t is a parameter, which is usually less than unity. When $t = 1$, the Toth isotherm reduces to the Langmuir isotherm. t characterizes the system heterogeneity. As it is deviated further away from unity the system is said to be more heterogeneous. The system heterogeneity could stem from the adsorbent or the adsorbate or a combination of both (Do, 1998).

The result of the model fitting with the Toth and Langmuir isotherms to the total data set (134 data points) of Table 4.2 is given in Table 4.3. The parameters are very similar and the minimal sum of squares is essentially equal. The Toth isotherm parameter is found to be very close to $t = 1$ for which the model reduces to the Langmuir isotherm. One model is not considerable better than the other and the Langmuir model was preferred due to the principle of parsimony².

The results obtained for the three samples of silicalite-1 and H-ZSM-5 with different Si/Al-ratios are very similar. From this data, no trend in the change of adsorption capacity with chemical composition can be concluded. Therefore, the three compounds can be considered to have identical adsorption capacities for propane. The saturation capacity reported is between 1.90 and 2.02 mol/kg, for pure silicalite-1 in the temperature range 298-308 K (Sun *et al.*, 1998; Zhu *et al.*, 2000b,a), being in the same range as found in the present study. The heat of adsorption was found to be $H_{ads}^0 = -43.1$ kJ/mol, which is similar to reported data (Hufton & Danner, 1993; Zhu *et al.*, 2000a). The condensation heat for propane in the temperature range of 5-60 °C is known to be -12 to -16 kJ/mol (Majer & Svoboda, 1985). This fact suggests that chemical adsorption rather than pore condensation is taking place.

²Preference for the least complex explanation for an observation

4.3 Isothermal Adsorption Model

4.3.1 Governing Model Equations

All mathematical models describing the behavior of an isothermal adsorption bed must include the following:

1. Adsorption isotherm
2. Mass balance for the gas phase
3. Mass balance inside the adsorbent

All these equations are coupled and need to be solved simultaneously. The boundary conditions depend on the specific process (e.g. temperature swing and pressure swing).

Assuming constant pressure and a single adsorbate these equations are as follows.

The adsorption equilibrium isotherm:

$$q = q(T, C^z) \quad (4.8)$$

where q is the amount adsorbed per volume of adsorbent, C^z is the gas phase concentration inside the pore and T is the temperature inside the pore.

The mass balance in the adsorbent depends on the pellet geometry. For a spherical pellet it becomes:

$$D_e \left(\frac{\partial^2 C^z}{\partial r^2} + \frac{2}{r} \frac{\partial C^z}{\partial r} \right) = \frac{\partial q}{\partial t} \quad (4.9)$$

where D_e is the effective diffusivity. The factor 2 in $2/r$ is replaced by 1 for cylindrical and 0 for platelet pellets. The derivation of this equation assumes that the accumulation of adsorptive in the void fraction inside the pellet ($\varepsilon_z \partial C^G / \partial t = 0$) can be neglected due to the small quantity relative to the adsorbate. This equation applies to sorbents of uniform pore structure.

The mass transport in the bulk gas phase can be described with convection and dispersion:

$$\frac{\partial C}{\partial t} = D_{ax} \frac{\partial^2 C}{\partial z^2} - \frac{\partial v C}{\partial z} - \frac{1 - \varepsilon}{\varepsilon} k_f a' (C - C_R^z) \quad (4.10)$$

where D_{ax} is the axial dispersion coefficient, v is the interstitial linear velocity, z is the axial position in the fixed-bed, ε is the bed porosity, k_f is the film mass transfer coefficient, a' is the external particle surface area and C_R^z is the gas adsorptive concentration at the outer adsorbent pellet surface. The gas phase concentration is assumed to be uniform in the radial direction and radial dispersion is thus neglected.

Equations 4.9 and 4.10 are coupled by the continuity at the pellet surface:

$$D_e \left(\frac{\partial C^z}{\partial r} \right)_R = k_f (C - C_R^z) \quad (4.11)$$

In order to solve this system of coupled partial differential equations several parameters need to be calculated and estimated. The physical parameters like porosities, ε , densities,

ρ , external surface area, a' , characteristic length, R and heat capacities, C_p are readily available or measurable. However, transport properties: D_e , D_{ax} and h , must be estimated from correlations based on gas flow, type of fixed-bed packing and pore structures.

The resistances to mass transfer inside and outside the adsorbent pellets can be important. The local rate of adsorption is assumed instantaneous because it approximates the collision frequency of the gas on the solid surface, which is much greater than the transport processes (Yang, 1997).

4.3.2 Classification

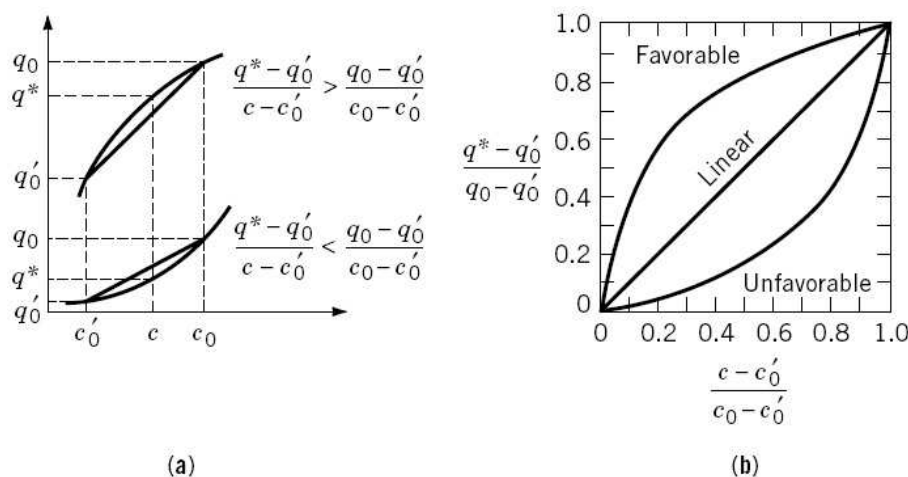


Figure 4.11: (a) Equilibrium isotherm and (b) dimensionless equilibrium diagram showing favorable, linear, and unfavorable isotherms. (Ruthven, 2001).

The dynamic behavior of an adsorption bed can be classified according to the nature of the mass transfer front and the complexity of the mathematical model required to describe the system. The nature of the mass transfer front is determined by the equilibrium relationship alone. For systems with linear or unfavorable isotherms (see Figure 4.11) the mass transfer zone (MTZ) broadens as the front propagates through the adsorption bed. This behavior is called dispersive or "proportionate pattern", since the width of the MTZ increases in direct proportion to the distance travelled through the bed. When the isotherm is favorable, the mass transfer front broadens in the initial region, but after some distance it attains a constant-pattern form and progresses with no further change of shape. The complexity of the mathematical model depends on the concentration level, the choice of rate equation and the choice of flow model. Single component systems can be classified according to the following scheme:

1. Equilibrium Relationship

- *Linear Isotherm:* Dispersive behavior. Analytic solutions for step or pulse response can generally be found.
- *Favorable Isotherm:* Concentration front approaches constant-pattern form. General analytic solutions for the breakthrough curve or pulse response is only possible in a few special cases.

- *Unfavorable Isotherm*: Dispersive behavior. Most commonly observed during desorption of a favorably adsorbed species. Analytic solutions are generally not possible.

2. Isothermal or Adiabatic

- *Isothermal*: Heat transfer resistance can be neglected. The spreading of the concentration front is only due to axial dispersion and mass transfer resistance.
- *Adiabatic*: Heat transfer between fluid and solid phase is slow and cause a broadening of the concentration front. A thermal front may be observed with a secondary MTZ.

3. Concentration Level of Adsorptive

- *Trace Systems*: The adsorptive is present in low concentration in an inert carrier. Changes in fluid velocity across the MTZ can be neglected.
- *Non-trace Systems*: The adsorptive is present in a high enough concentration to result in significant changes in fluid velocity.

4. Flow Model

- *Plug Flow*: Axial dispersion is neglected. The term $D_{ax}(\partial^2 C / \partial z^2)$ can be dropped from Equation 4.10, reducing it to a first-order hyperbolic equation.
- *Dispersed Plug Flow*: Axial dispersion is significant. The numerical solution of the system is more complex than above.

5. Complexity of Kinetic Model

- *Negligible Mass Transfer Resistance*: Instantaneous equilibrium is assumed at all points in the fixed-bed.
- *Single Mass Transfer Resistance*: Using a linear rate expression for the mass transfer: the linear driving force (LDF) approach. The rate coefficient is an overall effective mass transfer coefficient (lumped parameter).
- *Two Mass Transfer Resistances*: External fluid film resistance plus intraparticle diffusion or two internal diffusional resistances (macropore-micropore).
- *Three Mass Transfer Resistances*: External film plus two internal diffusional resistances in series.

In the current study the isotherm was found to follow the Langmuir model satisfactorily, which is a favorable isotherm. Furthermore, the system was isothermal and treated trace levels of adsorbent $< 0.3\%$. Even during desorption to the catalytic burner the mole fractions should be lower than 0.5% . In modeling the system, the deviation from plug

flow was too significant to be neglected. However, as will be shown later, the mathematical model described the deviation from plug flow by the tanks-in-series model. First, the kinetic models and secondly the discretization by the tanks-in series model will be discussed.

4.3.3 Instantaneous Mass Transfer

The simplest system to consider is an isothermal plug flow system with a trace of adsorptive in an inert carrier which is being adsorbed under conditions where mass transfer is negligible. In this case the concentration is uniform at any radial cut of the fixed-bed including the void of the adsorbent. The system can be described by only two coupled ordinary differential equations (ODEs): the mass balance in the gas phase (Equation 4.10):

$$\frac{\partial C}{\partial t} = -v \frac{\partial C}{\partial z} - \frac{1-\varepsilon}{\varepsilon} \rho_z \frac{\partial q}{\partial t} \quad (4.12)$$

where ρ_z is the adsorbent density, and a second mass balance for the accumulation in the adsorbent phase, using the chain rule and calculating $\partial q / \partial C$ from the definition of the Langmuir isotherm:

$$\frac{\partial q}{\partial t} = \frac{\partial q}{\partial C} \frac{\partial C}{\partial t} \quad (4.13)$$

$$\frac{\partial q}{\partial t} = \frac{q_m K R T}{(1 + K C R T)^2} \frac{\partial C}{\partial t} \quad (4.14)$$

Combining Equation 4.12 and 4.14 yields a single ODE describing the breakthrough curve:

$$\frac{\partial C}{\partial t} = \frac{-v}{1 + \frac{1-\varepsilon}{\varepsilon} \rho_z \frac{q_m K R T}{(1 + K C R T)^2}} \frac{\partial C}{\partial z} \quad (4.15)$$

Considering the same mass balance for a tanks-in-series model with N tanks, for the j^{th} tank:

$$\varepsilon V_j \frac{\partial C_j}{\partial t} = \dot{V} (C_{j-1} - C_j) - V_j (1 - \varepsilon) \rho_z \frac{\partial q_j}{\partial t} \quad (4.16)$$

$$\frac{\partial C_j}{\partial t} = \frac{1}{\tau_j} (C_{j-1} - C_j) - \frac{(1 - \varepsilon)}{\varepsilon} \rho_z \frac{\partial q_j}{\partial t} \quad (4.17)$$

$$\frac{\partial C_j}{\partial t} = \frac{1}{\tau_j} (C_{j-1} - C_j) - \frac{(1 - \varepsilon)}{\varepsilon} \rho_z \frac{\partial q_j}{\partial C_j} \frac{\partial C_j}{\partial t} \quad (4.18)$$

$$\frac{\partial C_j}{\partial t} = \frac{1}{\tau_j \left(1 + \left(\frac{(1-\varepsilon)}{\varepsilon} \rho_z \frac{\partial q_j}{\partial C_j} \right) \right)} (C_{j-1} - C_j) \quad (4.19)$$

$$\frac{\partial C_j}{\partial t} = \frac{1}{\tau_j \left(1 + \left(\frac{(1-\varepsilon)}{\varepsilon} \rho_z \frac{q_m K R T}{(1 + K C R T)^2} \right) \right)} (C_{j-1} - C_j) \quad (4.20)$$

$$\frac{\partial C_j}{\partial t} = \frac{1}{\tau_j + \Delta t_{ads}} (C_{j-1} - C_j) \quad (4.21)$$

where \dot{V} is the volumetric flow rate, Δt_{ads} is the "adsorption time" and $\tau_j = \epsilon V_j / \dot{V}$. This result (discretized for $N > 50$) is analogous to that of the plug flow fixed-bed adsorber in Equation 4.15. The result shows that in case of instantaneous mass transfer the apparent residence time of the adsorber is the hydraulic residence time plus the time needed for saturation of the adsorbent. The breakthrough curve will thus have the same shape as a step-curve in an empty reactor (or the response of an inert tracer) in dimensionless time, but will be retarded by Δt_{ads} due to the adsorption capacity of the system.

This simple system of isothermal plug flow with a trace of adsorptive in an inert carrier and negligible mass transfer is rare in practice. Indeed, it was not capable of describing the breakthrough curves of the current system. However, it provides insight into more complex systems.

4.3.4 Finite Mass Transfer

In practice, large adsorbent pellets are often desirable to keep the pressure drop low. Industrial adsorbents are usually larger than $250\text{--}420\ \mu\text{m}$ (Yang, 1997) and a model with instantaneous mass transfer is seldom accurate. Using zeolites as adsorbent will also lead to internal mass transfer influences, due to the small pore sizes and the accompanying low diffusivities.

Analytic solutions can be found for systems with plug flow. If the adsorption isotherm is linear, analytic solutions for the concentration profiles can be found by applying the Laplace transform method. For nonlinear isotherms numerical solutions are usually necessary.

Linear Isotherm

The intraparticle mass transfer can be described by a diffusion model (Equation 4.9), where the pellet is treated as a homogeneous phase in which diffusion takes place with a constant effective diffusivity, D_e . The most important of these models is that of Rosen (Rosen, 1952, 1954; Ruthven, 1984).

The Rosen Model

The rate of mass transfer in adsorption by a spherical pellet is assumed to be the combined rate of external film diffusion and internal pore diffusion. The isotherm is assumed linear. Further assumptions include: plug flow, isothermal constant flow velocity and constant effective diffusivity. An analytical solution was found for the effluent concentration with a step change in the inlet concentration to a clean bed.

The equations to be solved are the mass balance for the gas phase Equation 4.10 without the axial dispersion term, the intraparticle diffusion of Equation 4.9 with the volume-

average adsorbate concentration q :

$$q = \frac{3}{R^3} \int_0^R KC^z r^2 dr \quad (4.22)$$

The solution for the breakthrough curve is (Ruthven, 1984):

$$\frac{C}{C_0} = \frac{1}{2} + \frac{2}{\pi} \int_0^\infty \exp[-\xi H_1(\lambda)/5] \sin[2\lambda^2 \tau/15 - \xi H_2(\lambda)/5] \frac{d\lambda}{\lambda} \quad (4.23)$$

$$H_1(\lambda) = \lambda [\sinh(2\lambda) + \sin(2\lambda)] / [\cosh(2\lambda) - \cos(2\lambda)] - 1 \quad (4.24)$$

$$H_2(\lambda) = \lambda [\sinh(2\lambda) - \sin(2\lambda)] / [\cosh(2\lambda) - \cos(2\lambda)] \quad (4.25)$$

$$\xi = \frac{15D}{R^2} \frac{Kz}{v} \left(\frac{1 - \varepsilon}{\varepsilon} \right) \quad (4.26)$$

$$\tau = \frac{15D}{R^2} \left(t - \frac{z}{v} \right) \quad (4.27)$$

$$\frac{C}{C_0} = \frac{1}{2} \operatorname{erfc} \left(\frac{\xi - \tau}{2\sqrt{\xi}} \right) \quad (\text{asymptotic form for large } Z) \quad (4.28)$$

The solution is based on the assumption of a linear isotherm and the effect of nonlinearity of the isotherm can be significant.

Nonlinear Isotherm

A general analytic solution for a nonlinear (e.g. Langmuir isotherm) systems was derived by Thomas (Thomas, 1944). The model was derived for ion exchange in aqueous systems and assumed instantaneous diffusion steps (in both film and pores) with the rate-controlling step being the surface adsorption.

The Thomas model is based on the mass balance for the gas phase Equation 4.10 without the axial dispersion term and a pseudo second-order reaction kinetic rate law:

$$\frac{\partial q}{\partial t} = k[C(q_m - q) - \beta q(C_0 - C)] \quad (4.29)$$

and the solution to the system is (Ruthven, 1984):

$$\frac{C}{C_0} = \frac{J(\beta\xi, \tau)}{J(\beta\xi, \tau) + [1 - J(\xi, \beta\tau)] \exp[(\beta - 1)(\tau - \xi)]} \quad (4.30)$$

$$J(\alpha, \beta) = 1 - \int_0^\alpha \exp(-\beta - \alpha) I_0(2\sqrt{\beta\xi}) d\xi \quad (4.31)$$

$$\xi = \frac{kq_0 z}{v} \left(\frac{1 - \varepsilon}{\varepsilon} \right) \quad (4.32)$$

$$\tau = (kC_0) \left(t - \frac{z}{v} \right) \quad (4.33)$$

The parameter β defines the type of isotherm: $\beta = 0$ for an irreversible isotherm, $\beta = 1$ for a linear isotherm, $0 < \beta < 1$ for a favorable isotherm and $\beta > 1$ for an unfavorable isotherm.

While this analytical solution does provide insight into the system, it is based on an unrealistic rate expression. Theoretical breakthrough curves of nonlinear (and linear) systems may be calculated by numerical solution of the model equations (4.8 to 4.10) using standard finite difference methods or collocation methods.

4.3.5 Linear Driving Force Approach

To avoid the complexity of the diffusion solutions it is common practice to use the linear driving force (LDF) model with an overall effective rate constant. This approach eliminates the diffusion model for the adsorbent (Equation 4.9) and assumes that the overall rate of uptake is:

$$\frac{\partial q}{\partial t} = k_{LDF}(q^* - q) \quad (4.34)$$

where q is the average amount adsorbed in the adsorbent and q^* is the amount that would be adsorbed in equilibrium with the bulk gas concentration C . The LDF approximation was first suggested by Glueckauf & Coates (1947); Glueckauf (1955) who also proposed that the rate constant can be approximated for a spherical particle by:

$$k_{LDF} = \frac{15D_e}{R^2} \quad (4.35)$$

A series of mass transfer resistances, i.e. the external film diffusion, the macro-/meso-pore diffusion and the intracrystalline diffusion, can be approximated by (Ruthven, 1984):

$$\frac{1}{k_{LDF}K} = \frac{R}{3k_f} + \frac{R^2}{15\varepsilon_p D_e} + \frac{r_c^2}{15K D_c} \quad (4.36)$$

where D_c is the intracrystalline diffusivity and r_c is the crystal radius.

The LDF model of Equation 4.34 and 4.35 is based on the assumption of $D_e t / R^2 > 0.1$ to ensure that the interior is close enough to equilibrium. Since, the diffusion time constant (D_e / R^2) of zeolite crystals is in the order of 10^{-3} 1/s the application of the LDF model is often invalid for the initial uptake period.

The theoretical prediction of k_{LDF} depends on the adsorbent geometry. The diffusion in the adsorbent zeolite film on the fibers could be estimated as the diffusion in an infinite flat film, with diffusion from only one side (the gas side) and insulated on the other (the metal fiber side). The transient diffusion equation for such a flat film is:

$$\frac{\partial q}{\partial t} = D_e \frac{\partial^2 q}{\partial l^2} \quad (4.37)$$

where l is the coordinate perpendicular to the film surface. This direction varies from 0 to L , which is the thickness of the film. The volume-average concentration \bar{q} for a film with surface area A is given by:

$$\bar{q} = \frac{1}{AL} \int_0^L q A dl = \frac{1}{L} \int_0^L q dl \quad (4.38)$$

The accumulation rate of adsorbate is obtained by differentiating Equation 4.38:

$$\frac{d\bar{q}}{dt} = \frac{1}{L} \int_0^L \frac{dq}{dt} dl \quad (4.39)$$

Substituting Equation 4.37 into 4.39 yields:

$$\frac{d\bar{q}}{dt} = \frac{1}{L} \int_0^L \frac{d}{dl} \left(D_e \frac{dq}{dl} \right) dl = \frac{1}{L} D_e \frac{dq}{dl} \Big|_L \quad (4.40)$$

Several researches have found that the adsorbate concentration profile within the adsorbent pellet can be assumed parabolic (Liaw *et al.*, 1979; Yang & Doong, 1985; Tsai *et al.*, 1985; Do & Rice, 1986; Sircar & Hufton, 2000). The adsorbate concentration is thus approximated by a parabolic profile:

$$q = A + Bl^2 \quad (4.41)$$

where A and B are functions of time, but not of position. The volume-average concentration can thus be found by inserting Equation 4.41 in 4.38 which results in:

$$\bar{q} = \frac{1}{L} \int_0^L (A + Bl^2) dl = A + \frac{B}{3} L^2 \quad (4.42)$$

If it is assumed that the outer surface (L) is in equilibrium with the external gas concentration then $q_L = q^* = A + BL^2$. It follows that:

$$q^* - \bar{q} = \frac{2}{3} BL^2 \quad (4.43)$$

and

$$\frac{dq}{dl} = 2Bl \Rightarrow \left. \frac{dq}{dl} \right|_L = 2BL \quad (4.44)$$

Combining Equation 4.43 and 4.44 leads to:

$$q^* - \bar{q} = \frac{L}{3} \left. \frac{dq}{dl} \right|_L \quad (4.45)$$

Substituting Equation 4.45 into 4.40 finally gives:

$$\frac{d\bar{q}}{dt} = \frac{3D_e}{L^2} (q^* - \bar{q}) \quad (4.46)$$

For very thin zeolite films on the fibers this result is a good approximation of the mass transfer coefficient. However, the correct mathematical derivation of the mass transfer coefficient should consider the film as being cylindric. The solution to this problem can be derived analogously to the example above for the flat film. The mathematical transformations become more cumbersome due to the more complex geometry. The solution to the diffusion problem is (Patton *et al.*, 2004):

$$\frac{d\bar{q}}{dt} = \frac{4D_e(q^* - \bar{q})}{(1 - (r_i/r_o))(r_o^2 - r_i^2) - (1/r_o(r_o - r_i))[(1/2)(r_o^4 - r_i^4) - (4r_i/3)(r_o^3 - r_i^3) + r_i^2(r_o^2 - r_i^2)]} \quad (4.47)$$

The LDF approximation represents the desorption curves for any isotherm and the adsorption breakthrough curves for linear isotherms well, but it breaks down for the adsorption when the isotherms become highly nonlinear. Vermeulen (1953) developed a modified "quadratic driving force (QDF) approximation" which represents the diffusion model more accurately than the LDF model for nonlinear isotherms:

$$\frac{\partial q}{\partial t} = k_{QDF} \frac{q^{*2} - q^2}{2q} \quad (4.48)$$

where the quadratic driving force rate constant $k_{QDF} = \pi^2 D_e / R^2$ for a spherical particle. Although this expression describes the breakthrough behavior of a diffusion-controlled system well, the linear addition of the mass transfer resistances, which is a major advantage of the LDF model, is no longer possible with the nonlinear driving force model.

4.3.6 Tanks-in-Series Model with Linear Driving Force

In the current study of the two-step adsorption-incineration method using propane as a model molecule, the concentration by adsorption is only beneficial for a gas mole fraction below ≈ 3300 ppmv, since at higher concentrations the oxidation temperature ($T > 250^\circ\text{C}$) of an adiabatic catalytic burner can be sustained. This is discussed in Section 6.1. According to the isotherms in Figure 4.9, at temperatures higher than 20°C , the isotherm is nearly linear up to at least 1000 Pa or ≈ 10000 ppmv. The linear driving force model can thus be applied for this system. As discussed above, it is also necessary to estimate the diffusion time in the system, to assess the validity of the model.

From the definition of the Thiele modulus for a film we have:

$$\Phi = L \sqrt{\frac{k}{D_e}} \quad (4.49)$$

$$\begin{aligned} &\Updownarrow \\ \Phi^2 &= \frac{L^2}{D_e} k \end{aligned} \quad (4.50)$$

where L is the characteristic length of the adsorbent, the characteristic reaction time is given by the rate constant k and the characteristic diffusion time is L^2/D_e . The diffusivity in zeolites is specific to the system studied (i.e. type of diffusing molecule and type of zeolite), due to the small and well defined micro pores. The configurational diffusivity of propane in MFI-type zeolites is given in Table 4.4.

Table 4.4: Diffusivity of propane in MFI-type zeolites at 61°C and the diffusional activation energy, E_a . Adapted from (Kärger & Ruthven, 1992).

MFI-type	Method	D [m^2/s]	E_a [kJ/mol]
H-ZSM-5	NMR	$3 \cdot 10^{-9}$	7.5
Silicalite-1	Frequency response	$1.5 \cdot 10^{-11}$	~ 21
Silicalite-1	Square wave	$2.5 \cdot 10^{-9}$	6.7
Silicalite-1	Zero length column	$1.2 \cdot 10^{-11}$	13.0
Silicalite-1	Membrane	$7.3 \cdot 10^{-12}$	-

It is difficult to estimate the diffusivity in zeolites experimentally, which is seen by the variance of the measured values from different experimental measurement methods. The values are given for 61°C , so they are higher than can be expected at the isothermal adsorption temperature at room temperature. However, given the variance in the data it should be sufficient to estimate the diffusion time based on the lowest value of the diffusivity: $7 \cdot 10^{-12} \text{ m}^2/\text{s}$.

The thickness of the zeolite film grown on the SMF is taken as the characteristic length. The film thicknesses were estimated from SEM images and are shown in Table 4.5.

The diffusion time in the zeolite film at room temperature for the 10 wt.% loading sample is thus:

$$\frac{L^2}{D_e} = \frac{(2.75 \cdot 10^{-6} \text{ m})^2}{7.3 \cdot 10^{-12} \text{ m}^2/\text{s}} \approx 1 \text{ s} \quad (4.51)$$

With a diffusion time on the order of 1 s the LDF model should be valid after approximately 0.1 s according to the assumptions for Equation 4.35. Therefore, the LDF model

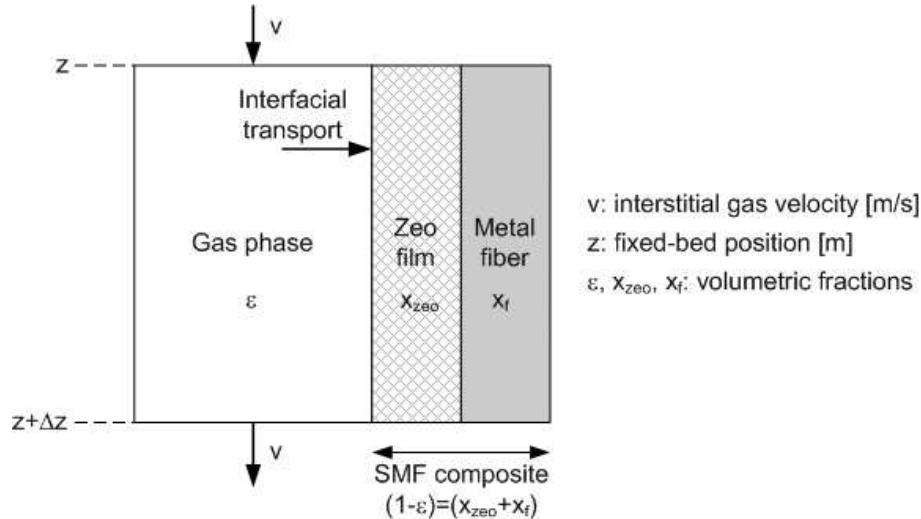
Table 4.5: Zeolite film thickness as a function of loading.

Zeolite loading wt. %	Composite diameter μm	Film thickness μm
0	20	0
5	23	1.5
10	25.5	2.75
19	29	4.5

should be able to describe the breakthrough curves of the studied system.

Initially, we proposed a tanks-in-series model using a lumped mass transfer coefficient for the film diffusion as a description of the system (Nikolajsen *et al.*, 2006). The derivation of this model is shown in Appendix A. However, the LDF model builds on the same principle of a single overall mass transfer coefficient, but is a simpler system with one ODE less for each tank. Furthermore, the LDF model can easily be changed to use a quadratic driving force in case of nonlinear isotherms with different VOCs or higher concentrations. Therefore, the tanks-in-series model with a linear driving force was used and the derivation of this model follows.

The adsorption process is described by the following mass balances and the linear driving force (LDF) approach. It is assumed that the adsorption on the solid phase is instantaneous and follows the Langmuir isotherm. The Langmuir parameters used in the simulations for the adsorption equilibrium, were determined experimentally by the transient response method as described in Section 4.2. Further assumptions include an isothermal bed, constant pressure, constant interstitial linear flow rate and the ideal gas law. A scheme of a control volume for the adsorber used for the derivation of the mass and energy balances is shown in Figure 4.12.

**Figure 4.12:** Scheme of a control volume for the adsorber.

The mass transport in the bulk gas phase can be described with convection and dispersion:

$$\frac{\partial C}{\partial t} = D_{ax} \frac{\partial^2 C}{\partial z^2} - v \frac{\partial C}{\partial z} - \frac{x_z \rho_z}{\varepsilon} \frac{\partial q}{\partial t} \quad (4.52)$$

where D_{ax} is the axial dispersion coefficient, v is the interstitial linear velocity, z is the axial position in the fixed-bed, x_z is the zeolite fraction in the fixed-bed and ρ_z is the density of the zeolite.

For deviations from plug flow the mass balance can be described either by the dispersion model or the tanks-in-series model, which are roughly identical for small deviations from plug flow (Levenspiel, 1996). Assuming plug flow (or small deviations from the same) and using the tanks-in-series model the axial dispersion term can be omitted:

$$\frac{\partial C}{\partial t} = -v \frac{\partial C}{\partial z} - \frac{x_z \rho_z}{\varepsilon} \frac{\partial q}{\partial t} \quad (4.53)$$

The linear driving force approach (LDF) can be used to simplify the mass transfer from the bulk gas to the adsorption surface. The LDF approach lumps the mass transfer resistances in series (external film transfer, internal pore diffusion and intrinsic rate of adsorption) together in one coefficient, which relates the amount of adsorbed species to the bulk gas concentration of adsorptive.

$$\frac{\partial q}{\partial t} = k_{LDF}(q^* - q) \quad (4.54)$$

where k_{LDF} is the LDF mass transfer coefficient and q^* is the maximum adsorption capacity of adsorbed species in dynamic equilibrium with adsorptive concentration C in the bulk gas phase. q^* is described by the Langmuir isotherm:

$$q^* = q_m \frac{KC}{1 + KC} \quad (4.55)$$

The Langmuir isotherm is temperature dependent according to the van't Hoff equation:

$$K = K' \exp \left\{ \frac{-\Delta H_{ads}^0}{R} \left(\frac{1}{T} - \frac{1}{T'} \right) \right\} \quad (4.56)$$

The temperature dependence of the mass transfer coefficient, k_{LDF} , can be described by an Arrhenius expression:

$$k_{LDF} = k'_{0,LDF} \exp \left\{ \frac{-E_{LDF}}{R} \left(\frac{1}{T} - \frac{1}{T'} \right) \right\} \quad (4.57)$$

where E_{LDF} is the activation energy for mass transfer and k'_{LDF} is the preexponential factor of the LDF mass transfer coefficient at the reference temperature T' .

The partial differential equation (PDE) describing the mass balance in the bulk gas phase (Equation 4.53) is discretized in order to reduce it to an ordinary differential equation (ODE). The fixed-bed is divided into N equal cells of height $\partial z = h/N$ and the equation is multiplied by the cell volume $\frac{V}{N}$:

$$\frac{V}{N} \frac{\partial C_j}{\partial t} = -\frac{V}{N} v \frac{(C_j - C_{j-1})}{h/N} - \frac{V}{N} \frac{x_z \rho_z}{\varepsilon} \frac{\partial q_j}{\partial t} \quad (4.58)$$

where C_j is the concentration in the j^{th} cell/tank. This reduces to:

$$\frac{V}{N} \frac{\partial C_j}{\partial t} = \frac{\dot{V}}{\varepsilon} (C_{j-1} - C_j) - \frac{V}{N} \frac{x_z \rho_z}{\varepsilon} \frac{\partial q_j}{\partial t} \quad (4.59)$$

$$\frac{\partial C_j}{\partial t} = \frac{N}{\tau} (C_{j-1} - C_j) - \frac{x_z \rho_z}{\varepsilon} \frac{\partial q_j}{\partial t} \quad (4.60)$$

where \dot{V} is the volumetric flow rate.

The initial and boundary conditions are:

$$C_j = 0, q_j = 0 \quad \text{at} \quad t = 0 \quad (4.61)$$

$$C_{j-1} = C_0 \quad \text{for tank } j = 1, t > 0 \quad (4.62)$$

The model equations are transformed to dimensionless form by introducing the following dimensionless variables:

$$f = \frac{C}{C_0} \quad (4.63)$$

$$\xi = \frac{q}{q_0} \quad (4.64)$$

$$\theta = \frac{t}{\tau_m} \quad (4.65)$$

$$\tau_m = \frac{mq_0}{\dot{V}C_0} \quad (4.66)$$

τ_m is a residence time based on the dynamic capacity of the adsorbent in equilibrium with the gas concentration C_0 . In dimensionless form the system becomes:

$$\frac{\partial f_j}{\partial \theta} = \frac{N\tau_m}{\tau}(f_{j-1} - f_j) - \frac{\tau_m}{\varepsilon\tau} \frac{\partial \xi_j}{\partial \theta} \quad (4.67)$$

$$\frac{\partial \xi_j}{\partial \theta} = \tau_m k_{LDF}(\xi_j^* - \xi_j) \quad (4.68)$$

The parameter τ_m was calculated from the isotherm results of the propane adsorption. The number of tanks, N , and the hydraulic residence time, τ , were found from a fit to the "empty" reactor response. The only parameter to be fitted in the model for the breakthrough curves was the LDF mass transfer coefficient, k_{LDF} . The response at the end of the reactor system is the concentration in the last tank, f_N . Equations 4.67 and 4.68 must be solved simultaneously, subject to the initial and boundary conditions in dimensionless form (Equation 4.61 and 4.62):

$$f_j = 0, \xi_j = 0 \quad \text{for} \quad \theta = 0 \quad (1 \leq j \leq N) \quad (4.69)$$

$$f_{j-1} = 1 \quad \text{for} \quad j = 1 \quad \text{and} \quad \theta > 0 \quad (4.70)$$

The set of 2 times N first order ordinary differential equations (ODEs) was solved using a FORTRAN program. The program uses the IVPAG routine of the IMSL MATH/library by Visual Numerics, Inc., which uses an algorithm based on the backward differentiation formulas (BDF), also known as Gear's stiff method. An example of the program code is found in Appendix B.

4.4 Adsorption Breakthrough Curves

The breakthrough experiments carried out serve as an example of the dynamics of the novel adsorbent material along with a mathematical model (Equations 4.67 to 4.70) capable of describing the breakthrough curve. The comparison of the simulation results with

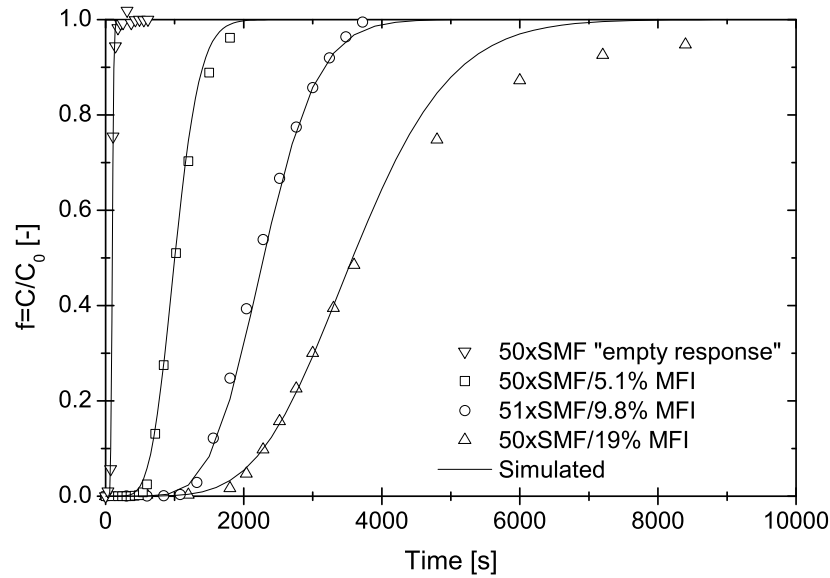


Figure 4.13: Breakthrough curves obtained in pilot adsorber. Isothermal, tanks-in-series, LDF model. Experimental conditions: 800 ppmv propane in Ar, 100 mL(STP)/min, atmospheric pressure and 30 °C.

the experimental data of the breakthrough curves from 50 SMF disks in the pilot reactor (see Section 3.3.3) are shown in Figure 4.13.

The hydrodynamic parameters of the model (number of tanks-in-series, N , and the hydraulic residence time, τ) were first fitted to the "empty" reactor response. The "empty" reactor was packed in a similar way as the normal reactor except that the SMF filters had no zeolite coating. In other words, the "empty" reactor had no adsorption capacity due to the zeolite coating, but the same hydrodynamics were assumed. The pressure drop over the SMF filters does increase with up to 100 % with the increased loading of zeolite. However, the column with the adsorbent was furthermore packed with glass beads, so even though the pressure drop over the active part of the adsorbers was not identical it was negligible in comparison with the rest of the column and the hydrodynamics of the four systems should be nearly identical.

The best fit was obtained with $N = 30$ and $\tau = 97$ s. These parameters describe the hydrodynamics and were used for the simulations of the breakthrough. With the adsorbent in the adsorber, the breakthrough is seen to be retarded. Approximately doubling the zeolite loading from 5.1 wt.% to 9.8 wt.% and again from 9.8 wt.% to 19 wt.% approximately doubles the mass of silicalite-1 in the bed and thus the adsorption capacity. In Figure 4.13 the observed breakthrough time is also seen to approximately double from one sample to the next. As the breakthrough time increases, an absolute broadening of the curve is seen, whereas the relative broadening, i.e. in dimensionless time θ , stays constant for identical mass transfer rates. The slope of the breakthrough curves in both absolute and dimensionless time depends on the mass transfer coefficient. A higher rate of mass transfer results in a steeper slope. However, the slope in absolute time also depends on the adsorption capacity of the system. To visually uncouple these two phenomena the breakthrough curves in dimensionless form are shown in Figure 4.14. The curves for

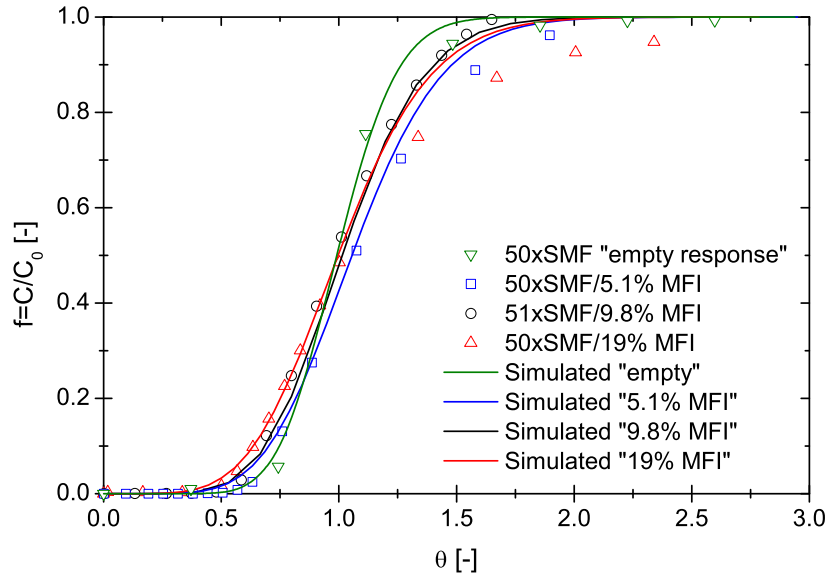


Figure 4.14: Breakthrough curves obtained in pilot adsorber in dimensionless time θ . Isothermal, tanks-in-series, LDF model. Experimental conditions: 800 ppmv propane in Ar, 100 mL(STP)/min, atmospheric pressure and 30 °C.

all four systems with largely differing mean residence times are seen to nearly overlap. In dimensionless form the F-curves/step-curves for the same hydrodynamics (identical number of tanks-in-series) should be identical, independent on the residence time of the system. Therefore, the increased broadening of the curves in real time is mainly due to the change in adsorption capacity and only to a minor degree due to a difference in the overall mass transfer resistance. However, there are small differences. The response of the "empty" adsorber with no capacity has the steepest curve and the adsorbent with the highest loading and thickest silicalite-1 film has the least steep curve. The differences are noticeable through the fitted parameter k_{LDF} and the true k'_{LDF} shown in Table 4.6.

The values of k_{LDF} were fitted with the hydrodynamics of the entire tubular reactor, while the mass transfer only takes place over a fraction of the total volume. The Damköhler I number relates the rate of consumption to the rate of transport:

$$DaI = \frac{\text{rate of consumption}}{\text{rate of transport}} = \tau k_{LDF} = \tau' k'_{LDF} \quad (4.71)$$

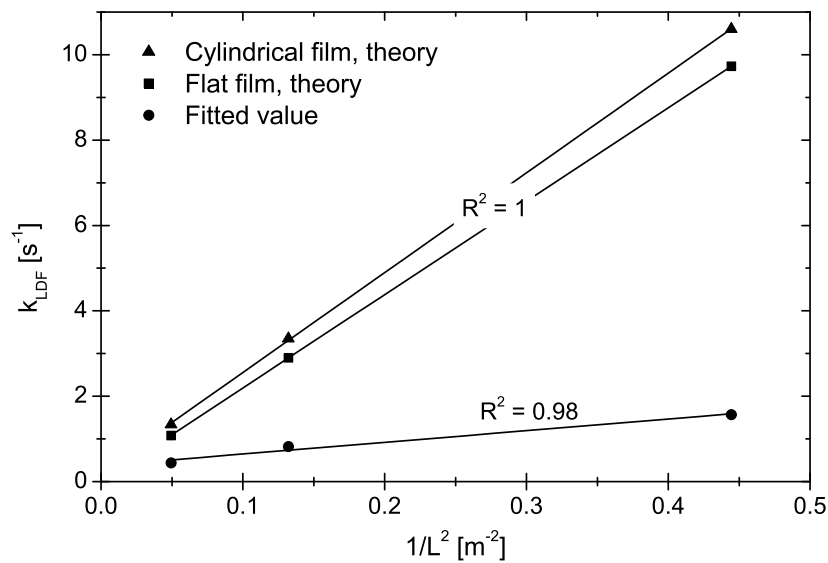
where the apostrophe, ' , denotes the parameter values relating to the active part of the adsorber. From the fitted values and the calculated τ' , the real k'_{LDF} was calculated.

Table 4.6: Experimentally determined values of k'_{LDF} . Number of tanks in model $N = 30$.

Parameter	Unit	Silicalite-1 loading		
		5.1 wt.%	9.8 wt.%	19 wt.%
d_f^\dagger	μm	23	25.5	29
L^\ddagger	μm	1.5	2.75	4.5
ε	-	0.776	0.723	0.643
τ_m	s	949	2255	3590
τ	s	97	97	97
k_{LDF}	$1/\text{s}$	$3.0 \cdot 10^{-2}$	$1.5 \cdot 10^{-2}$	$0.7 \cdot 10^{-2}$
τ'	s	1.85	1.77	1.53
k'_{LDF}	$1/\text{s}$	1.57	0.82	0.44
$D_e/L^2{}^b$	$1/\text{s}$	3.2	0.97	0.36
$k_{LDF, \text{film}} = 3D_e/L^2$	$1/\text{s}$	9.7	2.9	1.1
$k_{LDF, \text{cyl. film, Eqn. 4.47}}$	$1/\text{s}$	10.6	3.3	1.3
$\Phi = L\sqrt{k'_{LDF}/D_e}$	-	0.70	0.92	1.1
$\eta = \tanh \Phi/\Phi$	-	0.86	0.79	0.73

[†] Diameter of fiber composite (MFI/SMF)[‡] Film thickness^b The diffusion constant D_e/L^2 was calculated with $D_e = 7.3 \cdot 10^{-12} \text{ m}^2/\text{s}$ according to the discussion in Section 4.3.6.

The true values of the mass transfer coefficient k'_{LDF} are clearly seen to decrease with the increasing film thickness. An approximate doubling of the film thickness leads to half the size of the mass transfer coefficient. The trend should be explainable by the increasing film thickness according to the diffusion constant, since all other parameters with influence on the overall mass transfer rate are constant (constant flow rate leads to approximately constant external mass transfer rate and adsorption rate is assumed constant).

**Figure 4.15:** Predicted and fitted values of k_{LDF} .

Theoretically k'_{LDF} should equal $\omega D_e/L^2$, where ω depends on the geometry (sphere = 15, cylinder = 8, film = 3, cylindrical film = Eqn. 4.47) as discussed in Section 4.3.5. The estimated values are seen in Table 4.6 and plotted in Figure 4.15. As expected, the value of k_{LDF} is very similar for the flat film and the cylindrical film, due to the thin films. The fitted values of k_{LDF} follow the proportionality with $1/L^2$ very well with a determination coefficient of 0.98. However, the theoretically predicted values of k_{LDF} are approximately 3.5 times higher than the fitted values. The results obtained with the micromeritics setup for the temperature dependence (Table 4.9) predict a value of $k_{LDF} = 16 \pm 4.7 \text{ } 1/\text{s}$ for a film with 10 wt.% loading at 30 °C. This value on the other hand is about 5 times larger than the predicted value from $3D_e/L^2$. The theoretically predicted value falls in the range of the experimentally determined values. The difference between the values from the pilot and the micromeritics setup could be attributable to differences in flow rates or concentration differences. However, the flow rate difference should only affect the value of the external mass transfer coefficient.

The external mass transfer coefficient can be estimated from the mass transfer correlations as discussed in Section 5.3. k_f was estimated from the correlation of De Greef *et al.* (2005) in Table 5.14 and the values are given in Table 4.7 at 30 °C and yields $k_f = 0.05 \text{ m/s}$. Multiplied by the external surface area of the SMF with a diameter of $25.5 \text{ } \mu\text{m}$ results in $k_{ext} \approx 2100 \text{ } 1/\text{s}$. The external mass transfer is thus three orders of magnitude larger than the determined overall mass transfer rate and should not have any influence on the mass transfer rate.

Table 4.7: Parameters used for the estimation of the film mass transfer coefficient k_f .

Parameter	Unit	Value
T	°C	30
P	Pa	101325
\dot{V}	mL(STP)/min	100
v	m/s	0.013
ρ_{Ar}	kg/m ³	1.61
μ	Pa s	$2.29 \cdot 10^{-5}$
D_m	m ² /s	$1.20 \cdot 10^{-5}$
Re_d	-	0.023
Sc	-	1.3
Sh	-	0.112
k_f	m/s	0.049
a'	m ² /m ³	43450

The Thiele modulus, Φ , is defined for a chemical reaction, but an analogy can be made for adsorption. The adsorption could be considered as a "pseudo-irreversible first order reaction", since no product molecule is formed in the gas phase to produce a gas phase reaction equilibrium. The adsorption kinetics is first order in the gas phase adsorptive concentration. Considering the Thiele modulus as defined in Equation 4.50 the values have been calculated in Table 4.6. The effectiveness factor η can thus be calculated from the flat plate approximation $\eta = \tanh \Phi / \Phi$. The effectiveness factor should in this case describe the influence of diffusion on the gas concentration profile inside the zeolite film. $\eta = 1$ would mean that there is no internal diffusion influence, and that the concentration at any point

inside the film equals that on the external surface of the film. The values of η are calculated in Table 4.6 and vary from 0.73 to 0.86. These values are associated with much uncertainty mainly due to the estimation of the diffusivity in the silicalite-1 zeolite. However, since the breakthrough curves cannot be fitted with the instantaneous adsorption model 4.3.3, the value of the external mass transfer rate is 3 orders of magnitude larger than the overall value k'_{LDF} and since the local rate of adsorption can be considered instantaneous - the mass transfer influence must be related to diffusion in the zeolite film. Therefore, there must be small concentration gradients over the film. The advantage of using the proposed thin film of zeolite supported on SMF lies in the high efficiencies, η , obtained along with the low pressure drop. An optimization of the material is possible through the variation of the film thickness which affects the pressure drop, adsorption capacity and the overall adsorption rate constant.

A better estimation of the LDF mass transfer coefficient might be realized by decreasing the ratio of τ/τ' and thereby decreasing the error introduced by the conversion of k_{LDF} to k'_{LDF} . In the investigated setups $\tau/\tau' > 50$.

4.5 Activated Mass Transfer Coefficient

The isothermal tanks-in-series adsorption model with the LDF mass transfer coefficient was fitted to breakthrough curves at 5, 20, 40, 50 and 60 °C as shown in Figure 4.16. The measurements were made in the micromeritics reactor as described for the isotherm experiments in Section 3.3.2. The reactor was packed with 16 disks of SMF with 10 wt.% H-ZSM-5, Si/Al-ratio = 500. The propane mole fraction was 0.30 % and was fed at 76 mL(STP)/min. The model was fitted in the same way as described in the previous section. The breakthrough curves and the model predictions are seen in Figure 4.16.

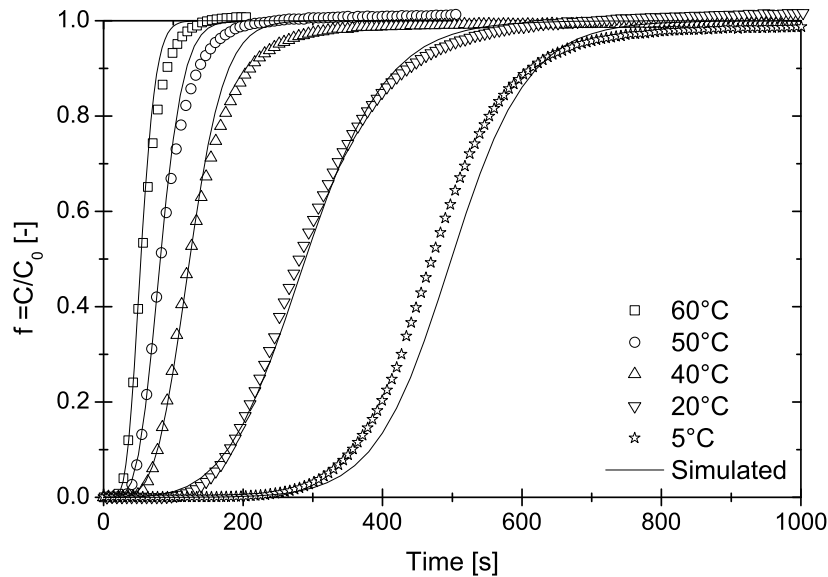


Figure 4.16: Fitting of the LDF rate constant k_{LDF} to breakthrough curves at 5, 20, 40, 50 and 60 °C.

The obtained values of τ and k_{LDF} are given in Table 4.8 and plotted in an Arrhenius

plot in Figure 4.17 and shows a good linear fit with a R^2 -value of 0.94.

Table 4.8: Experimentally determined values of k'_{LDF} . Number of tanks in model $N = 10$.

Parameter	Unit	Adsorption temperature				
		5 °C	20 °C	40 °C	50 °C	60 °C
τ_m	s	530	287	118	74.9	47.8
τ	s	12	12	12	12	10
k_{LDF}	1/s	$5.0 \cdot 10^{-2}$	$6.0 \cdot 10^{-2}$	$4.0 \cdot 10^{-1}$	1.0	5.0
τ'	s	0.240	0.191	0.178	0.173	0.168
k'_{LDF}	1/s	0.75	3.76	26.9	69.4	298

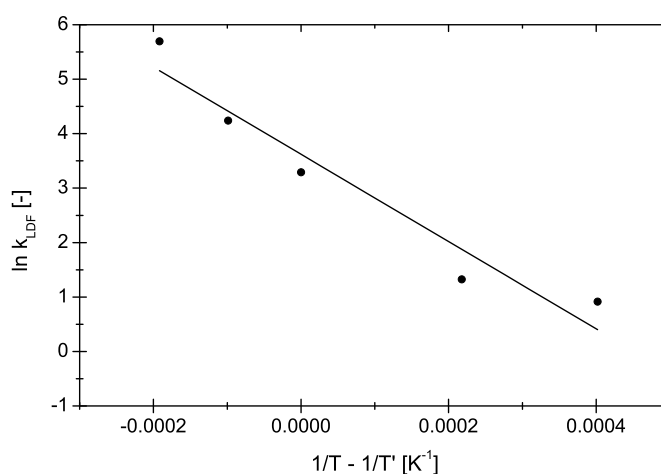


Figure 4.17: Arrhenius plot of the LDF rate constant k_{LDF} . Model fitted to breakthrough curves at 5 to 60 °C, with reference temperature $T' = 40$ °C.

The temperature dependency is described by Equation 4.57 and the parameters from the Arrhenius plot are given in Table 4.9. The value of k_{LDF} at 30 °C predicted from this relationship is 16 ± 4.7 1/s.

The activation energy of the LDF mass transfer coefficient E_{LDF} was found to be approximately 67 kJ/mol. This value is considerably higher than expected with the mass transfer resistance being solely in the zeolite film. The activation energy for diffusion of propane in MFI zeolite has been reported in the range 7 to 21 kJ/mol (Table 4.4). Even with the relatively large standard error, the experimental result is approximately 40 kJ/mol higher than for diffusion alone, which seems unlikely. An explanation might be an influence of activated adsorption onto the surface. However, a search for literature values of the energy of activation for the adsorption of alkanes in MFI zeolite was unsuccessful.

Table 4.9: LDF rate constant parameters. $T' = 40$ °C

Parameter	Unit	Value ($\pm\sigma$)
$k'_{0,LDF}$	1/s	37 ± 10
E_{LDF}	kJ/mol	67 ± 9.9

4.6 Pressure Drop

The pressure drop was measured in the laminar flow regime and shows a linear dependence on the flow rate (Figure 4.18).

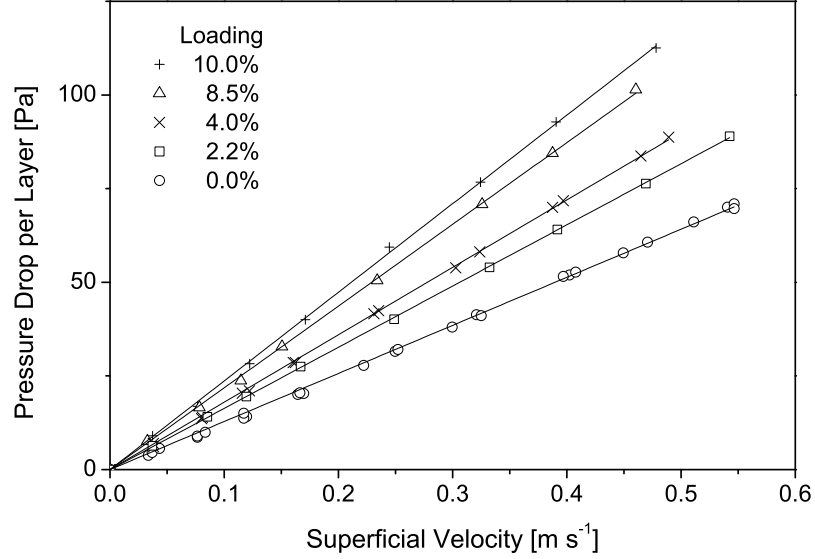


Figure 4.18: Pressure drop across stacked SMF filters as a function of the gas flow rate.

Darcy's law for the pressure drop in the laminar flow range was fitted to the data by a least-squares method, minimizing the sum of the squared residuals (SSR) between the model and the experimental data:

$$\frac{\Delta P}{\Delta h} = \frac{\mu \dot{V}}{kA} = \frac{\mu v}{k} \quad (4.72)$$

The variable in the model was the permeability factor, k . Figure 4.19 shows the expected falling tendency of the fitted permeability as a function of the zeolite loading on the SMF. Higher loading leads to a lower permeability and a higher pressure drop. Zeolite in the form of powder or particles can also be used in a fixed-bed for VOC adsorption, but the pressure drop will be much higher.

To compare the SMF with a conventional randomly packed bed of spheres the equivalent particle diameter could be calculated from the Ergun equation:

$$\frac{\Delta P}{\Delta h} = 150 \frac{(1 - \varepsilon)^2 \mu}{\varepsilon^3 d_p^2} v + 1.75 \frac{(1 - \varepsilon) \rho}{\varepsilon^3 d_p} v^2 \quad (4.73)$$

For low Reynolds numbers, i.e. the laminar regime, only the first term of the Ergun equation is relevant. Equating the laminar terms of the Ergun equation and Darcy's law allows the calculation of an equivalent particle diameter of the SMF. Assuming a bed porosity for the spheres of $\varepsilon = 0.4$ and $\varepsilon_{SMF} = 0.72$ with 10 wt.% loading. For the case

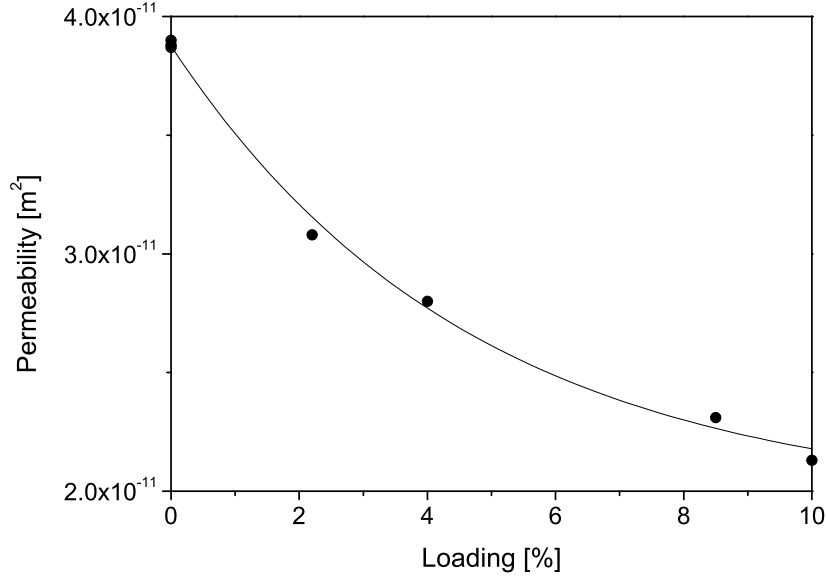


Figure 4.19: Permeability of SMF filters as a function of the zeolite loading.

of constant interstitial linear flow rate v :

$$\frac{\mu v}{k} = 150 \frac{(1 - \varepsilon)^2 \mu}{\varepsilon^3 d_p^2} v \quad (4.74)$$

\Updownarrow

$$d_p = \sqrt{150 \frac{(1 - \varepsilon)^2}{\varepsilon^3}} \sqrt{k} = 136 \mu\text{m} \quad (4.75)$$

and for constant superficial cross sectional area of the packed bed A and constant volumetric flow rate \dot{V} :

$$\frac{\mu \dot{V}}{k \varepsilon_{SMF} A} = 150 \frac{(1 - \varepsilon)^2 \mu}{\varepsilon^3 d_p^2} \frac{\dot{V}}{\varepsilon A} \quad (4.76)$$

\Updownarrow

$$d_p = \sqrt{150 \frac{(1 - \varepsilon)^2}{\varepsilon^3} \frac{\varepsilon_{SMF}}{\varepsilon}} \sqrt{k} = 183 \mu\text{m} \quad (4.77)$$

The pressure drop over the SMF with 10 wt.% loading and a diameter of $\sim 26 \mu\text{m}$ is thus comparable to that created by a packed bed of spheres with diameters 5-7 times larger. However, the dynamics of adsorbent particles with much bigger diameters will of course be very different.

The pressure drop over a fixed-bed of $1 \mu\text{m}$ spherical particles was estimated with the Ergun equation, porosity = 0.4. This particle size is in the same order of magnitude as the individual crystals in the zeolite film (Figure 4.2). When comparing the pressure drop in a randomly packed bed with the same mass of zeolite as on the SMF filters with 10 % loading, the pressure drop would be 3 orders of magnitude higher compared with the structured adsorber. However, conventional adsorbents are found in the form of spherical

beads of 2-3 mm diameter. It is clear that a zeolite film of $3\ \mu\text{m}$ has very different dynamics than spheres of 2-3 mm diameter. If spheres made entirely out of zeolite were employed the pressure drop would be much smaller, but the dynamics would change the breakthrough curve considerably and the amount of unused zeolite would increase. The pressure drop was therefore compared for two fixed-beds with identical mass of zeolite made up of the SMF based material and another made of 2 mm spheres with a $3\ \mu\text{m}$, active zeolite shell. In this case the internal mass transfer characteristics would be similar. It was found that the pressure drop of the fixed-beds is on the same order of magnitude in the laminar flow regime. The pressure drop is a factor 2 higher in the fixed-bed of SMF at a flow rate of $0.5\ \text{m/s}$. However, the packed bed of spheres is 50 times larger (volumetric basis) than that of SMF.

4.7 Conclusion

A novel, structured adsorber based on sintered metal fibers (SMF) coated by a thin, homogeneous MFI-type (ZSM-5, silicalite-1) zeolite film has been developed, tested and characterized. The zeolite/SMF composite is an efficient adsorbent for the removal of low concentration VOCs. When VOC breakthrough occurs, the adsorbent can be regenerated by desorbing the VOC. The chemical and physical analyses of the synthesized zeolite films correspond well with reported values for MFI zeolites in powder and supported form. The pressure drop across the filters was investigated and shows an increase with increasing loading. The low pressure drop characteristics lead to much more compact fixed-beds compared to using spherical beads with a similar thin zeolite film. The thin film of zeolite leads to a short diffusion path and lower resistance to internal mass transfer. Breakthrough curves of propane through fixed-beds of adsorbent were measured and compared with simulated results. The overall mass transfer coefficient k_{LDF} was found to depend on the temperature as well as the film thickness. The temperature dependence was described by an Arrhenius expression with the apparent activation energy of $E_{LDF} = 67 \pm 9.9\ \text{kJ/mol}$ and the rate constant $k_{LDF}^{40^\circ\text{C}} = 37 \pm 10\ 1/\text{s}$. The dependence on the film thickness follows the proportionality with $1/L^2$ very well. However, the fitted values were either too large or too small compared to the theoretical values. Results from one experimental setup gave larger values and smaller values were obtained from the other setup, but the theoretical values fall in the same range as those obtained from the measurements. The model simulations suggest that the adsorption rate is governed solely by internal pore diffusion in the zeolite. However, with the thin film the concentration gradients are very small, which was shown by the calculation of effectiveness factors from the Thiele modulus by analogy with chemical reaction in porous media.

Chapter 5

Oxidation Catalyst

For the combustion of VOC the SMF support was applied due to the numerous advantages as described in Section 2.2. Catalysts based on this support have previously been studied in our group: combustion catalysts have been developed with Raney-type catalysts based on metal grids (Yuranov *et al.* , 2002) and from SMF based catalysts with different zeolitic coatings (Yuranov *et al.* , 2003). These studies showed that Co_3O_4 was the most active oxide in comparison to the transition metal oxides of Cu, Mn and Cr as well as the noble metals Pt and Pd on various structured, fibrous supports for propane deep oxidation. Based on the promising results, it was decided to develop a novel type of structured catalyst made from a thin layer of finely powdered catalyst deposited on the SMF support. This was compared to a catalyst made from SMF with a film layer of silicalite-1 zeolite as support for the cobalt oxide. Furthermore, the influence of the support composition (AISI316L (SS), FeCrAlloy and Inconel 601) was investigated for catalysts with cobalt oxide impregnated directly on the oxidized SMF surface.

The three different groups of synthesized catalysts for the oxidation of propane are shown in Table 5.1. The group of powder coated SMF catalysts has two subgroups, since the fibers were either coated with inactive $\gamma\text{-Al}_2\text{O}_3$ -powder and then impregnated or they were coated with a fine powder of preimpregnated catalyst.

Table 5.1: Overview of the different groups of synthesized oxidation catalysts.

Support	SMF + Powder coating		SMF + silicalite film	Oxidized SMF
SMF material	AISI316L		AISI316L	AISI316L FeCrAlloy Inconel 601
Coating	$\gamma\text{-Al}_2\text{O}_3$ -powder	Catalyst-powder: CuO/MnOx or Co_3O_4 impregnated on Al_2O_3	silicalite-1 (=MFI)	-
Impregnation	Co_3O_4 , PtOx	-	Co_3O_4	Co_3O_4

The development and testing of these catalysts will be described in the current chapter. Section 5.1 is concerned with the preparation and characterization of the catalysts with cobalt oxide deposited on SMF directly or onto the silicalite-1/SMF composite. Section 5.2 is devoted to the development, powder adherence and optimization of the powder coating procedure, which was done by a design of experiments. Section 5.3 is considering

the mass transfer influences, which are important to assess before the activity and kinetics of the catalyst can be estimated.

5.1 Preparation and Characterization

5.1.1 Powder coatings

Powder of γ -alumina (Sigma-Aldrich, aluminium oxide, activated, neutral, Type 507C) and CK-302 was prepared by attrition milling and deposited according to the descriptions in Section 3.4.1. The details and the optimization of the deposition procedures are described in Section 5.2.

It was important that the powder size was considerably smaller than the fibers in order to form a continuous and stable powder layer. The deposited powder layer was analyzed by SEM images and the powder size distribution was evaluated by laser diffraction.

The SEM images clearly show that almost all of the deposited powder particles have sizes smaller than $1\ \mu\text{m}$, see Figures 5.1 and 5.2. The images also show that the powder film is completely covering the fibers.

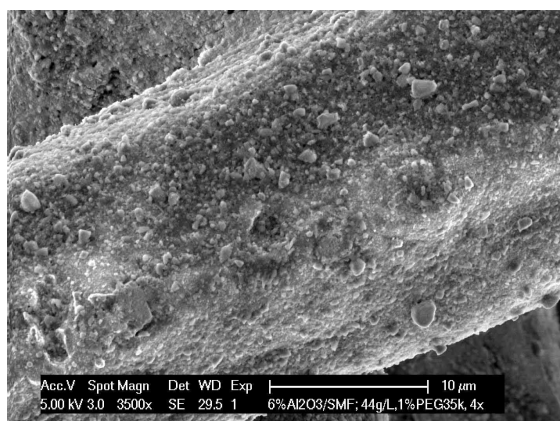


Figure 5.1: SEM: SMF after four powder depositions. Fine particles visible, homogeneous coverage.

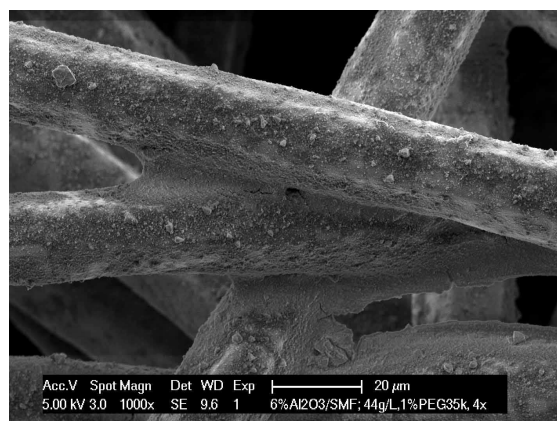


Figure 5.2: SEM: SMF after four powder depositions. Higher amounts of powder visible at intersections.

The equivalent diameter of the prepared powder was measured by laser diffraction (Malvern Mastersizer S). Figure 5.3 shows the volumetric particle distributions for two of the prepared powder suspensions and Table 5.2 shows three quantiles. The particle distributions of the two materials are on the same order of magnitude, but slightly different despite the identical preparation procedure. There could be two explanations of this difference. Firstly, the precision of these measurements are on the order of $\pm 30\%$ (Bowen, 2006). Especially, the measurements of CK-302 had a large uncertainty due to the mixture of phases and approximative information on the diffractive indices. Secondly, the different materials may have different hardnesses leading to different size distributions.

The particle distribution for CK-302 is bimodal. On a volumetric basis the larger particles were important. However, on a number basis they would be less important, and these big particles were agglomerating during the measurements. The results suggest that the obtained particle sizes were larger than desired. However, there is a large uncertainty on

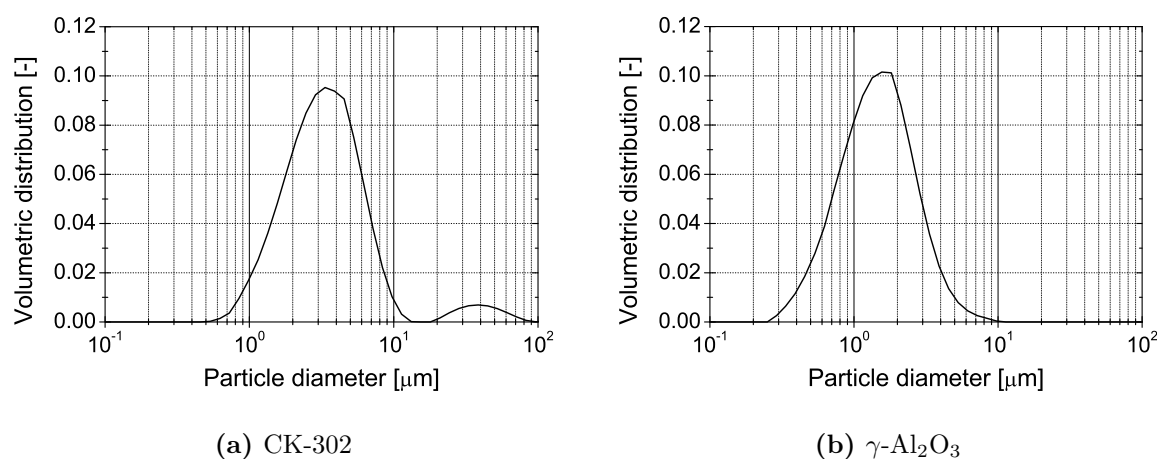


Figure 5.3: Particle size distribution measured by laser diffraction.

Table 5.2: Diameter of particles measured by laser diffraction. Fraction of particles with diameters smaller than:

	Quantile		
	10 %	50 %	90 %
CK-302	1.37 μm	3.10 μm	7.09 μm
$\gamma\text{-Al}_2\text{O}_3$	0.61 μm	1.35 μm	2.78 μm

these powder distribution measurements and the observations made by SEM (Figures 5.1 and 5.2) showed that almost all deposited particles were smaller than 1 μm . Due to the homogeneous powder coatings obtained, which were composed mainly of particles smaller than 1 μm as observed by SEM the procedure was not altered any further.

Incipient Wetness Impregnation

A $\text{Co}_3\text{O}_4/\gamma\text{-alumina}$ catalyst was prepared by incipient wetness impregnation (IWI), in which the amount of added solution is just sufficient to fill up the pore volume of the support particles. The IWI-catalyst was then attrition milled according to the procedure used for the CK-302 catalyst and the $\gamma\text{-alumina}$ powder as described in section 3.4.1. This catalyst was prepared to see the difference in activity between this (IWI) preimpregnated Co_3O_4 on alumina catalyst and that of the Co_3O_4 impregnated onto an already existing alumina powder coating on the SMF filters.

The catalyst was prepared from a batch of 50 g of the ball milled $\gamma\text{-alumina}$ (Sigma-Aldrich) dried at 150 $^\circ\text{C}$ for 14 hours. The dry powder was then impregnated twice with thorough manual mixing and drying (110 $^\circ\text{C}$, 17 h) after each impregnation. Sufficient solution of the required concentration of $\text{Co}(\text{NO}_3)_2(\text{aq})$ (ACROS Organics, Cobalt(II) nitrate hexahydrate, ACS reagent) was used to result in 18.8 wt.% Co_3O_4 after the final calcination (450 $^\circ\text{C}$, 1 h).

The powder was analyzed by XRD as shown in Figure 5.4. The support alone (grey) matches well with the reference spectrum for $\gamma\text{-alumina}$. The IWI-impregnated support

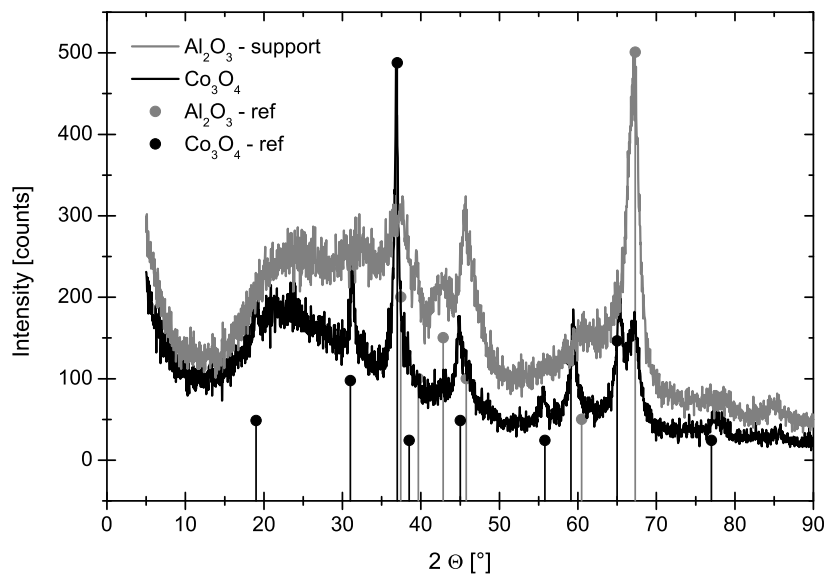


Figure 5.4: XRD spectra of γ -alumina support and 18.8 wt.% IWI- Co_3O_4 on that same support.

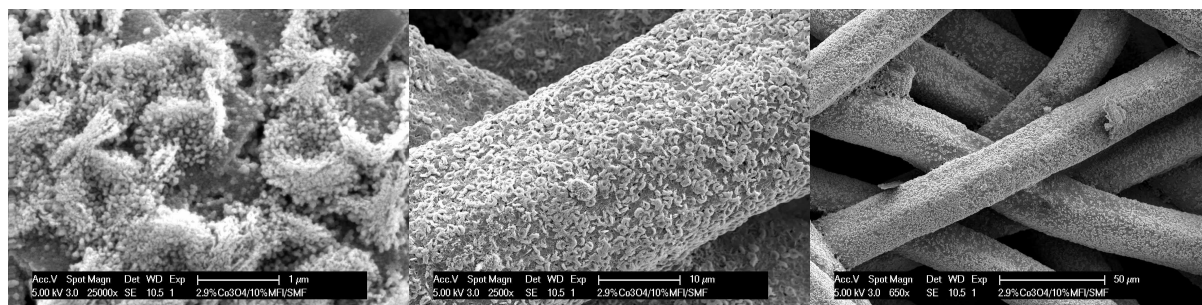


Figure 5.5: SEM: 2.9 wt.% Co_3O_4 impregnated on a 10 wt.% silicalite-1 film on SMF.

shows all the peaks of the reference spectrum of Co_3O_4 , still with the major peaks of the alumina support visible. No peaks of the reference spectra for Co , CoO or Co_2O_3 were visible. It could be concluded that the active phase of cobalt oxide is indeed Co_3O_4 .

5.1.2 Cobalt Oxide/Silicalite-1/SMF

Cobalt oxide was supported on stainless steel SMF covered with a 10 wt.% silicalite-1 film (identical to the adsorbent materials in Chapter 4) by impregnation with cobalt nitrate salt solution. The microporous film will absorb part of the salt solution, but as is seen in Figure 5.5 a large quantity of cobalt oxides (white circular shapes) are spread homogeneously on the outer surface of the silicalite-1/SMF composite.

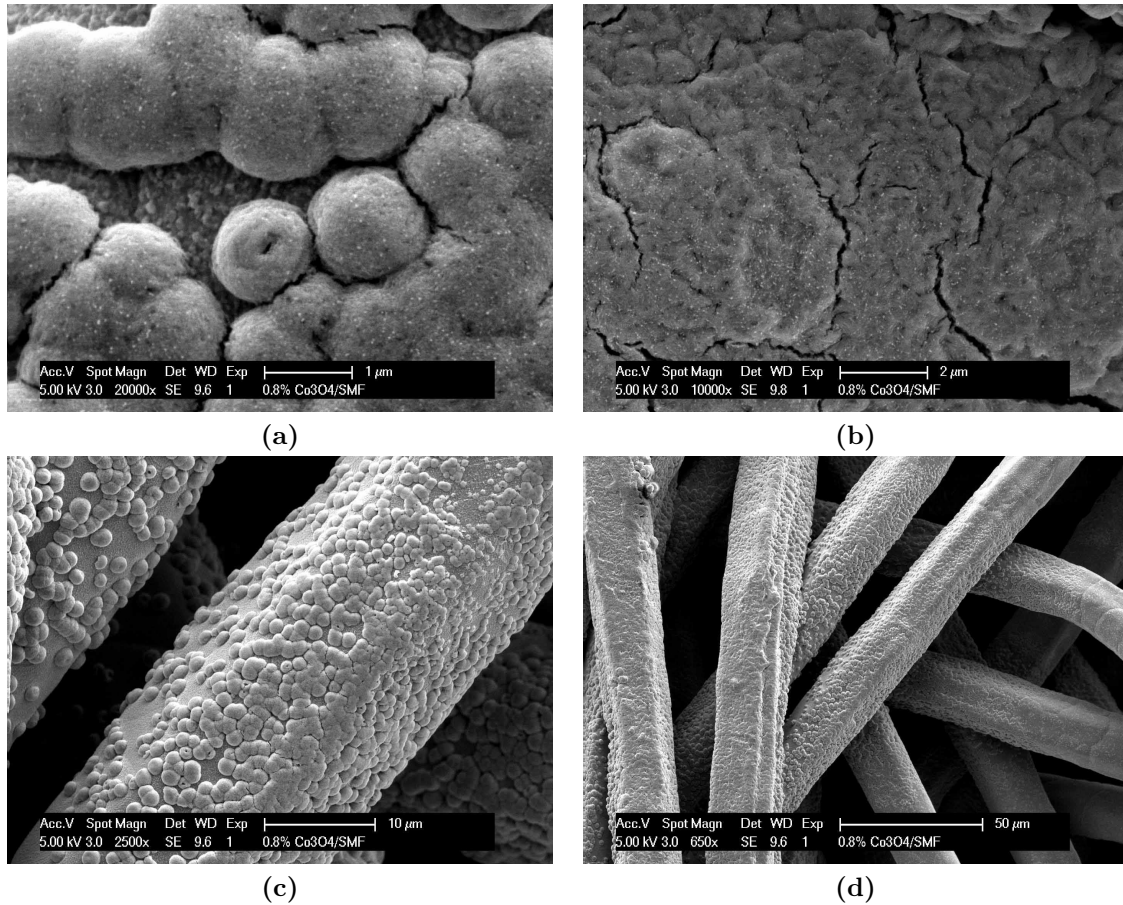


Figure 5.6: SEM: 0.8 wt.% Co_3O_4 impregnated directly on SMF (stainless steel).

5.1.3 Cobalt Oxide/Oxidized SMF

The simplest way of producing the SMF supported metal oxide catalyst is by impregnation of the oxidized SMF filters. The SEM images seen in Figure 5.6 show that the cobalt oxide spreads well over the fiber surfaces. There seems to be a higher concentration around the fiber intersections, where the liquid will tend to build up in order to minimize the liquid surface area during drying. The Co_3O_4 makes hemispheres where there is not enough material to completely cover the fibers. In areas with higher concentration the Co_3O_4 will actually form a thin layer which shows sub-micron sized cracks (Figure 5.6(b)). It was observed that the cobalt oxide spreads more homogeneously over the fibers with the zeolite film of the cobalt oxide/silicalite-1/SMF (Figure 5.5) than directly on the oxidized surface.

5.1.4 BET

The BET specific surface area (SSA_w) was measured for all powders. The results in Table 5.3 show that there is a slight loss of SSA_w as the original particles are milled. The change is not drastic and probably due to loss of mesoporous surfaces. A much larger loss of surface area is caused by the incipient wetness impregnation of γ -alumina with Co_3O_4 for which the SSA_w decreases from 155 to 118 m^2/g due to the filling of the pores.

Table 5.3: BET results for the employed powders.

Treatment	CK-302			γ -Al ₂ O ₃			IWI-Co ₃ O ₄ / γ -Al ₂ O ₃		
	SSA _w ^b [m ² /g]	r_p ^c [Å]	PSV ^d [cm ³ /g]	SSA _w [m ² /g]	r_p [Å]	PSV [cm ³ /g]	SSA _w [m ² /g]	r_p [Å]	PSV [cm ³ /g]
As received ^a	160	20-24	0.29	159	21	0.24	-	-	-
Ball milled	150	20	0.38	155	21	0.29	118	19	0.19
Attrition milled	146	20	0.31	154	21	0.25	-	-	-

^a CK-302 was received as spherical pellets $\varnothing = 3$ -4 mm. γ -Al₂O₃ was received as 150 mesh particles.

^b The BET specific surface area

^c Dominant pore radius

^d Pore specific volume

Table 5.4: Estimated values of the BET SSA_w [m²/g] of SMF filters with a powder or silicalite-1 coating. The loading is based on the mass of SMF support.

	CK-302	γ -Al ₂ O ₃	IWI	Silicalite-1
Powder/silicalite-1	146	154	118	350
Film/SMF				
Loading				
1 wt.%	1.4	1.5	1.2	3.5
5 wt.%	7.0	7.3	5.6	17
10 wt.%	13	14	11	32

For the powder coated SMF filters it is difficult to obtain reliable BET measurements due to the large amount of composite material required. Since the SSA of the filters alone is negligible and the deposited powder does not undergo a physico-chemical change the final catalyst SSA can be estimated directly from the amount of powder deposited on the SMF. Table 5.4 shows the estimated values of the BET SSA for powder-catalyst/SMF composites. The results are computed as a function of the loading and the powder or silicalite-1 specific surface area:

$$SSA_{w,composite} = \frac{x}{1+x} SSA_{w,coat} \quad (5.1)$$

where x is the loading on the SMF. Hence, a benefit of the porous film coating is obviously a large increase of the potential SSA available for the catalytic active phase as compared to a direct impregnation of the metal oxide on the SMF.

5.2 Coatings on SMF by Powder Deposition

The development of the powder coating method was optimized by using design of experiments (DOE). To discuss the chosen DOE scheme it must first be understood what should be obtained from the experiments as well as the importance and limitations of the influencing factors. The limitations will help define the levels of the factors.

5.2.1 Experimental Considerations

The goal was to deposit a homogeneous layer of the finely powdered catalyst on the SMF filters. This means that all of the fibers were coated. It was also important to maximize the loading while keeping the blocking of filter pores to a minimum. The loading could be increased by repeating the deposition procedure. The experimental procedure of the powder preparation and deposition is described in Section 3.4.1.

Five **factors** were identified which could have an effect on the loading:

1. **Polymer type**
2. **Powder suspension concentration**
3. **Polymer concentration**
4. **Calcination or no calcination between repeated depositions**
5. **Drying after deposition in air or vacuum**

Each of these factors could have an influence on the deposition and maybe on the activity of the catalyst as well. The advantages and disadvantages in relation to activity and deposition are discussed in the following:

1. **Polymer:** The type of polymer could have an effect on the activity due to an adverse effect on the specific surface area (SSA) (Germani *et al.* , 2006). It is also possible that the ashes after calcination could have an effect on the activity. An effect on the deposition could also be imagined due to viscosity effects.
2. **Suspension concentration:** This concentration should only have an effect on the deposition characteristics. The higher the concentration, the higher the viscosity and the higher the loading per deposition cycle. Unfortunately, higher concentrations lead to inhomogeneous deposition and blocking of pores. An optimum is expected.
3. **Polymer concentration:** Could enhance effects on the activity due to polymer type. The increased viscosity is believed to be important for the homogeneous spreading of powder on the fibers, but becomes a negative effect at higher concentrations due to blocking of pores and difficult deposition procedure.
4. **Calcination or no calcination between repeated depositions:** could have an effect on the spreading of the aqueous powder solution on the fiber surfaces due to different surface hydrophilicity characteristics. The calcination could also have a negative effect on the activity, due to deactivation. A temperature of 300 °C was chosen for sufficient removal of polymer and low influence on the activity.
5. **Drying after deposition in air or vacuum:** It was thought that the faster vacuum drying could help "freezing" and spreading the powder on the fiber surface.

It is possible to simply test all factors in a certain experimental design. However, this would be quite demanding especially since several types of polymers could be used. In

selecting the factors for the experimental design it is often advisable to do a screening experiment to find the most important factors. This is often done by a Hadamard design (Placket and Burman design). Here 5 factors could be tested at two levels in only eight experiments. This was not so useful in relation to the polymers where four levels were needed. Hence, the polymers were screened in an individual study and the best one was chosen. Using 1 wt.% of the polymers PEG 600, PEG 35,000 and PVP 360,000 in the suspensions compared to the catalyst without polymer it was found that the activity was ca. 30 % higher at the test conditions using the PEG 35,000 polymer, which was chosen for the development of the deposition method (see table 5.5).

Table 5.5: Polymer influence on catalyst activity. Catalysts tested at 350 °C, $0.10 \text{ mol}_{\text{C}_3\text{H}_8}/\text{m}^3$ (equivalent to 20 % conversion of 0.5 % propane in 15 % O_2 at atmospheric pressure).

Sample	Activity at 350 °C WHSV [$\text{g}_{\text{C}_3\text{H}_8}/\text{g}_{\text{cat}}\cdot\text{h}$]
No polymer	2.9
1 wt.% PEG 600	3.0
1 wt.% PEG 35,000	3.8
1 wt.% PVP 360,000	2.8

The remaining four factors could be tested at two levels, which led to a full factorial 2^4 design.

5.2.2 DOE Scheme

The aim of the experiments was to maximize the powder loading on the SMF without getting detrimental effects such as pore blocking and inhomogeneous coverage. The loading would then serve as the response of the experiments. A full 2^4 factorial design was chosen based on the discussion in the previous section 5.2.1. A full factorial design is constituted by an even number of fractional factorial designs. A 2^4 full factorial design consists of 16 experiments. These 16 experiments can be covered precisely by the two 2^{4-1} fractional factorial designs (generators: $\pm 4=123$), which each consists of 8 experiments. Hence, it is often wise to start the experiments with one of the fractional factorial design parts. This will not give full insight into the interactions between the factors, but it could give valuable information, which might lead to a better design or which could save some work.

In the present study there was not a large amount of time and money to be saved by starting with one of the fractional factorial designs. Therefore, the full factorial design was prepared from the beginning.

The following four factors were tested at the levels shown in table 5.6. The concentrations were chosen close to the highest possible levels in order to maximize the loading on the filters in a minimum of repeated depositions.

It is quite obvious that a filter impregnated with a suspension of higher powder concentration should result in a higher loading of powder. Therefore it was chosen to do the deposition four times with the lower concentration ($4 \cdot 33.3 \text{ g/L} = 133.2 \text{ a.u.}^1$) and three

¹a.u.: arbitrary units

Table 5.6: Values of factor levels.

Factor		Unit	Level	
			-1	1
x_1	Suspension concentration	g/L	33.3	44.4
x_2	PEG 35,000 concentration	wt.%	1	2
x_3	Calcination		Yes	No
x_4	Drying		Ambient	Vacuum

times with the higher concentration ($3 \cdot 44.4 \text{ g/L} = 133.2 \text{ a.u.}$) to obtain the same additive amount of loading and not simply observe the obvious effect of the concentration difference.

The deposition method was optimized using the loading of powder after the last calcination of the repeated depositions as the response. A full 2^4 factorial design leads to 16 experiments i.e. 16 different treatments as shown in Table 5.7. Each solution was used with 6 disks of SMF to increase the reliability of the experiments.

Table 5.7: Full 2^4 factorial design.

Experiment Number	Factors			
	Suspension conc.	PEG conc.	Calcination	Drying
1	-1	-1	-1	-1
2	-1	-1	-1	1
3	-1	-1	1	-1
4	-1	-1	1	1
5	-1	1	-1	-1
6	-1	1	-1	1
7	-1	1	1	-1
8	-1	1	1	1
9	1	-1	-1	-1
10	1	-1	-1	1
11	1	-1	1	-1
12	1	-1	1	1
13	1	1	-1	-1
14	1	1	-1	1
15	1	1	1	-1
16	1	1	1	1

5.2.3 Powder Layer Homogeneity

The homogeneity of the deposited powder was not good after one deposition. There would be large regions of the fibers with low or no powder coverage. In the vicinity of fiber intersections there was visibly more powder. This is probably due to the increased surface-solution interactions in these regions. Repeating the deposition would increase the loading and after three depositions the fibers were completely covered with powder and all appeared homogeneously covered. Figure 5.7 shows the calcined SMF, Figure 5.8

shows the SMF after one powder deposition, where the coverage is very inhomogeneous. Figure 5.1 and 5.2 show the fibers after four powder depositions, where the coverage appear homogeneous.



Figure 5.7: SEM: Clean SMF after calcination.

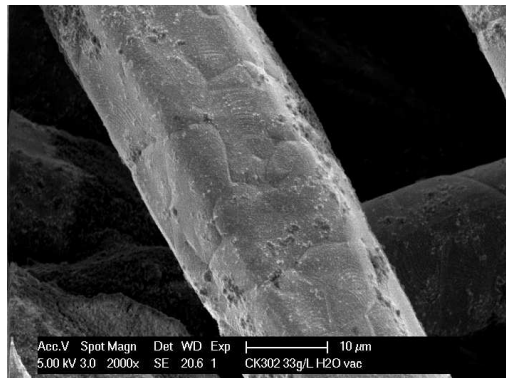


Figure 5.8: SEM: SMF after one powder deposition.

5.2.4 ANOVA and Linear Model

The results of the four chosen factors' effects on the loading were treated by an ANOVA using a MATLAB function (Fürbringer, 2006). Since there were 6 disks for each of the 16 possible treatments the data set consists of 96 data points. In general the depositions were reproducible, but with a significant standard deviation of up to 12 % of the average loading value for each experimental set. The model fitted to the experimental data is shown in equation 2.37. With main half effects and first order interaction half effects. The higher order effects were assumed to be negligible.

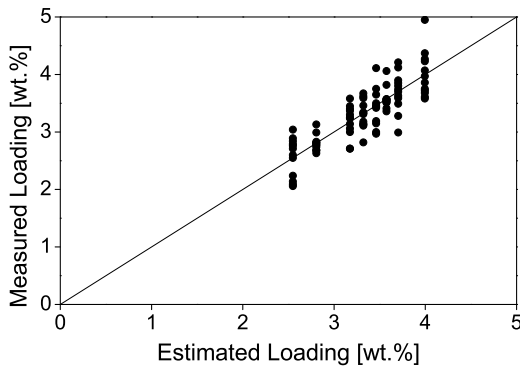
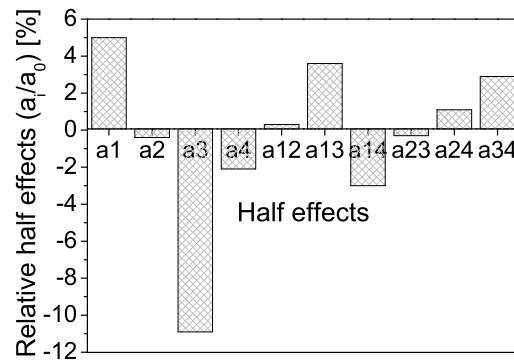
Table 5.8: ANOVA of powder deposition results.

	Effects	SS	DF	MS	F	P
Constant	3.32	1059.48	1			
a_1	0.16	2.60	1	2.6	29	0.0000
a_2	-0.01	0.01	1	0.015	0.17	0.6812
a_3	-0.36	12.48	1	12	141	0.0000
a_4	-0.07	0.46	1	0.46	5.2	0.0255
a_{12}	0.01	0.01	1	0.012	0.14	0.7115
a_{13}	0.12	1.39	1	1.4	16	0.0002
a_{14}	-0.10	0.98	1	0.98	11	0.0013
a_{23}	-0.01	0.01	1	0.011	0.12	0.7269
a_{24}	0.04	0.14	1	0.14	1.5	0.2171
a_{34}	0.10	0.90	1	0.9	10	0.0020
Residual		7.50	85	0.088		

From the results in Table 5.8 it is seen that all the effects that include the factor x_2 (the polymer concentration in the range [1; 2]wt.%) are nonsignificant, since the probabilities for them to be random are much higher than 5 %. After discarding the nonsignificant

Table 5.9: Final ANOVA of powder deposition results.

	Effects	SS	DF	MS	<i>F</i>	P
Constant	3.32	1059.48	1			
a_1	0.16	2.60	1	2.6	30	0.0000
a_3	-0.36	12.48	1	12	145	0.0000
a_4	-0.07	0.46	1	0.46	5.3	0.0238
a_{13}	0.12	1.39	1	1.4	16	0.0001
a_{14}	-0.10	0.98	1	0.98	11	0.0011
a_{34}	0.10	0.90	1	0.9	10	0.0018
Residual		7.68	89	0.086		

**Figure 5.9:** Parity plot (Model vs. data).**Figure 5.10:** Relative half effects.

effects, the ANOVA must be recomputed. The results of the recomputed model are shown in Table 5.9. The effect of recomputing the ANOVA is minimal, since the effects of the discarded factor were marginal and the number of data points was high. Finally, the significant model can be constructed from the rest of the factors as follows:

$$Y(\mathbf{x})[\text{wt.}\%] = 3.32 + 0.16x_1 - 0.36x_3 - 0.07x_4 + 0.12x_1x_3 - 0.10x_1x_4 + 0.10x_3x_4 \quad (5.2)$$

The predictions of the proposed model, Equation 5.2, are compared to all the results in Figure 5.9. It is seen, that there is a relatively high dispersion of the model results on the order of $\pm 20\%$, however the model describes the trend in the data very well. Compared to the average loading of the different sets of data the model errors are mostly smaller than 4% (see Table 5.10). The model is specific for the chosen factors and does not extrapolate directly to other concentrations for example. However, the ANOVA analysis gives us important information on the influence of the different factors on the loading.

The relative importance of the different factors is shown in Figure 5.10, where the half effects are compared to the constant effect a_0 . The most important factor is x_3 , the calcination between the depositions, since it is related to the highest relative half effect a_3 . To maximize the loading it is therefore very important to calcine the sample between the depositions. The calcination burns off the polymer, which might bind the powder stronger to the surface or which changes the surface properties (such as hydrophilicity) to better accept the powder suspension in the subsequent deposition step. The second

Table 5.10: Model results compared to deposition results.

Exp. No.	Factors				Mean result	Model predict.	Residual	Model Error
	Susp.	PEG	Calcin.	Drying				
Units	g/L	wt. %			wt. %	wt. %	wt. %	%
1	33.3	1	Yes	Ambient	3.55	3.70	-0.15	4.1
2	33.3	1	Yes	Vacuum	3.65	3.57	0.07	-2.0
3	33.3	1	No	Ambient	2.80	2.55	0.25	-9.7
4	33.3	1	No	Vacuum	2.73	2.81	-0.08	2.8
5	33.3	2	Yes	Ambient	3.83	3.70	0.13	-3.4
6	33.3	2	Yes	Vacuum	3.52	3.57	-0.05	1.4
7	33.3	2	No	Ambient	2.32	2.55	-0.23	9.0
8	33.3	2	No	Vacuum	2.86	2.81	0.06	-2.0
9	44.4	1	Yes	Ambient	4.11	3.99	0.12	-3.0
10	44.4	1	Yes	Vacuum	3.43	3.46	-0.03	0.9
11	44.4	1	No	Ambient	3.30	3.32	-0.02	0.6
12	44.4	1	No	Vacuum	3.11	3.17	-0.06	2.0
13	44.4	2	Yes	Ambient	3.90	3.99	-0.10	2.4
14	44.4	2	Yes	Vacuum	3.47	3.46	0.01	-0.2
15	44.4	2	No	Ambient	3.32	3.32	0.00	0.1
16	44.4	2	No	Vacuum	3.26	3.17	0.09	-2.7

most important factor is the suspension concentration x_1 . The higher concentration favors a higher loading. The effect of the drying x_4 is also significant. The highest loading is obtained by drying the samples at ambient temperature. The effect of the polymer concentration x_2 has no significant effect and does not even affect the deposition through linear interactions with the other factors. This does not necessarily mean that there is no potential effect of this factor. The analysis shows that there is no effect in the investigated interval [1; 2]wt.%, but it is still possible that there is an effect outside this interval. However, it is not likely in the near neighborhood and much higher concentrations are not practically realizable due to problems during the deposition. Three linear interactions between the three significant main effects are also important.

In order to maximize the loading on the filters by powder deposition it can be concluded that we need to use the maximum suspension concentration, dry the samples at ambient conditions and calcine between the depositions. Even though the polymer concentration was not found to be of high relevance the practical results (experiments 9 and 13 in Table 5.10) showed a slightly higher loading using 1 wt.% polymer. The work with the deposition method was continued with the optimized standard method (parameters shown in Table 5.11).

One factor (polymer concentration) turned out being non-significant. This could possibly have been foreseen with either the fractional factorial design approach or with a Hadamard type screening experiment. These approaches are therefore very important as the complexity and cost of the experiments increase.

Table 5.11: Standard deposition method.

Factor	Unit	Values
Suspension concentration	g/L	44.4
PEG 35,000 concentration	wt.%	1
Calcination		Yes
Drying		Ambient

5.2.5 Model Linearity

With a linear model it is good practice to use minimum three points to check the linearity². With a two level design one can only fit a linear model. It is therefore good practice to do the experiment at the zero levels of the factors, which is equivalent to the center point of the experimental space, to verify the linearity.

In the current study it was unfortunately not possible to do a check at the zero level of the four factors, since two factors are qualitative and have no zero level, see Table 5.6. It would still be possible to do a "zero" experiment with the remaining factors. However, in the current experiment there is one further limitation in that the experiment was designed to obtain a similar additive "exposure" to the powder in suspension, see section 5.2.2. The higher concentration suspension was used three times and the lower concentration, four times. Hence, at the "center point" $x_1 = 38.9$ g/L one would have to impregnate 3.42 times³ - which is not possible. Instead, the sample was coated three times and an extrapolation to 3.42 times gave the "quasi-experimental", "zero" result.

Table 5.12: Experimental "center point" and model linearity.

Experiment Number	Factors				Mean result	Model predict.
	Susp.	PEG	Calcin.	Drying		
Units	g/L	wt.%			wt.%	wt.%
2	33.3	1	Yes	Vacuum	3.65	3.57
6	33.3	2	Yes	Vacuum	3.52	3.57
10	44.4	1	Yes	Vacuum	3.43	3.46
14	44.4	2	Yes	Vacuum	3.47	3.46
3 depositions "zero"	38.9	1.5	Yes	Vacuum	3.14	
3.4 depositions "zero"	38.9	1.5	Yes	Vacuum	<i>3.58</i>	3.52

The extrapolated, hypothetical value of the powder loading after 3.42 depositions, is shown in *italic* in Table 5.12. The predicted value is slightly higher than the model predicted value and at the same level as experiments 2 and 6. With the error margin it is difficult

²Linearity with two points is not hard to obtain!

³The "zero" point of factor $x_1 = 38.9$ g/L. $3.42 \cdot 38.9$ g/L = 133 a.u., which is equal to the "powder exposure" level calculated in section 5.2.2.

to decide if the "zero" point value actually does confirm the linear model. However, we can exclude any strong nonlinear influences and it seems likely that the model is linear.

5.2.6 Powder Adherence

It is evident that the deposited layer of fine powder on the SMF must be stable during long time with respect to the adherence. Otherwise, the catalyst would lose its active phase and thereby its activity. In the lifetime of a catalyst it will be subjected to different kinds of stresses and shocks, e.g. during handling and transport as well as during use in the reactor, such as pressure, flow and temperature shocks. There exists no single universal test for the powder layer stability. The first of the following tests was inspired by previous, similar tests undertaken in our laboratory for the adhesion of powder layers in microchannels (Reuse, 2003; Rouge, 2001). The stability of the deposited powder layer was evaluated by the weight loss induced by three different tests:

- **Compressed air pressure shocks:** This test simulates the abrupt flow variations that could happen in a reactor. At ambient temperature the disks of SMF were placed flat on a SMF filter supported by a glass cup allowing the free flow of air through the sample. Compressed air (5 bar, 500 L/min, nozzle opening $\varnothing = 4$ mm) was blown through the sample at an angle of 90 °C and a distance of ca. 5 mm. The treatment was repeated several times according to the following pattern:

1. 10 pulses on one side
2. 10 pulses on both sides
3. 10 pulses both sides + 10 s both sides
4. 10 pulses both sides + 10 s both sides
5. 10 pulses both sides + 10 s both sides
6. 10 pulses both sides + 10 s both sides

Six optimized samples were tested by this procedure with a total of 110 pulses and 160 s of continuous flow per sample.

- **Ultra sonic bath:** This test is rigorous and is often used for characterizing the stability of deposited materials (Tribonet, 2006; Valentini *et al.*, 2001). At ambient temperature the samples were placed in distilled water and treated in an ultra sonic bath (47 kHz, 30 W) for 5 min. The samples were dried (110 °C, minimum 30 min) and weighed before and after this treatment, which was repeated 4 times. Four optimized samples were tested in this way for a total of 20 min of ultra sonic treatment.
- **Use in reactor:** This test shows how stable the catalyst layers will actually be during use. Five to six disks were placed in the pilot reactor, tested for their activity at 350 °C and taken out of the reactor again. The samples were weighed before and after. These samples have been exposed to some thermal stress and flow during real reaction conditions. However, it is believed that the main source of mechanical stress takes place during the emptying of the reactor where there is considerable friction with the reactor walls. This test cannot distinguish between the different

sources of stress, but is nevertheless useful in that it is not a simulation, but real reaction conditions. A total of 41 disks were tested in this way.

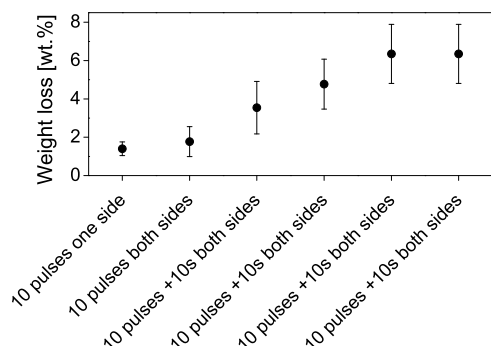


Figure 5.11: Powder coating weight loss after air pressure shocks. Error bars indicate the standard deviation.

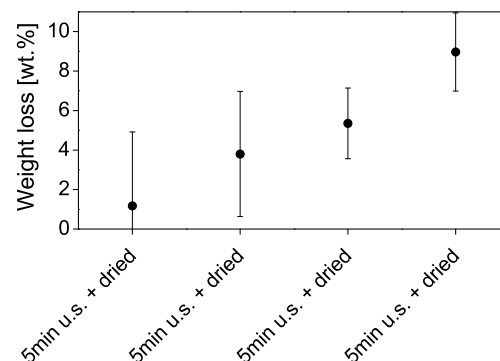


Figure 5.12: Powder coating weight loss after ultra sonic bath treatment. Error bars indicate the standard deviation.

The compressed air pressure shock test, Figure 5.11, showed that the powder layer is susceptible to the air flow pulses. However, the test conditions are much more severe than what can be expected in a real application. All six samples had a maximum weight loss after the fifth treatment, whereafter no further mass was lost. It is important to notice that the treatments became more severe after the first two treatments. The maximum weight loss was on the order of 7 wt.%, which is satisfactory in comparison to the adherence of powder dip coatings found in the literature: weight loss of ≈ 7 wt.% for powder coatings in metallic microchannels (Stefanescu *et al.*, 2006) and ≈ 10 –25 wt.% for powder coatings on metal slabs (Valentini *et al.*, 2001).

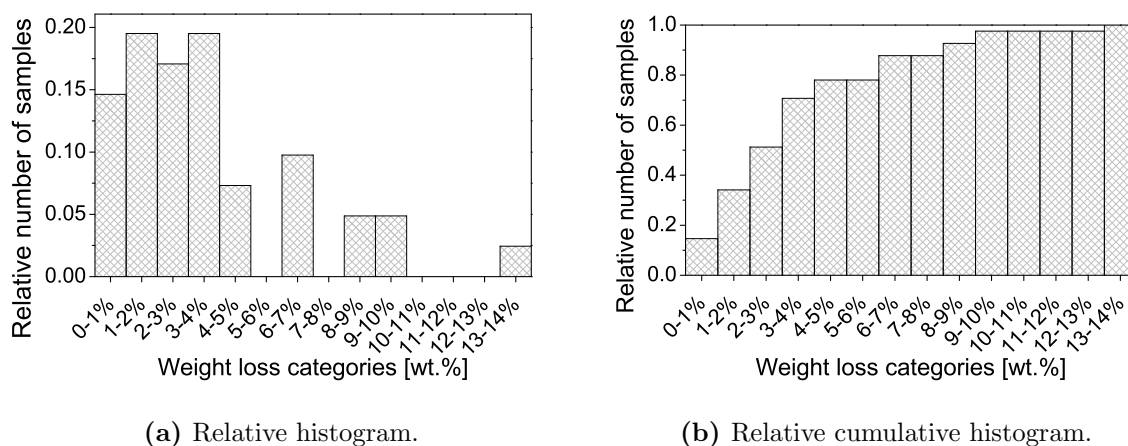
The ultra sonic test, Figure 5.12, shows a steady, but slow, loss of mass. It is not surprising that the powder will dissolve as it is not chemically bonded to the surface. The main conclusion of this test is that this type of catalyst is not suited for liquid phase reactions.

The last test was quite interesting, since it tests both thermal stresses and handling effects in real use, Figure 5.13. This test shows that even in handling most of the catalyst disks of SMF, more than 75 % of the samples, loose less than 4 wt.%. Especially, getting the catalyst out of the reactor is though due to friction with the walls and will cause some mechanical stresses.

The test results are positive and the deposited powder layers are quite stable. In practice it is possible to deposit an alumina layer, then blow off the loose part e.g. by compressed air pulses, before impregnating the active phase. In this way the active phase loss could be minimized.

5.3 Mass Transfer Limitations

When looking for the intrinsic kinetics or activity it is very important to know to which extent the measurements are influenced by mass transfer limitations. Ideally, mass trans-



(a) Relative histogram.

(b) Relative cumulative histogram.

Figure 5.13: Powder coating weight loss after use in pilot reactor.

fer limitations should be eliminated. In the laboratory this allows measuring the catalyst activity directly and in production the catalyst can then be used optimally.

In this section it is shown how the developed catalysts were influenced by mass transfer limitations.

5.3.1 External Mass Transfer Limitations

Experimental Test

The external mass transfer is the transport of reactants and products between the surface of the catalyst particle and the bulk phase by molecular diffusion. This type of transport can be described mathematically by the film model described in Section 2.5. The diffusion across the virtual "film", which is envisioned as a layer around the particle with a concentration gradient, depends on various parameters defining among others the "thickness" of the "film". The "film" thickness can be influenced by the flow rate of the fluid passing the object. A higher flow rate will lead to a thinner "film", which in turn leads to a steeper concentration gradient and a faster external transport of the molecules.

A classical way of determining experimentally if a catalyst is limited by external mass transfer under specific conditions is to vary the degree of agitation or the flow rate. For a reactor in a plug flow regime this is done by varying the flow rate proportionally to the volume or mass of the catalytic bed so as to keep the contact time constant. In a CSTR this can be done by keeping the residence time constant and changing the agitation. This would be the stirring intensity in a tank reactor. The employed tubular reactor could be operated in a PR regime or as a recycle reactor approaching an ideally mixed flow reactor (CSTR). The catalysts was tested for external mass transfer limitations by changing the flow rate over the catalyst by keeping the inlet flow rate constant and varying the flow rate of the recycle stream. The result is shown in Figure 5.14.

The experiment was carried out with six disks of 3.9 wt.% CK-302 powder on SMF_{SS} . The temperature was kept at 353°C , the inlet gas composition was $y_{\text{C}_3\text{H}_8, \text{in}} = 0.0050$, $y_{\text{O}_2, \text{in}} = 0.15$ in Ar and the inlet flow rate $\dot{V}_{\text{in}} = 88 \text{ mL(STP)}/\text{min}$. The recycle ratio, R , was

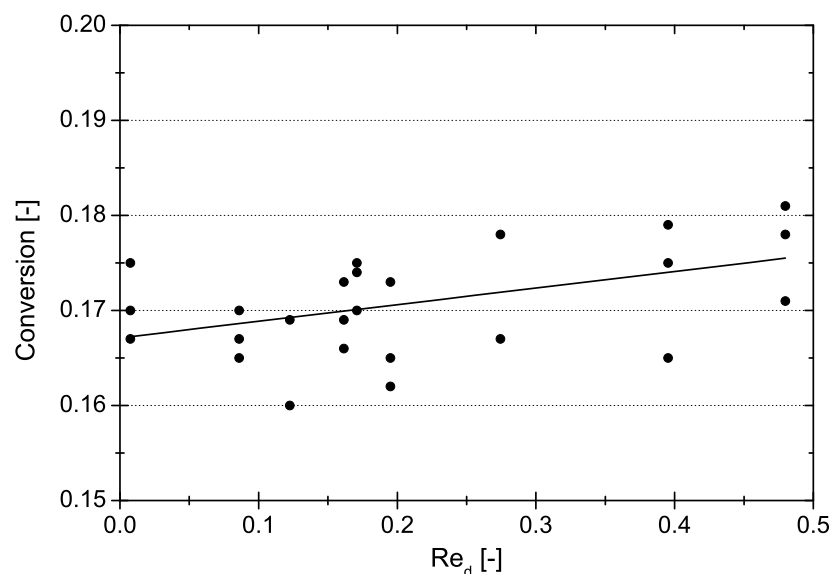


Figure 5.14: Conversion as a function of Re_d . 3.9 wt.%CK-302/SMF_{SS}.

varied between 0 (PFR) and 70. The conversion of the reaction was approximately 17% and the reactor was therefore approximately differential even in plug flow mode. The linear flow rate over the catalyst varied with the reflux ratio between 0.012 to 0.75 m/s.

A linear regression of the data gives $R^2 = 0.23$. The fit to the data is poor, however there is a tendency of a slight increase in the conversion and reaction rate as the flow rate is increased. The poor fit of the linear regression is a combination of the experimental error and the very low influence of the flow rate on the reaction rate. The conversion varies between 16 and 18% with a variance on the measurement of the conversion on the order of 0.5%. The influence of external mass transfer on the reaction rate at the current conditions is therefore negligible even at low flow rates.

Theoretical Test

For the experimental test described above the Carberry number with regards to the diffusion of propane, which is the largest of the reactant molecules and which appears in the lowest concentration, was evaluated theoretically. The main problem is to find a correlation for the mass transfer which is valid for the system. The work on mass and heat transfer coefficients for fibrous materials is scarce, but a number of correlations have been proposed for different types of fibrous materials. A selection of the proposed correlations are shown in Table 5.13.

Table 5.13: Mass transfer correlations for fibrous or cylindrical materials.

No.	Correlation	Re_d - regime	Material	Fiber diameter [μm]
1	$Sh = 0.94Re_d^{0.283}Sc^{1/3}$	[0.2; 100]	Pt-gauze	76-198
2	$Sh = 0.207Re_d^{0.758}Sc^{1/3}$	[1.0; 52.7]	wire-gauze	160
3	$Sh = 0.600Re_d^{0.513}Sc^{1/3}$	[50; 50,000]	single long cylinders	n/a
4	$Sh = 0.828Re_d^{0.49}Sc^{1/3}$	[0.01; 50]	fixed-bed of cylinders	n/a
5	$Sh = \frac{0.47}{\varepsilon}Re_d^{1/2}Sc^{1/3}$	[0.04; 0.64]	SMF	8-35
6	$j_D = \frac{1.6}{\pi} \left[\frac{1}{(1-\alpha)^2 K} \right]^{1/3} Re^{-2/3}$ $K = -\frac{1}{2} \ln \alpha - \frac{3}{4} + \alpha - \frac{\alpha^2}{4}$ $\alpha = 1 - \varepsilon_{bed}$	[0.01; 100]	fibrous filters	n/a

(continued)

No.	Fluid medium [†]	Type of transfer [‡]	Authors	Comments
1	g & l	h & m	Satterfield & Cortez (1970)	data from several references
2	g	h	Kolodziej & Lojewska (2005)	
3	g & l	-	Geankoplis (1993, p. 450)	$Re_d = \frac{v_{superficial} \rho d_p}{\mu 6(1-\varepsilon)0.91}$
4	g & l	-	Yoshida <i>et al.</i> (1962)	
5	l	m	De Greef <i>et al.</i> (2005)	
6	g	m	Ramarao & Tien (1989)	

[†] g: gas phase, l: liquid phase[‡] h: heat transfer, m: mass transfer

Heat transfer rates to a gas from stacks of woven screens were measured as early as 1956 by Coppage & London. However, Satterfield & Cortez (1970) found that the earlier literature data for heat transfer was erroneous at lower temperatures due to neglect of longitudinal heat conduction. Satterfield & Cortez (1970) studied the catalytic oxidation of hydrocarbons in excess air on platinum gauzes. They proved that the heat and mass transfer coefficients are related according to the Colburn analogy. Furthermore, the heat and mass transfer rates of the high porosity screens of gauze could be correlated by expressing the j -factor as a function of the Reynolds number based on the wire diameter rather than the hydraulic radius. They also found that the transport properties of screens are very similar to those of infinite cylinders. Satterfield & Cortez (1970) worked with fiber diameters from 76-198 μm and $Re_d \in [0.3; 20]$ and combined their own results with other literature data for both gas- and liquid-phase, heat- and mass-transfer covering $Re_d \in [0.2; 100]$ (Coppage & London, 1956; Dixon & Longfield, 1960; Gay & Maughan, 1963; Vogtlander & Bakker, 1963) to propose a general correlation, no. 1, in Table 5.13.

Kolodziej & Lojewska (2005) presents some of the most recent work in the area. They used 160 μm wire gauzes, gas flow with Reynolds numbers in the range 1.0 to 53 and measured heat transfer from electrically heated wires.

Their proposed correlation (no. 2, Table 5.13) estimates values of the mass transfer coefficient that are considerably lower than that of Satterfield & Cortez (1970) and the

infinite cylinders at lower Reynolds numbers.

Satterfield & Cortez (1970) found that there was very little difference between their correlation and that for a single infinite cylinder. A correlation for perpendicular gas and liquid flow past single long cylinders is given by Geankoplis (1993, p. 450). The data was taken from several references and the data scatter was considerable (up to $\pm 30\%$) and covers $50 < Re_d < 50000$ (no. 3, Table 5.13).

It could be imagined that a fixed-bed of sintered metal fibers could resemble a fixed-bed of long cylinders, with the exception of the bed porosity being considerably larger in a filter matrix. Such correlations include the one proposed by Yoshida *et al.* (1962) (no. 4, Table 5.13), which is valid for gases and liquids and $0.01 < Re_d < 50$.

There are very few studies of systems based on filters of metal fibers. A study was done by De Greef *et al.* (2005) with sintered metal fibers (Bekaert, Belgium - same supplier as in the current study) and fiber diameters of 8 to $35\ \mu\text{m}$, which is very similar to the current SMF filters employed. They found a correlation (no. 5, Table 5.13) based on liquid flow, but it is believed that it also holds for gas-flow as was the case in the early studies by Satterfield & Cortez (1970). The Reynolds number regime is not clearly defined, but seems to have covered $Re_d \in [0.04; 0.64]$.

Fibrous filters with void fractions from 0.6 to 0.992 were studied by Ramarao & Tien (1989) for the filtration of aerosols from gas flows over a flow range with $Re_d \in [0.01; 100]$. Their correlation (no. 6, Table 5.13) is based on the j_D -factor

$$j_D = \frac{Sh}{ReSc^{1/3}} = \frac{k_f}{v} Sc^{2/3} \quad (5.3)$$

includes α , the solid fraction of fibers in the bed and K , the hydrodynamic factor of Kuwabara flow (Lee & Liu, 1982).

For comparison of the six different mass transfer correlations, k_f has been calculated for each correlation and plotted against the Reynolds number in Figure 5.15. The values were obtained from estimated values at 300°C as shown in Table 5.14.

Table 5.14: Parameter values estimated at 300°C for comparison of mass transfer coefficients in Figure 5.15.

Parameter	Symbol	Unit	Value
Fiber diameter	d_f	μm	20
Diffusivity	D_m	m^2/s	$3.12 \cdot 10^{-5}$
Viscosity	μ	Pa s	$3.71 \cdot 10^{-5}$
Density	ρ	kg/m^3	0.93
Schmidt number	Sc	-	1.3

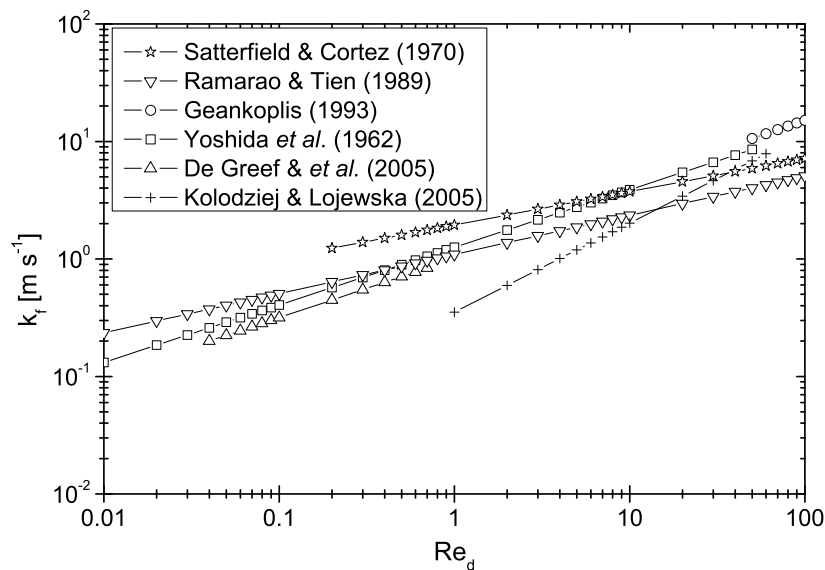


Figure 5.15: Comparison of the external mass transfer coefficient for fibrous material and cylinders predicted from a variety of correlations. Real experimental range of Re_d .

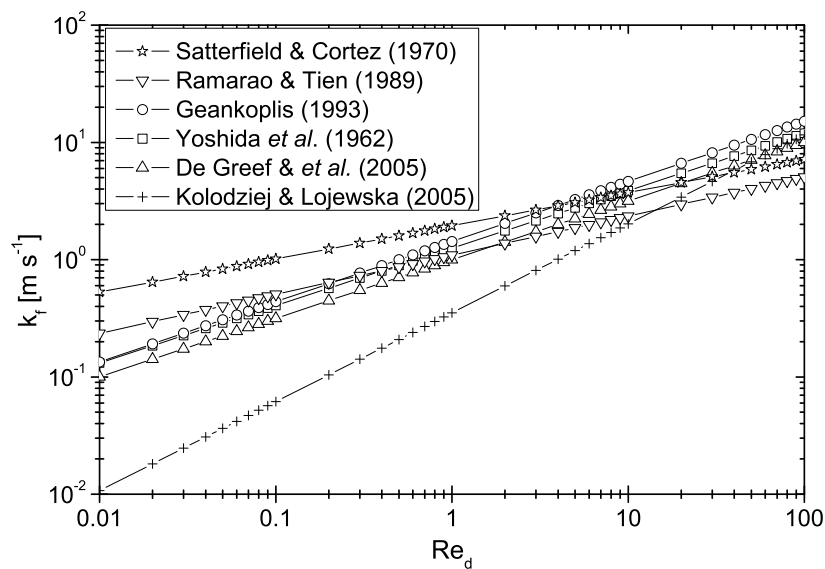


Figure 5.16: Comparison of the external mass transfer coefficient for fibrous material and cylinders predicted from a variety of correlations. Extrapolated values.

The correlation values in Figure 5.15 have been extrapolated in Figure 5.16 to cover the same range of Reynolds numbers. The trend in the data clearly shows that there are similarities between fibrous material including gauzes and infinite cylinders. The correlation of Satterfield & Cortez (1970) gives the highest values of k_f , but is still on the same order of magnitude as the rest. The other correlation, which stands out, is that of Kolodziej & Lojewska (2005), which results in considerably lower values of k_f for low values of Re_d , but coincides with the rest for $Re_d > 10$. This apparent discrepancy (in relation to the results of Satterfield & Cortez (1970)) is explained by significant differences in the gauze parameters and a possible homogeneous combustion contribution to the reaction rate at lower Reynolds numbers in the experiments of Satterfield & Cortez (1970). The latter does not seem likely, since Satterfield & Cortez (1970) based their final correlation on many different data obtained from different systems as discussed above.

Since the other four correlations seem to be very similar and one of these (De Greef *et al.*, 2005) is based on the exact same SMF as used in the current research project, their correlation (no. 5, Table 5.13) was considered most probable. The correlation of Kolodziej & Lojewska (2005), still possible and resulting in the lowest mass transfer coefficients was considered for a worst case scenario. The data used for the experimental test of presence of external mass transfer limitations shown in Figure 5.14 was also used to calculate the Carberry numbers based on the correlations no. 5, (De Greef *et al.*, 2005) and no. 2, (Kolodziej & Lojewska, 2005) of Table 5.13. The results are seen in Figure 5.17. The Carberry number

$$Ca_w = \frac{r_{w,observed}\rho_{cat}}{k_f a' C_{bulk}} \quad (5.4)$$

varies as a function of the Reynolds number, Re_d , due to the flow dependency of k_f . A higher flow rate results in a smaller Ca . The recycle ratio, R , varied from zero to a maximum of ca. 70.

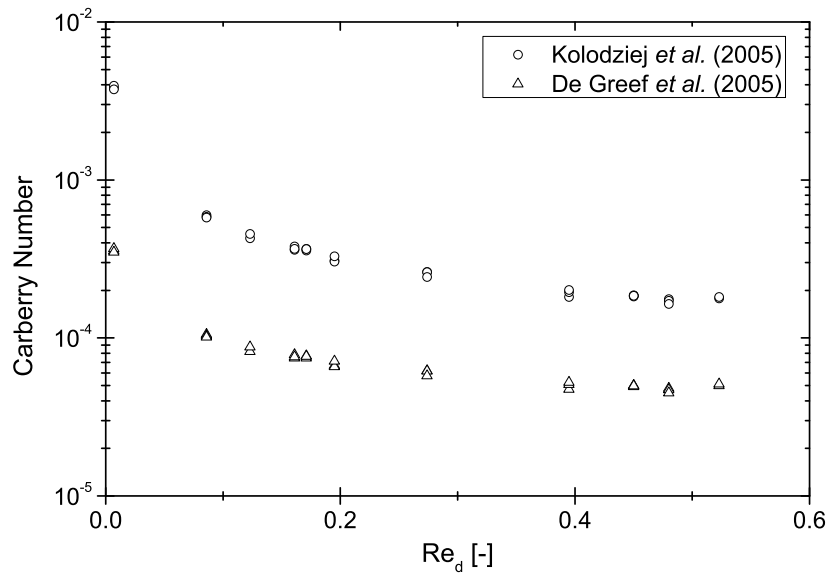


Figure 5.17: Carberry numbers at 350 °C as a function of the Re_d based on two different mass transfer correlations. 3.9 wt.%CK-302/SMF_{SS}.

The criteria for the existence of mass transfer limitations according to the Carberry number, Equation 2.18, depends on the order of reaction, which was found to be approximately $n = 0.6$ (see Appendix E). The deviation x of the observed reaction rate from the "intrinsic" reaction rate can thus be calculated from:

$$Ca \simeq \frac{x}{|n|} \quad (5.5)$$

A "worst case scenario" at the studied conditions of 350 °C, with no gas recycling (PFR mode, $R = 0$) and with the most conservative correlation for the mass transfer coefficient (no. 2, Table 5.13) the Carberry number is on the order of $4 \cdot 10^{-3}$ resulting in a deviation of the observed rate from the intrinsic reaction rate of approximately 0.2%. This result agrees well with the result of the experimental test above and confirms that external mass transfer was not a limiting factor for these types of catalysts.

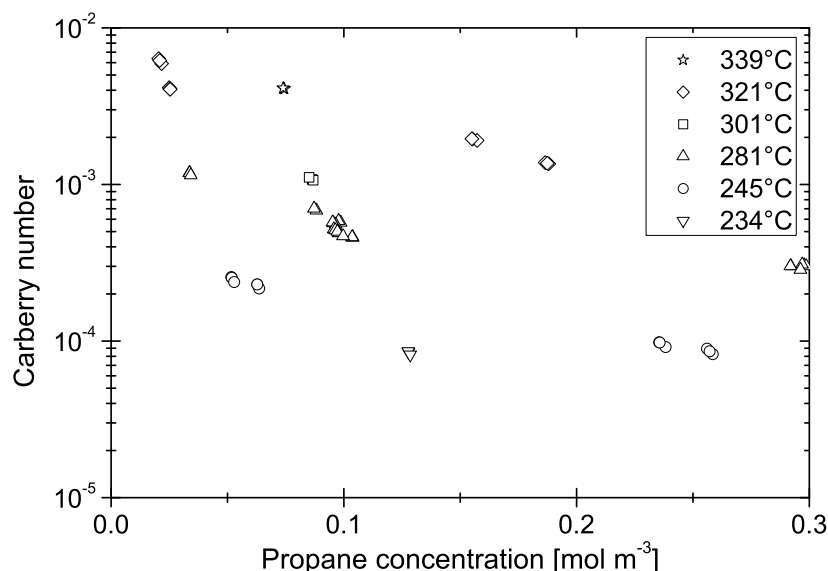


Figure 5.18: "Worst Case" Carberry numbers for the kinetic testing of 1.1 wt.% Co_3O_4 on stainless steel SMF.

Increasing external mass transfer limitations happen either when the reaction rate is very high or as the surrounding fluid approaches zero-flow (becomes stagnant). The low flow rates did not lead to mass transfer limitations as shown above. One of the most active catalysts in this study was the 1.1 wt.% Co_3O_4 impregnated directly on stainless steel SMF. The kinetics of this catalyst is discussed in Section 5.5. The estimated values of the Carberry numbers for this kinetic testing are shown in Figure 5.18. The experiments were done with maximum recycling ratio ($R = 70$) and nearly constant values of $Re_d \approx 0.4$ and $Sc \approx 1.3$ over the whole range. As above, the mass transfer coefficient of correlation no. 2 (Table 5.13) was used for a "worst case scenario" estimation. The Carberry number increases considerably with temperature as expected. Furthermore, there is a negative effect on the Carberry number from the increase in concentration, since the kinetic reaction order in propane is 0.4 (see Table 5.17) and so the Carberry number has a negative dependence on the concentration of approximately $C_{\text{C}_3\text{H}_8}^{-0.6}$. The maximum attained value of $Ca = 6.4 \cdot 10^{-3}$ results in a maximum deviation from the intrinsic reaction rate of 0.3%.

With a faster catalyst/reaction system based on fibrous materials it is off course possible to become rate limited by bulk diffusion. This was indeed how Satterfield & Cortez (1970) studied the mass transfer coefficients between 350 and 450 °C for VOC combustion over Pt wires.

5.3.2 Internal Mass Transfer Limitations

A classical experimental test for internal mass transfer is to vary the particle size. When limited by internal mass transfer the observed reaction rate will increase when using smaller particles until the limitations become unimportant. Similarly, the thickness of the catalytic film could be varied. This test is only effective if the active phase is dispersed homogeneously throughout the particles or film. With the impregnated SMF composites there is a risk that the active phase is primarily concentrated at the surface during drying, since not only the porous film, but the whole fiber matrix was saturated with the metal salt containing aqueous phase. Therefore, the internal mass transfer was estimated theoretically using the Weisz modulus.

Theoretical Test

The degree of internal mass transfer limitation was estimated by calculating the generalized Weisz modulus, Ψ , (Equation 2.20). Only the catalysts composed of a film of silicalite-1 or alumina on SMF have an internal pore structure and are thus susceptible to internal diffusion limitations. The most active catalyst tested was the 2.9 wt.% Co_3O_4 impregnated on a 10.4 wt.% silicalite-1 film on stainless steel SMF. This type of zeolite has a much smaller pore size, $d_{\text{pore}} \approx 5.5 \text{ \AA}$, compared to the $d_{\text{pore}} \approx 40 \text{ \AA}$ of the γ -alumina and is therefore much more prone to internal diffusion limitations. The estimated values of Ψ are given in Figure 5.19 as a function of temperature and concentration.

The diffusivity of propane in the silicalite-1 was estimated with the Bosanquet equation for the transitional regime between the Knudsen diffusivity and the configurational diffusivity. The configurational diffusivity of propane was estimated to $5 \cdot 10^{-9} \text{ m}^2/\text{s}$ (227-427 °C) from the measurements of Xiao & Wei (1992a). The molecular diffusivity of propane in Ar was estimated by the method of Fuller *et al.* (1966).

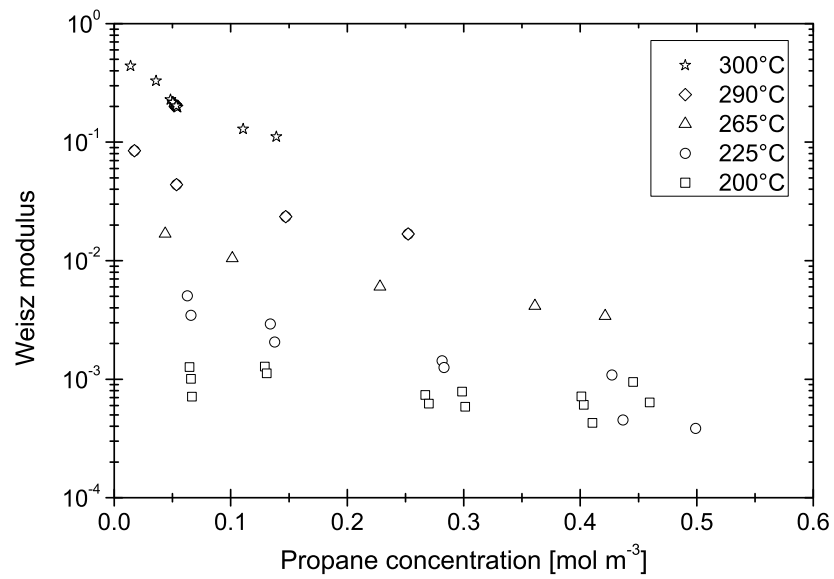


Figure 5.19: Weisz modulus for 2.9 wt.% Co_3O_4 on 10.4 wt.% silicalite-1 film on stainless steel SMF.

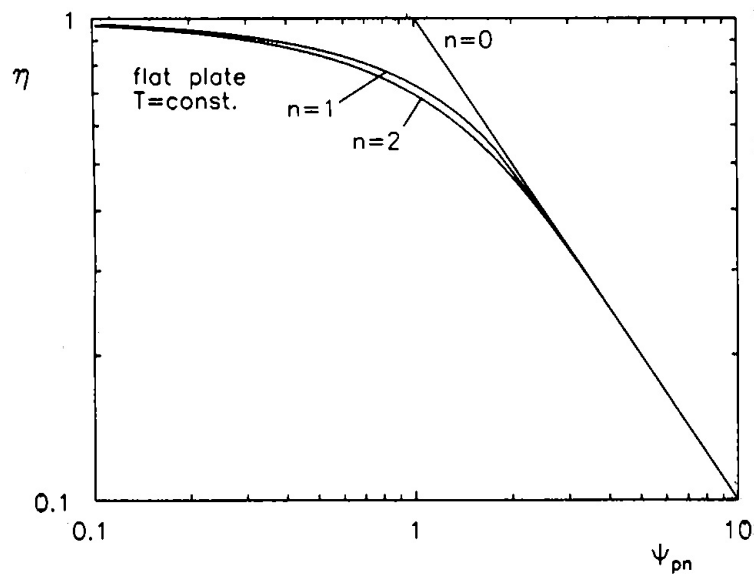


Figure 5.20: Effectiveness factor η as a function of the generalized Weisz modulus (Emig & Dittmeyer, 1997, p. 1218).

The results have to be compared with Figure 5.20, which shows the relationship between the effectiveness factor and the generalized Weisz modulus for an isothermal, irreversible reaction in a flat plate. From the values of the Weisz modulus in the former figure the effectiveness factor of the catalyst can be estimated. At 300 °C and the lowest propane concentration the highest value of $\Psi \approx 0.5$ was attained, which corresponds to an effectiveness factor of approximately 85 %. At all other temperatures (290 °C and below) Ψ was lower than 0.1 and the effectiveness factor practically unity and no diffusion limitations due to internal mass transfer should be encountered.

Using the MFI-type zeolite as porous structure on the SMF has the benefit of getting a large specific surface area of the catalyst, but could have the downfall of being prone to internal mass transfer limitations due to the small pore openings. The pore sizes in MFI-zeolites often lead to configurational diffusion, which can be several orders of magnitude slower than the Knudsen diffusion (Xiao & Wei, 1992a,b). In the current study with propane the diffusivity was only slightly lower than the Knudsen diffusivity. Larger molecules, higher temperatures and higher reaction rates could quickly lead to mass transfer limited conditions. In those conditions it becomes extremely important to control the film thickness to eliminate internal mass transfer limitations and keep the catalyst effectiveness high.

Catalysts composed of a γ -alumina powder layer as opposed to MFI-zeolite were screened as combustion catalysts (Section 5.4). These catalysts are less susceptible to internal mass transfer limitations due to the much larger pore size. Internal mass transfer limitations were never encountered for these catalysts even up to 350 °C.

5.4 Catalyst Screening

The catalyst screening was done according to the method described in Section 3.4.2.

5.4.1 Screening Results

Table 5.15: Composition of the screened catalysts. Catalysts A1 and A2 are the industrial catalyst CK-302.

	Active phase	wt.% in powder	wt.% in catalyst	Impregnated on	Deposited as powder on
A1	CuO/MnOx	20	20	γ -Al ₂ O ₃	-
A2	CuO/MnOx	20	1.1	γ -Al ₂ O ₃	SMF
B1	Co ₃ O ₄	19	19	γ -Al ₂ O ₃	-
B2	Co ₃ O ₄	19	0.8	γ -Al ₂ O ₃	SMF
C1	Co ₃ O ₄	-	0.8	SMF	-
C2	Co ₃ O ₄	-	4.1	SMF	-
D	Co ₃ O ₄	-	0.6	γ -Al ₂ O ₃ powder on SMF	-
E	Co ₃ O ₄	-	2.9	Silicalite-1 film on SMF	-
F	PtOx	-	0.8	γ -Al ₂ O ₃ powder on SMF	-

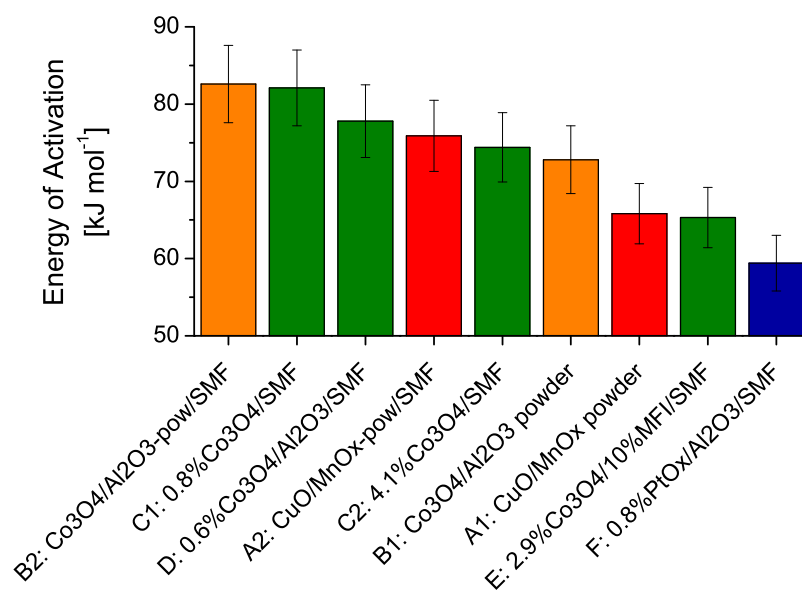


Figure 5.21: Activation energies of the screened catalysts. Error bars indicate 98 % confidence interval.

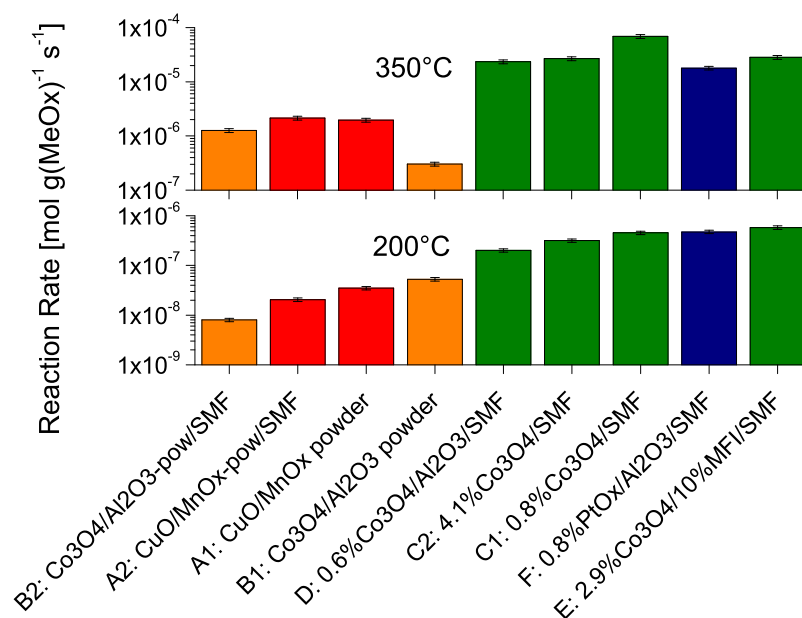


Figure 5.22: Activities of the screened catalysts at low and high temperature. Error bars indicate 98 % confidence interval.

The nine different catalysts that were screened are described in Table 5.15. The results of the activity testing are shown in Figures 5.21 and 5.22. The classification by activation energy shows that PtOx (catalyst F) has the lowest activation energy with $E_a = 59.4 \pm 3.6 \text{ kJ/mol}$. The second lowest activation energy is for 2.9 wt.% Co_3O_4 on the silicalite-1/SMF composite (catalyst E) with $E_a = 65.3 \pm 3.9 \text{ kJ/mol}$. These two catalysts are also among the catalysts showing the highest activity measured as reaction rate (Figure 5.22).

The activation energies give an idea about the most active catalyst, but the reaction rate considers also temperature and frequency factor and is what really counts for the assessment of the catalysts. Figure 5.22 shows a clear difference in the activity between the A and B (orange and red) catalysts and the C, D, E and F (green and blue) catalysts. There is an important structural difference between these two classes of catalysts. The A and B catalysts were made from preimpregnated and calcined catalysts, which were then attrition milled in aqueous phase and deposited on the SMF filters. The other catalysts were based on SMF filters (some with an inert film of silicalite-1 or γ -alumina), which were impregnated with the metal salts and then calcined.

Why are the A and B catalysts the least active? Catalyst A, which is the industrial CK-302 catalyst, contains CuO and MnOx and is optimized for organic solvents rather than propane according to the producer (Topsøe, 2006). There is a significant difference in the activation energy, which was countered by a difference in the frequency factor so that the activity was nearly identical between A1 and A2. The B catalysts were significantly less active than the rest of the Co_3O_4 containing catalysts. This is possibly due to loss of active phase during the attrition milling process in which it was necessary to centrifuge to retrieve the black, fine, powder in suspension. Another possibility is that a fraction of the active phase is not accessible due to "blocking" or filling of the smallest pores of the alumina. It was seen in section 5.1.4 that the specific surface area decreased by approximately 25 %, which could explain this effect.

All of the catalysts C, D, E and F have similarly high activities. Their synthesis method favors an even distribution of Co_3O_4 on the outer surface of the fibers. The porous coatings definitely absorb the impregnation solution, but the activity is probably similar for all cobalt oxide catalysts due to a large amount of easily accessible active phase on the surface. The outer layer of cobalt oxide was clearly visible in Figure 5.5.

Between the catalysts C, D and E there is only little difference in the activities and it was therefore decided to further research the simpler and cheaper type of catalyst with cobalt oxide deposited directly on the SMF, which is shown in Section 5.5.

5.5 Kinetics of Cobalt Oxide on SMF

Three different supports (SMF from: stainless steel, FeCrAlloy and Inconel) were impregnated with cobalt nitrate salt and calcined to obtain approximately 1.3 wt.% Co_3O_4 on the filters. The activity of the three different catalysts was assessed by the kinetics according to the theory described in Section 2.5. Temperature, oxygen and propane inlet mole fractions were varied according to a composite design of experiments to optimize the position of the data points. The inlet flow rate was varied in order to stay in the vicinity of conversions of 25 %. The inlet mole fraction of oxygen was varied in the range of inlet conditions shown in Table 5.16. The conditions were oxygen rich with inlet oxygen to

propane ratios ($y_{O_2,in}/y_{C_3H_8,in}$) higher than the stoichiometric ratio of 5. Three measurements of the concentrations were taken at steady state reached after ca. 45 min. The temperature range as well as the results of the least-square multi-parameter nonlinear regression of the power rate law (Equation 5.6) to the data are shown in Table 5.17.

Power Rate Law:

$$r = kC_{C_3H_8}^n C_{O_2}^m \quad [\text{mol/g}\cdot\text{s}] \quad (5.6)$$

Table 5.16: Inlet conditions for the chemical kinetics experiments.

	y_{O_2}	$y_{C_3H_8}$	$y_{O_2}/y_{C_3H_8}$
min	0.050	0.0025	5.8
max	0.175	0.0150	43

Table 5.17: Fitted parameters of power rate model.

Parameter	Units	FeCrAlloy	Inconel	AISI316L (SS)
Co ₃ O ₄ loading	wt. %	1.5	1.3	1.1
$k' \dagger$	$\left(\frac{\text{mol}}{\text{g}\cdot\text{s}}\right) \left(\frac{\text{m}^3}{\text{mol}}\right)^{(n+m)}$	$(2.1 \pm 0.3) \cdot 10^{-5}$	$(2.3 \pm 0.2) \cdot 10^{-5}$	$(2.6 \pm 0.2) \cdot 10^{-5}$
E_a	kJ/mol	87.5 ± 2.6	92.6 ± 1.7	92.4 ± 1.3
n		0.38 ± 0.04	0.47 ± 0.04	0.41 ± 0.02
m		0.30 ± 0.08	0.14 ± 0.06	0.18 ± 0.04
Temp. range	°C	[221; 323]	[221; 339]	[234; 339]
$ssq_{min} \ddagger$		0.57	0.63	0.18
Standard error*		0.094	0.097	0.057
Data points		68	71	60

\dagger Arrhenius frequency factor at reference temperature, $T' = 280^\circ\text{C}$ (see section 2.5.4).

\ddagger Minimal sum of squares of residuals.

* Approximate standard error on the output variable ($\ln r$).

The fit of the power rate law to the data is good. The approximate standard error on the output variable ($\ln r$) is on the order of 6 to 10 %. The good fit of the model is further verified by the parity plots of Figure 5.23, where most data points are seen to fall within $\pm 10\%$ of the model predictions.

The activation energy and the frequency factor of the Arrhenius equation are nearly identical for the three catalysts. However, the frequency factor is inversely proportional to the metal oxide loading, which was not identical on the three catalysts. This trend could be explained by a higher dispersion of active phase. A higher proportion of the available metal oxides will be on the surface of the metal oxide. It is quite certain that there is some influence of the supports on the kinetics, since there are large variations of the reaction orders in both oxygen and propane.

The kinetics of the three catalysts are compared for various experimental conditions in Figure 5.24. They have been compared over the studied range of temperatures for four different combinations of oxygen and propane mole fractions. The chosen mole fractions represented the extremities of the ranges for which every catalyst had been tested:

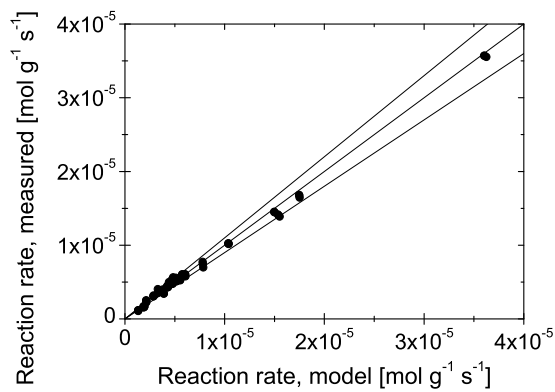
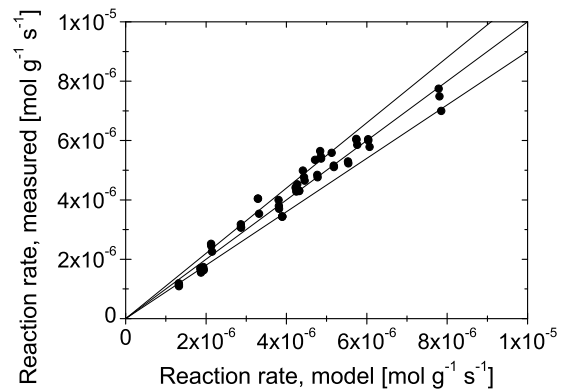
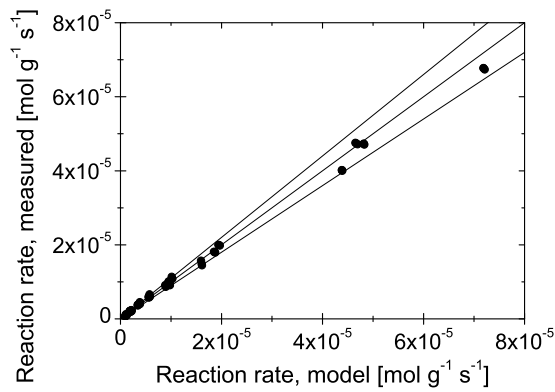
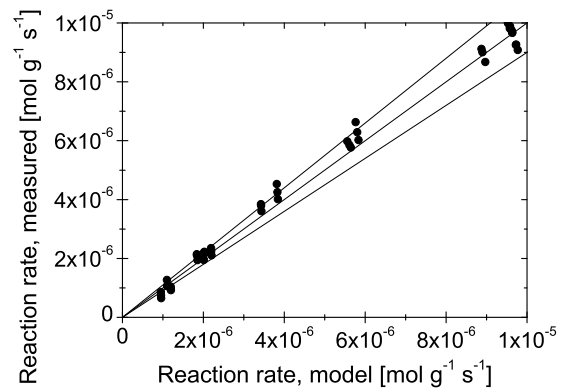
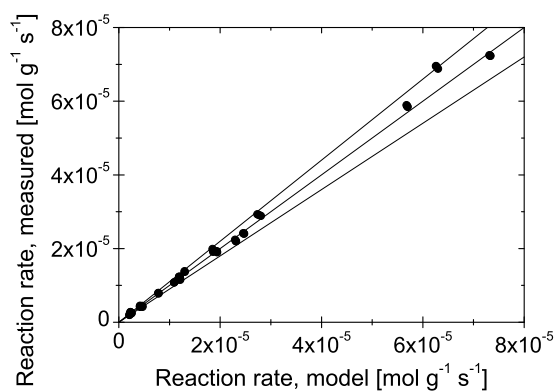
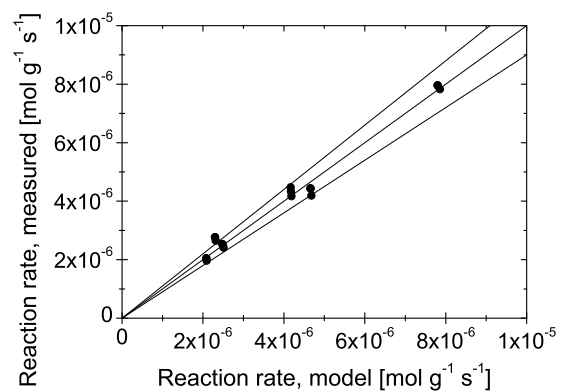
(a) Co_3O_4 on $\text{SMF}_{\text{FeCrAlloy}}$.(b) Co_3O_4 on $\text{SMF}_{\text{FeCrAlloy}}$. Zoom-in.(c) Co_3O_4 on $\text{SMF}_{\text{inconel}}$.(d) Co_3O_4 on $\text{SMF}_{\text{inconel}}$. Zoom-in.(e) Co_3O_4 on SMF_{SS} .(f) Co_3O_4 on SMF_{SS} . Zoom-in.

Figure 5.23: Parity plots of the power rate law model for the three different SMF materials. The three lines are giving *parity* and the $\pm 10\%$ of the model values. Plots on the right hand side are zoom-ins to the left hand plots.

- Low $y_{\text{C}_3\text{H}_8}=0.0013$, Low $y_{\text{O}_2}=0.047$
- Low $y_{\text{C}_3\text{H}_8}=0.0013$, High $y_{\text{O}_2}=0.167$
- High $y_{\text{C}_3\text{H}_8}=0.0110$, Low $y_{\text{O}_2}=0.047$
- High $y_{\text{C}_3\text{H}_8}=0.0110$, High $y_{\text{O}_2}=0.167$

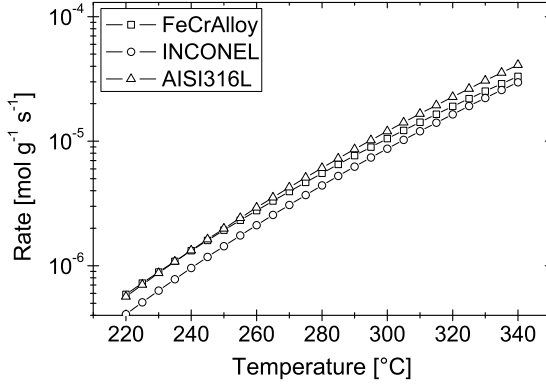
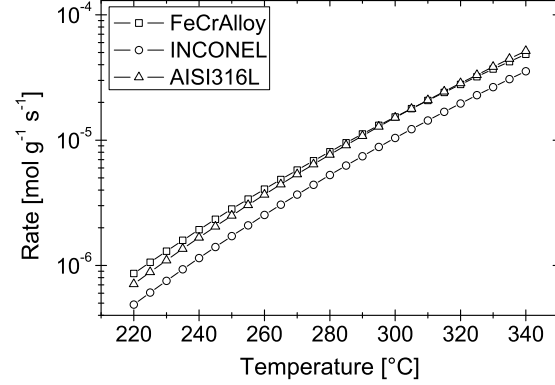
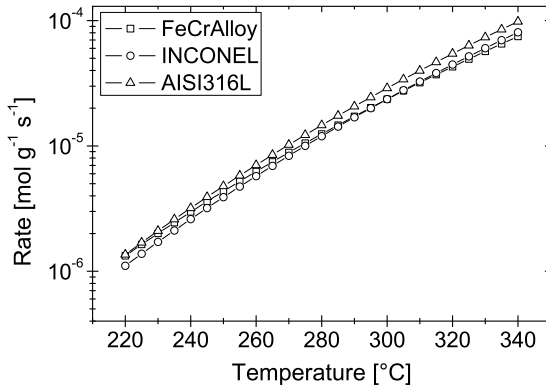
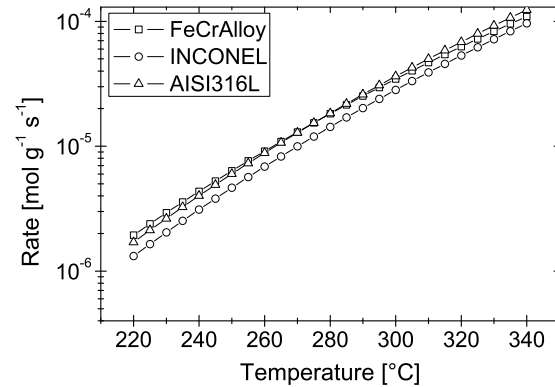
(a) Low $y_{\text{C}_3\text{H}_8}$; Low y_{O_2} (b) Low $y_{\text{C}_3\text{H}_8}$; High y_{O_2} (c) High $y_{\text{C}_3\text{H}_8}$; Low y_{O_2} (d) High $y_{\text{C}_3\text{H}_8}$; High y_{O_2}

Figure 5.24: Reaction rate vs. temperature for ≈ 1.3 wt.% Co_3O_4 on SMF of FeCrAlloy, inconel and stainless steel (AISI316L). $P = 1013$ mbar. Mole fractions [Low; High]: $y_{\text{C}_3\text{H}_8} = [0.0013; 0.0110]$, $y_{\text{O}_2} = [0.047; 0.167]$.

The reaction rate for the inconel based catalyst is mostly the lowest of the three in the test range. The reaction rates for the stainless steel (AISI316L) and the FeCrAlloy based catalysts are similar, but with some important differences. The FeCrAlloy based catalyst is more active at lower temperatures, due to the lower activation energy. Furthermore, this catalyst is favored by low propane concentrations and high oxygen concentrations in comparison to the AISI316L based catalyst. In the case of "Low $y_{\text{C}_3\text{H}_8}$, High y_{O_2} " the reaction rate at 220 °C is 21 % higher and it has the highest reaction rate until 310 °C. On the other hand with a "High $y_{\text{C}_3\text{H}_8}$, Low y_{O_2} " configuration and 340 °C the reaction rate of the AISI316L based catalyst is 32 % higher than that of the FeCrAlloy based catalyst.

A choice between these two best catalyst would thus have to depend on the specific conditions during use as well as other factors such as price and stability of base material and catalyst life time.

The **Mars-van Krevelen model** (MVK):

$$r = \frac{1}{\frac{5}{k'_{O_2} \exp\left(\frac{-E_{O_2}}{R}\left(\frac{1}{T} - \frac{1}{T'}\right)\right) C_{O_2}^n} + \frac{1}{k'_{HC} \exp\left(\frac{-E_{HC}}{R}\left(\frac{1}{T} - \frac{1}{T'}\right)\right) C_{HC}}} \quad [\text{mol/g}\cdot\text{s}] \quad (5.7)$$

was tested for the representation of the kinetics. The parameter fitting results for the 1.1 wt.% Co_3O_4 on SMF_{SS} are tabulated in Table 5.18 and the parity plot is shown in Figure 5.25.

Table 5.18: Fitted parameters of MVK model for the kinetics over 1.1 wt.% Co_3O_4 on SMF_{SS} .

Parameter	Units	Value
$k'_{O_2}{}^\dagger$	$(\text{mol/g}\cdot\text{s}) (\text{m}^3/\text{mol})^n$	$(8.1 \pm 0.8) \cdot 10^{-5}$
E_{O_2}	kJ/mol	87.6 ± 5.8
$k'_{HC}{}^b$	$(\text{mol/g}\cdot\text{s}) (\text{m}^3/\text{mol})$	$(3.5 \pm 0.4) \cdot 10^{-4}$
E_{HC}	kJ/mol	104 ± 8.3
n		0.28 ± 0.11
Temp. range	$^\circ\text{C}$	[234; 339]
$ssq_{min}{}^\ddagger$		0.51
Standard error*		0.096
Data points		60

[†] Arrhenius frequency factor at reference temperature, $T' = 280^\circ\text{C}$ (see section 2.5.4).

^b Arrhenius frequency factor at reference temperature, T' .

[‡] Minimal sum of squares of residuals.

* Approximate standard error on the output variable ($\ln r$).

The MVK model has been suggested as a kinetic model for the total combustion of hydrocarbons as discussed in Section 2.5.3 and the model has one more parameter than the power rate law. However, the power rate law describes the measured kinetics considerably better than the MVK model with a minimal sum of squares three times smaller for the same data set and the model discrepancy is obvious from the parity plot of Figure 5.25 compared to that of Figure 5.23. The power rate law results of Table 5.17 were used in the remainder of this study.

5.5.1 Surface Analysis

To better understand the reason for the activity differences between the three catalysts, the SMF filter surfaces were analyzed by X-ray photoelectron spectroscopy (XPS). Table 5.19 lists the composition of the three different catalysts and their respective supports.

A deconvolution of the cobalt peaks from the spectra showed no sign of metallic cobalt (Co^0), confirming that calcination of the cobalt impregnated catalysts leaves no metallic cobalt and that the active phase for the total oxidation is cobalt oxide. Three cobalt

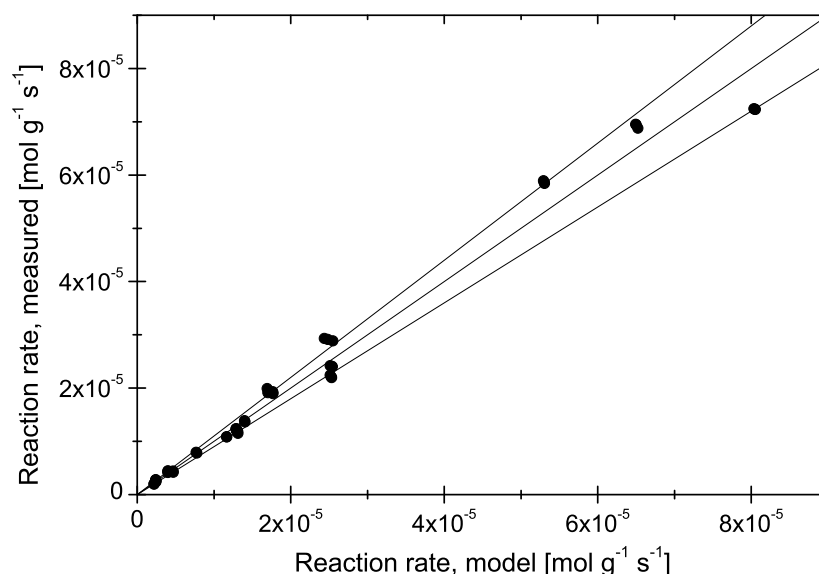


Figure 5.25: Parity plot of the Mars-van Krevelen model for the 1.1 wt.% Co_3O_4 on SMF_{SS} . The three lines are giving *parity* and the $\pm 10\%$ of the model values.

oxides are possible: CoO , Co_3O_4 and Co_2O_3 . The latter was not present in the samples, whereas it was not possible to distinguish between the peaks of CoO and Co_3O_4 , since the binding energies are too closely situated to one another. It was observed in the XRD spectrum of cobalt oxide impregnated powder (Section 5.1.1) that the active phase is predominantly Co_3O_4 .

The calcined supports alone showed no catalytic activity below $350\text{--}370^\circ\text{C}$, so the observed activity differences are not caused by the supports directly. However, the surface composition of the three catalysts vary considerably, which could explain the differences in activities. It is well known that mixed metal oxides often show higher activities than the single metal oxides (Spivey, 1987). It is thus possible that metals from the support diffuse to the surface during the calcination procedure, resulting in a partly mixed oxide surface. The XPS measurements show that, apart from the cobalt, there is a considerable amount of iron at the surface and minor amounts of nickel and chromium in the case of inconel. The diffusion of iron from the support surface to the catalyst surface seems to take place easier than that of nickel and chrome, since the impregnated surfaces were enriched with iron. This is seen particularly well from the calculations in the last row of Table 5.19, where the Co_3O_4 was subtracted from the calculations. Hence, the kinetics and the XPS measurements suggest that iron species at the catalyst surface has a positive effect on the activity.

Table 5.19: Composition (relative mass concentration, [wt.%]) of the SMF filter surfaces before and after impregnation with active phase (cobalt oxide).

Treatment	Element	Stainless steel	FeCrAlloy	Inconel
Bulk ^a	Co	0	0	0
	Fe	71.5	79.6	16.4
	Cr	16.5	20.0	23.0
	Ni	12.0	0.35	60.5
	O	-	-	-
	C	0.03	0.03	0.1
Calcined ^b	Co	0	0	0
	Fe	56.8	37.2	22.0
	Cr	0.7	13.0	11.6
	Ni	2.8	0.1	28.2
	O	33.0	44.2	33.2
	C	6.8	5.5	5.0
Impregnated ^c	Co	29.4	47.3	37.1
	Fe	37.1	22.3	17.1
	Cr	0.2	0.5	5.8
	Ni	0.0	1.8	7.6
	O	30.8	26.3	28.2
	C	2.6	1.8	4.4
Impregnated -(Co ₃ O ₄) ^d	Fe	61.8	62.7	34.5
	Cr	0.4	1.4	11.6
	Ni	0.0	4.9	15.3
	O	33.5	25.8	29.8
	C	4.2	5.2	8.8

^a Bulk composition, as given by the supplier: Southwest Screens & Filters (Sprimont, Belgium), now: Bekaert Fibre Technology (Zwevegem, Belgium).

^b Surface composition (XPS) after cleaning and calcination in air (see Section 3.1.2).

^c Surface composition (XPS) after impregnation and calcination to obtain ~1.3 wt.% Co₃O₄.

^d Surface composition (as ^c) with the surface composition of Co₃O₄ subtracted.

5.5.2 Deactivation

The effectiveness of a catalyst may change with use. The catalyst activity, a , can be defined as:

$$a = \frac{-r_A}{-r_{A0}} \quad (5.8)$$

where $-r_A$ is the reaction rate of reactant A over the catalyst and $-r_{A0}$ is the reaction rate with a fresh catalyst. Usually a starts at 1 and decreases with time.

For the irreversible n^{th} order reaction ($A \rightarrow B$) the reaction rate can be expressed as:

$$-r_A = kC_A^n a \quad (5.9)$$

where the deactivation is expressed as:

$$-\frac{da}{dt} = k_d C_i^m a^d \quad (5.10)$$

where k_d is the deactivation rate constant, superscript d is the order of deactivation and C_i is the concentration of material in the gas phase, either reactant A , product B or a poison P .

The deactivation was tested in the pilot reactor in CSTR mode. First, the kinetics of fresh catalyst was found in a series of short time runs, where a is considered constant (see Section 5.5). Afterwards, a long time run was performed with a constant inlet flow and inlet concentrations with mixed flow to check for the deactivation rate. This procedure allows the determination of a deactivation rate expression where $m = 0$, i.e. a concentration independent deactivation, which is usually the case for temperature induced changes to the catalyst surface. The deactivation expression (Equation 5.10) is thus:

$$-\frac{da}{dt} = k_d a^d \quad (5.11)$$

which in its integrated form is:

$$a = [1 + (d - 1)k_d t]^{1/1-d} \quad (5.12)$$

This expression was fitted to the reaction rate data as a function of time with the nonlinear least-squares parameter estimation program VA07AD (see Appendix D). The model parameters are shown in Table 5.20 and the decreasing activity, a , along with the model predictions are shown in Figure 5.26.

Table 5.20: Parameters of the deactivation rate expression with 2σ confidence levels (Equation 5.11 and 5.12).

Parameter	Unit	1.1 wt.% $\text{Co}_3\text{O}_4/\text{SMF}_{SS}$	2.9 wt.% $\text{Co}_3\text{O}_4/10\% \text{silicalite-1}/\text{SMF}_{SS}$
k_d	$1/\text{s}$	$(1.4 \pm 0.2) \cdot 10^{-5}$	$(1.4 \pm 0.2) \cdot 10^{-5}$
d	-	9.1 ± 0.8	11.3 ± 1.0

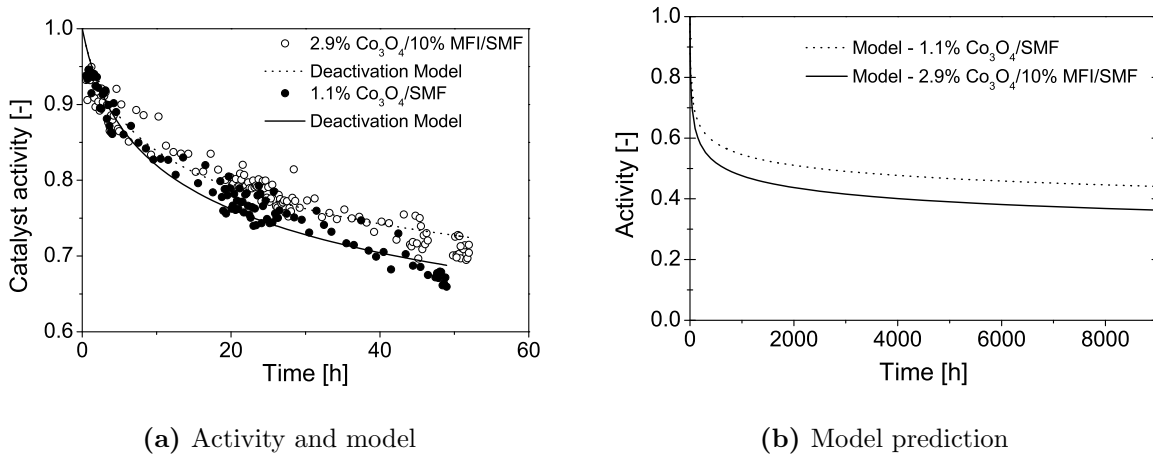


Figure 5.26: Catalytic activity as a function of time.

The stability of the two samples: 1.1 wt.% $\text{Co}_3\text{O}_4/\text{SMF}_{SS}$ and 2.9 wt.% $\text{Co}_3\text{O}_4/10\% \text{silicalite-1}/\text{SMF}_{SS}$ was investigated. The second sample was examined, since the cobalt

oxide spreads more evenly on the zeolite film, which could have a stabilizing effect on cobalt oxide.

The deactivation with both samples was very fast, but with a very high order of deactivation of approximately 10, the rate of deactivation is seen to slow down very fast as the deactivation progresses, as seen in Figure 5.26 (b). After 9000 hours (~ 1 year) on stream the deactivation model predicts an activity at 38 and 45 % of the initial activity for the two samples. The zeolite film might have a small stabilizing effect, but the deactivation rate is very similar and it would probably be better to chose the cheaper catalyst without the zeolite film.

The calcination of the dried, $\text{Co}(\text{NO}_3)_2$ impregnated samples was done at 450°C for 1 h in accordance with the procedure of Yuranov *et al.* (2003). Others have used similar calcination conditions for $\text{Co}(\text{NO}_3)_2$ impregnated samples ranging from 350 - 500°C and 2-4 h in air (Ji *et al.*, 2000; Barsan & Thyron, 2003; Chae *et al.*, 2004; Wyrwalski *et al.*, 2007). Chae *et al.* (2004) found that the catalytic activity of Co_3O_4 supported on Al_2O_3 depends very much on the type of precursor (cobalt-acetate or -nitrate salts) and on the calcination temperature (350 or 500°C). The higher calcination temperature led to lower activities due to sintering effects. However, even higher calcination temperatures have been used in the preparation of cobalt oxide. Depiak & Wierzba (1999) calcined a mixture of Co and Cr nitrate salts at 700°C for 5 h and Yuranov *et al.* (2002) used cobalt acetates and calcination at 650°C for 12 h to load metal grids with Co_3O_4 . The latter calcination method was used on a sample of 1.1 wt.% $\text{Co}_3\text{O}_4/\text{SMF}_{\text{SS}}$. This high temperature calcination strongly oxidizes the SMF surface as seen in Figure 5.27, where the cobalt oxide phase is no longer visible in comparison to the low temperature calcined samples in Figure 5.6.

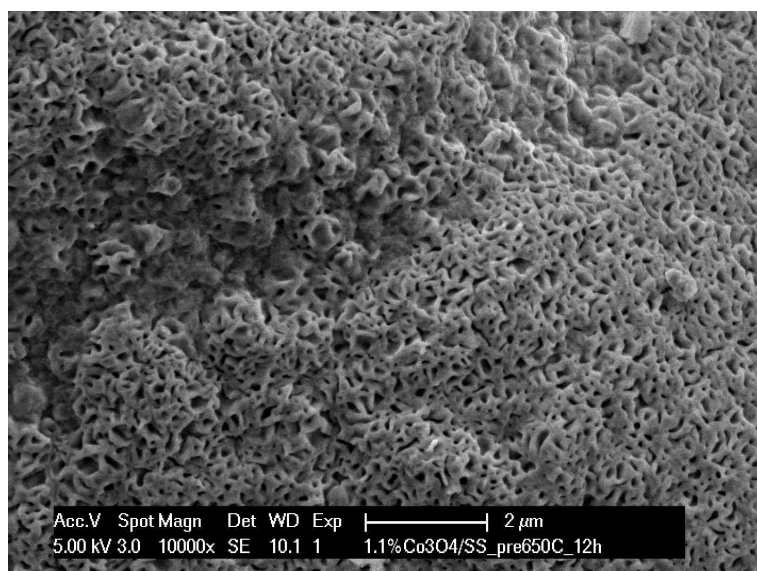


Figure 5.27: SEM image: 1.1 wt.% $\text{Co}_3\text{O}_4/\text{SMF}$ calcined at 650°C for 12 h.

In Figure 5.28 the deactivation of the three different Co_3O_4 samples discussed above are compared to the industrial catalyst CK-302 (copper and manganese oxide) as particles and as an attrition-milled powder supported on SMF. The catalysts were tested at similar conditions, but since the concentrations were not constant and identical between the samples the catalyst activity is expressed in terms of the rate constant (from the power

rate law Equation 2.27) assuming constant O_2 concentration:

$$k = \frac{r}{C_{C_3H_8}^n} \quad (5.13)$$

The reaction order in propane, n , was taken as 0.4 for Co_3O_4 (Table 5.17) and 0.6 for CK-302 (See Appendix E).

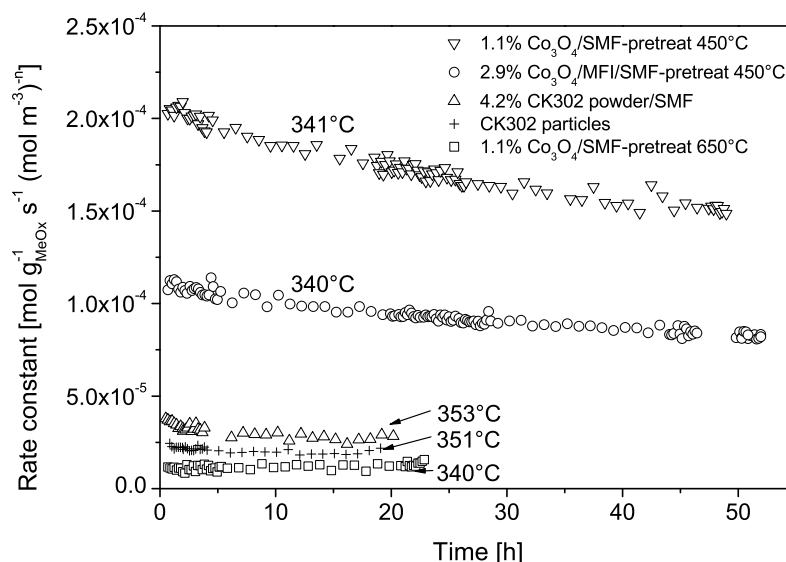


Figure 5.28: Comparison of the stability of different catalysts.

The high temperature calcined 1.1 wt.% Co_3O_4/SMF_{SS} was seen to be completely stable during the time on stream with an activity approximately one order of magnitude lower than the low temperature calcined 1.1 wt.% Co_3O_4/SMF and with a similar activity to the industrial catalysts CK-302. CK-302 catalysts showed a minor initial deactivation of approximately 20 %, before reaching a stable activity.

The Co_3O_4/SMF_{SS} catalyst has great potential for the oxidation of propane due to the high initial activity. With a deactivation over 1 year to approximately 40 % of the initial activity the catalyst would still be 3-4 times greater than the CK-302 catalysts with their initial activity. Furthermore, the stability of the Co_3O_4/SMF catalyst calcined at 650 °C for 12h shows that it will be very stable even with possible hot-spots formation in a fixed-bed reactor and finally, adding a second transition metal oxide could result in an even higher activity (Spivey, 1987; Depiak & Wierzba, 1999).

The Co_3O_4 /SMF could thus be optimized to achieve a stable and highly active, structured catalyst for the total oxidation of propane. The optimization parameters could for example be:

- SMF material (Stainless steel, FeCrAlloy)
- calcination temperature (450-650 °C)
- calcination time (2-12 h)
- cobalt oxide loading (1-5 wt.%)

The optimization could be done according to a 2^4 factorial design of experiments with a center point for each SMF material resulting in 18 experiments. However, this was not the scope of the current project.

5.6 Conclusion

Structured, fibrous catalysts for the destruction of VOCs by total oxidation were synthesized using sintered metal fibers (SMF) as support. These supports have the benefits of low pressure drop, high radial heat transfer conductivities leading to the avoidance of hot-spot formation, high geometric surface areas and corrosion resistance. The effect of modifying the support by the coating with an alumina layer or zeolite film was studied. These coatings increase the specific surface area of the support and could lead to higher dispersion and catalyst activity stability. Furthermore, the base support composition was varied (stainless steel, FeCrAlloy and inconel) for the catalysts with cobalt oxide supported directly on the SMF to investigate the support effect on the kinetics.

A method for coating the SMF with fine powder catalysts was developed and optimized by design of experiments. With the optimized deposition method three repeated dip-coatings in the powder suspension resulted in an average loading of 4.1 wt.%. The powder coating showed a very good mechanical stability on the SMF. By repeated air pressure pulses the maximum weight loss was ≈ 7 wt.% and after use in the reactor more than 75 % of the samples lost less than 4 wt.% of the powder coating. Furthermore, the powder coating increases the specific surface area considerably from $\sim 0.03 \text{ m}^2/\text{g}$ to $\sim 10 \text{ m}^2/\text{g}$ with 5 wt.% loading. The deposited powder was either a preimpregnated alumina catalyst or inert γ -alumina. The support with the coating of inert γ -alumina was subsequently impregnated with salts of cobalt and platinum to give a catalytically active phase upon calcination in air. The calcination in air resulted in Co_3O_4 as the catalytically active phase.

The catalytic screening showed that the most active catalysts for the combustion were those with cobalt oxide supported directly on the oxidized SMF or the silicalite-1/SMF composite. The powder-coat/SMF composites showed the lowest activities, especially samples with deposition of preimpregnated alumina powder. Several factors could have an influence on the lower activity: loss of specific surface area and pore blocking, loss of active phase during the aqueous attrition milling of the catalyst, less active copper and manganese oxides (in the case of CK-302) and possible support interaction between alumina and Co_3O_4 (Garbowski *et al.*, 1990).

The absence of mass transfer limitations allowed the determination of the kinetics of the most active and cheapest catalysts: Co_3O_4 supported on oxidized SMF. The kinetics were well described by a power rate law and showed significant differences between the catalysts with differing supports: stainless steel, FeCrAlloy and inconel. The results of the kinetic parameters are summarized in Table 5.21.

Table 5.21: Results of power rate law kinetics for the Co_3O_4 /SMF catalysts.

Parameter	Units	FeCrAlloy	Inconel	AISI316L
k'	$(\text{mol/g}\cdot\text{s}) (\text{m}^3/\text{mol})^{(n+m)}$	$(2.1 \pm 0.3) \cdot 10^{-5}$	$(2.3 \pm 0.2) \cdot 10^{-5}$	$(2.6 \pm 0.2) \cdot 10^{-5}$
E_a	kJ/mol	87.5 ± 2.6	92.6 ± 1.7	92.4 ± 1.3
n		0.38 ± 0.04	0.47 ± 0.04	0.41 ± 0.02
m		0.30 ± 0.08	0.14 ± 0.06	0.18 ± 0.04

Mainly the reaction orders varied between the catalysts. Overall, the inconel supported catalyst was the least active of the three. The FeCrAlloy supported catalyst was most active at lower temperature ($< 310^\circ\text{C}$), low $y_{\text{C}_3\text{H}_8} = 0.0013$ and high $y_{\text{O}_2} = 0.167$, whereas the stainless steel based catalyst was most active at high temperatures (350°C) and high propane mole fractions ($y_{\text{C}_3\text{H}_8} = 0.011$). The differences in activity seem to be explainable from the different surface compositions. The two most active catalysts have surfaces highly enriched with iron in comparison to the inconel supported catalyst. The FeCrAlloy catalyst have less iron, but more nickel at the surface than is the case with the stainless steel supported catalyst.

These very active catalysts (Co_3O_4 /SMF) deactivated fast, but with a high deactivation order. According to the concentration independent deactivation model the activity should level out around 40 % of the initial activity already after 3000 hours on stream. It was shown that by adapting the pretreatment method (increasing calcination time and temperature) the catalysts can be stabilized.

Catalysts based on Co_3O_4 supported directly on oxidized SMF are very active catalysts, are simple to prepare, would be able to withstand deactivation due to hot-spot formation, are very active and show good potential in relation to the industrial reference catalyst (CK-302, copper and manganese oxide supported on alumina).

Chapter 6

Two-Step Adsorption-Incineration

In this chapter a model will be developed for the coupling of desorption and total catalytic oxidation of propane in two separate fixed-beds. It is assumed that the fixed-beds are packed with the structured materials, i.e. SMF supported adsorbent and catalyst, that have been developed and described in the previous chapters.

The goal of the coupled process will be to incinerate the propane at an appropriate temperature in an adiabatic reactor, in order to stay below the emission limit of 25 ppmv (see Chapter 1).

First, the conditions of the catalytic reactor will be investigated. The desorber will be explored in terms of the different parameters influencing the desorption. For the coupling of the desorber and the reactor the goal will be to keep a constant propane concentration at the minimum needed for the adiabatic operating temperature of the catalytic fixed-bed reactor.

The desorber is described mathematically by two mass balances: one for the gas phase and one for the adsorbent phase. The desorption process is endothermic and the heat is provided from the combustion in the catalytic reactor. Therefore, an energy balance for the system is added and the temperature dependency of the mass transfer coefficient and the adsorption constant is accounted for by Arrhenius and van't Hoff expressions.

6.1 Catalytic Fixed-Bed Reactor

The catalyst for the combustion is the $\text{Co}_3\text{O}_4/\text{SMF}_{\text{FeCrAlloy}}$, which is the most active catalyst below 310°C and for low propane concentrations ($y_{\text{C}_3\text{H}_8} = 0.0013$) and high oxygen concentrations ($y_{\text{O}_2} = 0.167$). The assumptions for the catalytic fixed-bed reactor are:

- Plug flow hydrodynamics
- Thermodynamics of gas assumed equal to pure nitrogen.
- Negligible pressure drop
- Ideal gas law

- Adiabatic reactor
- The reactor will need to be heated for start-up and should afterwards be autothermal (e.g. via a concentric, counter-current double tubular reactor design).

An overall energy balance for the adiabatic reactor gives the outlet temperature as a function of the inlet concentration:

$$F_{in}(H_{in} - H_{out}) = F_{in}y_{C_3H_8,in}X\Delta H_r \quad (6.1)$$

For a constant pressure process the enthalpy change is given by:

$$\Delta H = \int_{T_{in}}^{T_{out}} C_p^G dT \quad (6.2)$$

where C_p^G is temperature dependent. In the present study the gas is assumed to have the properties of pure nitrogen for which C_p^G is approximately constant in the temperature range 25 to 400 °C. Therefore, the solution to the overall heat balance, Equation 6.1 and 6.2, results in a set of straight lines shown in Figure 6.1. The focus will be on two possible adiabatic reactor temperatures, 250 and 300 °C. To sustain these temperatures, a minimum mole fraction of propane is needed. This is found by solving for the propane mole fraction in the inlet as a function of the gas inlet temperature and gives the result shown in Figure 6.2. This relation can be used to control the gas conditions led to the reactor.

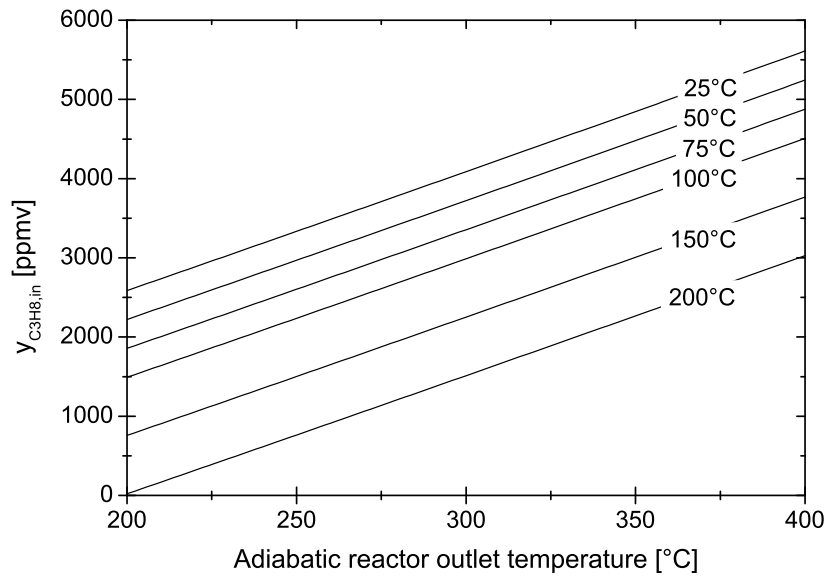


Figure 6.1: Relationship between the outlet temperature of an adiabatic catalytic reactor and the propane inlet concentration. Each line represents a different inlet temperature. Outlet mole fraction of propane = 20 ppmv.

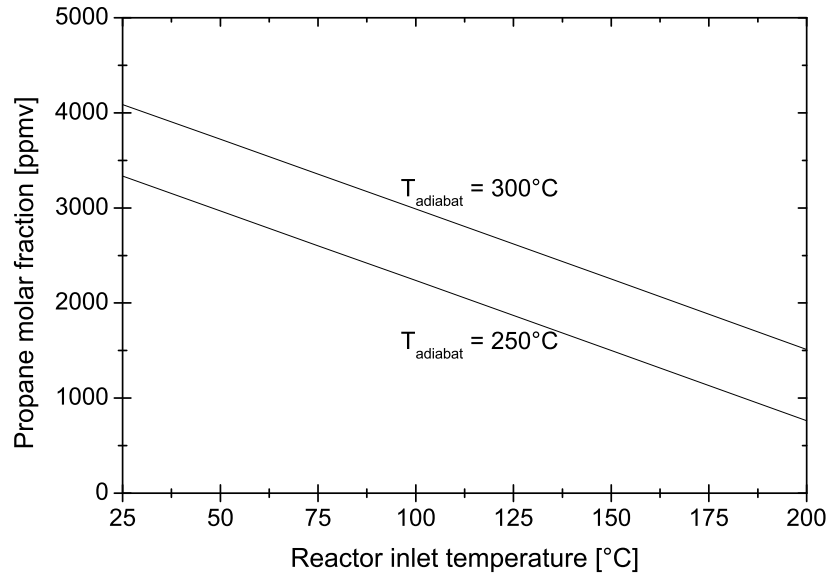


Figure 6.2: Propane mole fraction needed as a function of inlet gas temperature and the adiabatic reaction temperature desired.

6.2 Adiabatic Adsorption/Desorption Model

6.2.1 Governing Model Equations

All mathematical models describing the behavior of an adiabatic adsorption or desorption bed must include the adsorption equilibrium and mass balances described in Section 4.3:

1. The adsorption isotherm (Equation 4.8)
2. Mass balance for the gas phase (Equation 4.10)
3. Mass balance inside the adsorbent (Equation 4.9)

In addition the following energy balances are needed:

4. Energy balance for the gas phase
5. Energy balance inside the adsorbent

The energy balance inside a spherical pellet is:

$$k_e \left(\frac{\partial^2 T^z}{\partial r^2} + \frac{2}{r} \frac{\partial T^z}{\partial r} \right) = \rho^z C_p^z \frac{\partial T^z}{\partial t} + \Delta H \frac{\partial q}{\partial t} \quad (6.3)$$

where T^z is the temperature inside the pellet, k_e is the effective thermal conductivity of the pellet, ρ_z is the density of the solid adsorbent and C_p^z is the heat capacity of the solid phase and ΔH is the heat of adsorption (negative) or desorption (positive).

The energy balance for the bulk gas in the bed is:

$$\frac{\partial T}{\partial t} = k_{ax} \frac{\partial^2 T}{\partial z^2} - \frac{\partial vT}{\partial z} - \frac{1-\varepsilon}{\varepsilon} \frac{ha'}{\rho^G C_p^G} (T - T_R^z) \quad (6.4)$$

where T is the bulk gas temperature, k_{ax} is the axial thermal conductivity, superscript G denotes the properties of the gas phase and h is the film heat transfer coefficient. The axial thermal conductivity, which is analogous to axial dispersion, is usually negligible in a randomly packed bed.

Equations 6.3 and 6.4 are coupled by the relation:

$$k_e \left(\frac{\partial T^z}{\partial r} \right)_R = h(T - T_R^z) \quad (6.5)$$

where R indicates conditions at the particle surface.

6.2.2 Tanks-in-Series Model with Linear Driving Force

The adiabatic adsorption/desorption process for the zeolite/SMF-composite is described by the same mass balances as used for the isothermal adsorber with the linear driving force (LDF) approach. The control volume is identical to the one presented for the isothermal adsorption model in Figure 4.12.

The mass balance for the bulk gas phase is:

$$\frac{\partial C}{\partial t} = -v \frac{\partial C}{\partial z} - \frac{x_z \rho_z}{\varepsilon} \frac{\partial q}{\partial t} \quad (6.6)$$

The linear driving force approach is used to relate the amount of adsorbed species to the bulk gas concentration of adsorptive:

$$\frac{\partial q}{\partial t} = k_{LDF} (q^* - q) \quad (6.7)$$

q^* is the maximum adsorption capacity of adsorbed species in dynamic equilibrium with adsorptive concentration, C , in the bulk gas phase. q^* is described by the Langmuir isotherm:

$$q^* = q_m \frac{KC}{1 + KC} \quad (6.8)$$

For the adiabatic processes the Langmuir isotherm, through the adsorption constant K , must be temperature dependent via the van't Hoff expression:

$$K = K' \exp \left\{ \frac{-\Delta H_{ads}^0}{R} \left(\frac{1}{T} - \frac{1}{T'} \right) \right\} \quad (6.9)$$

and the mass transfer coefficient, k_{LDF} through the Arrhenius expression:

$$k_{LDF} = k'_{LDF} \exp \left\{ \frac{-E_{LDF}}{R} \left(\frac{1}{T} - \frac{1}{T'} \right) \right\} \quad (6.10)$$

The mass transfer coefficient k_{LDF} was fitted to adsorption breakthrough curves in Section 4.5. Since, adsorption and desorption are different processes the mass transfer coefficient

can differ between them. However, in the current study it was assumed that the same mass transfer coefficient can be used during the adsorption as well as during the desorption process.

Furthermore, an energy balance is needed to describe the adiabatic behavior. Considering the solid and gas phase in thermal equilibrium and neglecting the axial conductivity the following pseudo-homogeneous energy balance is obtained:

$$\left(\varepsilon \frac{P}{RT} C_p^G + x_z \rho_z C_p^z + x_f \rho_f C_p^f \right) \frac{\partial T}{\partial t} = -\varepsilon \frac{P}{RT} v C_p^G \frac{\partial T}{\partial z} + \Delta H x_z \rho_z \frac{\partial q}{\partial t} - Q \quad (6.11)$$

where x_f is the metallic fiber fraction in the fixed-bed, C_p is the heat capacity at constant pressure for the gas phase (G), zeolite (z) and metal fiber phase (f). ρ_f is the density of the metal fiber and Q is the energy flow rate from the system (heat loss), which is zero for an adiabatic system.

The axial conductivity in a fixed-bed reactor can often be neglected due to low heat conductivity of the porous bed material and heat transfer between particles taking place through their contact points and via the fluid phase (Yang, 1997; Kapteijn & Moulijn, 1997). When using SMF as a bed material the heat conductivity is an order of magnitude higher than with the normal inert metal oxides (alumina, silica, etc.), but the area of contact points between the fibers is still small. Furthermore, the layers of SMF can be slightly separated, further degrading the axial heat conductivity. In the adsorber, SMF_{SS} covered with a film of silicalite-1 was used. The thermal conductivity of the zeolite is $\approx 0.6 \text{ W/m}\cdot\text{K}$ at room temperature, which is two orders of magnitude lower than for stainless steel ($\approx 15 \text{ W/m}\cdot\text{K}$).

Radial heat conduction to the adsorber/desorber wall has the largest effect on minimizing the temperature gradients (Kapteijn & Moulijn, 1997, p. 1369). The radial heat transfer of the zeolite covered SMF is still significant due to the metallic core. According to Cahela & Tatarchuk (2001) the radial heat transfer is two times larger than in randomly packed beds, which is a big advantage of the structured, SMF fixed-bed reactors.

The partial differential equation (PDE) describing the mass balance in the bulk gas phase (Equation 6.6) is discretized in order to reduce it to an ordinary differential equation (ODE). The fixed-bed is divided into N equal cells of height $\partial z = h/N$ and the equation is multiplied by the cell volume V/N :

$$\frac{V}{N} \frac{\partial C_j}{\partial t} = -\frac{V}{N} v \frac{(C_j - C_{j-1})}{h/N} - \frac{V}{N} \frac{x_z \rho_z}{\varepsilon} \frac{\partial q_j}{\partial t} \quad (6.12)$$

where C_j is the concentration in the j^{th} cell/tank. This reduces to:

$$\frac{V}{N} \frac{\partial C_j}{\partial t} = \frac{\dot{V}}{\varepsilon} (C_{j-1} - C_j) - \frac{V}{N} \frac{x_z \rho_z}{\varepsilon} \frac{\partial q_j}{\partial t} \quad (6.13)$$

where \dot{V} is the volumetric flow rate. Analogously, the energy balance of Equation 6.11 for an adiabatic system is transformed to:

$$\begin{aligned} \frac{V}{N} \left(\varepsilon \frac{P}{RT_j} C_p^G + x_z \rho_z C_p^z + x_f \rho_f C_p^f \right) \frac{\partial T_j}{\partial t} \\ = \dot{V} \frac{P}{RT_j} C_p^G (T_{j-1} - T_j) + \frac{V}{N} \Delta H x_z \rho_z \frac{\partial q_j}{\partial t} \end{aligned} \quad (6.14)$$

The adiabatic adsorber and desorber can be described by a system of coupled ODEs given by the Equations: 6.7, 6.13 and 6.14. The total number of equations to solve the system will then be 3 times the number of tanks-in-series, N .

The initial and boundary conditions for a desorber with a fully saturated adsorption bed are:

$$C_j = C_0, q_j = q_0 \quad \text{at} \quad t = 0 \quad (6.15)$$

$$C_{j-1} = 0 \quad \text{for tank } j = 1, t > 0 \quad (6.16)$$

The model equations are transformed to dimensionless form by introducing the following dimensionless variables:

$$f = \frac{C}{C_0} \quad (6.17)$$

$$\xi = \frac{q}{q_0} \quad (6.18)$$

$$\theta = \frac{t}{\tau_m} \quad (6.19)$$

$$\tau_m = \frac{mq_0}{QC_0} \quad (6.20)$$

$$\zeta = \frac{T - T_0}{T_m - T_0} = \frac{T - T_0}{T_s} \quad (6.21)$$

where T_m is the maximum temperature of the inlet gas stream to the desorber (equal to the maximum design temperature for the catalytic reactor) and T_0 is the initial temperature of the desorber. For simplicity $T_s = (T_m - T_0)$.

In dimensionless form the system becomes:

$$\frac{\partial f_j}{\partial \theta} = \frac{N\tau_m}{\tau} (f_{j-1} - f_j) - \frac{\tau_m}{\varepsilon\tau} \frac{\partial \xi_j}{\partial \theta} \quad (6.22)$$

$$\frac{\partial \xi_j}{\partial \theta} = \tau_m k_{LDF} (\xi_j^* - \xi_j) \quad (6.23)$$

$$\begin{aligned} & \left(\frac{\varepsilon PC_p^G}{R[T_0 + T_s \zeta_j]} + x_z \rho_z C_p^z + x_f \rho_f C_p^f \right) T_s \frac{\partial \zeta_j}{\partial \theta} \\ &= \frac{\varepsilon \tau_m N PC_p^G}{\tau R[T_0 + T_s \zeta_j]} T_s (\zeta_{j-1} - \zeta_j) + \Delta H x_z \rho_z q_0 \frac{\partial \xi_j}{\partial \theta} \end{aligned} \quad (6.24)$$

This set of 3 times N first order ODEs (Equations 6.22-6.24) was solved using a FORTRAN program. The program uses the IVPAG routine of the IMSL MATH/library by Visual Numerics, Inc., which uses an algorithm based on the backward differentiation formulas (BDF), also known as Gear's stiff method. An example of the program code is found in Appendix C.

6.3 Modeling of Adsorption/Desorption System

6.3.1 Adiabatic Adsorber

In Chapter 4 the adsorber was considered isothermal, which is usually a good assumption for trace gas concentrations of adsorptive (Ruthven, 1984; Yang, 1997). The adiabatic model derived above was used to verify this assumption by comparing it to the isothermal model and the experiment with 51 pieces of SMF with 9.8 wt.% silicalite-1 loading. The result is shown in Figure 6.3 and the physical parameters used for the model are given in Table 6.1. In the adiabatic model, the adsorber heats up slightly. This temperature increase decreases the adsorption capacity, which leads to the breakthrough curve shifting to the left. Using the activated mass transfer coefficient the rate of mass transfer is slightly higher resulting in a slightly steeper breakthrough curve. The adiabatic model showed a maximum temperature increase at the outlet of 1.5 °C. With this temperature increase, a plateau for the outlet concentration at $f_N = 0.998$ and the adsorbate concentration at $\xi_N = 0.928$ is reached after ≈ 1 h.

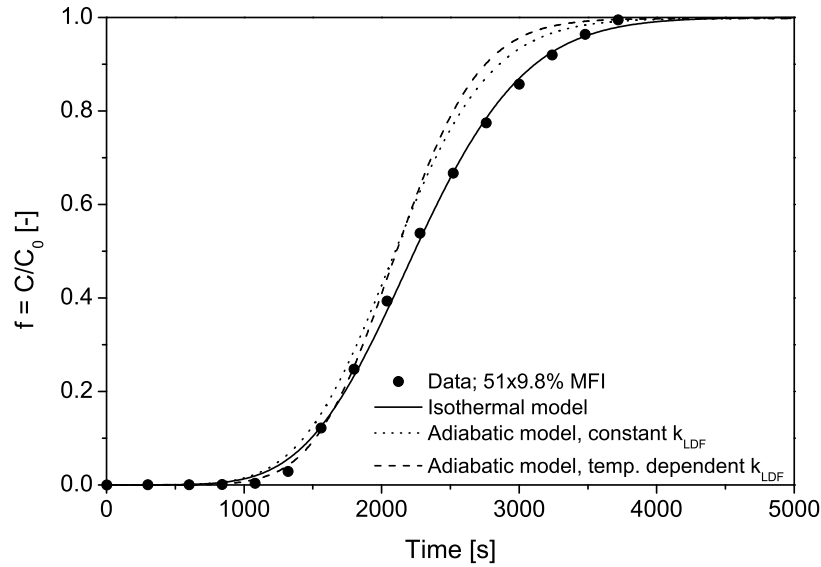


Figure 6.3: Adiabatic and isothermal adsorber models.

The model shows that this temperature plateau at the outlet is kept, until the temperature falls due to convection to the colder inlet gas. The bed is totally saturated after ≈ 33 h. This indicates that the heat capacity of the fixed-bed is very high in relation to the heat capacity of the heat carrier, which is the gas.

The slow change of temperature in the adsorber is due to the large heat capacity of the system $866 \text{ kJ/m}^3\cdot\text{K}$, mainly due to the fixed-bed. The heat capacity of the heat carrier, the gas, is only on the order of $1 \text{ kJ/m}^3\cdot\text{K}$.

Table 6.1: Thermodynamic and model parameters.

Parameter	Unit	Value
C_p^G	J/mol·K	29.2
C_p^z	J/kg·K	800
C_p^f	J/kg·K	500
ρ_z	kg/m ³	2160
ρ_f	kg/m ³	8000
ε	-	0.723
x_f	-	0.17
x_z	-	0.107
T_0	°C	30.0
T_m	°C	300.0

6.3.2 Adiabatic Desorber

Once adsorption breakthrough occurs, the adsorbent needs to be regenerated. The regeneration is driven by a change in the equilibrium conditions. Four basic methods are used in industry to regenerate the adsorbent by desorption, although combinations of these can also be used with advantage (Ruthven, 1984; Yon & Sherman, 2004):

1. **Thermal Swing:** Thermal swing is the regeneration of the adsorbent bed by heating. This is usually done with a stream of hot gas to a temperature at which the adsorbate is desorbed and removed by the fluid.
2. **Pressure Swing:** In a pressure swing process the desorption takes place by a reduction of the pressure at essentially constant temperature and purging the bed at low pressure. This operation is restricted to gaseous systems.
3. **Purge Gas Stripping:** The bed is regenerated at essentially constant temperature and pressure by purging with a nonadsorbing inert gas. This method is only useful for weakly adsorbed species. Otherwise, the quantity of purge gas becomes expensive. Furthermore, the desorbed species are normally only present at low concentrations in the purge gas and is therefore not useful for the recovery or concentration of the desorbate.
4. **Displacement Desorption:** The temperature and pressure of the bed is kept essentially constant and the desorbed species are being displaced by a stream containing a competitively adsorbed species, as in displacement chromatography. The method can be used in both liquid and gas systems. Steam stripping, which is widely used in the regeneration of solvent recovery systems using an activated carbon adsorbent, can be considered as a combination of thermal swing and displacement desorption.

The goal of the adsorption in the current study is to concentrate the VOC outlet stream enough to sustain the adiabatic reaction temperature in the catalytic combustion reactor. Figure 6.4 shows the need of heating the adsorbent in order to desorb with an increased concentration. The adsorbent in the previous section (6.3.1) has the indicated adsorbate

concentration of 13.4 mol/kg and is in equilibrium with a gas concentration of $\approx 80 \text{ Pa}$. However, a partial pressure of $\approx 400 \text{ Pa}$ is necessary for the adiabatic reactor at 300°C with an inlet temperature of 30°C . As indicated by the vertical bar, the temperature needs to be raised quickly to 60°C and even further as the desorption proceeds and the adsorbent is depleted in adsorbate (dashed arrow).

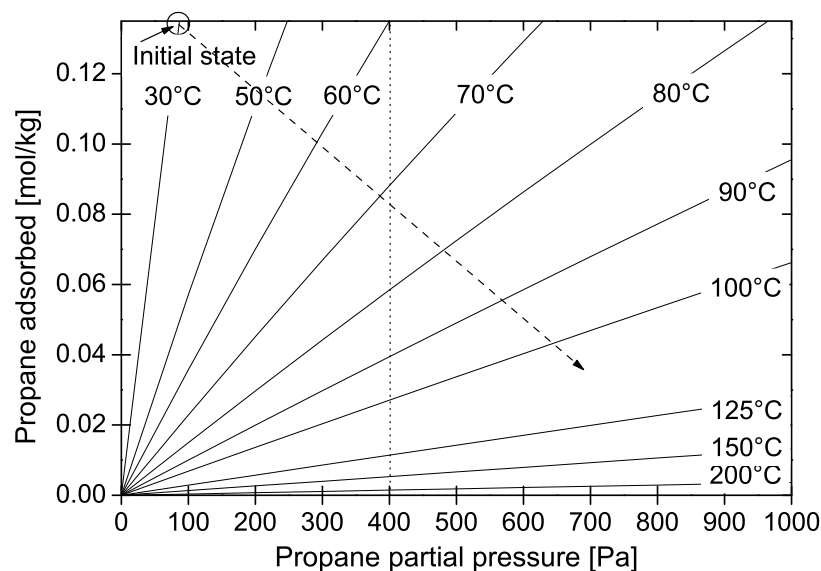


Figure 6.4: Langmuir isotherms for propane on the silicalite-1 film. Initial condition is for the saturated adsorbent in equilibrium with 800 ppmv at 30°C and 106 kPa. The vertical bar shows the partial pressure (400 Pa) necessary for the adiabatic reactor with an inlet temperature of 30°C .

Different options and models are considered to obtain this goal. All the methods use thermal swing to favorably change the equilibrium:

1. Thermal swing purging with hot gas from reactor; model with pseudo-homogeneous energy balance
2. Thermal swing purging with hot gas from reactor; model with film heat transfer
3. Thermal swing using steam as a high heat carrier in the fixed-bed
4. Thermal swing by preheating the desorber from the outside, purging with air for desorption (homogeneous distribution of adsorbate and adsorptive)

The different options are discussed in the following, where the simulations are made with the parameters from Table 6.1 and 6.2.

6.3.3 Desorption by Hot Gas

Thermal swing purging with hot gas exiting the catalytic reactor and entering the desorber at $T_m = 300^\circ\text{C}$ was simulated with the model proposed above (Equation 6.22-6.24) for the

Table 6.2: Desorption simulation parameters.

Parameter	Unit	Value
P	Pa	106000
R	J/mol·K	8.31415
τ	s	97
τ_m	s	2254
N	-	30
q_0	mol/kg	0.134
ΔH_{ads}^0	kJ/mol	-43.1
K'	1/Pa	$9.14 \cdot 10^{-4}$
\dot{V}	mL(STP)/min	10
m	kg	0.00100

case of a pseudo-homogeneous energy balance. Furthermore, the breakthrough profiles of the adsorptive and adsorbate from the isothermal adsorber were used as the initial conditions for the simulations. The flow rate for the desorption was taken as 10 % of the adsorption stream.

The simulation results in Figure 6.5 show the desorption process in time. The graphs on the left hand side (a, c, e) show the development of the bed profiles for the full model. In the right hand graphs (b, d, f) the same model neglects the heat capacity of the metal fibers ($C_p^f = 0$). With $C_p^f = 0$, the temperature profile is seen to progress faster. However, the effect of the heating on the adsorptive and adsorbate profiles is negligible and no concentration of the VOC takes place, since the heating is too slow compared to the gas flow rate. Both simulations show that it is problematic to use the gas as the heat carrier in this system, since the heat capacity ($1 \text{ kJ/m}^3 \cdot \text{K}$) of the gas is 3 orders of magnitude smaller than that of the fixed-bed ($866 \text{ kJ/m}^3 \cdot \text{K}$).

A model with a film heat transfer coefficient was then considered. If the heat transfer is not instantaneous and the model is no longer pseudo-homogeneous, the heat could travel through the fixed-bed and heat it more homogeneously to a lower temperature than 300°C , but still shifting the equilibrium.

The rate of heat transfer, \dot{Q} , depends on the interface surface area, a' , and the temperature difference between the fluid and the solid phase:

$$\dot{Q} = ha' \Delta T \quad (6.25)$$

where h is the film heat transfer coefficient.

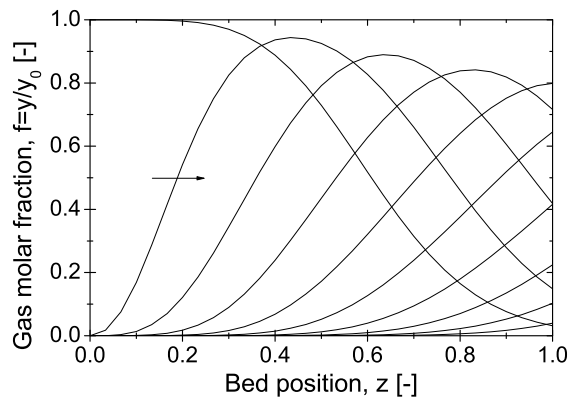
The energy balance was modified to cover the gas and the fiber-composite phases. The energy balance for the gas phase is:

$$\left(\frac{\varepsilon PC_p^G}{R(T_0 + T_s \zeta_j^G)} \right) \frac{\partial \zeta_j^G}{\partial t} = \frac{\varepsilon NPC_p^G}{\tau R(T_0 + T_s \zeta_j^G)} (\zeta_{j-1}^G - \zeta_j^G) - ha' (\zeta_j^G - \zeta_j^C) \quad (6.26)$$

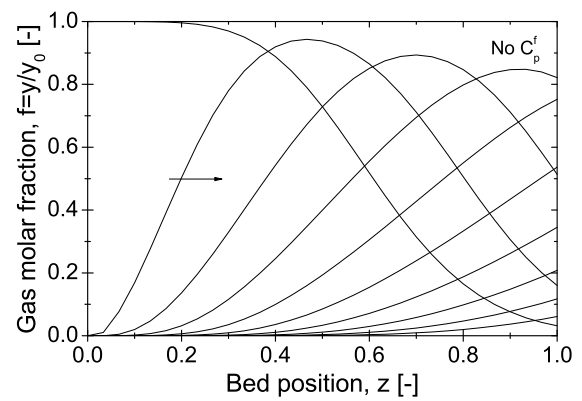
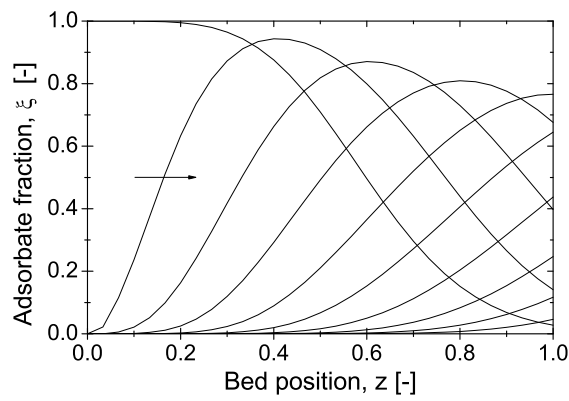
where the superscripts G and C refer to the gas and composite phases, respectively.

The energy balance for the solid, composite phase is:

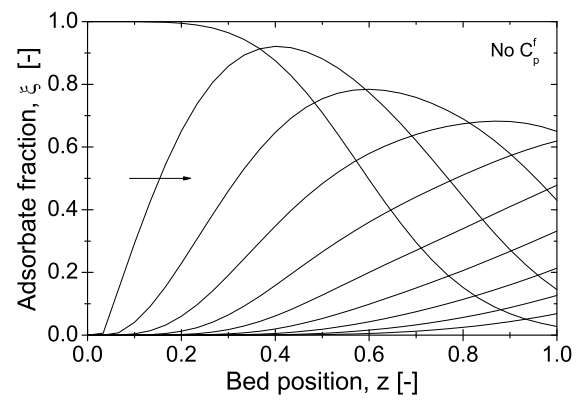
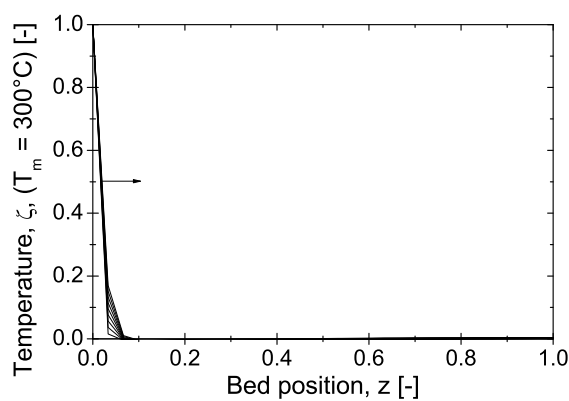
$$(x_z \rho_z C_p^z + x_f \rho_f C_p^f) T_s \frac{\partial \zeta_j^C}{\partial t} = \Delta H x_z \rho_z q_0 \frac{\partial \xi_j}{\partial t} + ha' T_s (\zeta_j^G - \zeta_j^C) \quad (6.27)$$



(a) Adsorptive fraction.

(b) Adsorptive fraction. $C_p^f = 0$.

(c) Adsorbate fraction.

(d) Adsorbate fraction. $C_p^f = 0$.

(e) Temperature profile.

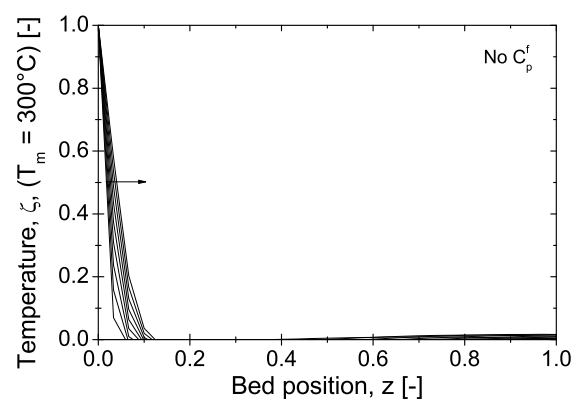
(f) Temperature profile. $C_p^f = 0$.

Figure 6.5: Bed profiles (pseudo-homogeneous energy balance model) for the adiabatic desorption of the isothermal adsorption bed after breakthrough. Each curve is 500 s apart in direction of the arrow, starting at $t = 0$. Gas flow rate is 10% of the adsorption flow rate at 10 mL(STP)/min, $T_0 = 30^\circ\text{C}$, $T_m = 300^\circ\text{C}$.

The film heat transfer coefficient was estimated from the Chilton-Colburn analogy:

$$j_H = j_D \quad (6.28)$$

and the expression of De Greef *et al.* (2005) for the mass transfer coefficient (see Section 5.3 and Table 5.13):

$$Sh = \frac{0.47}{\varepsilon} Re^{1/2} Sc^{1/3} \quad (6.29)$$

$$j_D = Sh Re^{-1} Sc^{-1/3} \quad (6.30)$$

$$j_H = Nu Re^{-1} Pr^{-1/3} \quad (6.31)$$

Combining these four relations yields:

$$Nu = \frac{hd_f}{k} = \frac{0.47}{\varepsilon} Re^{1/2} Pr^{1/3} \quad (6.32)$$

The Biot number for heat transfer has been estimated with the parameters of Table 6.3 from the following equation:

$$Bi_H = \frac{hd_f}{k_{SiO_2}} \quad (6.33)$$

The result of the Bi_H and the film heat transfer coefficient h as a function of the Reynolds number is shown in Figure 6.6.

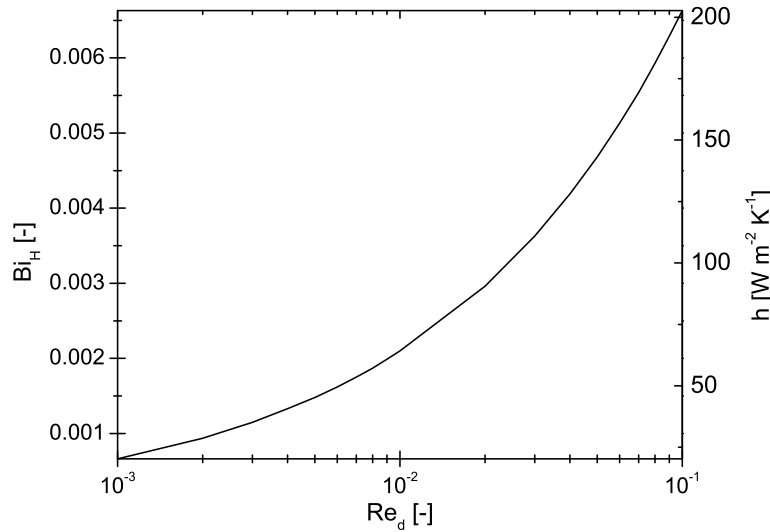


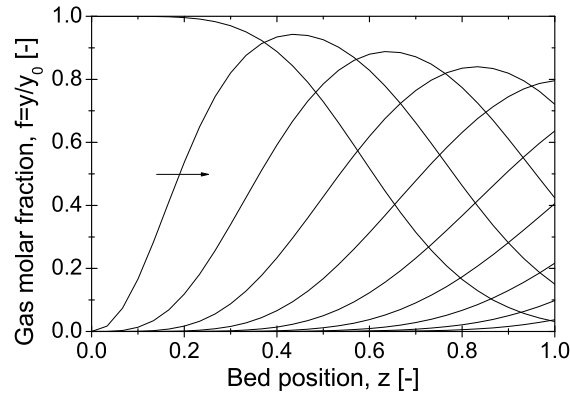
Figure 6.6: Bi_H and the film heat transfer coefficient as functions of Re_d .

With a $Re_d = 0.023$ (as calculated in Table 4.7) the $Bi_H = 1 \cdot 10^{-3} \ll 1$, which is equivalent to the main resistance of the heat transfer being due to the heat transfer between the two phases. Furthermore, this results in temperature gradients being negligible in the composite phase.

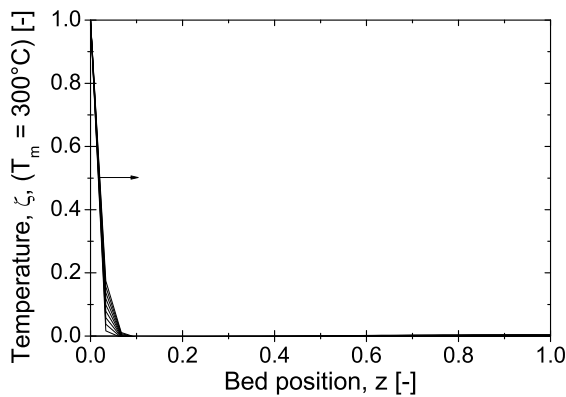
The results of the simulations of this heat transfer model are shown in Figure 6.7. The temperature profiles for the gas and composite phases with the predicted heat transfer coefficient are essentially identical. The heat transfer over the film is too effective to result in a temperature difference between the two phases. The model only predicted a temperature difference with a value of h being 3 orders of magnitude smaller than the estimated value.

Table 6.3: Parameters used for the calculation of the Bi_H . Values taken from (Lide, 2001).

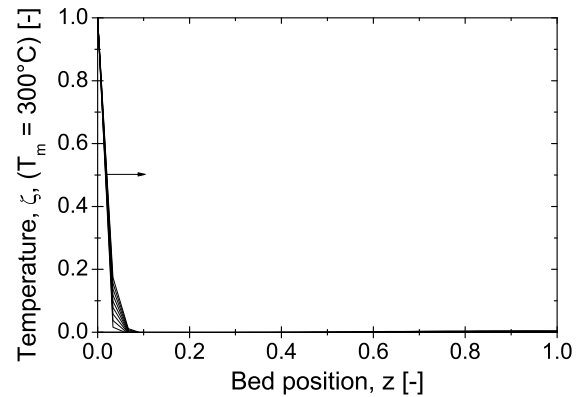
Parameter	Unit	Evaluation temperature [°C]	Value
k_{SiO_2}	W/m·K	50	1.3
k_{N_2}	W/m·K	27	$2.58 \cdot 10^{-2}$
d_f	μm	-	25.5
ε	-	-	0.723
C_p^G	J/mol·K	27	29.2
μ	Pa s	27	$2.29 \cdot 10^{-5}$
Pr	m^2/s	27	0.93



(a) Adsorptive fraction.



(b) Temperature profile. Gas phase.



(c) Temperature profile. Composite phase.

Figure 6.7: Bed profiles (film heat transfer model) for the adiabatic desorption of the isothermal adsorption bed after breakthrough. Each curve is 500 s apart in direction of the arrow, starting at $t = 0$. Gas flow rate is 10 % of the adsorption flow rate at $10 \text{ mL(STP)}/\text{min}$, $T_0 = 30^\circ\text{C}$, $T_m = 300^\circ\text{C}$.

It can therefore be concluded that the model with a pseudo-homogeneous energy balance is sufficient for describing the system and that the heat will have to be supplied in a different way to achieve the concentration of VOC in the gas stream.

6.3.4 Steam Purging

The problem of heating the fixed-bed with hot gas from the inside is the large difference in heat capacity of the gas and the solid phase. This problem might be overcome by using steam as the heat carrier due to the high latent heat of steam. Saturated steam at 100 °C has a heat of condensation of $2257 \text{ kJ/kg} = 1328 \text{ kJ/m}^3$. In comparison the heat of nitrogen gas supplied by cooling from 300 to 100 °C amounts to 202 kJ/kg or 124 kJ/m^3 ¹. The heat supplied by steam would be approximately 10 times larger than with dry, hot purging gas and would only heat the bed to 100 °C, which might be sufficient to achieve the concentration of VOC.

However, there are several disadvantages of using steam. The condensed steam will have to be removed in an additional drying stage, adding to the investment cost. Steaming is especially used for solvent recovery. In these processes the VOC is desorbed from the adsorbent and condenses along with the condensed steam on the external surfaces of the adsorbent. The liquid phases run off the vertical fixed-bed and can then be separated by decanting (Jedrzejak & Paderewski, 1988; Yon & Sherman, 2004). In the case of propane and light alkanes the solubility in water at 25 °C is very low ($6.7 \cdot 10^{-5} \text{ wt.}\%$ for propane and decreasing with increasing temperature) and the boiling points are low (-42.1 °C for propane) and there would not be a separation problem. However, using steaming for the desorption followed by the catalytic combustion would result in the discussed separation problems with other types of VOCs which are high boiling and/or soluble in water. Furthermore, the effect of high steam concentration on the catalyst would have to be investigated.

The advantage of using steam as a high heat carrier is followed by several disadvantages. This method of heating will therefore not be considered for the thermal swing desorption. Heating with steam would result in a highly concentrated gas of propane, since the saturated steam only drives off the propane, but does not dilute it. A similar effect could be achieved by external preheating of the fixed-bed without purging of the bed.

6.3.5 External Preheating

The desorber can be heated externally (for example with the reactor outlet gas) without passing a gas through the unit. Assuming that the heat was supplied from the combustion of desorbed propane from a previously saturated adsorber unit allows the calculation of the maximum temperature rise possible.

An overall heat balance on the reactor considers the amount of energy that can be released by total oxidation, the amount of energy used for the heat of desorption and the energy needed to heat the desorber to the desorption temperature:

$$n_{VOC}\Delta H_r = n_{VOC}^A(-\Delta H_{ads}^0) + (m_{bed}\hat{C}_p^{bed} + n^G C_p^G)\Delta T \quad (6.34)$$

¹Calculated with the gas inlet concentration at 300 °C

where \hat{C}_p^{bed} is the average heat capacity of the bed and

$$n_{VOC} = n_{VOC}^G + n_{VOC}^A \quad (6.35)$$

with n_{VOC} being the total moles of VOC in the bed comprised of VOC in both the gas (G) and the adsorbent (A) phase.

The maximum desorption temperature obtainable for a given system is a function of the adsorbate loading on the adsorbent, which again is a function of the concentration of VOC in the gas stream to be cleaned and the relative size of the mass transfer zone (MTZ). The MTZ is the part of the bed, where mass transfer takes place and hence, where the dimensionless concentration of adsorbate varies between 0 and 1. When the MTZ makes up a major part of an adsorbent bed, the equilibrium capacity is poorly utilized.

A longer adsorbent fixed-bed results in a smaller part of the total bed made up by the MTZ and the utilization of the adsorption capacity will tend to 1 as $L \rightarrow \infty$. However, a fully saturated bed can also be obtained by using a lead-trim configuration. The feed flows successively through a lead bed and then a trim bed. The lead bed is fully saturated before it is taken out of service to be regenerated. When a lead bed is removed from adsorption, the trim bed becomes the lead and a fully regenerated bed becomes the new trim bed.

A fully saturated adsorbent bed defines the maximum heat possible to generate from the adsorbed propane in the bed. The maximum temperature rise and the maximum desorber temperature possible, with no internal flow, as a function of the inlet fraction of propane to the adsorber was calculated from Equation 6.34 and the result is given in Figure 6.8.

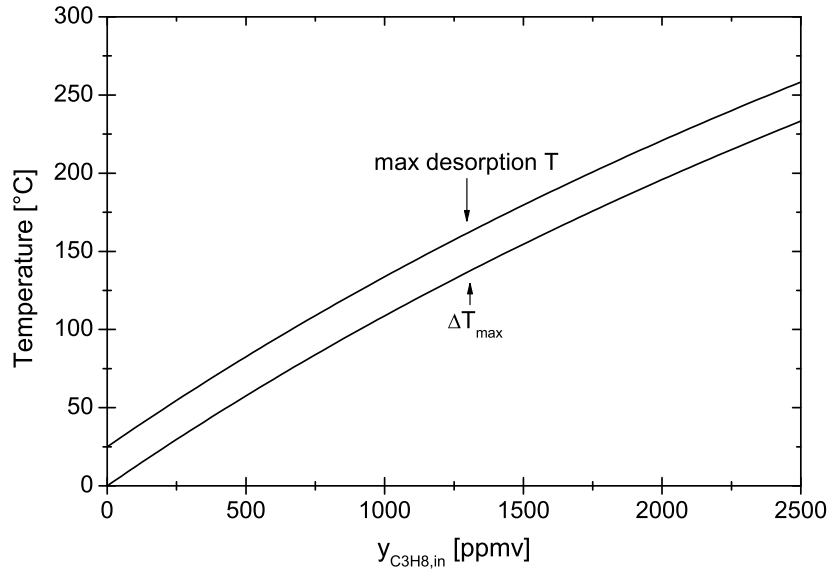


Figure 6.8: Maximum adiabatic temperature rise of the desorber with heat provided uniquely from oxidation of the adsorbate. $T_{ads} = 25^\circ\text{C}$.

An adiabatic temperature rise of the desorber to 100°C is achieved with only 675 ppmv propane in the inlet. The temperature needed for an efficient desorption is yet to be assessed. Assuming that the adsorption is isothermal at 25°C with $y_{C_3H_8,in} = 1000$ ppmv and that the adsorbent is completely saturated, the adsorption equilibrium results as

a function of the preheating temperatures were calculated. The calculations show the fraction of adsorbate that is desorbed, the respective gas mole fraction of propane and the corresponding desorber pressure (for a closed constant volume system) or the volume for a constant pressure process. The results are shown in Figure 6.9 and 6.10.

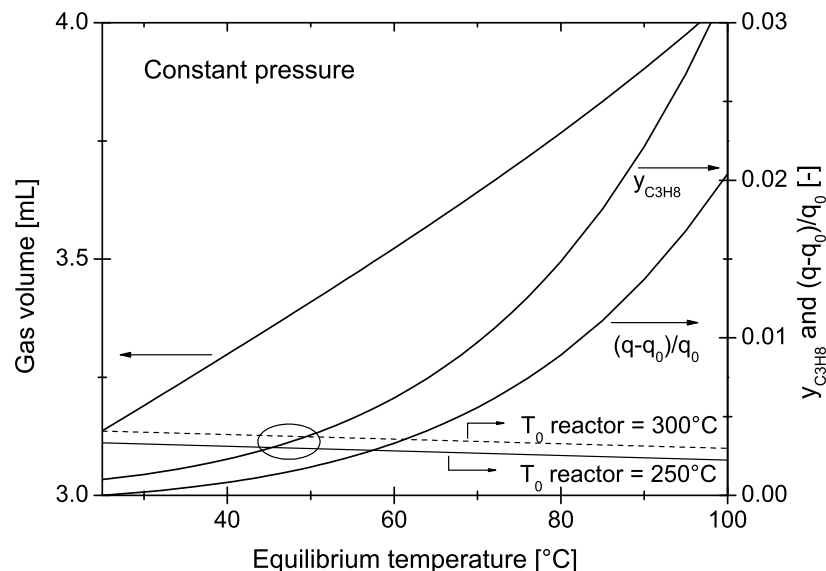


Figure 6.9: Preheating of desorber at constant pressure. Fully saturated adsorber at 25 °C and $y_{C_3H_8,in} = 1000$ ppmv.

Since, it is assumed that the propane was removed from air and the purge gas is air, there will be a very large excess of oxygen for the oxidation and the stream exiting the desorber will not need further dilution with air to meet the oxygen requirements before entering the incinerator. The desorbed mole fraction of propane needed, to keep the reactor at a certain constant temperature, depends on the temperature of the exiting stream as was shown in Figure 6.2. These curves have been superimposed in Figure 6.9 and 6.10. The intersections of the lines for the reactor operating at 250 and 300 °C and the line of $y_{C_3H_8}$ from the adsorption equilibrium at the preheated desorber temperature define the minimum preheating temperature needed to obtain the minimum propane mole fraction needed for the self sustaining reaction temperature. The intersection points are almost identical for the cases of constant volume and constant pressure desorption. The minimum mole fraction needed is ≈ 3700 ppmv and minimum $T_{des} = 50$ °C for a reactor temperature of 300 °C and ≈ 3000 ppmv and minimum $T_{des} = 46$ °C for a reactor temperature of 250 °C. The results show that it is only necessary to heat to approximately 50 °C in the current case to be above this limit. However, a higher initial temperature might be needed to ensure a continuing desorption at sufficiently high concentrations.

The previously developed model for the adiabatic desorption was used to simulate the desorption of the preheated desorber. This model does not take into account the initial differences from the batch wise preheating of the desorber resulting in increased pressure or volume in the initial phase of desorption. However, the error induced by this simplification is relatively small up to 80 °C, where the initial pressure or the initial gas volume release respectively is 20 % higher than assumed in the model for full adsorption of 1000 ppmv at 25 °C. Only 0.9 % of the adsorbate will have been released at the ini-

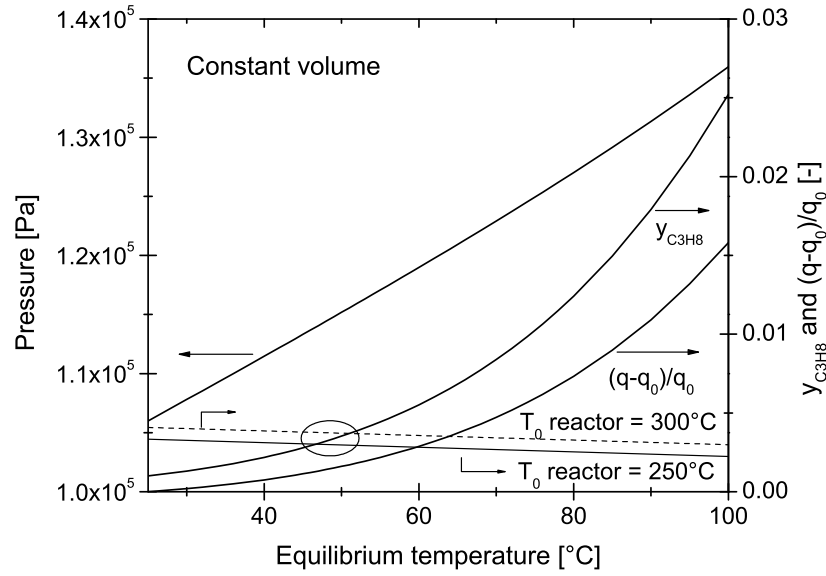


Figure 6.10: Preheating of desorber at constant volume. Fully saturated adsorber at 25 °C and $y_{C_3H_8,in} = 1000$ ppmv.

tial preheating temperature of 80 °C. The model can thus give a good estimation of the expected desorption behavior.

6.3.6 Parametric Study of Adiabatic Desorber

In this section the influence of important process parameters on the desorption is shown in detail. The investigated parameters were:

- \dot{Q} , desorption gas flow rate (1, 10, 100 1000 mL(STP)/min)
- T_0 , initial desorber temperature (45, 50, 55, 60, 65, 70, 80 °C)
- $y_{C_3H_8,in}$, inlet propane mole fraction to the adsorber (25, 250, 500, 650, 750, 1000, 2500 ppmv)

All the simulations considered the regeneration of an adsorber, fully saturated at 25 °C. The base case was considered as the desorption from an adsorber fully saturated with $y_{C_3H_8,in} = 1000$ ppmv, preheated to 60 °C and a desorption flow rate of 10 mL(STP)/min (= 10 % of the adsorption flow rate). Based upon this case, the parameters were varied one at a time. The influence of the parameters on the desorption process was evaluated by:

- Initial equilibrium mole fraction, $y_{C_3H_8,eq}$
- Desorption effectiveness, η_L : fraction of propane desorbed with $y_{C_3H_8} > y_{min,250^\circ C}$
- Desorption effectiveness, η_H : fraction of propane desorbed with $y_{C_3H_8} > y_{min,300^\circ C}$
- Maximum attainable adiabatic reactor temperature from the chemically stored energy of propane, T_{max}

For the simulation of the desorption curves it was assumed that the reactor is close to plug flow (number of tanks-in-series, $N = 100$), that the desorber is adiabatic, that air at 25 °C is used as purge gas and that the initial deviations from the ideal state in the model are negligible. The initial equilibrium conditions are assumed identical at any point in the desorber. The equilibrium conditions were calculated for the constant pressure case and the additional volume evolving from the equilibrium desorption was added to the exiting stream from the desorber.

The simulated desorption mole fraction profiles for the base case are shown in Figure 6.11. The initial equilibrium conditions for the base case were found to be a desorption of 0.33 % of the adsorbate resulting in a mole fraction of 6190 ppmv. Since the entire unit is at equilibrium, the exiting stream has this initial concentration for approximately 3000 s until the purge gas front reaches the outlet and the mole fraction drops sharply. Figure 6.11(a) shows the bed profiles during the desorption. A broadening of the mass transfer zone (MTZ) is observed, which is due to the nearly linear or slightly unfavorable isotherm during desorption (Ruthven, 1984).

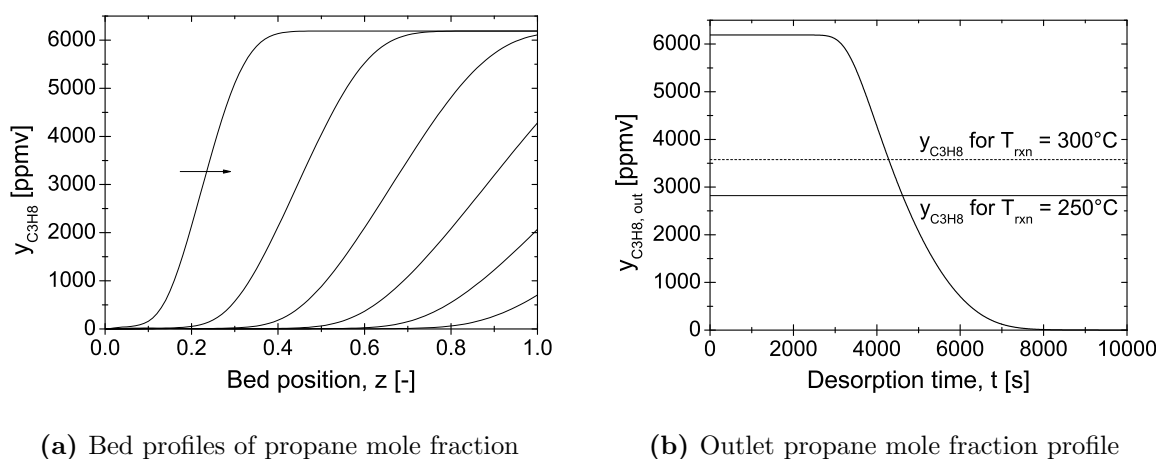


Figure 6.11: Base case: Full adsorption with $y_{C_3H_8, in} = 1000$ ppmv at 25 °C. Desorption from preheated unit at 60 °C and 10 mL(STP)/min, 1000 s between each profile.

The fraction of the desorbed propane, with a mole fraction above the minimum level necessary to sustain the adiabatic temperature of the reactor at either 250 or 300 °C, was calculated by integrating the part of the outlet mole fraction higher than these values. These effectiveness factors of the desorption are named η_L and η_H for the low (L) and high (H) reaction temperatures. In the base case $\eta_L = 0.913$ and $\eta_H = 0.876$.

Desorption Flow Rate

During thermal purging the flow rate is usually decreased compared to the adsorption stream. This is done to increase the concentration of VOC in the outlet. With the current model of the preheated desorber there was no influence of the flow rate (1 to 1000 mL(STP)/min) on the outlet concentration and the desorption time changes linearly with the flow rate. This is due to the fact that the mass transfer is very fast because of the short diffusion path in the thin zeolite film. Larger zeolite particles and higher flow

rates should result in lower gas phase concentrations as a result of higher diffusion times and lower residence time.

With the thin zeolite film as adsorbent the desorption flow rate can be varied over a large range without effects on the VOC outlet concentration. The rate of desorption can thus easily be adapted to the adsorption cycle and the VOC concentration to the catalytic combustor can be adjusted by dilution with air.

Initial Preheating Desorption Temperature

The preheating temperature of the desorber influences the desorption through the equilibrium over the adsorbent. The capacity of the adsorbent decreases with increasing temperature resulting in higher gas mole fractions of the VOC. This fact is clearly seen from Figure 6.12.

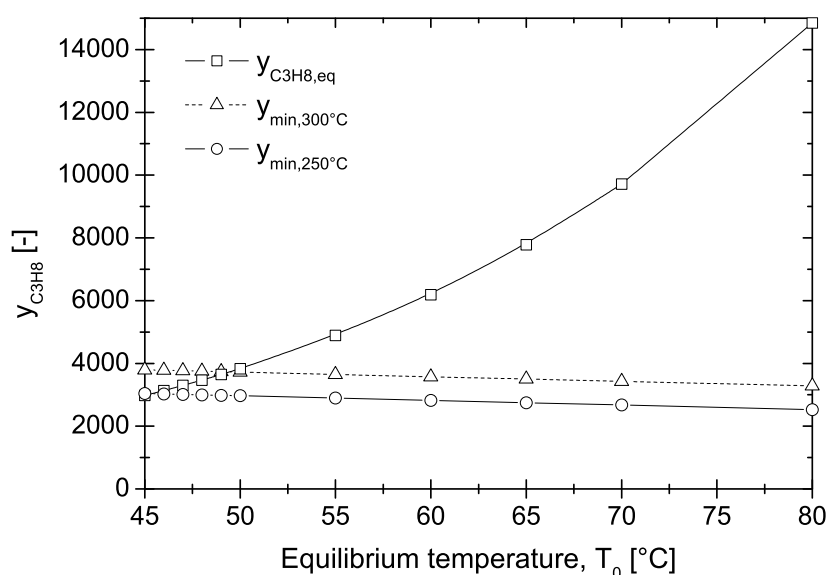


Figure 6.12: Propane mole fraction as a function of equilibrium temperature and propane mole fraction needed in the combustion reactor as a function of the equilibrium temperature in the desorber. Full adsorption with $y_{C_3H_8,in} = 1000$ ppmv at 25 °C.

The figure also shows the minimum mole fractions of propane needed to sustain a combustion temperature of 250 and 300 °C, respectively. The intersection of these lines with the equilibrium line defines the minimum preheating temperature necessary. In the case of full adsorption with $y_{C_3H_8,in} = 1000$ ppmv at 25 °C the minimum preheating temperature is approximately 49 °C to sustain the high combustion temperature and 45 °C for the low combustion temperature.

The desorption mole fraction profiles at the outlet of the desorber are seen in Figure 6.13. The area under the desorption curves is constant, but the shape changes due to the preheating. A higher temperature leads to a higher initial mole fraction of propane in the desorber. A higher temperature also results in a faster regeneration of the adsorbent and a steeper drop in the outlet concentration. The steepness of this drop is of importance to the effectiveness of the desorption. A steep drop results in a more effective desorption as

depicted in Figure 6.14. The effectiveness tends to 1 for $T_0 \rightarrow \infty$ and drops rapidly close to the limit of the minimum temperature needed for the combustion.

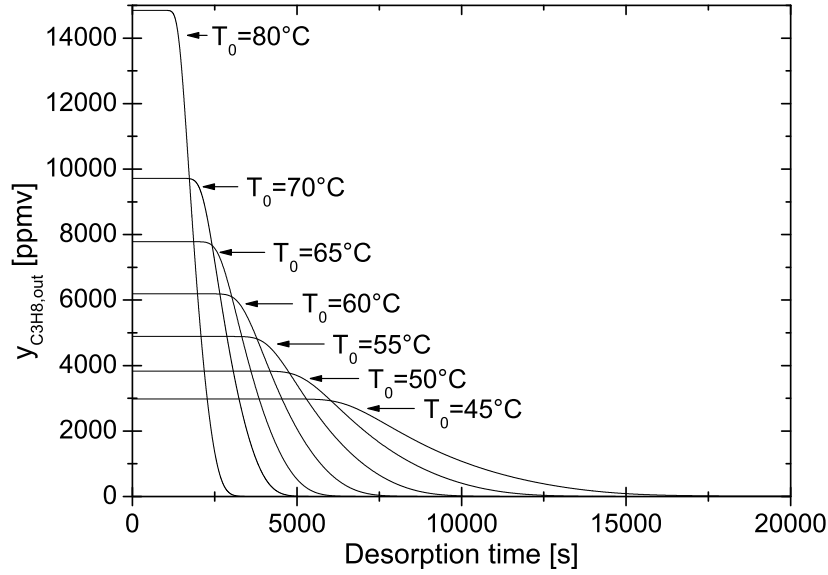


Figure 6.13: Desorption outlet mole fraction as a function of time and initial, equilibrium, preheating temperature, T_0 . $\dot{V} = 10 \text{ mL(STP)}/\text{min}$.

With the base case loading for adsorption with $y_{\text{C}_3\text{H}_8,\text{in}} = 1000 \text{ ppmv}$ at 25°C a very high effectiveness of desorption can easily be achieved autothermally, since the adiabatic preheating temperature is $\approx 138^\circ\text{C}$ as calculated in Figure 6.8.

Adsorptive Concentration

The initial, equilibrium mole fraction of propane during the desorption depends on the loading of the adsorbent, which is determined by the concentration of propane in the inlet to the adsorber and the adsorption temperature. The mole fraction during desorption depends on the mole fraction of propane fed to the adsorber as given in Figure 6.15. With adsorption at 25°C and desorption at 60°C the minimum mole fraction of propane needed to sustain the oxidation temperature in the reactor is 456 ppmv for a reactor temperature of 250°C and 578 ppmv for 300°C .

The desorber outlet profiles as a function of the adsorption inlet concentration is shown in Figure 6.16. In similarity with the results of the preheating temperature in Figure 6.13, the desorber outlet mole fraction of propane is kept constant until the purge gas wave reaches the outlet and a steep drop in the concentration is observed. However, the area under the curves is not identical, since the amount of propane adsorbed varies. The behavior of the effectiveness of desorption in Figure 6.17 is also similar to that of the preheating in Figure 6.14. However, the convergence towards unity as a function of the adsorptive concentration is much slower, since a favorable change in steepness of the concentration drop at the outlet is not pronounced. Therefore, the effectiveness is nearly constant at high propane mole fractions and drops steeply in proximity of the minimum limit for the mole fraction needed for the adiabatic combustion.

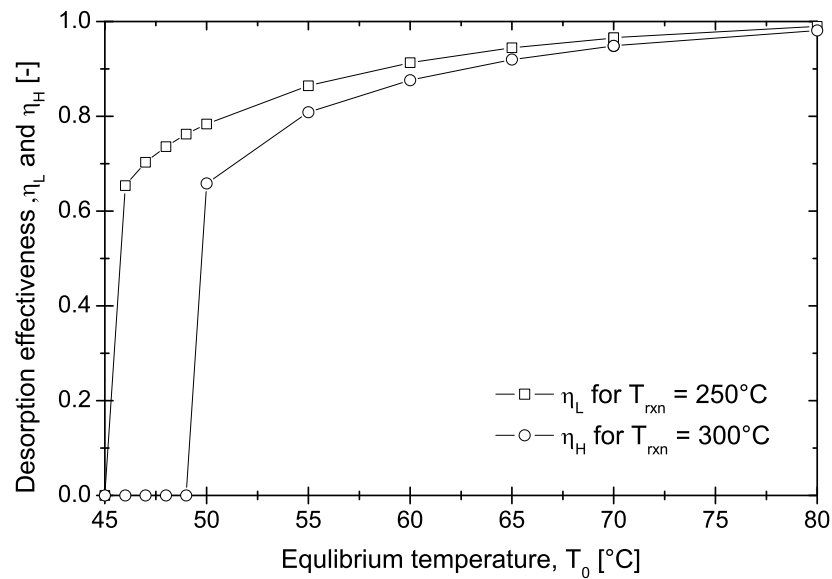


Figure 6.14: Desorption effectiveness as a function of the initial, equilibrium, preheating temperature, T_0 . $\dot{V} = 10 \text{ mL(STP)}/\text{min}$

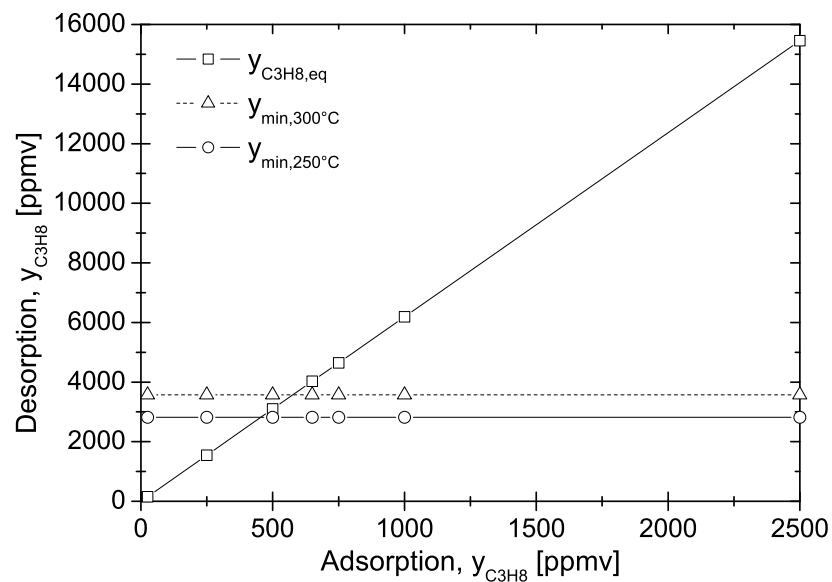


Figure 6.15: Desorber outlet mole fraction as a function of the propane mole fraction to the adsorber. Adsorption at 25°C , desorption at 60°C and $\dot{V} = 10 \text{ mL(STP)}/\text{min}$.

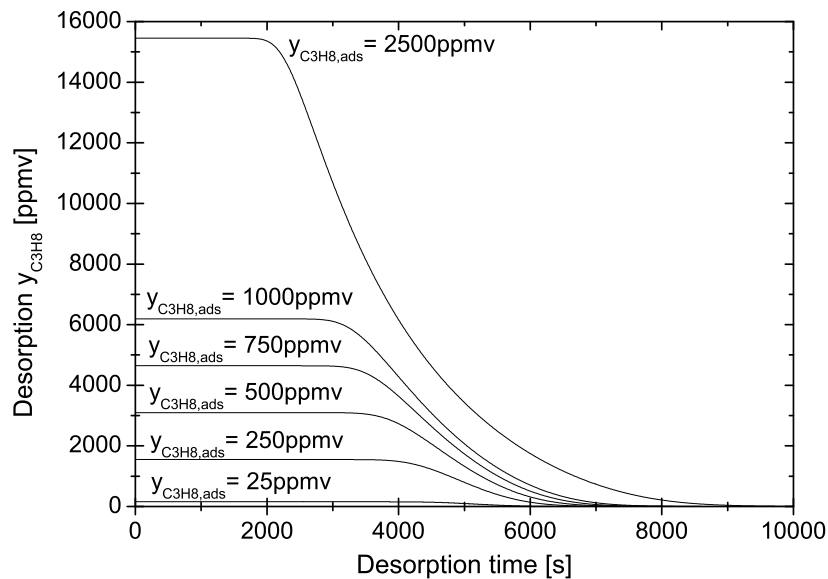


Figure 6.16: Desorber outlet mole fraction as a function of time and propane mole fraction to the adsorber. Adsorption at 25 °C, desorption at 60 °C and $\dot{V} = 10 \text{ mL(STP)}/\text{min}$.

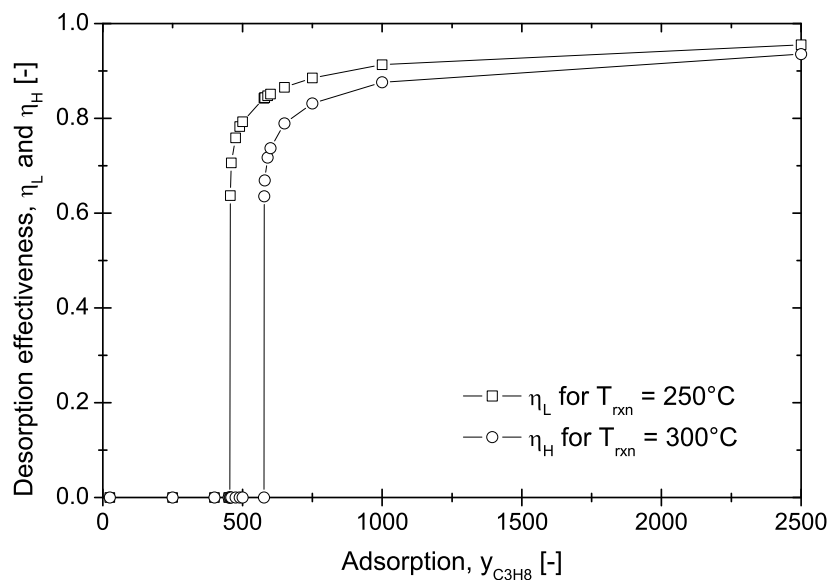


Figure 6.17: Desorption effectiveness as a function of the propane mole fraction to the adsorber. Adsorption at 25 °C, desorption at 60 °C and $\dot{V} = 10 \text{ mL(STP)}/\text{min}$.

The parametric study of the desorption from a preheated, fully saturated adsorber shows that the flow rate has no influence on the desorption characteristics other than the desorption time. At very low flow rates the axial diffusivity would become more important if the tube diameter stays constant and the mathematical model would have to account for this. The adsorptive concentration to the adsorber defines the adsorbate loading. The loading is very important for the effectiveness of desorption and to the possibility of running an autothermal process. A higher loading results in a higher effectiveness of desorption and the possibility of running an autothermal process. This parameter cannot be controlled as it is defined by the upstream processes and the question is rather to find the limiting VOC concentration for the autothermal process.

Autothermal Regime

Finally, the only parameter to control, when using preheating of the desorber to force a concentration of the VOC, is the preheating temperature. The preheating temperature can easily be calculated for a specific loading and desired effectiveness of desorption as shown above. The heat can always be added with an external source. However, the autothermal propane mole fraction limit is more interesting in relation to energy savings. The limit is defined as the propane mole fraction which, upon desorption, provides sufficient thermal energy to preheat the desorber to a temperature, where the concentration of the desorbed propane is adequate to sustain a given combustion temperature (250°C or 300°C for this study). The calculations assume adiabatic conditions and the results are shown graphically in Figure 6.18.

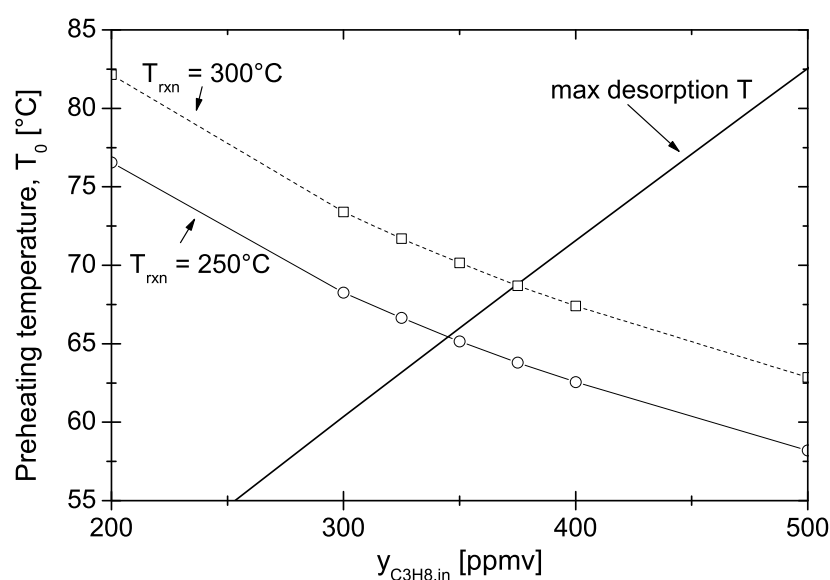


Figure 6.18: Autothermal regime. Maximum adiabatic desorption temperature as a function of the inlet mole fraction to the adsorber ($T_{ads} = 25^{\circ}\text{C}$) compared to the initial, equilibrium mole fraction as a function of preheating temperature.

The figure shows the intersection of two types of lines. The maximum adiabatic temperature attainable as a function of the propane mole fraction fed to the adsorber. This is the

same curve calculated for the overall energy balance in Figure 6.8. The two other lines define the preheating temperature necessary to provide a sufficiently high propane mole fraction in the desorber outlet to sustain the combustion reaction temperature over the catalyst at either 250 °C or 300 °C as a function of the mole fraction fed to the adsorber. It is seen that for a lower feed concentration of propane a higher preheating temperature is needed to sustain the combustion temperature.

The theoretical, autothermal regime is the range of propane mole fractions for which the maximum adiabatic desorber temperature attainable is greater than or equal to the preheating temperature necessary for sustaining the adiabatic combustion temperature. For a combustion temperature of 250 °C the minimum propane mole fraction is ≈ 350 ppmv and for 300 °C a slightly higher mole fraction of 375 ppmv is needed.

The practical propane concentrations will be somewhat higher, since the system was simplified for this theoretical analysis. Adiabatic conditions are difficult to obtain, since heat losses are unavoidable, but do become negligible with a decreasing external specific surface area of the reactor, i.e. for large reactors. The heat capacity of the adsorber walls was not included in the overall energy balance and could increase the average system heat capacity up to a factor of two, depending on material, geometry and wall thickness. Lastly, the maximum desorption temperature calculated from the overall energy balance assumes that all the chemical energy stored in the adsorber is released. However, the intersection of the two energy balance lines in Figure 6.18 defines the mole fraction at which the effectiveness of desorption (as in Figure 6.17) drops to zero. In the near region of this limiting mole fraction the effectiveness factor is therefore low, but rises quickly to above 0.8. In an autothermal regime the maximum attainable temperature rise would be approximately proportional to this effectiveness of desorption. This means that the energy balance for the maximum desorption temperature would shift down and that the minimum mole fraction needed for an autothermal regime would increase.

Based on the simplifications in the desorption model, it is reasonable to expect that the minimum propane mole fraction level for an autothermal process should be at least the double of the theoretically calculated minimum value, i.e. 700 ppmv to sustain a combustion temperature of 250 °C.

The desorption can be undertaken until the bed is fully regenerated. This would require heat addition to the catalytic combustor. A more economical option would be to stop the desorption before it is complete, at the point where the propane mole fraction becomes too low to sustain the adiabatic combustion temperature. The desorber would then have to be cooled before reuse as adsorber and the adsorption should then be done in the reverse direction of the desorption to avoid the emission of VOC from the not completely regenerated adsorber.

6.4 Conclusion

The benefit of coupling adsorption with catalytic combustion for the removal of VOC in low concentration is the possibility of concentrating the VOC by forced desorption. The concentration of the VOC can be necessary in order to combust it without adding further heat from an external source (electrical heating or additional chemical energy in the form of gaseous combustibles). The concentration should be done by thermal swing, allowing

for the use of the thermal energy from the adsorbed VOC. A theoretical treatment of the two-step adsorption-incineration process was undertaken to investigate the feasibility of the coupled system and the conditions for an autothermal process.

It was assumed that the catalytic incinerator was kept at a constant temperature of either 250 °C or 300 °C. The goal of the desorber was to supply the propane with a feasible concentration and temperature. A mathematical model was developed to describe the adiabatic desorption. The hydrodynamics was described by a tanks-in-series model and the gas-solid mass transfer by the linear driving force approach.

Concentrating the propane by heating the fixed-bed with a hot gas proved impossible. The heat capacity of the zeolite/metallic fiber matrix was approximately 3 orders of magnitude higher than the heat capacity of the hot gas. This characteristic ensured an isothermal adsorption, but also resulted in an insufficient rate of heating of the desorber. According to the simulations the propane would be flushed out of the desorber in front of the heat wave, without any concentration of the propane. This behavior is partly due to the large difference of the heat capacities, but also due to the very fast diffusion in the thin zeolite film on the fibers.

A heat carrier with a higher heat capacity could be used to avoid this problem. Steam has a heat capacity approximately 10 times higher than that of hot air. However, this method of heating was not considered due to the increased process complexity and separation problems of water and VOC.

Preheating the desorber with the heat evolved from the catalytic combustion showed interesting potential. The fully saturated adsorber would be heated to a certain temperature at which equilibrium and homogeneous conditions were assumed in the entire desorber. This approach allows a precise control of the outlet mole fraction of propane as a function of the inlet mole fraction to the adsorber and the equilibrium preheating temperature. The effectiveness of the desorption, defined as the fraction of propane desorbed with a mole fraction greater than or equal to the minimum level needed to sustain the minimum adiabatic temperature of the combustion, depends largely on the equilibrium temperature, but also on the initial loading of the desorber. A higher preheating temperature and a higher initial loading leads to a more effective desorption process.

The theoretical limit of an autothermal two-step adsorption-incineration process with propane was found to be a minimum propane mole fraction of ≈ 350 ppmv for a combustion temperature of 250 °C and a slightly higher mole fraction of 375 ppmv for $T_{rxn} = 300$ °C. Close to this limit the effectiveness of the desorption would be relatively low (60-80 %), and the adsorbent cannot be completely regenerated in an autothermal process. In such a process the partly regenerated adsorbent would have to be cooled and used in the adsorption mode with reverse flow compared to the desorption flow.

Chapter 7

Chemical Kinetics by Design of Experiments

In this chapter the development of a new method for estimation of chemical kinetics based on a design of experiments (DOE) called "central composite design" (CCD) will be described. The developed method optimizes spatial placements of the experimental measurement points, decreasing the variance and thereby increasing the model validity for a similar number of data points taken by a traditional one-factor-at-a-time (OFAT) design.

The OFAT design was once regarded as the correct way to conduct experiments and is still widely used (Box *et al.* , 2005). It is called so, since only one factor is varied while the rest of the factors of a "standard setting" are kept constant. It is used because it allows the experimenter to determine individual effects unambiguously as they are changed. However, this OFAT design results in less information from a similar amount of data points chosen by a DOE and no information is gained on interactions between the factors (Gunter, 1993). For a given model (linear, linear with interactions, quadratic), the arrangement of the measurement points can be optimized in order to minimize the variance of the fitted model over the experimental space. The literature gives a series of designs for this purpose, which all have their benefits and drawbacks (Fürbringer, 2005).

Design of experiments has also been used in the field of catalysis for many years. Applications cover, among others, catalytic reactors (Nordin *et al.* , 1995), catalyst formulation and preparation (Dawson & Barnes, 1992; Weckhuysen *et al.* , 2000; Tagliabue *et al.* , 2003), catalytic kinetic modeling (Hunter & Mezaki, 1967; Barsan & Thyron, 2003) and optimization of process variables in catalytic systems (Deeng *et al.* , 2004; Sjoblom *et al.* , 2005).

The kinetic modeling studies by Hunter & Mezaki (1967) and Barsan & Thyron (2003) used two different methods for distinguishing between different reaction mechanisms and reaction networks. Hunter & Mezaki used a method for sequential planning of the experiments (Box & Hill, 1967). Barsan & Thyron used a CCD with extra points in the star design to actually combine an OFAT with a full factorial design. The OFAT part of the design allowed them to visualize the effects of the different factors. However, the choice of replicating the CCD design for three temperatures as opposed to incorporating them into the CCD design as a fourth factor might have led to abundant data. Furthermore, the CCD design was used on a highly nonlinear system, which might lead to non optimal

measurement points.

Both kinetic modeling studies discussed above show methods for the determination of reaction networks. No studies have been found in the literature for the optimization of experimental studies of an irreversible reaction like the total oxidation of propane considered in this work. However, it was thought that a design of experiments can be used to choose the optimal measurement points for a predefined model and thereby optimizing the information retrieved by experimentation.

The chemical kinetics represented by the power rate law (Equation 7.1) is a highly non-linear model, which can be linearized by transforming it by the logarithm. By linearizing the model any design of experiment model can be used to find the optimum measurement points. A factorial design could be used, but tests only the factors at two levels. In order to get a more precise model more data would be needed. Looking towards response surface methodology the Box-Wilson centered composite design, commonly called central composite design, tests each factor at five levels and shows a quite constant variance over the whole experimental space.

7.1 Models and Experimental Design

7.1.1 Design Factors

The kinetic model to be fitted to the data is the power rate law:

$$r = kC_{\text{C}_3\text{H}_8}^n C_{\text{O}_2}^m \quad [\text{mol/g}\cdot\text{s}] \quad (7.1)$$

The data for the reaction rate was obtained from a recycle reactor modeled as a CSTR, for which the performance equation is:

$$r = \frac{F_{\text{C}_3\text{H}_8, \text{in}} X}{m_{\text{cat}}} \quad [\text{mol/g}\cdot\text{s}] \quad (7.2)$$

During the experiments a number of variables can be controlled:

- Total inlet flow rate, F_{in}
- Catalyst mass, m_{cat}
- Temperature, T
- Propane inlet mole fraction, $y_{\text{C}_3\text{H}_8, \text{in}}$
- Oxygen inlet mole fraction, $y_{\text{O}_2, \text{in}}$
- Recycle ratio, R

furthermore the pressure is a parameter with influence on the system:

- Pressure, P

The recycle ratio was kept at a maximum to keep the system in a mixed flow regime. The maximum concentration gradient over the fixed-bed was 1 % and so the system was always in a mixed flow state.

The reactor pressure depends on the atmospheric pressure and the gauge pressure, which is a function of the inlet flow rate. The pressure along with the temperature defines the gas concentration according to the ideal gas law:

$$C = \frac{n}{V} = \frac{P}{RT} \quad (7.3)$$

The gas concentrations for component i over the catalyst is $C \cdot y_i$ (not $C \cdot y_{i,in}$) and cannot be controlled directly.

The experimental variables with effect on the chemical reaction kinetics that must be controlled according to the experimental design are called the **design factors** and were:

- Temperature, T .
- Propane outlet mole fraction, $y_{\text{C}_3\text{H}_8}$.
- Oxygen outlet mole fraction, y_{O_2} .

To achieve the desired gas concentrations over the catalyst the experimental designs were made for a specific conversion ($X = 0.25$), which was then obtained by varying the residence time ($\tau \cong m_{\text{cat}}/F_{\text{in}}$) in terms of the catalyst mass and inlet flow rate employed as well as the inlet mole fractions of propane and oxygen.

The experimental values were varied within the following intervals:

- Temperature, $T \in [250; 400]^\circ\text{C}$.
- Propane outlet mole fraction, $y_{\text{C}_3\text{H}_8} \in [0.0025; 0.0150]$.
- Oxygen outlet mole fraction, $y_{\text{O}_2} \in [0.050; 0.200]$.

7.1.2 Experimental details

The catalyst used for the experiments was the industrial catalyst: CK-302, Haldor Topsøe, Lyngby, DK (Section 3.4.1). The catalyst was crushed and fractionated by sieving into two fractions: $[160; 200]\mu\text{m}$ and $[200; 315]\mu\text{m}$. The catalyst was diluted with inert quartz particles with the same size in a ratio (catalyst:quartz) of minimum 1:2. The fixed-bed height varied between 0.5 and 2.4 cm. The smaller particles were used at temperatures above 325°C to avoid internal mass transfer effects, which were not observed. No fast catalyst deactivation was observed at 400°C up to 3 hours on stream.

At least three measurements were taken at steady state conditions. This was done in order to verify that steady state had been attained, but served also as a quantitative measure of the measurement error/system stability. The experimental designs were verified with both one point (the last measurement point) and with the three steady state points in order to see the effect on the model predictions.

7.1.3 One-Factor-at-a-Time

The OFAT design is often used, since it is simple and allows the easy use of graphical methods for finding the activation energy (Arrhenius plot) and reaction orders.

The OFAT design has a "star shape" with the measurement points equidistantly distributed between their extremes as represented in Figure 7.1. The actual design used for the experiments is shown in Table 7.1. Note that the factors are simply varied linearly in their real space as is done in most research.

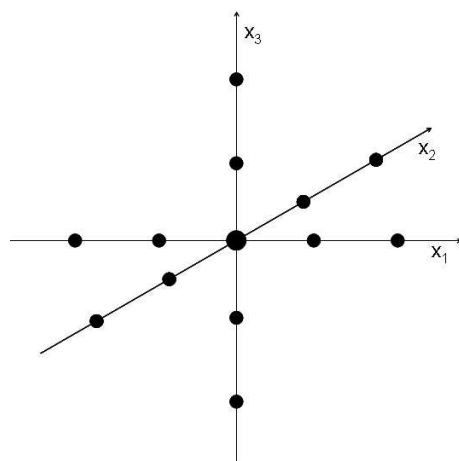


Figure 7.1: One-factor-at-a-time design.

Table 7.1: Conventional OFAT experimental design.

Exp. no.	Coded variables			Real variables		
	x_1	x_2	x_3	T [°C]	$y_{\text{C}_3\text{H}_8, \text{in}}$ [%]	$y_{\text{O}_2, \text{in}}$ [%]
1	-1	0	0	250.0	0.875	12.50
2	-0.5	0	0	287.5	0.875	12.50
3	0	0	0	325.0	0.875	12.50
4	0.5	0	0	362.5	0.875	12.50
5	1	0	0	400.0	0.875	12.50
6	0	-1	0	325.0	0.250	12.50
7	0	-0.5	0	325.0	0.563	12.50
8	0	0	0	325.0	0.875	12.50
9	0	0.5	0	325.0	1.188	12.50
10	0	1	0	325.0	1.500	12.50
11	0	0	-1	325.0	0.875	5.00
12	0	0	-0.5	325.0	0.875	8.75
13	0	0	0	325.0	0.875	12.50
14	0	0	0.5	325.0	0.875	16.25
15	0	0	1	325.0	0.875	20.00

These experiments were used for comparison with the data obtained from the central composite design.

7.1.4 Central Composite Design

The Box-Wilson central composite design (CCD) is obtained by merging a star design with a factorial design as shown in Figure 7.2.

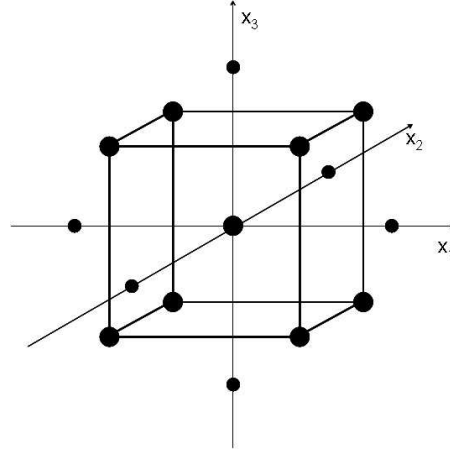


Figure 7.2: Central composite design.

The matrix of the experiments of the CCD thus takes the form (in coded variables) as shown in Table 7.2. The factorial part of the matrix, N_{fact} , can be either full or fractional, the star runs, N_{α} , are symmetrical points on the axes and a number of center points, N_0 , must be chosen.

Table 7.2: Central composite design matrix.

	Factors			
Number	x_1	x_2	\cdots	x_N
N_{fact}	± 1	± 1	\cdots	± 1
N_{α}	$-\alpha$	0	\cdots	0
	α	0	\cdots	0
	0	$-\alpha$	\cdots	0
	0	α	\cdots	0
	0	0	\cdots	0
	0	0	\cdots	0
	0	0	\cdots	$-\alpha$
	0	0	\cdots	α
N_0	0	0	\cdots	0
	\cdots	\cdots	\cdots	\cdots
	0	0	\cdots	0

To keep the property of isovariance per rotation (the variance of the model coefficients is independent from the axis orientation) and the orthogonality (the effects are estimated independently) the radius α of the star matrix and the number of runs at the center N_0 must be chosen according to the data of Table 7.3.

Table 7.3: Optimal relation between the number of factors N , the number of factorial experiments N_{fact} , the number of star points N_α , the radius α and the number of runs at the center N_0 . Adapted from (Feneuille *et al.*, 1983).

N		2	3	4	5
Factorial design		2^2	2^3	2^4	2^5
N_{fact}		4	8	16	32
N_α		4	6	8	10
α	$N_0 = 1$	1.0	1.215	1.414	1.596
	$N_0 = 2$	1.078	1.287	1.483	1.662
	$N_0 = 3$	1.147	1.353	1.547	1.724
	$N_0 = 4$	1.210	1.414	1.607	1.784

The kinetic model was linearized as shown in the following. Combining the two relations (Equations 7.1 and 7.2) describing the reactor system and the kinetics model and using a reference temperature T' yields:

$$\frac{F_{in} y_{C_3H_8, in} X}{m_{cat}} = k'_0 \exp \left[-\frac{E_a}{R} \left(\frac{1}{T} - \frac{1}{T'} \right) \right] (C y_{C_3H_8})^n (C y_{O_2})^m \quad [\text{mol/g.s}] \quad (7.4)$$

This relation is transformed by the conversion, X (the model response), and by the ideal gas law to only contain the input variables ($T, y_{C_3H_8, in}$ and $y_{O_2, in}$) and the measured parameter of the pressure, P :

$$\begin{aligned} & \frac{F_{in} y_{C_3H_8, in} X}{m_{cat}} \\ &= k'_0 \exp \left[-\frac{E_a}{R} \left(\frac{1}{T} - \frac{1}{T'} \right) \right] \left(\frac{P}{RT} y_{C_3H_8, in} (1 - X) \right)^n \left(\frac{P}{RT} y_{O_2, in} - 5X y_{C_3H_8, in} \right)^m \end{aligned} \quad (7.5)$$

For simplicity, the response and variable names are transformed into the nomenclature of design of experiments (see Section 2.6.1) given in Table 7.4.

Table 7.4: Variable names in the DOE design and the chemical reaction kinetics model.

	DOE coded	DOE natural	Physico-chemical
Response	Y	Y	X
	x_1	u_1	T
Factors	x_2	u_2	$y_{C_3H_8, in}$
	x_3	u_3	$y_{O_2, in}$

Equation 7.5 then becomes:

$$\frac{F_{in} u_2 X}{m_{cat}} = k'_0 \exp \left[-\frac{E_a}{R} \left(\frac{1}{u_1} - \frac{1}{T'} \right) \right] \left(\frac{P}{R u_1} u_2 (1 - X) \right)^n \left(\frac{P}{R u_1} u_3 - 5X u_2 \right)^m \quad (7.6)$$

This expression is linearized by taking the logarithm:

$$\begin{aligned} & \ln \left(\frac{F_{in} u_2 X}{m_{cat}} \right) \\ &= \ln k'_0 - \frac{E_a}{R} \left(\frac{1}{u_1} - \frac{1}{T'} \right) + n \ln \left(\frac{P}{R u_1} u_2 (1 - X) \right) + m \ln \left(\frac{P}{R u_1} u_3 - 5X u_2 \right) \end{aligned} \quad (7.7)$$

Which is identical to the linear relationship

$$z = a_0 + a_1x_1 + a_2x_2 + a_3x_3 \quad (7.8)$$

where

$$z = \ln \left(\frac{F_{in}u_2X}{m_{cat}} \right) \quad (7.9)$$

$$a_0 = \ln k'_0 \quad (7.10)$$

$$a_1 = -\frac{E_a}{R} \quad (7.11)$$

$$a_2 = n \quad (7.12)$$

$$a_3 = m \quad (7.13)$$

and the coded variables \mathbf{x} (vary linearly (between 1 and -1 in the factorial design)) equal:

$$x_1 = \frac{1}{u_1} - \frac{1}{T'} \quad (7.14)$$

$$x_2 = \ln \left(\frac{P}{Ru_1} u_2 (1 - X) \right) \quad (7.15)$$

$$x_3 = \ln \left(\frac{P}{Ru_1} u_3 - 5Xu_2 \right) \quad (7.16)$$

In the current study a design with one center point was chosen resulting in the experimental design presented in Table 7.5.

Table 7.5: Composite experimental design with one center point (DOE composite, $N_0 = 1$).

Design parts	Exp. no.	Coded variables			Real variables		
		x_1	x_2	x_3	T [°C]	$y_{C_3H_8,in}$ [%]	$y_{O_2,in}$ [%]
Factorial	1	-1	-1	-1	260.5	0.27	4.72
	2	-1	-1	1	260.5	0.27	15.58
	3	-1	1	-1	260.5	1.16	5.84
	4	-1	1	1	260.5	1.16	16.70
	5	1	-1	-1	383.3	0.33	5.81
	6	1	-1	1	383.3	0.33	19.17
	7	1	1	-1	383.3	1.43	7.18
	8	1	1	1	383.3	1.43	20.54
Star	9	-1.215	0	0	250.0	0.54	8.70
	10	1.215	0	0	400.0	0.70	11.19
	11	0	-1.215	0	315.6	0.25	9.34
	12	0	1.215	0	315.6	1.50	10.90
	13	0	0	-1.215	315.6	0.61	5.00
	14	0	0	1.215	315.6	0.61	20.00
Center	15	0	0	0	315.6	0.61	9.79

7.1.5 Full Factorial Design

As mentioned above a part of the CCD is a factorial design as shown in Figure 7.3. The 2^3 full factorial part of the design is the first eight experiments of the design in Table 7.5.

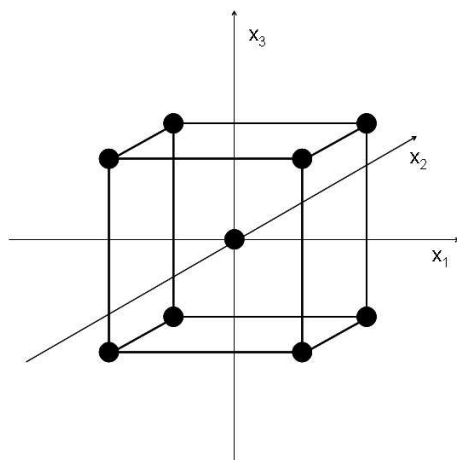


Figure 7.3: Full 2^3 factorial design with center point.

7.2 Results and Discussion

The comparison of the different designs has been done by four different parameters:

1. **Approximate standard error of model**

The parameter estimation program (see Section 2.5.4 and Appendix D) estimates the approximate standard error of the output variable. The smaller the standard error, the better.

2. **ssq_{min}**

The parameter estimation program calculates the minimal sum of squares of the residuals. The smaller the ssq for a model with the same number of experiments, the better. This information is similar to the information of the model standard error, but can only be used to compare the fits to the same number of data since every data point is accompanied with error and an increase in the ssq_{min} .

3. **2σ -levels**

The parameter estimation program calculates the 2σ -levels as a measure for the variance of the estimated parameters. The smaller the variance, the better.

4. **ANOVA: F -test and probability**

An ANOVA calculates the probability of each factor to be purely noise. The smaller the probability of being noise, the better.

OFAT and Central Composite Designs

One of the main challenges in the current study of experimental design was to achieve gas partial concentrations of propane and oxygen as close to the design values as possible. This

was mainly due to the change of reactor pressure with the change of flow rates to obtain the design value of 25 % conversion. The measurement points' distribution according to their original designs are shown in Figure 7.4. The figures show that the measurements were taken in very close proximity of the design values and that it was indeed possible to follow the design.

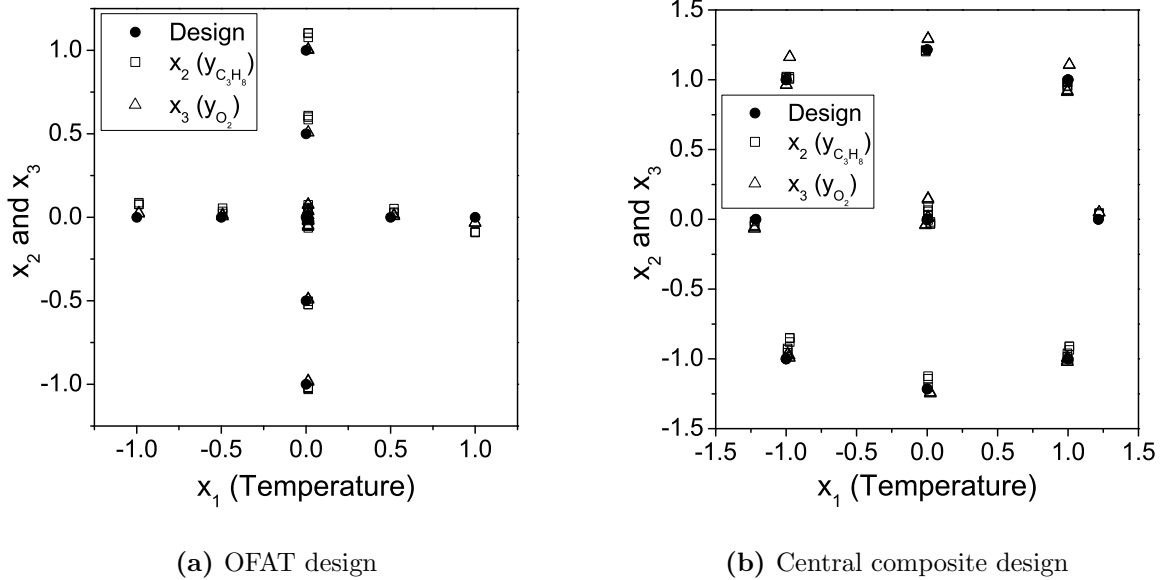


Figure 7.4: Design and measurement points in coded variables.

The experimental results of the conversion as a function of temperature, inlet concentrations of propane and oxygen, as well as the reactor residence time, were varied according to the experimental designs described above. The power rate law was fitted with a four parameter nonlinear regression model to the obtained results from each design. These results are shown in Table 7.6 for the OFAT and CCD experimental designs. The model was also fitted to the total 90 data points used for the four designs, the results of which are shown in Table 7.7.

When comparing the results for the OFAT and CCD designs it is quickly noted that there is a very large difference in the quality of the fit of the power rate law model to the data of the two designs. Focusing first at the one point experiments it is seen, that the model fits the CCD data with a ssq_{min} less than one quarter of the OFAT data. The variance on the estimated parameters represented by the 2σ -confidence levels, show how well the parameters have been estimated. The values of the four parameters are very similar, but in the case of the OFAT design the variance is three to four times greater. Finally, the estimated model standard error predicts half the model error in the case of CCD.

Table 7.6: Results of 4 parameter nonlinear regression of power rate law to OFAT and CCD data for kinetics.

	Parameter	OFAT		DOE Composite, $N_0 = 1$	
		Par. value [*]	Rel. err. ^b	Par. value [*]	Rel. err. ^b
1 point	Std. err. [‡]	0.101		0.047	
	ssq_{min} [*]	0.113		0.024	
	k' [†]	$(8.9 \pm 2.6) \cdot 10^{-7}$	29 %	$(8.2 \pm 0.8) \cdot 10^{-7}$	9.6 %
	E_a [‡]	85.0 ± 5.1	6.0 %	87.1 ± 1.4	1.6 %
	n	0.53 ± 0.14	27 %	0.49 ± 0.04	8.1 %
	m	0.28 ± 0.16	58 %	0.23 ± 0.04	20 %
	Data points	15		15	
3 points	Std. err. [‡]	0.096		0.058	
	ssq_{min} [*]	0.376		0.138	
	k' [†]	$(8.6 \pm 1.4) \cdot 10^{-7}$	16 %	$(8.0 \pm 0.5) \cdot 10^{-7}$	6.8 %
	E_a [‡]	85.9 ± 2.8	3.2 %	87.4 ± 0.9	1.1 %
	n	0.49 ± 0.08	16 %	0.48 ± 0.03	6.0 %
	m	0.24 ± 0.09	38 %	0.24 ± 0.03	13 %
	Data points	45		45	

^{*} Parameter values with (\pm) 2σ -confidence levels

^b Relative error: $(2\sigma\text{-confidence level})/\text{parameter value} \cdot 100\%$

[‡] Approximate standard error on the output variable $(\ln r)$

^{*} Minimal sum of squares of residuals

[†] Arrhenius frequency factor at reference temperature = 325 °C (see Section 2.5.4). Unit: $(\text{mol}/(\text{g}\cdot\text{s})) (\text{m}^3/\text{mol})^{(n+m)}$

[‡] Unit: kJ/mol

When looking at the results for three repetitions of the measurement points the trends between the two designs are similar to those discussed for one measurement at each design point. Repeating the measurements three times adds more certainty to the model as it gives a better measure of the variance related to the experiments. This shows in the form of the relatively smaller 2σ -confidence levels for both designs. Repeating the measurement three times was easy in this experimental setup and did not cost much extra (time or money). In that case it is best to use all data available. However, in a different case where each experimental point has an important value the measurements cannot all be repeated. In this case, model validity can be added by repeating the center point only (see Table 7.3).

When fitting the power rate law model to the total amount of data produced by the two designs above we end up with a model fit to the data, which falls somewhere between the two results of the individual designs. This is shown in Table 7.7. The results are very similar to those of the central composite design with three measurement points. Adding the results from the OFAT experiment adds results at three more temperatures and different gas concentrations. However, it does not change the result to any better fit, since most data are taken at similar conditions to those of the CCD (center and star points) and since the OFAT data showed more variance. If starting with a central composite design and needing additional information this illustrates the importance of the design of experiments choosing the location of the future data points. To simply mix in the new data points according to the OFAT star design does not produce any more significant information.

Table 7.7: Results of 4 parameter nonlinear regression of power rate law to all results used for the kinetics of CK-302.

Parameter	Par. value [*]	Rel. err. ^b
Std. err. [#]	0.082	
ssq_{min} [*]	0.577	
k' [†]	$(8.46 \pm 0.64) \cdot 10^{-7}$	7.5 %
E_a [‡]	87.2 ± 1.2	1.3 %
n	0.49 ± 0.03	6.7 %
m	0.25 ± 0.04	15 %
Data points	90	

^{*} Parameter values with $(\pm) 2\sigma$ -confidence levels^b Relative error: $(2\sigma\text{-confidence level})/\text{parameter value} \cdot 100\%$ [#] Approximate standard error on the output variable $(\ln r)$ ^{*} Minimal sum of squares of residuals[†] Arrhenius frequency factor at reference temperature = 325 °C
(see section 2.5.4). Unit: $(\text{mol}/(\text{g}\cdot\text{s})) (\text{m}^3/\text{mol})^{(n+m)}$ [‡] Unit: kJ/mol

The fourth way of comparing the models is via the F -test. When doing an analysis of variance (ANOVA) the probability of the different factors to be purely noise is calculated via the F -test. The criteria for determining whether the effects of the factors are significant depends on the application. The results of the ANOVA on the power rate law model in the form of Equation 7.8 are given in Table 7.8 for the CCD with one point. The model only predicts linear contributions, but the ANOVA was first used to check for eventual linear interactions and quadratic influences. As seen in the table the probabilities for any of these effects can be excluded as they cannot be distinguished from noise (minimum 61 % probability of being noise).

Table 7.8: ANOVA of full model with linear interactions and second order contributions for the one point CCD experiment.

	Effects	SS	DF	MS	F	P
a_0	-15.1718	3432.57	1	$3.4 \cdot 10^3$	$8 \cdot 10^5$	$3.4 \cdot 10^{-14}$
a_1	1.8371	36.49	1	36	$8.5 \cdot 10^3$	$2.9 \cdot 10^{-9}$
a_2	0.3589	1.26	1	1.3	$2.9 \cdot 10^2$	$1.3 \cdot 10^{-5}$
a_3	0.1408	0.23	1	0.23	54	0.00075
a_{12}	0.0065	0.00	1	0.00025	0.057	0.82
a_{13}	-0.0020	0.00	1	$7 \cdot 10^{-5}$	0.016	0.90
a_{23}	-0.0095	0.00	1	0.00092	0.21	0.66
a_{11}	0.0022	0.00	1	$7.6 \cdot 10^{-6}$	0.0018	0.97
a_{22}	0.0108	0.00	1	0.00037	0.086	0.78
a_{33}	0.0161	0.00	1	0.0013	0.3	0.61
Residual		0.02	5	0.0043		

The non-significant contributions can thus be discarded, the ANOVA redone and the results for the significant factors shown in Table 7.9 show that the model can be verified without question. The values of the effects do not give the sought values directly due

to the variable transformations of Section 7.1.4. However, through retransformation the exact same values of the four model parameters are found as by the nonlinear regression shown in Table 7.6 for the one point CCD.

Table 7.9: Final ANOVA of linear model for the one point CCD experiment.

	Effects	SS	DF	MS	F	P
a_0	-15.1503	3432.57	1	$3.4 \cdot 10^3$	$1.5 \cdot 10^6$	0
a_1	1.8373	36.49	1	36	$1.6 \cdot 10^4$	0
a_2	0.3588	1.26	1	1.3	$5.7 \cdot 10^2$	$8.2 \cdot 10^{-11}$
a_3	0.1416	0.23	1	0.23	$1 \cdot 10^2$	$6.1 \cdot 10^{-7}$
Residual		0.02	11	0.0022		

The ANOVA of the three point CCD shown in Table 7.10 shows with even more certainty the validity of the model, which is coherent with the lowest relative 2σ -levels found for this experimental design in Table 7.7.

Table 7.10: Final ANOVA of linear model for the three point CCD experiment.

	Effects	SS	DF	MS	F	P
a_0	-15.1498	10297.42	1	$1 \cdot 10^4$	$3.1 \cdot 10^6$	0
a_1	1.8435	110.13	1	$1.1 \cdot 10^2$	$3.3 \cdot 10^4$	0
a_2	0.3506	3.62	1	3.6	$1.1 \cdot 10^3$	0
a_3	0.1461	0.74	1	0.74	$2.2 \cdot 10^2$	0
Residual		0.14	41	0.0034		

The ANOVA of the model fit to the OFAT design shown in Table 7.11 shows the worst fit of the two experimental designs. The first three factors clearly pass the test, but a_3 which represents the reaction order in oxygen has a 5% probability of being noise. For many engineering applications this would just be satisfactory. Nevertheless, it shows that the noise in the OFAT design has much more influence on the results than in the central composite design.

Table 7.11: Final ANOVA of linear model for the one point OFAT experiment.

	Effects	SS	DF	MS	F	P
a_0	-14.6670	3211.93	1	$3.2 \cdot 10^3$	$1.9 \cdot 10^5$	0
a_1	2.1339	11.04	1	11	$6.4 \cdot 10^2$	$4.4 \cdot 10^{-11}$
a_2	0.3949	0.42	1	0.42	24	0.00046
a_3	0.1817	0.08	1	0.081	4.7	0.053
Residual		0.19	11	0.017		

The parity plots shown in Figure 7.5 show that the fitted power rate law models describe the chemical kinetics well. Both parity plots show all 45 measurement points and it is seen that most data points fall within the $\pm 10\%$ of the model values. Again, it is seen that the data obtained from the CCD fit the model better. The parity plots also give a

hint as to why the OFAT is not as effective in giving a good model fit. Most data points fall in a relatively narrow range of reaction rates, since only the temperature change will result in large reaction rate changes. The noise on the data thus becomes difficult to differentiate from the real effects of the parameters. In the parity plots (c) and (d) for the central composite design the data is much better spread over the entire range of reaction rates.

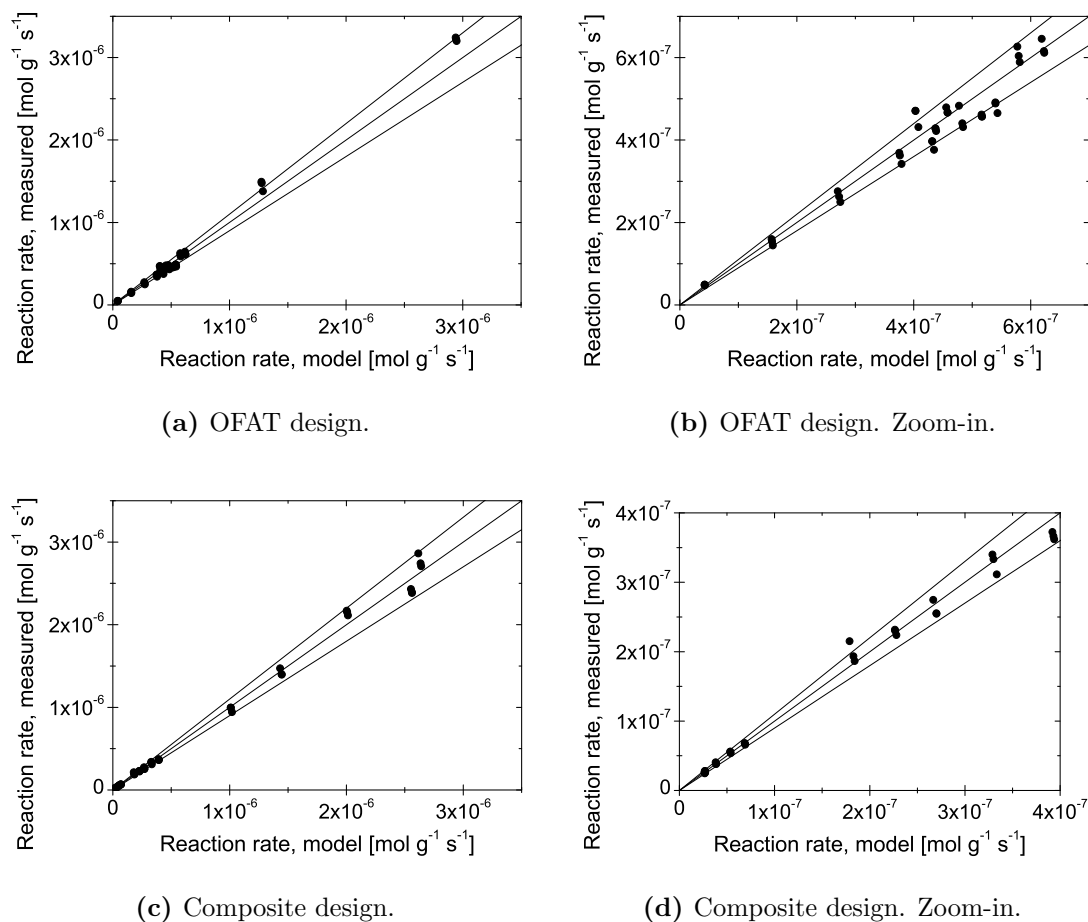


Figure 7.5: Parity plots of the power rate law model for the two different experimental designs: OFAT and CCD. The three lines are giving *parity* and the $\pm 10\%$ of the model values. Plots on the right hand side are zoom-ins to the left hand plots.

It is thus very clear that the central composite design of experiments produces much better results than the OFAT design in terms of the model fitting due to minimization of the effects of naturally occurring noise.

Full Factorial Design

Since the central composite design is constructed of a full factorial and a star design it could be interesting to see if for example the full factorial design alone would be capable of predicting satisfactorily the parameters of the power rate law. The results of the nonlinear regression of the model to the data of the full factorial design with and without the center point is shown in Table 7.12.

Table 7.12: Results of 4 parameter nonlinear regression of power rate law to factorial design data for kinetics.

	Parameter	Factorial		Factorial, $N_0=1$	
		Par. value [*]	Rel. err. ^b	Par. value [*]	Rel. err. ^b
1 point	Std. err. [‡]	0.023		0.033	
	ssq_{min} [*]	0.0020		0.0053	
	k' [†]	$(8.8 \pm 0.5) \cdot 10^{-7}$	5.5 %	$(8.8 \pm 0.7) \cdot 10^{-7}$	7.8 %
	E_a [‡]	87.9 ± 0.8	0.9 %	87.9 ± 1.1	1.3 %
	n	0.52 ± 0.02	4.4 %	0.52 ± 0.03	6.0 %
	m	0.23 ± 0.03	11 %	0.23 ± 0.04	16 %
	Data points	8		9	
3 points	Std. err. [‡]	0.042		0.043	
	ssq_{min} [*]	0.035		0.043	
	k' [†]	$(8.7 \pm 0.5) \cdot 10^{-7}$	5.8 %	$(8.7 \pm 0.5) \cdot 10^{-7}$	6.0 %
	E_a [‡]	88.0 ± 0.8	0.9 %	88.0 ± 0.8	1.0 %
	n	0.51 ± 0.02	4.7 %	0.51 ± 0.02	4.9 %
	m	0.24 ± 0.03	11 %	0.24 ± 0.03	12 %
	Data points	24		27	

^{*} Parameter values with $(\pm) 2\sigma$ -confidence levels

^b Relative error: $(2\sigma\text{-confidence level})/\text{parameter value} \cdot 100\%$

[‡] Approximate standard error on the output variable $(\ln r)$

^{*} Minimal sum of squares of residuals

[†] Arrhenius frequency factor at reference temperature = 325 °C (see section 2.5.4). Unit: $(\text{mol}/(\text{g}\cdot\text{s})) (\text{m}^3/\text{mol})^{(n+m)}$

[‡] Unit: kJ/mol

The results of the four different cases are very similar. Adding the center point hardly changes the results, which shows that the points of the factorial design were already well chosen. However, as previously discussed (Section 5.2.5) it is always wise to use minimum three points when predicting linear relationships. These four factorial designs give essentially the same results as found with the best fit to the CCD. It is important to note, that with only 8 measurements (1 point full factorial design) essentially the same result is obtained for all four parameters as with the 45 measurements according to the 3 point CCD. However, the variable space is larger and the influence of occasional erroneous data is not as important in the larger experimental design.

7.3 Conclusion

The chemical kinetics for the total oxidation of propane were modeled by the power rate law. A classical one-factor-at-a-time (OFAT) and central composite design (CCD) of experiments were used to collect the necessary data. It was clearly shown that the best experimental design for determining the parameters of the power rate law was the CCD. With the same number of data the CCD yields a model fit with a sum of squares of residuals, ssq_{min} , three to four times smaller than with the OFAT design. Furthermore, the variance, 2σ -level, on the four parameters is also three to four times smaller for the CCD.

The main benefits of using the OFAT design is its simplicity and the possibility of graph-

ically determining the parameters. By plotting the data from an OFAT design it is also possible to visually check for changes in the variables over the variable domain, which could take place in case of a change in reaction mechanism or mass transfer limitations. However, if the design points of the CCD are precisely chosen it is also possible to make linear plots at the axes (3 points) and at the factorial design levels ± 1 (2 points) to do the same check as with the OFAT, but the model parameters have to be determined either by a multiple parameter regression or by the ANOVA as shown in this study.

The message is to start with the star design of the CCD to get a feeling for the effects of the variables and add a full factorial design to get the spatially well dispersed data points minimizing the variance of the model.

Improvements could be achieved in getting experimental values even closer to the design values. In the current system this could be realized by adding a valve at the outlet to control the reactor pressure. A constant reactor pressure for all experiments could also be realized with a constant flow rate, varying the residence time through the catalyst mass. This would be very time consuming in the current experimental setup, but could be an option for a smaller, easier to handle and faster responding system. For a liquid continuous system it should also be possible to change the residence time without great effect on the reactant concentrations and thus realize measurement points precisely at the design values.

Chapter 8

Conclusion

Novel, structured types of adsorbent and catalysts have been developed for the removal of volatile organic compounds (VOCs) in low concentration from effluent gasses. Both the adsorbent and the catalysts were supported on sintered metal fibers (SMF), which have several engineering advantages over conventional, pelletized supports:

- Low pressure drop, due to the high porosity of the SMF.
- High thermal conductivity, diminishing temperature gradients in the fixed-bed.
- Very high external, geometric surface area, due to the small fiber diameter.

The novel, structured adsorbent consisted of a thin, homogeneous, crystalline film of MFI-type zeolite (silicalite-1 and ZSM-5) grown in a well controlled manner by the seed-film method. The support was first seeded with nano-sized silicalite-1 crystals, which serves to nucleate the film growth on the metallic surface during a hydrothermal synthesis at 125 °C. After 24 h the synthesis results in a 3 μm film and 10 wt.% silicalite-1 on the SMF with a specific surface area of 30 m^2/g . The Si/Al-ratio was varied between ∞ and ~ 200 , by varying the aluminate concentration in the synthesis solution. The adsorption equilibrium of propane was described well by the Langmuir isotherm, with a saturation capacity of $1.83 \pm 0.06 \text{ mol/kg}$ and a heat of adsorption of $\Delta H_{ads}^0 = -43.1 \text{ kJ/mol}$.

The thin zeolite film leads to very low resistance to internal mass transfer during the adsorption and desorption, which optimizes the use of the adsorber fixed-bed and diminishes the problems of tailing during the desorption. The mass transfer during the adsorption was characterized by a linear driving force (LDF) mass transfer coefficient, which was found to have an activation energy of $E_{LDF} = 67 \pm 10 \text{ kJ/mol}$ and to be proportional to $1/L^2$. These results were obtained from isothermal breakthrough curves measured as a function of temperature and film thickness. A mathematical model, based on a tanks-in-series model with a LDF mass transfer description, successfully described the breakthrough behavior. Increasing the film thickness leads to lower mass transfer rates and a higher adsorption capacity, but also results in a higher pressure drop. The pressure drop was measured and the permeability was calculated in the laminar flow regime. Compared to a randomly packed fixed-bed of spheres, the equivalent diameter for a constant volumetric flow rate and cross sectional area was $d_p = 180 \mu\text{m}$, for a fiber diameter of $d_f = 26 \mu\text{m}$ at 10 wt.% zeolite loading. For a similar pressure drop the fibrous SMF thus allows the

utilization of a media with a characteristic length one order of magnitude smaller than with a conventional support.

The structured catalysts were all using SMF as support. Different metal oxides were tested as active phase and cobalt oxide was found to be the most active (compared to PtOx and mixed manganese/copper oxides). The active phase for the propane oxidation was deposited on the support in different manners. The metal oxides were synthesized onto the support directly on the metal fiber surface, by impregnation onto a 10 wt.% MFI film on SMF or as a finely, powdered catalyst deposited as a film on the fibers. The deposition of a finely powdered catalyst was a new method of loading the SMF with an active phase, which was developed in this study and showed a good adherence with a maximum weight loss of 7 wt.%.

From a series of screening experiments the most active catalysts were found to be those with Co_3O_4 impregnated directly onto the fibers. The influence of the base material (stainless steel (SS), FeCrAlloy and inconel) was investigated through kinetic experiments and surface analysis by XPS.

The stainless steel and FeCrAlloy supports had similar activities, surpassing that of the inconel supported catalyst, which probably can be attributed to a Co_3O_4 surface enriched with iron from the support. The chemical kinetics were determined from a novel and efficient experimental design, which increases the precision of the kinetic parameters by a factor four compared to the same number of experiments conducted by a conventional one-factor-at-a-time design. The catalysts were tested up to 350 °C. Mass transfer limitations were absent and the kinetics was described best with the power rate law in comparison to the Mars-van Krevelen model.

Between the 1.1 wt.% Co_3O_4 /SMF_{SS} and 1.5 wt.% Co_3O_4 /SMF_{FeCrAlloy} catalyst the Fe-CrAlloy supported catalyst had the highest normalized activity at low temperature (< 310 °C), low propane mole fraction (0.13 %) and high oxygen concentration (16.7 %). The apparent activation energy for this catalyst was found to be 87.5 ± 2.6 kJ/mol, with reaction orders in propane of 0.38 ± 0.04 and in oxygen of 0.30 ± 0.08 . The very active catalysts (Co_3O_4 /SMF) deactivated quickly, but with a high deactivation order. According to the concentration independent deactivation model the activity should level out at about 40 % of the initial activity already after 3000 hours on stream. It was shown, that by adapting the pretreatment method (increasing calcination time and temperature) the catalysts can be stabilized.

When VOCs occur in concentrations too low to sustain the combustion temperature over the catalyst the, so-called "two-step adsorption-incineration" method can be used to remove the VOC. In a first step the VOC is removed from the gas stream by adsorption and in a second step the VOC is desorbed with a higher concentration so that it can be oxidized over the catalyst and sustain the oxidation temperature. The coupling of the adsorption with the desorption and catalytic combustion was investigated theoretically with a model for the adiabatic behavior of the desorber. Purging the desorber with a hot gas cannot result in the concentration of the VOC, due to the high heat capacity of the fixed-bed and the efficient heat transfer. A different approach consisting in preheating the desorber, thereby changing the adsorption equilibrium in favor of high gas concentrations, was investigated. For this method, the objective was to keep a steady propane concentration in the desorber outlet, appropriate for sustaining a minimum temperature needed in the adiabatic combustion reactor. The minimum theoretical propane mole fraction for an

autothermal process was found to be 350 ppmv to sustain a catalytic incinerator at 250 °C. Furthermore, the model showed that the very low internal diffusion resistance of the film does not lead to any adverse effects such as tailing and low efficiency of desorption.

8.1 Outlook

The oxidation catalyst based on Co_3O_4 supported directly on oxidized SMF, showed good potential in comparison to the industrial reference catalyst (copper and manganese oxide supported on alumina). The catalyst is very active, simple to prepare and can withstand deactivation due to hot-spot formation. However, an optimization of the SMF material, metal loading, calcination time and temperature would be needed in order to address the deactivation issue of the catalyst synthesized in the current study and to find the most active combination for this application. This optimization could be done advantageously with a design of experiments.

The good heat conductivity of the SMF, the large geometric surface area and the low pressure drop makes SMF based catalysts and adsorbents ideal candidates for use in microreactors. The SSA_v of the reactor packing is on the order of $50,000 \text{ m}^2/\text{m}^3$ compared to monoliths with approximately $2,000 \text{ m}^2/\text{m}^3$. Microreactors are often made from a stack of metal plates with etched or machined microchannels. The microchannels often have irregularities, especially after the introduction of the catalytically active phase, which can result in flow maldistributions between the channels and a nonuniform conversion. Further advantages from using SMF as opposed to microchannel plates include: lower cost of production and ease of scale-up.

Another interesting application is the possibility of making a two- or multi-layered type of catalyst. The "seed-film" method is very versatile and MFI-zeolite films have been grown on metals, silicon, silica and alumina among others (Hedlund *et al.*, 1999; Sterte *et al.*, 2001; Hedlund *et al.*, 2004). It is possible to grow different layers of ZSM-5 in several steps or different layers, e.g. alumina covered with a ZSM-5 layer. In this fashion, an egg-shell type catalyst could be synthesized, where different reactant diffusivities through the ZSM-5 could be exploited. An example is the selective catalytic reduction (SCR) of NO_x with hydrocarbons e.g. propene. The role of the outer layer of ZSM-5 would be to permeate the NO and oxygen selectively, while adsorbing the propene. The bottom layer should then be a catalyst for the oxidation of NO to NO_2 . This can be done e.g. by noble metals (Pt or Au) on alumina or in a ZSM-5 ion-exchanged with transition metals such as Cu, Co, Mn or Fe. The reduction of NO_2 with the adsorbed propene would take place during the diffusion of NO_2 through the outer layer. This principle has been proven to increase the activity of the SCR DeNOx process as compared to a single layer catalyst (Kang *et al.*, 2006).

Appendix A

Temporal Point Model

The fixed-bed reactor system was modeled based on a previously proposed tanks-in-series model for the adsorption of heavy metals in a fluidized bed (Yang & Renken, 2000). The simplified model in this study uses the tanks-in-series model to describe the hydrodynamics and a lumped mass transfer coefficient for the gas-film diffusion to the solid phase. It is assumed, that the adsorption on the solid phase is instantaneous and follows the Langmuir isotherm. The Langmuir parameters used in the simulations for the adsorption equilibrium, were determined experimentally by the transient response method as described in Section 4.2. The material balances in the following are shown for the j^{th} tank. The mass balance for the bulk gas phase for the adsorptive (propane), mixed flow is:

$$\frac{dC_j^b}{dt} = N \frac{C_{j-1}^b - C_j^b}{\tau} - \frac{a'k_{lump}}{\varepsilon} (C_j^b - C_j^s) \quad (\text{A.1})$$

Where k_{lump} is the overall gas-film mass transfer coefficient and N is the number of tanks-in-series. The concentration of adsorptive at the surface of the fibers was calculated from the mass balance at the gas-solid interphase:

$$\varepsilon \frac{dC_j^s}{dt} = a'k_{lump} (C_j^b - C_j^s) - (1 - \varepsilon) \rho \frac{dq_j}{dt} \quad (\text{A.2})$$

The accumulation in the solid phase is related to the interphase concentration and derived from the Langmuir isotherm:

$$\frac{dq_j}{dt} = k_f \left(C_j^s (q_m - q_j) - \frac{1}{K} q_j \right) \quad (\text{A.3})$$

The initial and boundary conditions are:

$$C_j^b = 0, C_j^s = 0, q_j = 0 \quad \text{at} \quad t = 0 \quad (\text{A.4})$$

$$C_{j-1}^b = C_0 \quad \text{for tank } j = 1, t > 0 \quad (\text{A.5})$$

The following dimensionless variables are introduced:

$$f = \frac{C}{C_0} \quad (\text{A.6})$$

$$\xi = \frac{q}{q_0} \quad (\text{A.7})$$

$$\theta = \frac{t}{\tau_m} \quad (\text{A.8})$$

$$\tau_m = \frac{mq_0}{QC_0} \quad (\text{A.9})$$

τ_m is a residence time based on the dynamic capacity of the adsorbent in equilibrium with the gas concentration C_0 . The system in dimensionless variables is as follows:

$$\frac{df_j^b}{d\theta} = \frac{N\tau_m}{\tau}(f_{j-1}^b - f_j^b) - \frac{a'k_{lump}\tau_m}{\varepsilon}(f_j^b - f_j^s) \quad (\text{A.10})$$

$$\frac{df_j^s}{d\theta} = \frac{a'k_{lump}\tau_m}{\varepsilon}(f_j^b - f_j^s) - \frac{\tau_m}{\tau} \frac{d\xi_j}{d\theta} \quad (\text{A.11})$$

$$\frac{d\xi_j}{d\theta} = \frac{k_fm q_0}{Q}(f_j^s(\xi_m - \xi_j) - (\xi_m - 1)\xi_j) \quad (\text{A.12})$$

The parameter τ_m was calculated from the isotherm results of the propane adsorption. The number of tanks, N , and the hydraulic residence time, τ , were found from a fit to the "empty" reactor response. The only parameter to be fitted in the model for the breakthrough curves was the lumped mass transfer coefficient, k_{lump} . The response at the end of the reactor system is the concentration in the last tank, f_N . Equations (A.10), (A.11) and (A.12) must be solved simultaneously subject to the initial and boundary conditions given by Equation (A.4) ($f_j^b, f_j^s, \xi_j = 0$ for $\theta = 0$ ($1 \leq j \leq N$)) and Equation (A.5) ($f_{j-1}^b = 1$ for $j = 1$ and $\theta > 0$). The set of 3 times N first order ordinary differential equations (ODEs) was solved using a FORTRAN program. The program uses the IVPAG routine of the IMSL MATH/library by Visual Numerics, Inc., which uses an algorithm based on the backward differentiation formulas (BDF), also known as Gear's stiff method.

Appendix B

Isothermal Adsorption Breakthrough Program

Here follows an example of the FORTRAN 90 program code for the calculation of isothermal adsorption breakthrough curves.

```
PROGRAM TIS30_LDF

!*****
USE IMSL F90
!*****
! N=NUMBER OF DIFFERENTIAL EQUATIONS; N=2*M, where M is number of tanks in series
!*****
INTEGER MXPARM, N
PARAMETER (MXPARM=50, N=60)
! SPECIFICATIONS FOR PARAMETERS
INTEGER MABSE, MBDF, MSOLVE
PARAMETER (MABSE=1, MBDF=2, MSOLVE=2) !MSOLVE = 1 (for user-Jacobian), 2 (for numerical-Jacobian)
! SPECIFICATIONS FOR LOCAL VARIABLES
INTEGER IDO, ISTEP, NOUT
REAL A(1,1), PARAM(MXPARM), T, TEND, TOL, Y(N)
! SPECIFICATIONS FOR SUBROUTINES
EXTERNAL IVPAG, SSET, UMACH
! SPECIFICATIONS FOR FUNCTIONS
EXTERNAL FCN, FCNJ
! Global constants and variables
COMMON /PAR/ YO, aKLDF, EQF, M, TAU, TAUM, aK, CO, QO, ADSM, PORB, RGAS, TEMP
!*****
! START MAIN PROGRAM
!*****
CALL UMACH (2, NOUT)
! Open files
OPEN (UNIT=11, FILE='TIS30_LDF_505%.OUT')
! Define constants
!*****
M = 30 !number of tanks in series "see top/CHANGE N, set N=2*M"
!*****
! Experimental values
RGAS = 8.31415 ! [J/(mol*K)]
P = 106000.0 ! [Pa]
TEMP = 33.0 + 273.15 ! [K]
FRAC = 0.000800 !mole fraction of adsorbate [-]
QSTP = 6.0 !molar flow rate [L(STP)/h]
aMADS = 0.0102735 !total mass of adsorbent [kg]
aLOAD = 0.0505 !loading (fraction of support) [-]
PORB = 0.776E0 !SMF bed porosity (0%=0.83, 5%=0.776, 10%=0.723)
QMAX = 1.85 !maximum adsorption capacity [mol/kg]
HADS = -43100.0 !heat of adsorption [J/mol]
aK0 = 3.44E-11 !pre-exponential Arrhenius factor [Pa^-1]
```

```

! Calculate parameters
QVOL = QSTP*(101325.0*TEMP)/(P*273.15)/(3600.0*1000.0) !actual volumetric flowrate [m^3/s]
CGAS = P/(RGAS*TEMP) !gas concentration at P and Temp [mol/m^3]
CO = CGAS*FRAC !inlet concentration [mol/m^3]
aK = aK0*EXP(-HADS/(RGAS*TEMP)) !adsorption constant [Pa^-1]
Q0 = QMAX*aK*P*FRAC/(1.0+aK*P*FRAC) !maximum adsorption capacity at P + T, LANGMUIR [mol/kg]
ADSM = aMADS/(1.0+aLOAD)*aLOAD !mass of adsorbent phase[kg]
TAUM = ADSM*Q0/(QVOL*CO) !saturation time [s]
EQF = QMAX/Q0 !equilibrium factor [-]
! Parameter to fit
TAU = 97.0 !OVERALL hydraulic residence time [s]
aKLDF = 3.0E-2 !Linear driving force coefficient [s-1]
!*****
! Set initial conditions:
! Time
T = 0.0
! Tank, adsorbate concentrations
DO I=1,N
Y(I) = 0.0
ENDDO
! Inlet concentration
Y0 = 1.00
! Set error tolerance
TOL = 1.0E-7
!*****
! Set PARAM to defaults
CALL SSET (MXPARM, 0.0, PARAM, 1)
! Select absolute error control
PARAM(10) = MABSE
! Select BDF method
PARAM(12) = MBDF
! Select chord method and a user-provided Jacobian.
PARAM(13) = MSOLVE
PARAM(4) = 10000
!*****
! Print header
WRITE (11,99998)
! Set step size
IDO = 1
ISTEP = 0
SSIZE = 50 !15
MAXSTEP = 60

10 CONTINUE
ISTEP = ISTEP + 1
TEND = ISTEP*SSIZE
TIME = TEND
! The array a(*,*) is not used.
CALL IVPAG (IDO, N, FCN, FCNJ, A, T, TEND, TOL, PARAM, Y)
IF (ISTEP .LE. MAXSTEP) THEN
WRITE (11,'(I6,F12.4,2F13.5)') ISTEP, TIME, Y(M), Y(2*M)!, Y(3*M)!, M !Y(1), Y(2), Y(3), Y(4)
! Final call to release workspace
IF (ISTEP .EQ. MAXSTEP) IDO = 3
GO TO 10
END IF
99998 FORMAT (4X, 'ISTEP', 5X, 'TIME', 8X, 'Y(M)', 8X, 'Y(2M)')
END
!*****
! In the following there are 2 types of diff. eqns. for each tank:
! They are stored in the solution vector Y(3N) in 3 blocks:
! Y1: Y(1,N) = mass balance on each tank
! Y2: Y(N+1,2N) = mass balance on adsorbent
!*****
SUBROUTINE FCN (N, T, Y, YPRIME)
! SPECIFICATIONS FOR ARGUMENTS
INTEGER N
REAL T, Y(N), YPRIME(N)
COMMON /PAR/ Y0, aKLDF, EQF, M, TAU, TAUM, aK, CO, Q0, ADSM, PORB, RGAS, TEMP

! YEQL is the adsorbate concentration in equilibrium with the bulk gas concentration
YEQL = EQF*aK*CO*Y(1)*RGAS*TEMP/(1.E0+aK*CO*Y(1)*RGAS*TEMP)
YPRIME(M+1) = aKLDF*(YEQL-Y(M+1))
YPRIME(1) = M/(PORB*TAU)*(Y0-Y(1)) - TAUM/(PORB*TAU)*(YPRIME(M+1))

```

```

      IF (M .GT. 1) THEN
      DO I=2,M
! YEQL is the adsorbate concentration in equilibrium with the bulk gas concentration
      YEQL = EQF*aK*CO*Y(I)*RGAS*TEMP/(1.E0+aK*CO*Y(I)*RGAS*TEMP)
      YPRIME(M+I) = aKLDF*(YEQL-Y(M+I))
      YPRIME(I)    = M/(PORB*TAU)*(Y(I-1)-Y(I)) - TAUM/(PORB*TAU)*(YPRIME(M+I))
      ENDDO
    ENDIF

      RETURN
    END
!*****
      SUBROUTINE FCNJ (N, T, Y, DYPDY)
!          SPECIFICATIONS FOR ARGUMENTS
      INTEGER N
      REAL T, Y(N), DYPDY(N,*)
      COMMON /PAR/ YO, aKLDF, EQF, M, TAU, TAUM, aK, CO, QO, ADSM, PORB, RGAS, TEMP

!          SPECIFICATIONS FOR SUBROUTINES
      EXTERNAL SSET
!          Clear array to zero
      CALL SSET (N**2, 0.0, DYPDY, 1)
!          Compute partials

      RETURN
    END

```


Appendix C

Adiabatic Adsorption/Desorption Program

Here follows an example of the FORTRAN 90 program code for the calculation of adiabatic adsorption and desorption.

```
PROGRAM TIS_LDF
!*****
USE IMSL90
!*****
! N=NUMBER OF DIFFERENTIAL EQUATIONS; N=3*M, where M is number of tanks in series
!*****
INTEGER MXPARM, N
PARAMETER (MXPARM=50, N=300)
! SPECIFICATIONS FOR PARAMETERS
INTEGER MABSE, MBDF, MSOLVE
PARAMETER (MABSE=1, MBDF=2, MSOLVE=2) !MSOLVE = 1 (for user-Jacobian), 2 (for numerical-Jacobian)
! SPECIFICATIONS FOR LOCAL VARIABLES
INTEGER IDO, ISTEP, NOUT
REAL A(1,1), PARAM(MXPARM), T, TEND, TOL, Y(N)
! SPECIFICATIONS FOR SUBROUTINES
EXTERNAL IVPAG, SSET, UMACH
! SPECIFICATIONS FOR FUNCTIONS
EXTERNAL FCN, FCNJ
! Global constants and variables
COMMON /PAR1/ YEQ, YCO, YTO, aKLD, EQF, M, TAU, TAUM, aK, aKO, CO, QO, ADMS, PORB, RGAS, P, TEMP, TM
COMMON /PAR2/ TO, TS, PORF, PORZ, CPG, CPZ, CPF, RHOZ, RHOF, HADS, aKLDFO, ELDF, TREF, VOL, QSTP, FYO
!*****
! START MAIN PROGRAM
!*****
CALL UMACH (2, NOUT)
! Open files
OPEN (UNIT=11, FILE='TIS30_LDF_DESORBER.OUT')
OPEN (UNIT=12, FILE='TIS_LDF_PARAMETERS.OUT')
OPEN (UNIT=13, FILE='TIS_LDF_DESORBER_PROFILES.OUT')
! Print headers
WRITE (11,99998)
WRITE (13,99997)
99998 FORMAT (4X, 'ISTEP', 5X, 'TIME', 8X, 'Y(M)', 8X, 'Y(2M)')
99997 FORMAT (4X, 'TIME', 5X, 'POSITION, z', 8X, 'Fj', 10X, 'XIj', 10X, 'ZETAj')
! Define constants
!*****
M = 100 !number of tanks in series "see top/CHANGE N, set N=3*M"
!*****
! Experimental values
RGAS = 8.31415D0 ![J/(mol*K)]
P = 106000.D0 ![Pa]
aMADS = 0.0112891 !total mass of adsorbent [kg]
aLOAD = 0.09755 !loading (fraction of support) [-]
```

```

DISKS = 51.DO
PORB = 0.723DO      !SMF bed porosity (0%=0.83, 5%=0.776, 10%=0.723)
PORF = 0.17DO      !metal fiber fraction of bed
PORZ = 1.DO-PORB-PORF !zeolite film fraction of bed
QMAX = 1.85DO      !maximum adsorption capacity [mol/kg]
HADS = -43100.DO   !heat of adsorption [J/mol]
aK0 = 3.44D-11     !preexponential Arrhenius factor [Pa^-1]
aKLDF0 = 37.DO     !preexponential Arrhenius factor [s^-1]
ELDF = 67000.DO    !activation energy of LDF mass transport [J/mol]
TREF = 40.DO + 273.15DO !reference temperature for LDF [K]
! Physical parameters
  CPG = 29.2DO      !heat capacity of gas (N2) [J/mol/K]
  CPZ = 800.DO      !heat capacity of zeolite [J/kg/K]
  CPF = 500.DO      !heat capacity of zeolite [J/kg/K]
  RHOZ = 2162.DO    !density of zeolite [kg/m3]
  RHOF = 8000.DO    !density of metal fiber [kg/m3]
! Adsorption parameters
  TEMP = 25.DO + 273.15DO !adsorption temperature [K]
  FYO = 1000.D-6      !molar fraction of adsorptive [-]
  QSTP = 6.DO         !molar flow rate [L(STP)/h]
! Calculate parameters
  QVOL = QSTP*(101325.DO*TEMP)/(P*273.15DO)/(3600.DO*1000.DO) !actual volumetric flowrate [m^3/s]
  CGAS = P/(RGAS*TEMP) !gas concentration at P and Temp [mol/m^3]
  CO = CGAS*FYO !inlet concentration [mol/m^3]
  aK = aK0*EXP(-HADS/(RGAS*TEMP)) !adsorption coefficient at partial pres. of ads. and Temp [Pa^-1]
  QO = QMAX*aK*P*FYO/(1.DO+aK*P*FYO) !max adsorption capacity at P and Temp, Langmuir isotherm [mol/kg]
  ADSM = aMADS/(1.DO+aLOAD)*aLOAD !mass of adsorbent phase[kg]
  TAUM = ADSM*QO/(QVOL*CO) !saturation time [s]
  EQF = QMAX/QO !equilibrium factor [-]
  VOL = 3.1415927/4.DO*0.019DO**2*DISKS*0.3D-3*PORB !bed void volume [m^3]
  VOCT = QO*ADSM + VOL*CO !total VOC in system [mol]
! Desorption parameters
  TM = 60.DO + 273.15DO !'maximum' temperature of desorber (=max inlet) [K]
  TO = TEMP !'minimum' temperature of desorber (=initial T) [K]
  TS = TM-TO !scaling temperature [K]
  QSTP = 6.DO*1.D-1 !desorption molar flow rate [L(STP)/h]
  QMOL = RGAS*273.15DO*1.D3/101325.DO ! 22.41 L(STP)/mol
! Preheating equilibrium parameters, constant pressure
  YEQ = 6189.750080D-6 !equilibrium molar fraction [-]
  XIEQ = 0.9966881236DO !equilibrium adsorbate fraction [-]
  VEQ = 7.003643211D-7 !equilibrium moles desorbed at constant P [m^3]
  YMINL = 3703.6-14.693*(TM-273.15DO) !minimum concentration for reactor at 250C
  YMINH = 4457.7-14.719*(TM-273.15DO) !minimum concentration for reactor at 300C
  VOCTE = QO*XIEQ*ADSM + P*VOL*YEQ/(RGAS*TM) + VEQ !nitial VOC in system = VOCT, OK [mol]
! Maximum adiabatic temperature rise with heat supplied from VOC
  DHR = 2043130.DO !reaction enthalpy [J/mol]
  EHDES = QO*ADSM*-HADS !enthalpy for desorption
  EHRXN = VOCT*DHR !reaction enthalpy
  CPSYS = VOL/PORB*(CGAS*CPG*PORB+PORZ*CPZ*RHOZ+PORF*CPF*RHOF) !Cp of the system
  DTMAX = (EHRXN-EHDES)/CPSYS !max adiabtic temp rise from VOC
!*****
! Inlet concentration
  YCO = 0.DO
! Inlet temperature
  YTO = 1.D-10 ! [0,1]=[T0,TM] Room temp air
! Set initial conditions:
! Time
  T = 0.0
! Adsorptive (gas) concentrations
  DO I=1,(M)
    Y(I) = 1.DO
  ENDDO
! Adsorbate (solid) concentrations
  DO I=(M+1),(2*M)
    Y(I) = XIEQ
  ! Y(I) = 1.DO
  ENDDO
! Tank temperatures [C]
  DO I=(2*M+1),N
    Y(I) = 1.DO ! [0,1]=[T0,TM] Preheated to max temperature
  ENDDO
! skips text line in data file with isothermal adsorber breakthrough profiles
! DO I=1,1

```

```

!      READ(12,*)
!      ENDDO
! reads data for adsorbate and adsorptive concentrations
!      DO I=1,M
!          READ(12,*) TANK, BRTIME, Y(I),Y(M+I)
!      ENDDO
! Writing initial outlet conditions
      WRITE (11,'(I6,F12.4,3F13.5)') 0, 0.0, Y(M)*YEQ*1.D6, Y(2*M), Y(3*M)*TS+T0-273.15D0
! Writing initial bed profiles
      Z = 0.D0
      WRITE (13,'(F12.2,F12.5,3F13.5)') T, Z, 1.D0*YEQ*1.D6, 1.D0, 1.D0*TS+T0-273.15D0
DO I=1,M
      Z = 1.D0*I/M
      WRITE (13,'(F12.2,F12.5,3F13.5)') T, Z, Y(I)*YEQ*1.D6, Y(M+I), Y(2*M+I)*TS+T0-273.15D0
ENDDO
WRITE (13,*)
! Set error tolerance
      TOL = 1.0E-7
!*****
! Set PARAM to defaults
      CALL SSET (MXPARAM, 0.0, PARAM, 1)
! Select absolute error control
      PARAM(10) = MABSE
! Select BDF method
      PARAM(12) = MBDF
! Select chord method and
! a user-provided Jacobian.
      PARAM(13) = MSOLVE
      PARAM(4) = 10000
!*****
! Set step size
      IDO = 1
      ISTEP = 0
      SSIZE = 10 !15 ! [s]
      MAXSTEP = 10000
! Time interval for bed profiles
      TINT = 500/SSIZE !time interval [s]
      PINT = TINT      !initializing
! Integration initialization
      SUMH = 0.D0
      YYH = Y(M)
      SUML = 0.D0
      YYL = Y(M)
      SUMT = 0.D0
      YYT = Y(M)

      10 CONTINUE
      ISTEP = ISTEP + 1
      TEND = ISTEP*SSIZE
      TIME = TEND
! The array a(*,*) is not used.
      CALL IVPAG (IDO, N, FCN, FCNJ, A, T, TEND, TOL, PARAM, Y)
! Writing outlet conditions
      IF (ISTEP .LE. MAXSTEP) THEN
          WRITE (11,'(I6,F12.4,3F13.5)') ISTEP, TIME, Y(M)*YEQ*1.D6, Y(2*M), Y(3*M)*TS+T0-273.15D0
! Writing bed profiles
          IF(ISTEP .EQ. PINT) THEN
              PINT = PINT + TINT
              Z = 0.D0
              WRITE (13,'(F12.2,F12.5,3F13.5)') T, Z, 0.D0, 0.D0, 0.D0*TS+T0-273.15D0
DO I=1,M
              Z = 1.D0*I/M
              WRITE (13,'(F12.2,F12.5,3F13.5)') T, Z, Y(I)*YEQ*1.D6, Y(M+I), Y(2*M+I)*TS+T0-273.15D0
          ENDDO
          WRITE (13,*)
          ENDF
! Integration of outlet concentration by trapezoidal rule
          IF(YMINH .LE. (Y(M)*YEQ*1.D6)) THEN
              SUMH = SUMH + YYH +Y(M)
              TMINH = TIME
          ENDF
          YYH = Y(M)
          IF(YMINL .LE. (Y(M)*YEQ*1.D6)) THEN

```

```

      SUML = SUML + YYL +Y(M)
      TMINL = TIME
      ENDIF
      YYL = Y(M)
! Total integration for check
      SUMT = SUMT + YYT +Y(M)
      YYT = Y(M)
! Final call to release workspace
      IF (ISTEP .EQ. MAXSTEP) IDO = 3
      GO TO 10
      ENDIF
! Integration of outlet concentration by trapezoidal rule
      IF(YMINH .LE. (YEQ*1.D6)) THEN
        FRACH = (SSIZE/2.D0*SUMH*YEQ*QSTP/(QMOL*3600.D0) + VEQ)/VOCT !VOC desorbed with conc>yminH [mol]
      ELSE
        FRACH = 0.D0
      ENDIF
      IF(YMINL .LE. (YEQ*1.D6)) THEN
        FRACL = (SSIZE/2.D0*SUML*YEQ*QSTP/(QMOL*3600.D0) + VEQ)/VOCT !VOC desorbed with conc>yminL [mol]
      ELSE
        FRACL = 0.D0
      ENDIF
      FRACT = (SSIZE/2.D0*SUMT*YEQ*QSTP/(QMOL*3600.D0) + VEQ)/VOCT !VOC desorbed in total [mol]
! Write parameters
      WRITE (12,99996)
99996 FORMAT (4X, 'YC3,0', 6X, 'TMAX', 7X, 'V', 6X, 'YEQ', 7X, 'YMINL', 5X, 'YMINH', 4X, 'FRAC(YMINL)', 1X,
& 'FRAC(YMINH)', 1X, 'FRAC(TOTAL)', 2X, 'TIME(YMINL)', 2X, 'TIME(YMINH)', 2X, 'TMAX,OVERALL', 2X, 'XIEQ')
      WRITE (12,'(6F10.2, 3F12.8, 2F12.2, F17.2, F12.8)') FYO*1.D6, (TM-273.15D0), (QSTP*1000/60), (YEQ*1D6),
& YMINL, YMINH, FRACL, FRACH, FRACT, TMINL, TMINH, (DTMAX+T0-273.15D0), XIEQ
      END
!*****
! In the following there are 3 types of diff. eqns. for each tank:
! They are stored in the solution vector Y(3N) in 3 blocks:
!
! Y1: Y(1,N)      = mass balance on each tank, molar fraction
! Y2: Y(N+1,2N)   = mass balance on adsorbent
! Y3: Y(2N+1,3N)  = pseudo-homogeneous energy balance
!
!*****
      SUBROUTINE FCN (N, T, Y, YPRIME)
! SPECIFICATIONS FOR ARGUMENTS
      INTEGER N
      REAL T, Y(N), YPRIME(N)
      COMMON /PAR1/ YEQ, YCO, YTO, aKLD, EQF, M, TAU, TAUM, aK, aKO, CO, QO, AD, PORB, RGAS, P, TEMP, TM
      COMMON /PAR2/ T0, TS, PORF, PORZ, CPG, CPZ, CPF, RHOZ, RHOF, HADS, aKLDFO, ELDF, TREF, VOL, QSTP, FYO
!
! calculation of temperature dependent terms for each cell
      aK = aKO*EXP(-HADS/(RGAS*(TO+TS*Y(2*M+1)))) !adsorption coefficient at partial pres. of ads. and Temp [Pa-1]
      aKLD = aKLDFO*EXP(-ELDF/RGAS*(1.D0/(TO+TS*Y(2*M+1))-1.D0/TREF))
      TAU = VOL*P*273.15D0*3.6D6/(QSTP*101325.D0*(TO+TS*Y(2*M+1)))
! YEQL is the adsorbate concentration in equilibrium with the bulk gas concentration
      YEQL = EQF*aK*P*YEQ*Y(1)/(1.D0+aK*P*YEQ*Y(1))
! model for first cell
      YPRIME(M+1) = aKLD*(YEQL-Y(M+1))
      YPRIME(1) = M/(TAU)*((TO+TS*Y(2*M+1))/YTO*YCO-Y(1))
& - RGAS*(TO+TS*Y(2*M+1))*PORZ*RHOZ*QO/(P*PORB*YEQ)*(YPRIME(M+1))
      YPRIME(2*M+1) = ((PORB*M*P*CPG*TS)/(TAU*RGAS*(TO+TS*Y(2*M+1)))*(YTO-Y(2*M+1))
& +PORZ*RHOZ*QO*(-HADS)*YPRIME(M+1)) / (((PORB*P*CPG)/(RGAS*(TO+TS*Y(2*M+1)))+PORZ*RHOZ*CPZ+PORF*RHOF*CPF)*TS)
!
      IF (M .GT. 1) THEN
        DO I=2,M
! calculation of temperature dependent terms for each cell
          aK = aKO*EXP(-HADS/(RGAS*(TO+TS*Y(2*M+I)))) !adsorption coefficient at partial pres. of ads. and Temp [Pa-1]
          aKLD = aKLDFO*EXP(-ELDF/RGAS*(1.D0/(TO+TS*Y(2*M+I))-1.D0/TREF))
          TAU = VOL*P*273.15D0*3.6D6/(QSTP*101325.D0*(TO+TS*Y(2*M+I)))
! YEQL is the adsorbate concentration in equilibrium with the bulk gas concentration
          YEQL = EQF*aK*P*YEQ*Y(I)/(1.D0+aK*P*YEQ*Y(I))
! model for subsequent cells
          YPRIME(M+I) = aKLD*(YEQL-Y(M+I))
          YPRIME(I) = M/(TAU)*((TO+TS*Y(2*M+I))/(TO+TS*Y(2*M+I-1))*Y(I-1)-Y(I))
& - RGAS*(TO+TS*Y(2*M+I))*PORZ*RHOZ*QO/(P*PORB*YEQ)*(YPRIME(M+I))
          YPRIME(2*M+I) = ((PORB*M*P*CPG*TS)/(TAU*RGAS*(TO+TS*Y(2*M+I)))*(Y(2*M+I-1)-Y(2*M+I))
& +PORZ*RHOZ*QO*(-HADS)*YPRIME(M+I)) / (((PORB*P*CPG)/(RGAS*(TO+TS*Y(2*M+I)))+PORZ*RHOZ*CPZ+PORF*RHOF*CPF)*TS)
        END DO
      END IF

```

```
ENDDO
ENDIF

      RETURN
      END

!*****
      SUBROUTINE FCNJ (N, T, Y, DYPDY)
! SPECIFICATIONS FOR ARGUMENTS
      INTEGER N
      REAL T, Y(N), DYPDY(N,*)
      COMMON /PAR1/ YEQ, YCO, YTO, aKLDf, EQF, M, TAU, TAUM, aK, aKO, CO, QO, ADSM, PORB, RGAS, P, TEMP, TM
      COMMON /PAR2/ TO, TS, PORF, PORZ, CPG, CPZ, CPF, RHOZ, RHOF, HADS, aKLDFO, ELDF, TREF, VOL, QSTP, FYO

! SPECIFICATIONS FOR SUBROUTINES
      EXTERNAL SSET
! Clear array to zero
      CALL SSET (N**2, 0.0, DYPDY, 1)

      RETURN
      END
```


Appendix D

Parameter Estimation Program

Here follows the FORTRAN 77 program code for the parameter fitting by a least squares method.

The following is a listing of the subroutines and their functions.

- VA07AD: Solves the minimization problem (i.e. Equation 2.33). VA07AD was modified in order to perform an under-relaxation, if the program made too big of a step that would cause the parameters to become zero.
- FM02AD, MA10AD: Help routines from the Harwell library
- RESID: Subroutine, called by VA07AD. The residuals $\ln y - \ln \hat{y}$ for Equation 2.33 are calculated here.
- LSQ: Subroutine, called by VA07AD. The derivatives (Jacobian matrix) of the residuals are calculated here. This was solved by a numerical routine calculating the central derivatives of the current solution vector.
- DTEST: Subroutine that calculates the standard deviation of the output variable, the 2σ -confidence intervals and the parameter correlation matrix, when minimization procedure is done.
- MODEL: Subroutine for the evaluation of the model.

```
PROGRAM PARAMETER_ESTIMATION
  IMPLICIT DOUBLE PRECISION (A-H,O-Z)
C *****
C NUMBER OF PARAMETERS TO FIT
C   NPAR=3
C NUMBER OF DATA POINTS FOR FITTING
C   NDAT=68
  PARAMETER (NDAT=68,NPAR=4)
  DIMENSION X(NPAR),AA(NPAR,NPAR),R(NDAT),D(NPAR),AUX(NDAT)
  DIMENSION EPS(NPAR)
  EXTERNAL RESID,LSQ
  COMMON/A/DR(NDAT,NPAR),RATE(NDAT),T(NDAT),CPROP(NDAT),COXY(NDAT)
  COMMON/B/ALR(NDAT),RGAS,TC
  COMMON/RES/XOLD(NPAR),L
C EPS CONTAINS THE CONVERGENCE CRITERIA FOR THE PARAMETERS
C In the convergence criteria the VA07AD code was modified to test the
c parameter change in relation to it's value. EPS-values for all parameters
c must be identical. The precision of all parameters is given by EPS,
c eg. EPS(i) = 0.001 results in a precision of 0.001.
```

```

DATA EPS /.000001,.000001,.000001,.000001/
C-----
OPEN(UNIT=10,FILE='FECRALLOY.DAT')      !INPUT FILE
OPEN(UNIT=6,FILE='FECRALLOY_RES_4PAR.OUT') !OUTPUT FILE OF FITTED PARAMETERS
L=0
C CONSTANTS
  RGAS=8.31415D0  ![m^3*Pa/(mol*K)] and [J/(mol*K)] The gas constant
TC =573.15D0  ![K] Center temperature for the rescaling of the frequency factor
C SKIPS TWO LINES IN DATAFILE
  DO I=1,2
    READ(10,*)
  ENDDO
C READS DATA AND CALCULATES THE LOG OF THE LEFT SIDE
  DO I=1,NDAT
    READ(10,*) RATE(I),T(I),CPROP(I),COXY(I)
    ALR(I)=DLOG(RATE(I))
  ENDDO
C INITIAL GUESS OF PARAMETERS
  X(1)=6.0D-5      !k0 [mol/(g*s)]      Frequency factor
  X(2)=88000.D0    !Ea [J/mol]      Activation energy
  X(3)=0.36D0      !n [-]      Reaction order in propane
  X(4)=0.05D0      !m [-]      Reaction order in oxygen
C MAXFN, MODE, IPRINT AND DLT ARE PARAMETERS FOR THE ADJUSTMENT ROUTINES
  MAXFN=150
  MODE=1
  IPRINT=1
  DLT=.0001
C WHEN INIT IS 1, DTEST CHECKS THE CALCULATION OF THE ANALYTICAL DERIVATIVES
  INIT=1
  CALL DTEST(RESID,LSQ,NDAT,NPAR,X,R,AA,D,AUX,DLT,INIT)
  write(*,*) 'First call to DTEST finished. Now running VA07AD'

  CALL VA07AD(RESID,LSQ,NDAT,NPAR,X,R,SS,AA,D,EPS,IPRINT,MAXFN,MODE)
  write(*,*) 'VA07AD finished. Now calling DTEST again'
C WHEN INIT IS -1, DTEST RETURNS THE FULL EVALUATION OF THE PARAMETER FIT
  INIT=-1
  CALL DTEST(RESID,LSQ,NDAT,NPAR,X,R,AA,D,AUX,DLT,INIT)
  write(*,*) 'DTEST finished'
  STOP
  END
C*****
SUBROUTINE RESID(M,N,X,R,IFL)
  IMPLICIT DOUBLE PRECISION (A-H,O-Z)
  PARAMETER (NDAT=68,NPAR=4)
  DIMENSION X(NPAR),R(NDAT),ALI(NDAT)
  COMMON/A/DR(NDAT,NPAR),RATE(NDAT),T(NDAT),CPROP(NDAT),COXY(NDAT)
  COMMON/B/ALR(NDAT),RGAS,TC
  COMMON/RES/XOLD(NPAR),L
C Calculation of the residual for each data point as a function of
C the current value of the X-vector.
  DO I=1,NDAT
    NRED=I
    CALL MODEL(NRED,X,AMOD)
    ALI(I)=AMOD
    R(I)=ALI(I)-ALR(I)
  ENDDO
  RETURN
  END
C*****
SUBROUTINE LSQ(M,N,X,R,A,V)
  IMPLICIT DOUBLE PRECISION (A-H,O-Z)
  PARAMETER (NDAT=68,NPAR=4)
  DIMENSION X(NPAR),R(NDAT),A(NPAR,NPAR),V(NPAR),XP(NPAR),
& R2(NDAT),R1(NDAT),XCALL(NPAR),RH(NDAT),RL(NDAT)
  COMMON/A/DR(NDAT,NPAR),RATE(NDAT),T(NDAT),CPROP(NDAT),COXY(NDAT)
  COMMON/B/ALR(NDAT),RGAS,TC
  COMMON/RES/XOLD(NPAR),L
C Calculation of Jacoby matrix in A DO-loop over all measurements
  DO I=1,NDAT
    NRED=I
    CALL MODEL(NRED,X,AMOD1)
    R1(I)=AMOD1-ALR(I)
  ENDDO

```

```

      XPERM=0.000001D0
      DO I=1,NDAT
        DO J=1,NPAR
          DX=X(J)*XPERM
          X(J)=X(J)+DX
          NRED=I
          CALL MODEL(NRED,X,AMOD2)
          R2(I)=AMOD2-ALR(I)
          X(J)=X(J)-DX
          DR(I,J)=(R2(I)-R1(I))/DX
        ENDDO
      ENDDO
C BELOW HERE: Calculation of coefficients A(I,J) and V(I) in the normal equations
C THIS MUST NOT BE CHANGED
      DO I=1,NPAR
        V(I)=FM02AD(M,DR(1,I),1,R(1),1)
        DO J=1,I
          A(I,J)=FM02AD(M,DR(1,I),1,DR(1,J),1)
        ENDDO
      ENDDO
      RETURN
      END
!C*****-----*****
      SUBROUTINE MODEL(NRED,X,AMOD)
C Here the calculation of the MODEL value is done
      IMPLICIT DOUBLE PRECISION(A-H,O-Z)
      PARAMETER (NDAT=68,NPAR=4)
      DIMENSION X(NPAR)
      COMMON/A/DR(NDAT,NPAR),RATE(NDAT),T(NDAT),CPROP(NDAT),COXY(NDAT)
      COMMON/B/ALR(NDAT),RGAS,TC
      COMMON/RES/XOLD(NPAR),L

      AMOD = DLOG(X(1))-(X(2)/RGAS)*(1.DO/T(NRED)-1.DO/TC)    !4 PARAMETERS
& +X(3)*DLOG(CPROP(NRED))+X(4)*DLOG(COXY(NRED))
      END

```


Appendix E

Kinetics of CK-302

The kinetics of the total oxidation of propane was determined for the industrial VOC combustion catalyst CK-302 (see Section 3.4.1). The kinetics was estimated for the catalysts in two forms:

1. CK-302 particles, size: 200-315 μm
2. CK-302 fine powder supported on SMF (see Sections 3.4.1, 5.2 and 5.4)

The two catalysts were tested in the pilot reactor (Section 3.2.2) with recycle. The temperature was varied between 230 and 352 $^{\circ}\text{C}$ for the first catalyst and 326 and 376 $^{\circ}\text{C}$ for the second, due to a lower catalyst mass. At each constant temperature, steady state conditions were obtained with different inlet gas compositions $y_{\text{C}_3\text{H}_8, \text{in}} \in [0.005; 0.010; 0.015]$ and a constant oxygen mole fraction in large excess at 0.15. The outlet concentration of propane, $C_{\text{C}_3\text{H}_8}$, varied between 0.06 and 0.39 mol/m^3 .

The power rate law:

$$r = kC_{\text{C}_3\text{H}_8}^n \quad (\text{E.1})$$

was fitted to the data using the parameter estimation program (see Appendix D). The results are shown in Table E.1.

Table E.1: Fitted parameters of power rate model.

Parameter	Units	CK-302 particles	CK-302 powder/SMF
$k' \dagger$	$(\text{mol}/\text{g}\cdot\text{s}) (\text{m}^3/\text{mol})^{(n+m)}$	$(0.41 \pm 0.22) \cdot 10^{-5}$	$(0.30 \pm 0.09) \cdot 10^{-5}$
E_a	kJ/mol	60.5 ± 9.1	88.2 ± 12.2
n		0.57 ± 0.26	0.59 ± 0.14
Temp. range	$^{\circ}\text{C}$	[230; 352]	[326; 376]
$ssq_{\min} \ddagger$		1.07	0.72
Standard error*		0.26	0.18
Data points		19	25

\dagger Arrhenius frequency factor at reference temperature = 300 $^{\circ}\text{C}$ (see section 2.5.4).

\ddagger Minimal sum of squares of residuals.

* Approximate standard error on the output variable ($\ln r$).

References

- Abdullah, A. Z., Abu Bakar, M. Z., & Bhatia, S. 2003. A kinetic study of catalytic combustion of ethyl acetate and benzene in air stream over Cr-ZSM-5 catalyst. *Industrial & Engineering Chemistry Research*, **42**(24), 6059–6067.
- Aguado, Sonia, Polo, Ana C., Bernal, Maria P., Coronas, Joaquin, & Santamaria, Jesus. 2004. Removal of pollutants from indoor air using zeolite membranes. *Journal of Membrane Science*, **240**(1-2), 159–166.
- Ahlstrom-Silversand, A. F., & Odenbrand, C. U. I. 1999. Modelling catalytic combustion of carbon monoxide and hydrocarbons over catalytically active wire meshes. *Chemical Engineering Journal*, **73**(3), 205–216.
- Allen, David T. 2004. Air Pollution. *Pages 787–815 of: Seidel, A. (ed), Kirk-Othmer Encyclopedia of Chemical Technology*, 5th edn., vol. 1. Hoboken, New Jersey: John Wiley & Sons, Inc.
- Andersson, M. P., Bligaard, T., Kustov, A., Larsen, K. E., Greeley, J., Johannessen, T., Christensen, C. H., & Norskov, J. K. 2006. Toward computational screening in heterogeneous catalysis: Pareto-optimal methanation catalysts. *Journal of Catalysis*, **239**(2), 501–506.
- Argauer, R. J., & Landolt, G. R. 1969. *Crystalline Zeolite ZSM-5 and Method of Preparing the Same*. Patent no. US 3 702 886.
- Atwood, G. A., Greene, H. L., Chintawar, P., Rachapudi, R., Ramachandran, B., & Vogel, C. A. 1998. Trichloroethylene sorption and oxidation using a dual function sorbent/catalyst in a falling furnace reactor. *Applied Catalysis, B: Environmental*, **18**(1-2), 51–61.
- Barrer, R. M. 1979. Chemical Nomenclature and Formulation of Compositions of Synthetic and Natural Zeolites. *Pure and Applied Chemistry*, **51**(5), 1091–1100.
- Barsan, M. M., & Thyron, F. C. 2003. Kinetic study of oxidative dehydrogenation of propane over Ni-Co molybdate catalyst. *Catalysis Today*, **81**(2), 159–170.
- Bart, H. J., & Von Gemmingen, U. 2005. Adsorption. *In: Ullmann's Encyclopedia of Industrial Chemistry*, online edn., vol. 1. Weinheim: Wiley-VCH.
- Bates, D.M., & Watts, D.G. 1988. *Nonlinear Regression Analysis and its Applications*. Wiley Series in Probability and Mathematical Statistics. New York: John Wiley and Sons, Inc.

- Beers, Annemarie E. W., Nijhuis, T. A., Aalders, N., Kapteijn, F., & Moulijn, J. A. 2003. BEA coating of structured supports-performance in acylation. *Applied Catalysis A: General*, **243**(2), 237–250.
- Bein, T. 1996. Synthesis and applications of molecular sieve layers and membranes. *Chemistry of Materials*, **8**(8), 1636–1653.
- Bielanski, A., & Haber, J. 1991. *Oxygen in Catalysis*. New York: Dekker.
- Bligaard, T., Norskov, J. K., Dahl, S., Matthiesen, J., Christensen, C. H., & Sehested, J. 2004. The Bronsted-Evans-Polanyi relation and the volcano curve in heterogeneous catalysis. *Journal of Catalysis*, **224**(1), 206–217.
- Blocki, S. W. 1993. Hydrophobic Zeolite Adsorbent - a Proven Advancement in Solvent Separation Technology. *Environmental Progress*, **12**(3), 226–230.
- Boreskov, G. K. 1982. *Page 39 of:* Anderson, J. R., & Boudart, M. (eds), *Catalysis Science and Technology*, vol. 3. New York: Springer-Verlag.
- Bosanquet, C. H. 1944. *British TA Report BR-507*.
- Bowen, P. 2006 (August). *Powder Technology Laboratory, EPFL, (Pers. comm.)*.
- Box, G. E. P., & Hill, W. J. 1967. Discrimination among Mechanistic Models. *Technometrics*, **9**(1), 57.
- Box, G.E.P., & Draper, N.R. 1987. *Empirical Model-Building and Response Surfaces*. Wiley Series in Probability and Mathematical Statistics. New York: John Wiley and Sons, Inc.
- Box, G.E.P., Hunter, J.S., & Hunter, W.G. 2005. *Statistics for Experimenters*. 2nd edn. New Jersey: John Wiley & Sons, Inc.
- Breck, D. W. 1974. *Zeolite Molecular Sieves*. New York: Wiley.
- Brunauer, S., Emmett, P. H., & Teller, E. 1938. Adsorption of gases in multimolecular layers. *Journal of the American Chemical Society*, **60**, 309–319.
- Bundesministerium für Umwelt, Naturschutz und Reaktorsicherheit. 2002 (24. Juli 2002). *Erste Allgemeine Verwaltungsvorschrift zum BundesImmissionsschutzgesetz (Technische Anleitung zur Reinhaltung der Luft TA Luft)*. Tech. rept. Publisher: Carl Heymanns Verlag KG, Luxemburger Strae 449, 50939 Kln (Tel.: 0221/943730).
- Busca, G., Guidetti, R., & Lorenzelli, V. 1990. Fourier-Transform Infrared Study of the Surface-Properties of Cobalt Oxides. *Journal of the Chemical Society-Faraday Transactions*, **86**(6), 989–994.
- Busca, Guido. 1996. Infrared studies of the reactive adsorption of organic molecules over metal oxides and of the mechanisms of their heterogeneously-catalyzed oxidation. *Catalysis Today*, **27**(3-4), 457–496.
- Cahela, Donald R., & Tatarchuk, Bruce J. 2001. Permeability of sintered microfibrinous composites for heterogeneous catalysis and other chemical processing opportunities. *Catalysis Today*, **69**(1-4), 33–39.

- Campbell, Larry E., & Sanders, Michele W. 1999. *Sequential adsorptive capture and catalytic oxidation of volatile organic compounds in a reactor bed*. Patent no. 9948593.
- Cellier, C., Ruaux, V., Lahousse, C., Grange, P., & Gaigneaux, E. M. 2006. Extent of the participation of lattice oxygen from gamma-MnO₂ in VOCs total oxidation: Influence of the VOCs nature. *Catalysis Today*, **117**(1-3), 350–355.
- Chae, J. O., Moon, S. I., Lee, D. Y., Choi, I. C., Pyagai, R., & Demidiouk, V. 2004. Influence of cobalt precursors on the catalytic activity of the cobalt oxide/Al₂O₃ catalysts. *Reaction Kinetics and Catalysis Letters*, **83**(2), 369–375.
- Chau, Joseph Lik Hang, Wan, Yu Shan Susanna, Gavrilidis, Asterios, & Yeung, King Lun. 2002. Incorporating zeolites in microchemical systems. *Chemical Engineering Journal*, **88**(1-3), 187–200.
- Chilton, T. H., & Colburn, A. P. 1934. Mass transfer (absorption) coefficients - Prediction from data on heat transfer and fluid friction. *Industrial and Engineering Chemistry*, **26**, 1183–1187.
- Chorkendorff, I., & Niemantsverdriet, J. W. 2003. *Concepts of Modern Catalysis and Kinetics*. Weinheim: Wiley-VCH.
- Coppage, J. E., & London, A. L. 1956. *Chem. Eng. Progr.*, **52**(2), 57F–63F.
- Coronas, J., & Santamaria, J. 1999. Separations using zeolite membranes. *Separation and Purification Methods*, **28**(2), 127–177.
- Coronas, J., & Santamaria, J. 2004a. State-of-the-art in zeolite membrane reactors. *Topics in Catalysis*, **29**(1-2), 29–44.
- Coronas, J., & Santamaria, J. 2004b. The use of zeolite films in small-scale and micro-scale applications. *Chemical Engineering Science*, **59**(22-23), 4879–4885.
- Cybulski, A., & Moulijn, J. (eds). 2006. *Structured Catalysts and Reactors*. 2nd edn. Chemical Industries. Boca Raton: CRC Press, Taylor & Francis Group.
- Dai, F. Y., Suzuki, M., Takahashi, H., & Saito, Y. 1988. In: Occelli, M. L., & Robson, H. E. (eds), *Zeolite Synthesis*. ACS symposium series. Los Angeles, California: Washington, DC : American Chemical Society, 1989.
- Dalla Betta, R. A., Schlatter, J. C., Lane, D. R., & Durieux, D. O. 1994. *Self-contained system for controlling gaseous emissions from dilute organic sources and a process for using that system*. Patent no. 5308457.
- Dawson, E. A., & Barnes, P. A. 1992. A New Approach to the Statistical Optimization of Catalyst Preparation. *Applied Catalysis a-General*, **90**(2), 217–231.
- De Greef, J., Desmet, G., & Baron, G. 2005. Micro-fiber elements as perfusive catalysts or in catalytic mixers - Flow, mixing and mass transfer. *Catalysis Today*, **105**(3-4), 331–336.
- Deeng, Khoo Daw, Mohamed, Abdul Rahman, & Bhatia, Subhash. 2004. Process optimization studies of structured Cu-ZSM-5 zeolite catalyst for the removal of NO using design of experiments (DOE). *Chemical Engineering Journal*, **103**(1-3), 147–157.

- Deng, S. G., & Lin, Y. S. 1995. Sulfur-Dioxide Sorption Properties and Thermal-Stability of Hydrophobic Zeolites. *Industrial & Engineering Chemistry Research*, **34**(11), 4063–4070.
- Depiak, A. M., & Wierzba, I. 1999. An experimental investigation of oxidation of common gaseous fuels over cobalt oxide/chromium oxide catalyst in a packed-bed reactor. *Pages 187–191 of: ETCE'99, Proceedings of the ASME Energy Sources Technology Conference.*
- Derouane, Eric G. 1998. Zeolites as solid solvents. *Journal of Molecular Catalysis A: Chemical*, **134**(1-3), 29–45.
- Dixon, J. K., & Longfield, J. E. 1960. *Catalysis*. vol. 7. New York: Reinhold.
- Do, D. D., & Rice, R. G. 1986. Validity of the Parabolic Profile Assumption in Adsorption Studies. *Aiche Journal*, **32**(1), 149–154.
- Do, Duong D. 1998. *Adsorption Analysis: Equilibria and Kinetics*. Series on Chemical Engineering, vol. 2. London: Imperial College Press.
- Dollimore, D., & Heal, G. R. 1964. Improved Method for Calculation of Pore Size Distribution from Adsorption Data. *Journal of Applied Chemistry of the USSR*, **14**(3), 109–114.
- Ehrfeld, W., Hessel, V., & Haverkamp, V. 2003. Microreactors. *Pages 1–31 of: Ullmann's Encyclopedia of Industrial Chemistry*, 6th edn., vol. 22. Weinheim: Wiley-VCH.
- Emig, G., & Dittmeyer, R. 1997. Simultaneous Heat and Mass Transfer and Chemical Reaction. *Pages 1209–1252 of: Ertl, G., Knözinger, H., & Weitkamp, J. (eds), Handbook of Heterogeneous Catalysis*, vol. 3. Weinheim, Germany: VCH.
- EPA. 2007. <http://www.epa.gov/radon/healthrisks.html>. U.S. Environmental Protection Agency.
- Farrauto, R. J., & Bartholomew, C. H. 1997. *Fundamentals of Industrial Catalytic Processes*. 1st edn. London: Blackie Academic & Professional.
- FDA. 1988. *Maximum Acceptable Level of Ozone, Code of Federal Regulations, Title 21, Part 801.415*. Washington, D.C.: U.S. Food and Drug Administration (FDA).
- Feneuille, D., Mathieu, D., & Phan-Tan-Luu, R. 1983. *Méthodologie de la recherche expérimentale. Tome I: outil mathématiques; Tome 2: surface de réponse*. Laboratoire de prospective réactionnelle et d'analyse de l'information, IPSOI rue Henri-Poincaré, 13397 Marseille, France.
- Fino, D., Specchia, S., Saracco, G., & Specchia, V. 2006. Catalytic Filters for Flue Gas Cleaning. *Pages 553–579 of: Moulijn, A. Cybulski, & J. (eds), Structured Catalysts and Reactors*, 2nd edn. Boca Raton: CRC Press, Taylor & Francis Group.
- Finocchio, E., Busca, G., Lenzelli, V., & Escibano, V. S. 1996. FTIR studies on the selective oxidation and combustion of light hydrocarbons at metal oxide surfaces .2. Propane and propene oxidation on Co₃O₄. *Journal of the Chemical Society-Faraday Transactions*, **92**(9), 1587–1593.

- Fuller, E.N., Schettler, P.D., & Giddings, J.C. 1966. A New Method for Prediction of Binary Gas-Phase Diffusion Coefficients. *Industrial and Engineering Chemistry*, **58**(5), 19–27.
- Fürbringer, J-M. 2005 (January 2005). *Course: Design of Experiments (PR02)*.
- Fürbringer, J-M. 2006 (February). *Matlab function for doing ANOVA: "anova_fact.m" (pers. comm.)*.
- Gangwal, S. K., Mullins, M. E., Spivey, J. J., Caffrey, P. R., & Tichenor, B. A. 1988. Kinetics and Selectivity of Deep Catalytic-Oxidation of N-Hexane and Benzene. *Applied Catalysis*, **36**(1-2), 231–247.
- Garbowski, E., Guenin, M., Marion, M.-C., & Primet, M. 1990. Catalytic properties and surface states of cobalt-containing oxidation catalysts. *Applied Catalysis*, **64**, 209–224.
- Gay, B., & Maughan, R. 1963. *Int. J. Heat Mass Transfer*, **6**, 277–87.
- Geankoplis, C. J. 1993. *Transport Processes and Unit Operations*. 3rd edn. New Jersey: Prentice Hall P T R.
- Germani, G., Stefanescu, A., Schuurman, Y., & van Veen, A.C. 2006. Preparation and Characterization of Porous Alumina-Based Catalyst Coatings in Microchannels. *Page 317 of: Abstracts, Book of (ed), 19th International Symposium on Chemical Reaction Engineering, ISCRE19*. Potsdam/Berlin, Germany: DECHEMA.
- Ghoshal, A. K., & Manjare, S. D. 2002. Selection of appropriate adsorption technique for recovery of VOCs: an analysis. *Journal of Loss Prevention in the Process Industries*, **15**(6), 413–421.
- Glueckauf, E. 1955. Theory of Chromatography .10. Formulae for Diffusion into Spheres and Their Application to Chromatography. *Transactions of the Faraday Society*, **51**(11), 1540–1551.
- Glueckauf, E., & Coates, J. I. 1947. Theory of Chromatography .4. the Influence of Incomplete Equilibrium on the Front Boundary of Chromatograms and on the Effectiveness of Separation. *Journal of the Chemical Society*, 1315–1321.
- Gunter, B.H. 1993. How Statistical Design Concepts Can Improve Experimentation in the Physical Sciences. *Computers in Physics*, **7**(3), 262–272.
- Haber, J. 1997. *Studies in Surface Science and Catalysis*, **110**, 1.
- Hedlund, Jonas, Schoeman, Brian J., & Sterte, Johan. 1997. Synthesis of ultra thin films of molecular sieves by the seed film method. *Studies in Surface Science and Catalysis*, **105**, 2203–2210.
- Hedlund, Jonas, Mintova, Svetlana, & Sterte, Johan. 1999. Controlling the preferred orientation in silicalite-1 films synthesized by seeding. *Microporous and Mesoporous Materials*, **28**(1), 185–194.
- Hedlund, Jonas, Ohrman, Olov, Msimang, Velaphi, van Steen, Eric, Bohringer, Walter, Sibya, Sifiso, & Moller, Klaus. 2004. The synthesis and testing of thin film ZSM-5 catalysts. *Chemical Engineering Science*, **59**(13), 2647–2657.

- Himmelblau, D.M. 1970. *Process analysis by statistical methods*. New York: Wiley.
- Hopper, M.J. 1978. *Harwell subroutine library : a catalogue of subroutines*. Harwell: Computer Science and Systems Division and the Reprographic Department, United Kingdom Atomic Energy Authority.
- Huften, J. R., & Danner, R. P. 1993. Chromatographic Study of Alkanes in Silicalite - Equilibrium Properties. *AIChE Journal*, **39**(6), 954–961.
- Hunter, W. G., & Mezaki, R. 1967. An Experimental Design Strategy for Distinguishing among Rival Mechanistic Models - an Application to Catalytic Hydrogenation of Propylene. *Canadian Journal of Chemical Engineering*, **45**(4), 247–249.
- IUPAC. 1997. *Compendium of Terminology*.
- Jansen, J. C., Koegler, J. H., van Bekkum, H., Calis, H. P. A., van den Bleek, C. M., Kapteijn, F., Moulijn, J. A., Geus, E. R., & van der Puil, N. 1998. Zeolitic coatings and their potential use in catalysis. *Microporous and Mesoporous Materials*, **21**(4-6), 213–226.
- Jaswal, I. S., Mann, R. F., Juusola, J. A., & Downie, J. 1969. Vapor-Phase Oxidation of Benzene over a Vanadium Oxide Catalyst. *Canadian Journal of Chemical Engineering*, **47**(3), 284.
- Jedrzejak, A., & Paderewski, M. 1988. Investigation of adsorption-desorption cycles in a fixed bed of adsorbent. *International chemical engineering*, **28**(4), 707–712.
- Ji, L., Lin, J., & Zeng, H. C. 2000. Metal-support interactions in Co/Al₂O₃ catalysts: A comparative study on reactivity of support. *Journal of Physical Chemistry B*, **104**(8), 1783–1790.
- Kang, Chan-Soon, You, Young-Jae, Kim, Ki-Joong, Kim, Tae-hee, Ahn, Seong-Jun, Chung, Kyong-Hwan, Park, Nam-Cook, Kimura, Shoichi, & Ahn, Ho-Geun. 2006. Selective catalytic reduction of NO_x with propene over double wash-coat monolith catalysts. *Catalysis Today*, **111**(3-4), 229–235.
- Kapteijn, F., & Moulijn, J. A. 1997. Laboratory Catalytic Reactors: Aspects of Catalyst Testing. *Pages 1359–1376 of: Ertl, G., Knözinger, H., & Weitkamp, J. (eds), Handbook of Heterogeneous Catalysis*, vol. 3. Weinheim, Germany: VCH.
- Kärger, J., & Ruthven, D. M. 1992. *Diffusion in zeolites and other microporous solids*. New York: John Wiley & Sons, Inc.
- Khan, Faisal I., & Ghoshal, Alok Kr. 2000. Removal of Volatile Organic Compounds from polluted air. *Journal of Loss Prevention in the Process Industries*, **13**(6), 527–545.
- Kittrell, J.R. 1970. *Advances in Chemical Engineering*, **8**, 98.
- Kiwi-Minsker, L., & Renken, A. 2005. Microstructured reactors for catalytic reactions. *Catalysis Today*, **110**(1-2), 2–14.
- Kokotailo, G. T., & Meier, W. M. 1979. Pentasil Family of High Silica Crystalline Materials. *Page 133 of: Townsend, R. P. (ed), The properties and applications of zeolites*, vol. Special Publ. No. 33. London: The Chemical Society.

- Kolb, Gunther, & Hessel, Volker. 2004. Micro-structured reactors for gas phase reactions. *Chemical Engineering Journal*, **98**(1-2), 1–38.
- Kolodziej, Andrzej, & Lojewska, Joanna. 2005. Optimization of structured catalyst carriers for VOC combustion. *Catalysis Today*, **105**(3-4), 378–384.
- Kondratenko, EV, & Perez-Ramirez, J. 2006. Mechanism and Kinetics of Direct N₂O Decomposition over Fe-MFI Zeolites with Different Iron Speciation from Temporal Analysis of Products. *American Chemical Society*, **published on the web**.
- Kullavanijaya, E., Trimm, D. L., & Cant, N. W. 2000. Adsocat: adsorption/catalytic combustion for VOC and odour control. *Studies in Surface Science and Catalysis*, **130A**(International Congress on Catalysis, 2000, Pt. A), 569–574.
- Kullavanijaya, Emwajee, Cant Noel, W., & Trimm David, L. 2002. The treatment of binary VOC mixtures by adsorption and oxidation using activated carbon and a palladium catalyst. *Journal of Chemical Technology and Biotechnology*, **77**(4), 473–480.
- Kummer, J. T. 1980. Catalysts for automobile emission control. *Progress in Energy and Combustion Science*, **6**(2), 177–199.
- Langmuir, Irving. 1918. The Adsorption of Gases on Plane Surfaces of Glass, Mica and Platinum. *J. Am. Chem. Soc.*, **40**(9), 1361–1403.
- Lassinantti, Magdalena, Jareman, Fredrik, Hedlund, Jonas, Creaser, Derek, & Sterte, Johan. 2001. Preparation and evaluation of thin ZSM-5 membranes synthesized in the absence of organic template molecules. *Catalysis Today*, **67**(1-3), 109–119.
- Lee, K. W., & Liu, B. Y. H. 1982. Theoretical-Study of Aerosol Filtration by Fibrous Filters. *Aerosol Science and Technology*, **1**(2), 147–161.
- Levenspiel, Octave. 1996. *The Chemical Reactor Omnibook*. Fifth edn. Corvallis, Oregon: OSU Book Stores, Inc.
- Liaw, C. H., Wang, J. S. P., Greenkorn, R. A., & Chao, K. C. 1979. Kinetics of Fixed-Bed Adsorption - New Solution. *Aiche Journal*, **25**(2), 376–381.
- Lide, David R. 2001. *CRC Handbook of Chemistry and Physics*. 82nd edn. Boca Raton: CRC Press.
- Louis, B., Reuse, P., Kiwi-Minsker, L., & Renken, A. 2001a. Synthesis of ZSM-5 coatings on stainless steel grids and their catalytic performance for partial oxidation of benzene by N₂O. *Applied Catalysis A-General*, **210**(1-2), 103–109.
- Louis, B., Kiwi-Minsker, L., Reuse, P., & Renken, A. 2001b. ZSM-5 coatings on stainless steel grids in one-step benzene hydroxylation to phenol by N₂O: Reaction kinetics study. *Industrial & Engineering Chemistry Research*, **40**(6), 1454–1459.
- Louis, B., Subrahmanyam, C., Kiwi-Minsker, L., Viswanathan, B., Buffat, P. A., & Renken, A. 2002. Synthesis and characterization of MCM-41 coatings on stainless steel grids. *Catalysis Communications*, **3**(4), 159–163.

- Maier, Wilhelm F., & Schlangen, Jorg W. A. 1993. Efficiency of air cleaning by catalytic afterburning with electric heaters. *Catalysis Today*, **17**(1-2), 225–233.
- Majer, V., & Svoboda, V. 1985. *Enthalpies of Vaporization of Organic Compounds: A Critical Review and Data Compilation*. Oxford: Blackwell Scientific Publications.
- Mars, P., & van Krevelen, DW. 1954. Oxidations Carried out by the Means of Vanadium Oxide Catalysts. *Chem Eng Technol*, **3** (special supplement), 41–59.
- Matatov-Meytal, Yu., & Sheintuch, M. 2002. Catalytic fibers and cloths. *Applied Catalysis A: General*, **231**(1-2), 1–16.
- Maxwell, I. E. 1996. *Studies in Surface Science and Catalysis*, **101**, 1.
- McCabe, W. L., Smith, J. C., & Harriott, P. 1993. *Unit Operations of Chemical Engineering*. New York: McGraw-Hill, Inc.
- McInnes, R.G. 1995. Explore New Options for Hazardous Air Pollutant Control. *Chemical Engineering Progress*, 36–48.
- Meeyoo, V., Lee, J. H., Trimm, D. L., & Cant, N. W. 1998. Hydrogen sulfide emission control by combined adsorption and catalytic combustion. *Catalysis Today*, **44**(1-4), 67–72.
- Meier, W. M., Olson, D. H., & Baerlocher, Ch. 1996. *Atlas of zeolite structure types*. 4th rev. ed edn. London: Elsevier.
- Meille, Valerie. 2006. Review on methods to deposit catalysts on structured surfaces. *Applied Catalysis A: General*, **315**, 1–17.
- Meindersma, G. W., & de Haan, A. B. 2002. Economical feasibility of zeolite membranes for industrial scale separations of aromatic hydrocarbons. *Desalination*, **149**(1-3), 29–34.
- Mies, M. J. M., van den Bosch, J. L. P., Rebrov, E. V., Jansen, J. C., de Croon, M. H. J. M., & Schouten, J. C. 2005. Hydrothermal synthesis and characterization of ZSM-5 coatings on a molybdenum support and scale-up for application in micro reactors. *Catalysis Today*, **110**(1-2), 38–46.
- Monnerat, B., Kiwi-Minsker, L., & Renken, A. 2001. Hydrogen production by catalytic cracking of methane over nickel gauze under periodic reactor operation. *Chemical Engineering Science*, **56**(2), 633–639.
- Morigami, Y., Kondo, M., Abe, J., Kita, H., & Okamoto, K. 2001. The first large-scale pervaporation plant using tubular-type module with zeolite NaA membrane. *Separation and Purification Technology*, **25**(1-3), 251–260.
- Morlec, Jean, Travers, Christine, & Dezael, Claude. 1993. *Treatment of malodorous and/or toxic gases*. Patent no. 2691375.
- Narayanan, S., Sultana, Asima, Meriaudeau, P., & Naccache, C. 1996. Synthesis, characterization and evaluation of ZSM-5 zeolites of different SiO₂/Al₂O₃ with and without template. *Catalysis: Modern Trends, [Papers presented at the National Symposium on Catalysis], 12th Bombay, Dec. 19-22, 1994*, 204–208.

- Neyestanaki, A. K., & Lindfors, L. E. 1995. Catalytic combustion of propane and natural gas over silica-fibre supported catalysts. *Combustion Science and Technology*, **111**, 303–320.
- Nijkamp, M.G., Raaymakers, J.E.M.J., van Dillen, A.J., & de Jong, K.P. 2001. Hydrogen storage using physisorption - materials demands. *Applied Physics A*, **72**(5), 619 – 623.
- Nikolajsen, K., Kiwi-Minsker, L., & Renken, A. 2006. Structured fixed-bed adsorber based on zeolite/sintered metal fibre for low concentration VOC removal. *Chemical Engineering Research & Design*, **84**(A7), 562–568.
- Nordin, A., Eriksson, L., & Ohman, M. 1995. No Reduction in a Fluidized-Bed Combustor with Primary Measures and Selective Noncatalytic Reduction - a Screening Study Using Statistical Experimental-Designs. *Fuel*, **74**(1), 128–135.
- O’Connell, M., Norman, A. K., Huttermann, C. F., & Morris, M. A. 1999. Catalytic oxidation over lanthanum-transition metal perovskite materials. *Catalysis Today*, **47**(1-4), 123–132.
- Ohrman, O., Nordgren, U., Hedlund, J., Creaser, D., & Sterte, J. 2001. Structured zeolite ZSM-5 coatings on ceramic packing materials. *Studies in Surface Science and Catalysis*, **135**(Zeolites and Mesoporous Materials at the Dawn of the 21st Century), 3200–3207.
- Patton, A., Crittenden, B. D., & Perera, S. P. 2004. Use of the linear driving force approximation to guide the design of monolithic adsorbents. *Chemical Engineering Research & Design*, **82**(A8), 999–1009.
- Perry, Robert H., Green, Don W., & Maloney, James O. 1997. *Perry’s Chemical Engineers’ Handbook*. 7th edn. New York: McGraw-Hill cop.
- Persson, A. E., Schoeman, B. J., Sterte, J., & Otterstedt, J. E. 1994. The synthesis of discrete colloidal particles of TPA-silicalite-1. *Zeolites*, **14**(7), 557–567.
- Pope, D., Walker, D. S., & Moss, R. L. 1976. Evaluation of cobalt oxide catalysts for the oxidation of low concentrations of organic compounds in air. *Atmospheric Environment*, **10**(11), 951–956.
- Ramarao, B. V., & Tien, C. 1989. On the Extension of Mass-Transfer J-Factor Correlation to the Collection Efficiency of Fibrous Filters. *Aerosol Science and Technology*, **11**(1), 58–64.
- Rebrov, E.V., De Croon, M.H.J.M., Schouten, J.C., Seijger, G.B.F., Calis, H.P.A., & Van den Bleek, C.M. 2001. The preparation of highly ordered single layer ZSM-5 coating on prefabricated stainless steel microchannels. *Applied Catalysis A: General*, **206**(1), 125–143.
- Reuse, P. 2003. *Production d’Hydrogène dans un Réacteur Microstructuré. Couplage Thermique entre le Steam Reforming et l’Oxydation Totale du Méthanol*. Ph.D., École Polytechnique Fédérale de Lausanne.
- Rosen, J. B. 1952. Kinetics of a Fixed Bed System for Solid Diffusion into Spherical Particles. *Journal of Chemical Physics*, **20**(3), 387–394.

- Rosen, J. B. 1954. General Numerical Solution for Solid Diffusion in Fixed Beds. *Industrial and Engineering Chemistry*, **46**(8), 1590–1594.
- Rouge, A. 2001. *Periodic Operation of a Microreactor for Heterogeneously Catalysed Reactions: The Dehydration of Isopropanol*. Ph.D., École Polytechnique Fédérale de Lausanne.
- Ruthven, D. M. 2001. Adsorption. *Pages 582–617 of: Kirk-Othmer Encyclopedia of Chemical Technology*, 5th edn., vol. 1. Hoboken, New Jersey: John Wiley & Sons, Inc.
- Ruthven, Douglas M. 1984. *Principles of Adsorption and Adsorption Processes*. New York: John Wiley & Sons, Inc.
- Salden, Axel, & Eigenberger, Gerhart. 2001. Multifunctional adsorber/reactor concept for waste-air purification. *Chemical Engineering Science*, **56**(4), 1605–1611.
- Satterfield, C. N. 1970. *Mass transfer in heterogeneous catalysis*. Cambridge, Massachusetts: M.I.T. Press.
- Satterfield, C. N. 1991. *Heterogeneous Catalysis in Industrial Practice*. 2nd edn. New York: McGraw-Hill.
- Satterfield, C. N., & Cortez, D. H. 1970. Mass Transfer Characteristics of Woven-Wire Screen Catalysts. *Industrial & Engineering Chemistry Fundamentals*, **9**(4), 613.
- Satterfield, C.N. 1980. *Heterogeneous Catalysis in Practice*. Chemical Engineering Series. New York: McGraw-Hill.
- Schoubye, Peter Carl Semestedt. 1980 (5/6/1980). *Method and apparatus for the removal of oxidizable pollutants from gases*. Patent no. GB2051761 (IPC Class).
- Seijger, G. B. F., Oudshoorn, O. L., van Kooten, W. E. J., Jansen, J. C., van Bekkum, H., van den Bleek, C. M., & Calis, H. P. A. 2000. In situ synthesis of binderless ZSM-5 zeolitic coatings on ceramic foam supports. *Microporous and Mesoporous Materials*, **39**(1-2), 195–204.
- Shimadzu-Corporation. *Atomic Absorption Spectrophotometry Cook Book*.
- Shiraishi, Fumihide, Yamaguchi, Shunsuke, & Ohbuchi, Yusuke. 2003. A rapid treatment of formaldehyde in a highly tight room using a photocatalytic reactor combined with a continuous adsorption and desorption apparatus. *Chemical Engineering Science*, **58**(3-6), 929–934.
- Shore, Lawrence, Farrauto, Robert J., Deeba, Michel, Lampert, Jordan K., & Heck, Ronald M. 2001. *Compositions for abatement of volatile organic compounds and apparatus and methods using the same*. Patent no. 0143854 or US6319484.
- Sircar, S., & Hufton, J. R. 2000. Why does the Linear Driving Force model for adsorption kinetics work? *Adsorption-Journal of the International Adsorption Society*, **6**(2), 137–147.
- Sjoblom, Jonas, Papadakis, Klaus, Creaser, Derek, & Odenbrand, C. U. Ingemar. 2005. Use of experimental design in development of a catalyst system. *Catalysis Today*, **100**(3-4), 243–248.

- Sokolovskii, V. D. 1990. Principles of Oxidative Catalysis on Solid Oxides. *Catalysis Reviews-Science and Engineering*, **32**(1-2), 1–49.
- Spivey, J. J. 1987. Complete Catalytic-Oxidation of Volatile Organics. *Industrial & Engineering Chemistry Research*, **26**(11), 2165–2180.
- Spivey, J. J., & Butt, J. B. 1992. Literature review: deactivation of catalysts in the oxidation of volatile organic compounds. *Catalysis Today*, **11**(4), 465–500.
- Stefanescu, A., van Veen, A.C., Duval-Brunei, E., & Mirodatos, C. 2006. Wall coating of a Ni/Al₂O₃ catalyst for steam reforming of fuel in an on-board processor. *Pages 311–12 of: Abstracts, Book of (ed), 19th International Symposium on Chemical Reaction Engineering, ISCRE19*. Potsdam/Berlin, Germany: DECHEMA.
- Sterte, J., Hedlund, J., Creaser, D., Ohrman, O., Zheng, W., Lassinantti, M., Li, Q. H., & Jareman, F. 2001. Application of the seed-film method for the preparation of structured molecular sieve catalysts. *Catalysis Today*, **69**(1-4), 323–329.
- Sun, M. S., Shah, D. B., Xu, H. H., & Talu, O. 1998. Adsorption equilibria of C-1 to C-4 alkanes, CO₂, and SF₆ on silicalite. *Journal of Physical Chemistry B*, **102**(8), 1466–1473.
- Tagliabue, M., Carluccio, L. C., Ghisletti, D., & Perego, C. 2003. Multivariate approach to zeolite synthesis. *Catalysis Today*, **81**(3), 405–412.
- Takeuchi, Yasushi, Iwamoto, Hayato, Miyata, Norio, Asano, Seiichi, & Harada, Masashi. 1995. Adsorption of 1-butanol and p-xylene vapor and their mixtures with high silica zeolites. *Separations Technology*, **5**(1), 23–34.
- Teller, Aaron J. 2000. *Integrated catalytic/adsorption process for destroying volatile organic compounds*. Patent no. 6051199.
- Thomas, H. C. 1944. Heterogeneous ion exchange in a flowing system. *Journal of the American Chemical Society*, **66**, 1664–1666.
- Topsøe, Haldor. 2006.
<http://www.topsoe.com/site.nsf/all/BBNN-5PFH76?OpenDocument>.
- Tornqvist, A., Skoglundh, M., Thormahlen, P., Fridell, E., & Jobson, E. 1997. Low temperature catalytic activity of cobalt oxide and ceria promoted Pt and Pd: -influence of pretreatment and gas composition. *Applied Catalysis B: Environmental*, **14**(1-2), 131–145.
- Treacy, M.M.J., & Higgins, J.B. 2001. *Collection of simulated XRD powder patterns for zeolites*. 4th rev. ed. edn. Amsterdam: Elsevier.
- Tribolet, P. 2006. *Nanofibres de carbone sur filtre métallique comme support catalytique structuré*. Ph.D., École Polytechnique Fédérale de Lausanne.
- Tribolet, P., & Kiwi-Minsker, L. 2005a. Carbon nanofibers grown on metallic filters as novel catalytic materials. *Catalysis Today*, **102-103**, 15–22.

- Tribolet, P., & Kiwi-Minsker, L. 2005b. Palladium on carbon nanofibers grown on metallic filters as novel structured catalyst. *Catalysis Today*, **105**(3-4), 337–343.
- Tsai, M. C., Wang, S. S., Yang, R. T., & Desai, N. J. 1985. Temperature-Swing Separation of Hydrogen Methane Mixture. *Industrial & Engineering Chemistry Process Design and Development*, **24**(1), 57–62.
- Tucker, W. Gene. 2004. Air Pollution and Control, Indoor. *Pages 816–839 of: Seidel, A. (ed), Kirk-Othmer Encyclopedia of Chemical Technology*, 5th edn., vol. 1. Hoboken, New Jersey: John Wiley & Sons, Inc.
- Tyuliev, G., & Angelov, S. 1988. The nature of excess oxygen in $\text{Co}_3\text{O}_{4+\epsilon}$. *Applied Surface Science*, **32**(4), 381–391.
- Ulla, M. A., Mallada, R., Coronas, J., Gutierrez, L., Miro, E., & Santamaria, J. 2003. Synthesis and characterization of ZSM-5 coatings onto cordierite honeycomb supports. *Applied Catalysis a-General*, **253**(1), 257–269.
- Valentini, Michela, Groppi, Gianpiero, Cristiani, Cinzia, Levi, Marinella, Tronconi, Enrico, & Forzatti, Pio. 2001. The deposition of $[\gamma]\text{-Al}_2\text{O}_3$ layers on ceramic and metallic supports for the preparation of structured catalysts. *Catalysis Today*, **69**(1-4), 307–314.
- Vermeulen, T. 1953. Theory for Irreversible and Constant-Pattern Solid Diffusion. *Industrial and Engineering Chemistry*, **45**(8), 1664–1670.
- Vogtlander, P. H., & Bakker, C. A. P. 1963. An Experimental Study of Mass Transfer from a Liquid Flow to Wires and Gauzes. *Chemical Engineering Science*, **18**(9), 583–589.
- Vorob'eva, M. P., Greish, A. A., Ivanov, A. V., & Kustov, L. M. 2000. Preparation of catalyst carriers on the basis of alumina supported on metallic gauzes. *Applied Catalysis A: General*, **199**(2), 257–261.
- Wan, Y. S. S., Gavriilidis, A., & Yeung, K. L. 2003. 1-Pentene epoxidation in titanium silicalite-1 microchannel reactor - Experiments and modelling. *Chemical Engineering Research & Design*, **81**(A7), 753–759.
- Wan, Yu Shan Susanna, Chau, Joseph Lik Hang, Gavriilidis, Asterios, & Yeung, King Lun. 2001. Design and fabrication of zeolite-based microreactors and membrane microseparators. *Microporous and Mesoporous Materials*, **42**(2-3), 157–175.
- Weckhuysen, B. M., Verberckmoes, A. A., Debaere, J., Ooms, K., Langhans, I., & Schoonheydt, R. A. 2000. In situ UV-Vis diffuse reflectance spectroscopy - on line activity measurements of supported chromium oxide catalysts: relating isobutane dehydrogenation activity with Cr-speciation via experimental design. *Journal of Molecular Catalysis a-Chemical*, **151**(1-2), 115–131.
- Weisz, P. B. 1973. Zeolites - New Horizons in Catalysis. *Chemtech*, 498–505.
- Wloch, E., Lukaszczyk, A., Zurek, Z., & Sulikowski, B. 2006. Synthesis of ferrierite coatings on the FeCrAl substrate. *Catalysis Today*, **114**(2-3), 231–236.

- Wyrwalski, F., Lamonier, J. F., Siffert, S., Gengembre, L., & Aboukais, A. 2007. Modified Co₃O₄/ZrO₂ catalysts for VOC emissions abatement. *Catalysis Today*, **119**(1-4), 332–337.
- Xiao, Jirong, & Wei, James. 1992a. Diffusion mechanism of hydrocarbons in zeolites—I. Theory. *Chemical Engineering Science*, **47**(5), 1123–1141.
- Xiao, Jirong, & Wei, James. 1992b. Diffusion mechanism of hydrocarbons in zeolites—II. Analysis of experimental observations. *Chemical Engineering Science*, **47**(5), 1143–1159.
- Yang, J. Z., & Renken, A. 2000. Heavy metal adsorption to a chelating resin in a binary solid fluidized bed. *Chemical Engineering and Technology*, **23**(11), 1007–1012.
- Yang, R. T. 1997. *Gas Separation by Adsorption Processes*. Series on chemical Engineering, vol. 1. London: Imperial college Press.
- Yang, R. T., & Doong, S. J. 1985. Gas Separation by Pressure Swing Adsorption - a Pore-Diffusion Model for Bulk Separation. *Aiche Journal*, **31**(11), 1829–1842.
- Yon, Carmen M., & Sherman, John D. 2004. Adsorption, Gas Separation. *Pages 617–663 of: Seidel, A. (ed), Kirk-Othmer Encyclopedia of Chemical Technology*, 5th edn., vol. 1. Hoboken, New Jersey: John Wiley & Sons, Inc.
- Yoshida, F., Ramaswami, D., & Hougen, O. A. 1962. Temperatures and Partial Pressures at the Surfaces of Catalyst Particles. *AIChE Journal*, **8**(1), 5–11.
- Yu Yao, Yung-Fang. 1974. The oxidation of hydrocarbons and CO over metal oxides : III. Co₃O₄. *Journal of Catalysis*, **33**(1), 108–122.
- Yu Yao, Yung-Fang. 1975. The oxidation of CO and C₂H₄ over metal oxides : V. SO₂ effects. *Journal of Catalysis*, **39**(1), 104–114.
- Yuranov, I., Dunand, N., Kiwi-Minsker, L., & Renken, A. 2002. Metal grids with high-porous surface as structured catalysts: preparation, characterization and activity in propane total oxidation. *Applied Catalysis B: Environmental*, **36**(3), 183–191.
- Yuranov, I., Kiwi-Minsker, L., & Renken, A. 2003. Structured combustion catalysts based on sintered metal fibre filters. *Applied Catalysis B: Environmental*, **43**(3), 217–227.
- Yuranov, I., Renken, A., & Kiwi-Minsker, L. 2005. Zeolite/sintered metal fibers composites as effective structured catalysts. *Applied Catalysis a-General*, **281**(1-2), 55–60.
- Zagoruiko, Andrey N., Kostenko, Oleg V., & Noskov, Alexander S. 1996. Development of the adsorption-catalytic reverse-process for incineration of volatile organic compounds in diluted waste gases. *Chemical Engineering Science*, **51**(11), 2989–2994.
- Zhu, W., Kapteijn, F., & Moulijn, J. A. 2000a. Adsorption of light alkanes on silicalite-1: Reconciliation of experimental data and molecular simulations. *Physical Chemistry Chemical Physics*, **2**(9), 1989–1995.
- Zhu, W., Kapteijn, F., & Moulijn, J. A. 2000b. Equilibrium adsorption of light alkanes in silicalite-1 by the inertial microbalance technique. *Adsorption-Journal of the International Adsorption Society*, **6**(2), 159–167.

- Zwinkels, M. F. M., Jaras, S. G., Menon, P. G., & Griffin, T. A. 1993. Catalytic Materials for High-Temperature Combustion. *Catalysis Reviews-Science and Engineering*, **35**(3), 319–358.

Curriculum Vitae

EDUCATION

2003 - 2007 Ecole Polytechnique Federale de Lausanne, Switzerland
Ph.D. in Chemical Engineering
at the Laboratory of Chemical Reaction Engineering

1994 - 2002 The Technical University of Denmark, Kgs. Lyngby, Denmark
Master of Science in Chemical Engineering
Specialization: chemical engineering, chemical reactor simulation

1997 - 1998 Washington State University, Pullman, WA, USA
Exchange student in chemical engineering program

WORK EXPERIENCE

2003 - 2007 EPFL, Lausanne, Switzerland
Assistant/researcher

1999 Paul Scherrer Institute, Villigen, Switzerland
3 month internship

Papers

- K.M. Nikolajsen, L. Kiwi-Minsker and A. Renken. Structured Fixed-Bed Adsorber Based on Zeolite/Sintered Metal Fibre for Low Concentration VOC Removal. Chemical Engineering Research and Design, 84(A7): 562-568, 2006.

Oral Presentations

- K.M. Nikolajsen, L. Kiwi-Minsker and A. Renken. Novel Structured Adsorbent and Catalytic Material for the Removal of VOCs. CAMURE-5/ISMR-4, 15-18 June 2005, Portorož, Slovenia.

Posters

1. K.M. Nikolajsen, L. Kiwi-Minsker and A. Renken. Novel Structured Adsorber and Cobalt Oxide Catalysts for the Removal of Low Concentration VOCs. EUROPACAT 8, 26-31 August 2007, Turku/Åbo, Finland. *Accepted*.
2. K.M. Nikolajsen, L. Kiwi-Minsker and A. Renken. Novel Structured Adsorber and Cobalt Oxide Catalysts for the Removal of VOC. ISCRE19, 3-6 September 2006, Potsdam/Berlin, Germany.
3. K.M. Nikolajsen, L. Kiwi-Minsker and A. Renken. Novel Structured Adsorbent and Catalytic Material for the Removal of VOCs. CAMURE-5/ISMR-4, 15-18 June 2005, Portorož, Slovenia.
4. K.M. Nikolajsen, L. Kiwi-Minsker and A. Renken. Structured Fixed-Bed Adsorber Based on Zeolite/Sintered Metal Fiber for Low Concentration VOC Removal. Conférence universitaire de Suisse occidentale, Séminaire hors-ville en chimie inorganique et génie chimique, Modern Concepts for Environmentally Benign Synthesis, 11-15 September 2005, Villars, Switzerland.
5. K.M. Nikolajsen, L. Kiwi-Minsker and A. Renken. Novel Structured Adsorbent and Catalytic Material for Removal of VOCs. Conférence universitaire de Suisse occidentale, Séminaire hors-ville en chimie inorganique et génie chimique, Frontiers in Catalysis, 28 September - 2 October 2003, Champéry, Switzerland.